Development of optical coherence tomography for monitoring the glaucoma laser surgery

Masreshaw-Demelash Bayleyegn

UNIVERSITE PARIS-SUD

ÉCOLE DOCTORALE: STITS
Laboratoire Charles Fabry, Institut d'Optique

DISCIPLINE PHYSIQUE

THÈSE DE DOCTORAT

soutenue le 20/12/2012

par

Masreshaw-Demelash BAYLEYEGN

Tomographie par cohérence optique pour la chirurgie laser du glaucome

Directeur de thèse :   **Arnaud DUBOIS**   Professeur (Institut d'Optique)

<u>**Composition du jury**</u> :

Rapporteurs :   Benoît-Claude FORGET   Professeur (Université Paris-Descartes)
               Jean-Marc FRIGERIO   Professeur (Université Pierre et Marie Curie)
Examinateurs :   Gaël LATOUR   MC (Université Paris-Sud)
               Sandrine LEVEQUE-FORT   CR (HDR) (Université Paris-Sud)
               Karsten PLAMANN   Professeur (LOA, ENSTA ParisTech)

Dedication

*I wish to dedicate this dissertation and all my subsequent titles and achievements to my mother **Wudie Temesgen** and my father **Demelash Bayleyegn**. Gasha and Eme, I am very lucky and so proud to be your son; I love you forever!!!*

Acknowledgment

First of all, I would like to thank the dissertation committee **Arnaud DUBOIS (Prof)**, **Benoît-Claude FORGET (Prof), Jean-Marc FRIGERIO (Prof), Gaël LATOUR (PhD), Sandrine LEVEQUE-FORT (HDR)** and **Karsten PLAMANN (Prof)** for reviewing this report which testifies the doctoral research work that I did in the Biophotonics group of Laboratoire Charles Fabry – Institut d'Optique *Graduate School* (LCFIO).

It was a great honor and pleasure to be a PhD student in LCFIO, one of the leading research institutes of optics in Europe. And I would like to express my immense gratitude and respect specifically to my supervisor Professor **DUBOIS Arnaud** for his trust to offer me the PhD position in his team that has opened me the door for new opportunities. During the course of my PhD, despite of his busy schedules, he has maintained his invaluable discussion, supervision and advice. In parallel, he has also given me full autonomy of my PhD work. I also appreciate his special editing skills and immediate feedbacks that I used to receive during writing this dissertation and other scientific papers. I also thank and appreciate **Delphine SACCHET (PhD)** for the continuous support she offered me during my master internship which helped me build my confidence in setting up my own experimental setups afterwards. I wish to acknowledge **Houssine MAKHLOUF (PhD)** for bringing in an alternative numerical spectral calibration method and for his fruitful contribution during writing scientific papers.

I would like to thank **Patrick GEORGES (Laser group leader)** for his effort in securing my PhD grant and all the laser group research staffs for creating such a friendly research environment that helped me decide to stay in LCFIO for my PhD. I am also thankful to **Michael CANVA (Biophotonics group leader)** for all the administrative work he has done mainly during the last few months of my PhD.

Without a well-coordinated collaboration with other partners, this PhD work would have been incomplete. I therefore wish to acknowledge all partners of the NOUGAT project for their active participation. I would like to specifically thank **Karsten PLAMANN (OPS group leader, LOA)** for organizing and leading the NOUGAT project. My special gratitude and appreciation go to **Caroline CROTTI (PhD)** for her invaluable contribution for the success of the project, mainly for her role in coupling the laser surgery system with the OCT imaging system. Despite of her busy schedules, even after the project ended, she has remained

available all the time. She has always been very helpful in addressing all the issues I had concerning the laser surgery setup. I also wish to thank **Jean-Lou CHARLES (mechanics)** for the precise mechanical work that he did during coupling of the two systems. I also thank **Fatima ALAHYNE (Engineer)** for all the contributions she made during my efforts to control the galvanometric mirror. I also thank **Laura KOWALCZUK (PhD, Biologist)** for explaining and demonstrating me the parts of the eye by dissecting a pig eye.

Finally, I convey my collective and individual acknowledgements to all members of the Biophotonics group. I thank **Julien MOREAU (PhD)** for his kick-off explanation of LabView at start of my PhD. I also thank **Karen PERONI (PhD)** for taking a leading role in organizing my PhD defense. My special thanks go to **Maha CHAMTOURI (PhD student)** for being one of the few closest and best friends I ever made during my PhD stay, and I would like to take this opportunity to wish you all the best for your manuscript and the upcoming PhD defense. I also thank Antoine **FEDRERCI (PhD student)** for his kind and honest personality. With all the progresses that you are making on your experimental setup, I am sure that you will get good results soon and enjoy the remaining PhD work. I also thank the PhD students **Alexandra SEREDA, Mitradeep SARKAR** and **Nicolas FISZMAN** for all the fun we together had and I wish you all a successful career.

Last but not the least; I thank my family for their unconditional love and support. Nothing else can make me be happier than being part of a family with full of affection and trust! Above all, I would like thank the Almighty God for His divine intervention in my academic endeavor and for giving me all the ability, strength and endurance to be able to go through all the way and successfully accomplish my PhD!

Table of Contents

x

Abbreviations

ADC – Analog-to-Digital Converter

ALT – Argon Laser Trabeculoplasty

AM – Amplitude Modulation

ANR – Agence Nationale de la Recherche

ANSI – American National Standards Institute

BBO – Beta Barium Borate

CCD – Charge-Coupled Device

CNRS – Centre National de la Recherche Scientifique

CT – Computed Tomography

DR – Dynamic Range

ENSTA – École Nationale Supérieure de Techniques Avancées

FD-OCT – Fourier-Domain Optical Coherence Tomography

FOV – Field Of View

FWC – Full-Well Capacity

FWHM – Full Width at Half Maximum

GOI – Gated Optical image Intensifier

GPIB – General Purpose Interface Bus

GUI – Graphical user Interface

HMO – Health Maintenance Organization

IOP – Intraocular pressure

LASIK – Laser Assisted in-situ Keratomileusis

LBO – Lithium TriBOrate

LCI – Low Coherence Interferometry

LOA – Laboratoire d'Optique Appliquée

LSC – Line Scan Camera

LTP – Laser Trabeculoplasty

MFP – Mean Free Path

MRI – Magnetic Resonance Imaging

NA – Numerical Aperture

NIR – Near InfraRed

NOUGAT – Nouvel OUtil pour la chirurgie du Glaucome Assistée par laser femtoseconde et

Tomographie par cohérence optique

NPDS – Non-Penetrating Deep Sclerectomy

OCT – Optical Coherence Tomography

OPA – Optical parametric Amplification

OPD – Optical Path Difference

OPG – Optical Parametric Generation

PDT – Photodynamic therapy

PSF – Point-spread function

QE – Quantum Efficiency

SC – Schlemm's Canal

SD-OCT – Spectral-Domain Optical Coherence Tomography

SEM – Scanning Electron Microscope

SLD – Superluminescent Diode

SLT – Selective Laser Trabeculoplasty

SNR – Signal-to-Noise Ratio

SPD – Spectral Power Density

SS-OCT – Swept-source Optical Coherence Tomography

TD-OCT – Time-Domain Optical Coherence Tomography

TM – Trabecular Meshwork

TPSF – Temporal Point Spread Function

WLC – White Light Continuum

Introduction

This PhD thesis has been conducted within the framework of a project funded by the French National Research Agency entitled "NOUGAT". NOUGAT is an acronym that stands for "*Nouvel OUtil pour la chirurgie du Glaucome Assistée par laser femtoseconde et Tomographie par cohérence optique*" translated into English as "*new tool for glaucoma surgery assisted by femtosecond laser and optical coherence tomography*". The project has been funded by "l'Agence Nationale de la Recherche - ANR" (ANR-08-TECS-012, program TecSan) and run in collaboration by the following partners: Laboratoire d'Optique Appliquée (LOA, ENSTA ParisTech, École polytechnique, CNRS), Laboratoire Charles Fabry – Institut d'Optique *Graduate School*, the company "Amplitude Systèmes" and the *Laboratoire Biotechnologie et Œil* of the "Hôtel-Dieu" hospital and Paris Descartes University in Paris.

Owing to the advent of compact and convenient laser systems, biomedical optics has become a very active research field. This multidisciplinary field has triggered the establishment of collaboration among scientists, engineers and medical doctors to work together for the development of optical devices that will allow physicians and medical researchers to understand, detect and treat human diseases non-invasively. Today, lasers are widely used in clinics and hospitals not only for diagnostic purposes but also for performing laser therapy[1]. Most diagnostic optical imaging techniques that allow early detection of various diseases use lasers as a light source. Cancer treatment using photodynamic therapy (PDT), cardiovascular disease treatment using laser thrombolysis and treatment of macular degeneration using laser coagulation are, on the other hand, few examples where lasers can directly be used in treatment of diseases. Lasers are also being routinely and widely used by ophthalmologists for refractive surgery, an eye surgery that corrects common refractive errors of the human eye (myopia, hyperopia and astigmatism) in order to avoid the use of eye glasses or contact lenses. The most commonly performed all-laser refractive surgery is Femto-LASIK (Laser-Assisted *in-situ* Keratomileusis), a procedure where a *femtosecond laser* (instead of a mechanical *microkeratome*[2]) is used to create a corneal flap and then an *excimer laser* (instead of *cryolathe*[3]) is employed to perform a corneal ablation for reshaping the cornea in

---

[1] Laser therapy: any treatment using intense beams of light to precisely cut, burn, or destroy tissue.
[2] Microkeratome: an instrument with an oscillating steel blade.
[3] Cryolathe: a device used for freezing and grinding human cornea tissue to change its refractive power.

order to correct the refractive error. Because of a greater accuracy in flap size, shape and thickness, a corneal flap created by the Femto-LASIK procedure is considered by many ophthalmologists as a significant improvement over the traditional LASIK procedure that uses a microkeratome. In addition, the Femto-LASIK treatment does not need hospitalization and reduces the amount of medication.

Motivation

The success of femtosecond lasers in refractive surgery has motivated research activities in LOA and Institut d'Optique on the extension of this technology for the treatment of another form of eye disorder called glaucoma. Glaucoma is the damage of the optic nerve that is usually associated with an increased internal pressure of the eye. The disease can lead to a decreased field of vision and eventually to blindness. It is the second cause of blindness in the world with more than 80 million people affected (~ 1 million in France) and approximately 6 million blind. The standard clinical treatment of glaucoma, after unsuccessful administration of eyedrops, is performing incisional surgery. In this treatment method, the ophthalmologist uses a surgical tool to mechanically cut an artificial channel in the eye (usually through the sclera) in order to drain out some liquid and decrease the elevated eye pressure. However, due to post-surgical complications like wound healing and scarring, this conventional method has a low global success rate. In comparison, as ultrashort pulse laser surgery may be performed in volume and is *a priori* less invasive and less susceptible of causing scarring, glaucoma surgery using femtosecond laser would be a novel technique to supplement the conventional glaucoma surgery.

The challenge

Refractive error surgery involves performing incisions in a transparent cornea at shallow depth (~ 110 µm). Commercially available solid state lasers are routinely used for that purpose. On the other hand, for efficient laser treatment of glaucoma, one needs to send a laser beam through the strongly scattering tissues of sclera and focus it at a depth[4] of ~ 1 mm with enough power and good beam quality for the laser incision to happen. As a result, the development of all-laser-based tool for glaucoma treatment has been a major challenge mainly due to optical scattering and the complex nature of the glaucoma disease itself.

---

[4] This depth refers to the region in the limbus where the draining liquid experiences high resistance which leads to pressure rise in the eye and damage of the optic nerve (glaucoma).

Our approach

The development of a glaucoma laser surgery tool can be decomposed into two main tasks:
  i) Development of a surgery laser source itself
  ii) Development of an imaging system to monitor the on-going laser surgery in real-time

The aim of the NOUGAT project was to develop a new tool that uses an optimized ultrashort pulse laser to make the glaucoma surgery and an imaging system based on optical coherence tomography (OCT) to monitor the intervention in real-time. LOA has worked on the femtosecond laser optimization as well as laser incision experiments on healthy and pathological cornea and sclera. They have demonstrated that the laser incision depth in highly scattering sclera and pathological cornea can be enhanced by using an optimized femtosecond laser source at $1.65\,\mu m$ central wavelength. The Biophotonics group of Laboratoire Charles Fabry – Institut d'Optique, where I belong to, was in charge of developing a non-invasive and fast OCT system capable of resolving the Schlemm's[5] canal in order to monitor the laser surgery in real-time.

Scope

This PhD work was mainly about the development of the imaging system in the framework of the NOUGAT project. Under the supervision of Prof. Arnaud DUBOIS, I have been working on the development and utilization of Fourier-domain OCT (FD-OCT) for imaging the Schlemm's canal, the circular channel found nearly $800\,\mu m$ inside the strongly scattering corneal limbus where the laser surgery was intended to be performed for treating glaucoma. In collaboration with LOA, we have also worked on the coupling of the laser incision system with the OCT imaging system in order to demonstrate real-time imaging of the laser surgery in human cornea. Since my work has been mainly experimental, emphasis in this dissertation will be given to the technical issues and experimental aspects of FD-OCT. However, a great care has been taken during writing this dissertation to provide adequate theoretical background of OCT to the reader.

---

[5] A circular channel situated in the corneal limbus that plays an important role for controlling glaucoma. Laser surgery is intended to be performed in this region (see chapter 1, section 1.3).

Organization of the dissertation

This dissertation is organized in 5 chapters. The first chapter is intended to give a short overview of the human eye, glaucoma and its diagnosis and treatment methods. The chapter starts with an introduction to the structure of the human eye. The development of the most common types of glaucoma and parts of the eye that play a crucial role in treatment of glaucoma are presented. Some of the existing glaucoma treatment methods and their drawbacks are also mentioned. In this chapter, we also introduce the new method of glaucoma treatment that we have proposed in the NOUGAT project in order to supplement or replace the existing inefficient and risky conventional glaucoma surgery methods.

The second chapter is about the principles and techniques of OCT. To have an overall idea about what can be done with OCT, the comparison of OCT with other imaging systems is presented first, and some of the unique features of OCT are indicated. Starting from a simple two-wave interferometer, the basic theory and mathematical formulation of low-coherence interferometry is addressed. Qualitative explanation and mathematical derivation of the most important OCT parameters are given. The different types of OCT modalities are presented. As time-domain OCT (TD-OCT) was the first OCT to be invented, we evaluate TD-OCT based on the OCT parameters and indicate its limitations for applications that require fast imaging. Finally, a short overview of Fourier-domain OCT (FD-OCT) and its potential for real-time imaging is indicated.

The imaging system developed for the NOUGAT project was based on the FD-OCT modality. This is because FD-OCT is faster and more sensitive than TD-OCT. The detailed principle of spectral-domain OCT (SD-OCT), one of the two FD-OCT modalities, is discussed in detail in chapter 3. As SD-OCT is a spectrometer-based system, the design of an optimal spectrometer for high-resolution SD-OCT is an important step in the development of SD-OCT. A set of design procedures needed to develop SD-OCT is presented in this chapter.

In chapter 4, the experimental setup of the high-resolution SD-OCT developed in the laboratory is explained. Characterization of the system's performance is presented and compared to the theoretically predicted values. The experimental results of depth dependent degradation of axial resolution and sensitivity fall-off are also given. The importance of spectral calibration and zero padding for improving the sensitivity fall-off and axial resolution are demonstrated. A comparison of our system with a commercial FD-OCT working at the

same wavelength is presented. Finally, images of the Schlemm's canal and also of other samples are shown to illustrate the performance of the system.

In the last chapter, chapter 5, we present the demonstration of monitoring the laser incision in real-time using OCT. To do that, the surgical laser and the OCT imaging system were coupled. The technical details of coupling and the results obtained are the main subject of the chapter. Moreover, the role of optimizing the laser wavelength for enhancing the incision depth in the strongly scattering sclera and edematous cornea is mentioned. Looking at the laser-tissue interaction, the reasons why ultrashort lasers are preferred for our application are also explained in this chapter.

Finally, conclusion and perspectives constitute the last chapter of the dissertation. The main research outcomes are summarized, and the planned future work is indicated.

In the appendix part, the challenges of large-depth and high-resolution optical imaging in turbid media are presented. The concept of light attenuation due to absorption and scattering, and its fundamental limit on the depth of imaging in biological tissues are discussed. Various ways of enhancing the imaging depth including coherence-gating, as implemented in OCT, are highlighted.

Chapter 1 - Glaucoma: the disease and its treatment

1.1   Introduction

Sight is the most important sense used to observe and learn about the environment in which we live. The optical organ that gives us the sense of sight is the eye. To see an object, the light emitted by or reflected from the object should enter our eye. When such light rays enter the normal eye, it undergoes refractions by various optical interfaces before it is finally focused on the back lining of the eye (called the retina) that contains the light sensing tissues called the photoreceptor cells. When light is focused on the retina, the photoreceptor cells convert light rays into nerve impulses. These nerve impulses are then processed and transmitted to the visual centers of brain through the optic nerve for interpretation (as shown in Figure 1.1).
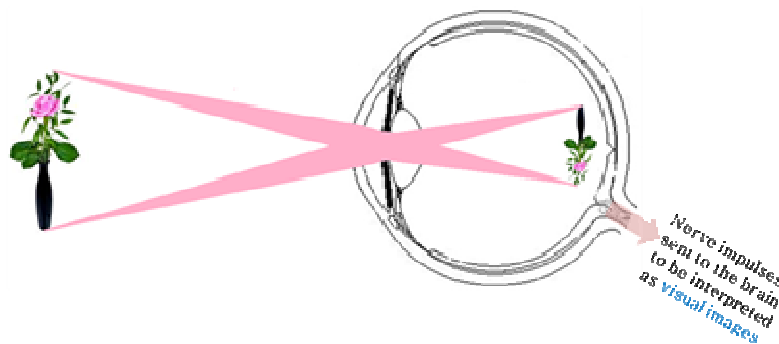
Figure 1.1 Image formation by the eye.

The signals received by the brain are eventually interpreted within fraction of a second as visual images to enable us to see the world. We can then not only tell the size, shape, color, and texture of an object but also we know how close it is, whether it's standing still or coming toward us, and how quickly it's moving, etc.

A group of eye disorders that damages the retina in general and causes a visual impairment is collectively called glaucoma. Glaucoma is a complicated eye disorder that may take as short as few days or as long as several years for the damage to be noticeable. It is the second leading cause of blindness in the world. To help understand the development, diagnosis and treatment of glaucoma, a short overview of the structure of the eye is presented below.

1.2   The structure of the eye

The human eye is a sophisticated sensing organ which allows the detection of light and the transmission of nerve impulses to the brain. While its structure is amazingly complex, the size of the entire eyeball is small with an approximate sagittal diameter or length of 23–24 mm and a transverse diameter of 23 mm. Figure 1.2 shows the structure of human eye and the main optical components.

The cornea and sclera together form the supporting wall of the eyeball. The cornea is the transparent front part of the eyeball which covers the iris and pupil. It is the window of the eye. A tear film normally coats the cornea, keeping the eye moist. The sclera is the white part of the eye that is continuous with the cornea. It is a non-transparent, dense, fibrous outer coating that forms the posterior five sixths of the outer coating of the eyeball. The sclera is perforated by numerous nerves, blood vessels and the optic nerve, and is covered by the bulbar conjunctiva and the episclera. The episclera is situated immediately under the bulbar conjunctiva and is rich with blood vessels which nourish the underlying sclera [1].
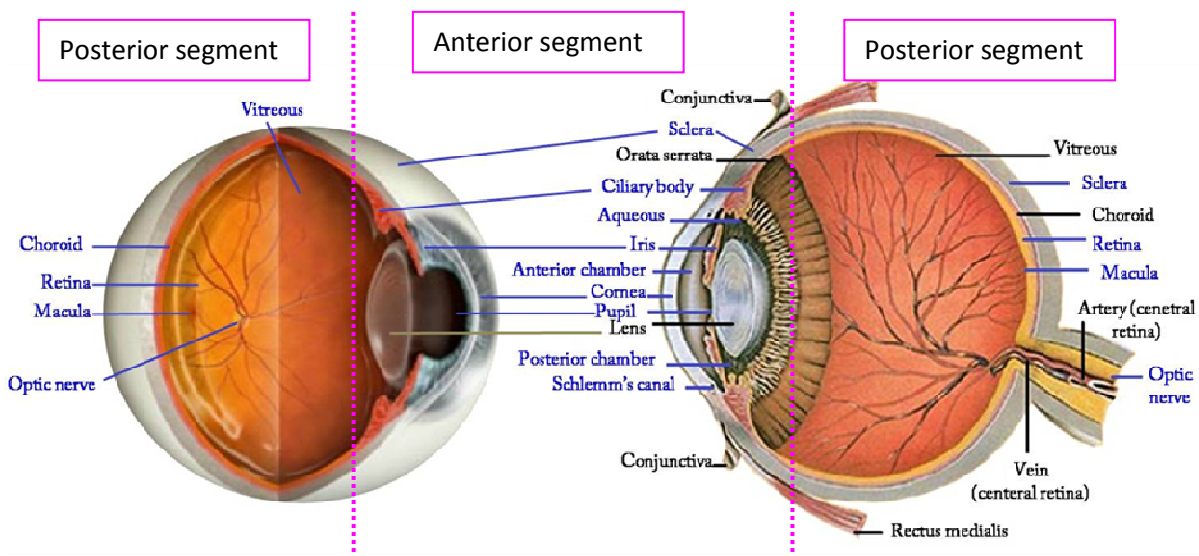
Figure 1.2 Structure of human eye [2]. The parts of the eye involved in glaucoma are marked in blue color.

The inside part of the eye can be categorized into two segments: anterior and posterior. The anterior segment is the front one-third of the eye that includes the front eye structures such as the cornea, iris ciliary body and the lens. The anterior segment is further divided into two chambers: the anterior and the posterior. The iris separates the anterior chamber from the posterior chamber. The anterior chamber is the fluid space between the cornea and the iris, and the posterior chamber is located between the iris and the crystalline lens. The iris is a thin

circular structure behind the cornea. It gives the color of the eye (as blue, brown etc) and controls the size of the pupil, the opening in the middle of the iris that appears black. Depending on the brightness of illumination, the muscles attached to the iris expand and contract automatically to adjust size of the pupil and control the amount of light reaching the retina. In bright light, the pupil gets narrower and in dim light it widens. The pupil also gets smaller during focusing for near vision to sharpen the focus by reducing aberration. The support of the iris is the ciliary body. The ligaments (called zonule fibers) that are used to suspend the transparent crystalline lens are also attached to the ciliary body. Depending on the distance of the objects that we are looking at, these suspensory ligaments contract or relax to change the focal length of the biconvex lens and fine-tune the focus. This dynamic accommodation allows the human eye to focus on objects at various distances and to form a sharp real image on the retina (the light sensor).

It is important to mention here that the lens is not the only refracting element involved in image formation. When light enters the normal eye, it first undergoes refraction at the cornea. The cornea is in fact the first and the most powerful refracting element of the optical system of the eye. It contributes 2/3 of the optical power of the eye, while the crystalline lens contributing to the remaining 1/3 (see table 1.1).

Table 1.1 Optical characteristics of the main elements of human eye involved in image formation [3].

Structures of the eye	Anterior radius of curvature	Posterior radius of curvature	Focusing power	Refractive index
Cornea	7.8 mm	6.8 mm	43 diopter	1.377
Aqueous humor	……	……	……	1.337
Crystalline lens	10 mm	6 mm	20 diopter	1.413
Vitreous humor	……	……	……	1.336

The cornea along with the tear film has an optical power of approximately 43 diopters and lens has 20 diopters[6]. The total convergence power of the eye is 58.7 diopters. It is approximately 4 diopters less than the sum of the individual powers ($43 + 20 = 63$) due to the distance between the cornea and the lens (depth of the anterior chamber) [4]. Even though the cornea contributes to most of the optical power of the eye, it has a fixed focal length. This explains why refractive eye surgery is often done on cornea using excimer lasers to reshape the curvature of the cornea and modify its refractive state to reduce or cure common vision

---

[6] The optical power of a lens or curved mirror, measured in units of diopter (m^{-1}), is given as the reciprocal of the focal length f' (1/f') where f' is in meters.

disorders such as myopia (nearsightedness), hyperopia (farsightedness) and astigmatism.

In addition to supporting the iris and suspensory ligaments, the ciliary body also constantly produces a fluid called aqueous humor. It is secreted to the posterior chamber and reaches the anterior chamber via the pupil of the eye and fills both chambers of the anterior segment of the eye. The fluid is responsible for providing nourishment to the front eye structures, removing waste products and maintaining the pressure of the eye. The intersection of the iris and the cornea is called the drainage angle. It is in this location that most of the fluid leaves the eye through the trabecular meshwork, mesh-like porous structure found next to the anterior chamber that permits the aqueous humor to drain from the eye and flow into a canal called Schlemm's canal. Connected to several veins, the role of the Schlemm's canal is to allow proper fluid drainage and maintain a healthy eye pressure. Most glaucoma cases happen when this fluid is not properly removed from the eye, causing elevation of eye pressure that will ultimately damage the optic nerve (see section 1.3.2).

The posterior segment corresponds to the posterior two-thirds of the eye located behind the anterior segment. It includes the vitreous chamber (a large cavity filled with non-refracting gel-like structure), the retina, choroid and optic nerve. The retina is a lining of light sensitive-tissues (photoreceptor cells) at the back of the eye. The retina has similar function as photographic film of traditional cameras (or electronic sensors of digital cameras).The outer layers of the retina are supplied with oxygen and nourishment by the choroid, a vascular layer that lies between retina and sclera. Close to center of the retina, we find an oval shaped highly pigmented yellow spot called the macula. Near its center, the macula consists of the fovea that contains the largest concentration of cone cells responsible for central and high-resolution vision. In human eye, the retina is composed of a millions of specialized light sensitive photoreceptor cells called rods and cones. Rods are responsible for peripheral and dim light vision. They provide black-and-white vision. Cones provide central, bright light, fine detail vision. They support perception of color. Central retina is cone-dominated whereas peripheral retina is rod-dominated. The light received by these photoreceptor cells is converted into nerve impulses, which are then processed and sent through the nerve fibers to the visual region of the brain to be interpreted as visual images. The nerve fibers leave the eyeball at the optic disk (optic nerve head) and reach the brain through the optic nerve. The optic nerve is part of the central nervous system and is responsible for connecting the retina to the brain. It is very delicate and is susceptible for permanent damage with a slight change in the internal

pressure of the eye. Any damage to the optic nerve affects transmission of these signals and hence causes visual impairment. Such eye disorder is called glaucoma.

1.3 Glaucoma

Glaucoma refers to a group of eye disorders characterized by the damage of the optic nerve and can lead to a decreased field of vision and eventually blindness. When damage to the optic nerve occurs, blind spots develop in the visual field of the eye. Blind spots are like blind CCD pixels of a digital camera. As blind spots lack light detecting photoreceptor cells, light striking the blind spots will not generate nerve impulses and fails to deliver the corresponding information to the brain. Hence the information falling on the blind spots is in fact lost. The damage of the optic nerve often starts at periphery, leading to a gradual decreasing of field of vision. If it continues uncontrolled, glaucoma can progressively damage the central vision and possibly lead to total blindness eventually. Glaucoma is one of the main causes of blindness in the world. Globally, 110 million people are affected (~ 1 million in France) by glaucoma and as many as 6 million individuals are totally blind in both eyes from this disease [3].

1.3.1 Risk factors

The exact cause of optic nerve damage from glaucoma is not fully understood, but it is associated with some mechanical compression and/or decreased blood flow of the optic nerve. While everyone is at risk for glaucoma, certain people are at a much higher risk and need to be checked more frequently by their eye doctor. Risk factors for glaucoma include history of elevated intraocular pressure, age, family history of glaucoma, history of injury to the eye, race, thin cornea, genetics, diabetes, high blood pressure, myopia, hyperopia, etc. Most cases of glaucoma are usually associated with an elevated intraocular pressure (IOP) of the eye.

1.3.1.1 Elevation of IOP

The major risk factor of most glaucoma cases, and the focus of its treatment, is increased IOP. But it does not mean that a person with normal IOP is free from developing glaucoma. Usually, an elevated IOP above the normal physiological range (8-22 mm Hg) and its fluctuation can lead to the damage of the delicate optic nerve. This pressure elevation results from extra accumulation of aqueous humor in the front eye. Aqueous humor is a clear natural fluid (similar to blood plasma) that is responsible for providing nourishment to the front eye structures, removing waste products and maintaining the IOP as well shape of the eye. Nutrition of the eye structures and maintenance of IOP are critical for a normal visual process.

Aqueous humor is continuously secreted in the ciliary body on a diurnal curve with a rate of 2-3 µl/min [5]. It first enters the posterior chamber (volume 60 µl) and reaches the anterior chamber (volume 250 µl) through the pupil of the eye (see Figure 1.3).
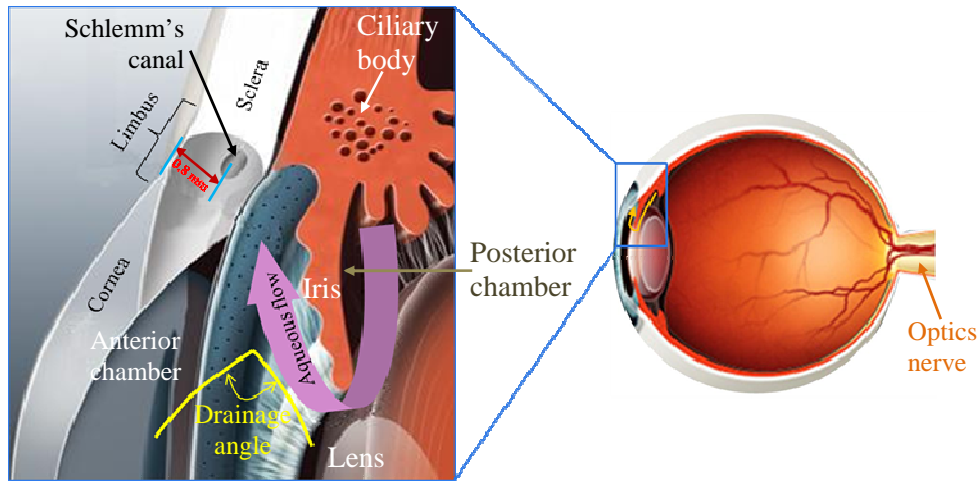
Figure 1.3 Schematic diagram of aqueous humor flow cycle in human eye, picture adapted from [6].

Aqueous humor undergoes a natural refreshment cycle (with 2 - 3 hrs of turnover). After supplying nutrients to the front eye structures such as the lenses and cornea, the used-up one should be removed from the eye while an equal amount of new fluid is being produced. The fluid drains through draining channels located in the front of the eye in an area between the cornea and the iris called the iridocorneal angle, or simple the drainage angle (see Figure 1.3). In this angle, there are two pathways through which outflow of the aqueous humor can occur: non-conventional and conventional.

1. **The non-conventional (or uveoscleral) pathway:** refers to the exit of the aqueous humor from the anterior chamber through intercellular spaces among ciliary muscle fibers by diffusion. In human eye, this pathway contributes a minority outflow ($< 15\%$) to the overall aqueous humor drainage.

2. **The Conventional (or trabecular) pathway**: refers to the exit of the aqueous humor from the anterior chamber through a well–structured porous tissue known as the trabecular meshwork. This pathway is the main outflow ($> 85\%$) route in human eye and its outflow rate is IOP dependent. After crossing the trabecular meshwork, aqueous humor reaches Schlemm's canal, named after the German anatomist Friedrich Schlemm (1795 – 1858), from which it directly drains to the blood veins. Schlemm's canal is an endothelial-lined annular vessel having ∼ 0.25 mm diameter and situated at ∼ 0.8 mm depth in the corneoscleral junction of the limbus (the joint

point of cornea and sclera). Schlemm's canal plays a predominant role in the regulation and stability of the IOP [7].

Anything that slows or blocks the flow of this fluid out of the eye causes IOP to build up. In most cases of glaucoma, IOP is often found to be above the healthy pressure range.

1.3.2 Types of glaucoma

Depending on the type of outflow disruption the fluid may encounter, there are two main types of glaucoma: closed-angle glaucoma and open-angle glaucoma.

i. **Closed-angle glaucoma**: occurs when the aqueous humor outflow is disrupted due to the obstruction at the anterior chamber drainage angle. In this type of glaucoma, the periphery of the iris sticks with the lens (see Figure 1.4) resulting in the inability of the aqueous humor to flow from the posterior to the anterior chamber. As a consequence, the rise of pressure in the posterior chamber pushes the final roll and root of the iris against the cornea thereby physically **closing** the drainage angle that is located at the interface between the cornea and root of iris, and suddenly blocking the fluid from having access to the drainage system of the eye. This results in a rapid accumulation of aqueous humor and causes an acute and painful buildup of pressure in the eye. Closed-angle glaucoma is a less common but dangerous type of glaucoma which needs immediate medical intervention.

ii. **Open-angle glaucoma**: It is by far the most common type of glaucoma ($> 85\%$ of glaucoma cases). In this type of glaucoma, the drainage angle is **open** and looks normal (see Figure 1.4) but the conventional drainage system, meaning the trabecular meshwork (TM), becomes clogged from inside, disrupting the aqueous humor outflow. TM is a sponge-like porous filtration meshwork located in the drainage angle of the eye, right next to the anterior chamber. The aqueous humor from anterior chamber has to cross all the way through the tiny intercellular spaces of TM to reach the Schlemm's canal from which it directly drains to the blood veins to leave the eye. In open-angle glaucoma, these tiny draining channels inside TM become clogged, resulting in a decreased outflow rate of the aqueous humor, and leading to a chronic and painless buildup of pressure in the eye that will gradually damage the optic. The exact cause of this malfunctioning of the trabecular meshwork is unknown.

a) The two main types of glaucoma

b) The damaged optic nerve manifests as 'cupping' or excavation of the optic nerve head
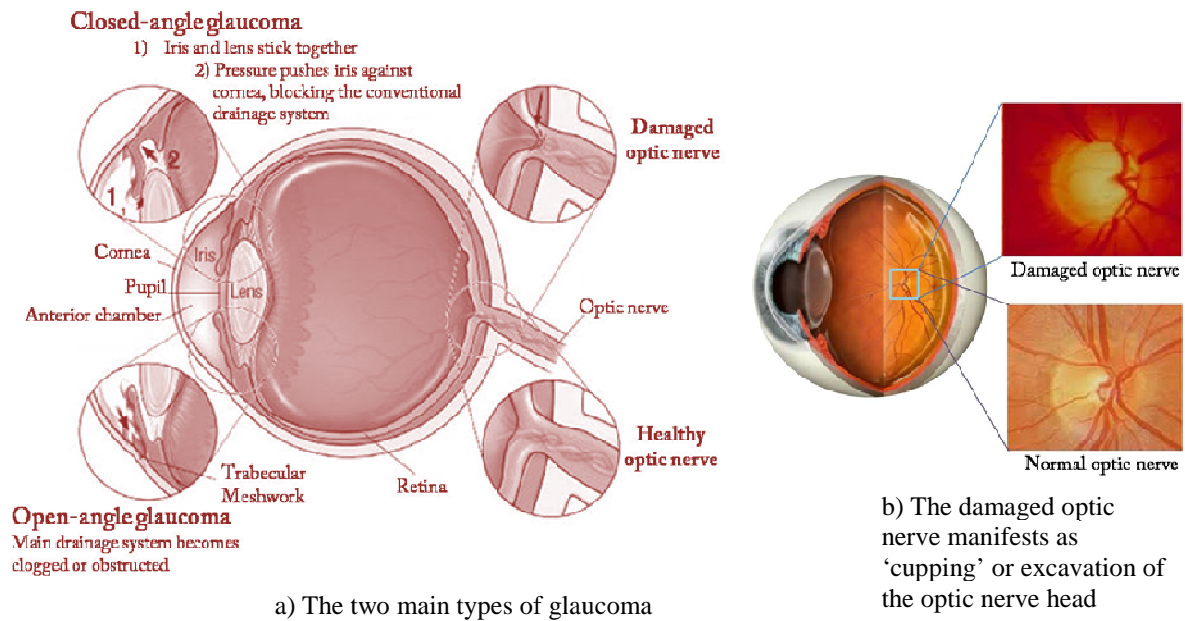
Figure 1.4 Glaucoma and its damage to the optic nerve [8]. In the normal eye, aqueous humor is produced at a rate of 2 to 3 microlitres per minute. Any obstruction at the anterior chamber drainage angle (angle closure) or clogging of the drainage system (open angle) means that the rate of aqueous drainage will be less than the rate of production. This results in build-up of aqueous fluid and elevation of the intraocular pressure, thereby damaging the optic nerve and leading to blindness.

1.4 Symptoms and diagnosis of glaucoma

1.4.1 Symptoms

Open-angle glaucoma and acute closed-angle glaucoma, the two most common types of glaucoma, have completely different symptoms. For open-angle glaucoma (majority of glaucoma cases), there are no early perceptible symptoms until the optic nerve is permanently damaged and peripheral vision is irreversibly lost. The damage typically starts with peripheral vision and it may take years for the disease to damage the central vision. Open-angle glaucoma often has no pain. As a result, victims of glaucoma experience no early symptom until noticeable irreversible vision loss occurs. For this reason, glaucoma is sometimes referred to as the *silent thief of vision*. Hence as everyone is prone to glaucoma, a regular eye examination is important. At intermediate and advanced stages (Figure 1.5 c & d), the patient eventually starts to notice a narrowing field of vision and some kind of tunnel vision.
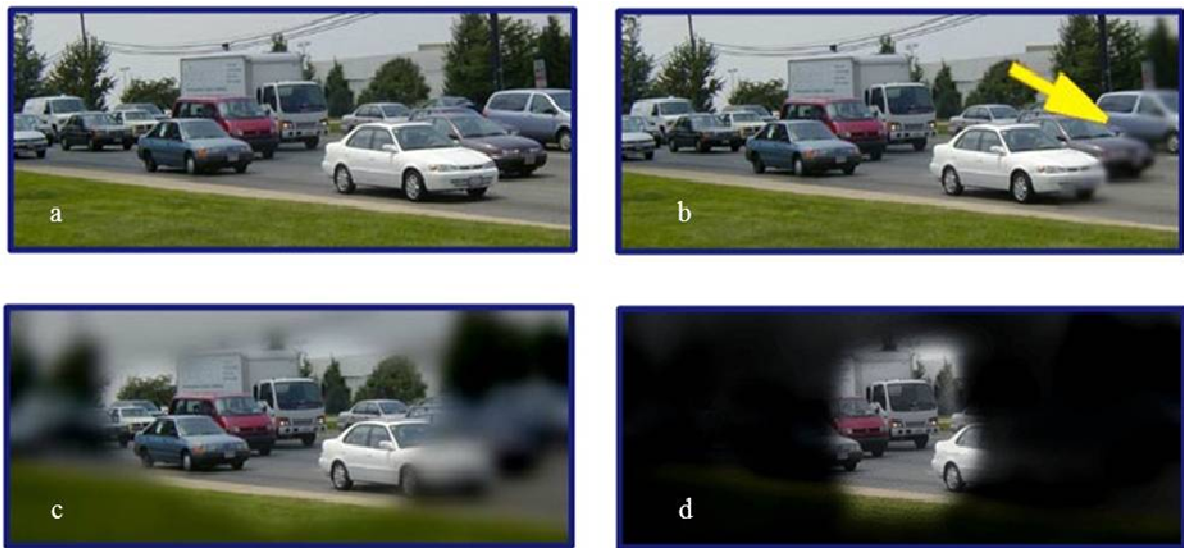
Figure 1.5 Comparison of healthy and impaired visions at different levels of open-angle glaucoma [9] a) Example of normal vision b) Early symptom: may include a gradual and often imperceptible failing of puerperal (side) vision. c) Intermediate symptom: as the disease progresses, the central vision may still clear, however peripheral vision begins to fail d) Advanced symptom (tunnel vision): only a small central field of vision remains. If the entire optic nerve is damaged, then total blindness may result afterwards.

However for acute closed-angle glaucoma, the symptoms may come and go at first, or steadily become worse and include: severe eye pain, nausea and vomiting (accompanying the severe eye pain), sudden onset of visual disturbance, often in low light, decreased and blurred vision, rainbow-like halos around lights, reddening of the eye, eye feels swollen. When such symptoms persist, it is recommended that a person should visit an ophthalmologist for further diagnosis.

1.4.2 Diagnosis

The fact that little or no physical symptom is observed until the first sign of vision loss makes early detection of glaucoma difficult. Glaucoma examination can be performed by a combination of different techniques. These tests are not stand-alone diagnostic methods on their own but the information obtained from such tests can be combined with the patient's history and can greatly help the ophthalmologist to make decision. Tests should include measurement of eye pressure, thickness of the cornea, anterior chamber angle examination, examination of the optic nerve and measurement of field of vision. Table 1.2 summarizes the glaucoma tests.

Table 1.2 Summary of possible glaucoma diagnosis [10].

Technique	What is measured	Procedure
Tonometry	Internal pressure of the eye (IOP)	The eye is numbed via eye drops. The examiner then uses a tonometer to measure the inner pressure of the eye through pressure applied by a warm puff of air or a tiny tool.
Pachymetry	Thickness of cornea	The examiner places a pachymeter gently on the front of the eye to measure its thickness.
Gonioscopy	Drainage angle where iris meets cornea	Eye drops are utilized to numb the eye. A hand held contact lens with a mirror is placed gently on the eye. It allows the examiner to see the angle between the cornea and the iris.
Ophthalmoscopy	Shape and color of optic nerve	The pupil is dilated via the application of eye drops. Using a small magnification device with a light on the end, the examiner can examine the magnified optic nerve.
Perimetry	Complete field of vision	The patient looks straight ahead and is asked to indicate when light passes the patients peripheral field of vision. This allows the examiner to map the patient's field of vision.
Nerve fiber analysis	Thickness of the nerve fiber layer	Using one of several techniques such as OCT, the nerve fibers are examined.

1.5 Current glaucoma treatment methods

Glaucoma cannot be cured and its damage to the optic nerve cannot be restored. However its progress can be controlled. For the moment, the only treatments available for glaucoma work by lowering pressure in the eye; either by decreasing the production of fluid or increasing its outflow. Even in patients with normal IOP but with early signs of the disease, lowering pressure has been shown to significantly slow down the progression of nerve damage [11]. Most antiglaucoma drugs are delivered as eyedrops, which may need to be used once or several times a day. When the use of eyedrops is no longer sufficient, surgical and laser treatments can be used to allow excess fluid to flow out of the eyes.

1.5.1 Eyedrops
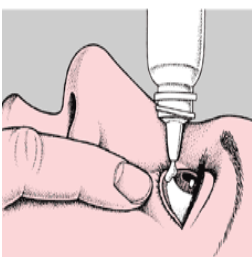
Eyedrops are in most cases the first choice of glaucoma treatment. The ophthalmologist

chooses the right eyedrop, and at the beginning the treatment usually starts with a single type of eyedrop, then depending on the progress of glaucoma, intraocular pressure and other parameters, the treatment may progressively involve combination different types of eyedrops. The target of glaucoma treatment, as mentioned above, is either to decrease

the production of the aqueous humor in the ciliary body or increase its rate of outflow by opening up the drainage system. For example, *beta-blockers* (yellow or blue bottle caps,

Figure 1.6) which are most often used to treat open-angle glaucoma help lower the IOP by reducing the production of aqueous humor. On other hand, *miotics,* another group of glaucoma medications, can lower the IOP by narrowing the iris muscles and constricting the pupil. This action pulls the iris away from the trabecular meshwork and allows the aqueous humor to gain access to the drainage channels.

Figure 1.6 Different types of eyedrops [8].

The four main classes of lowering the IOP are: beta-blockers, prostaglandin analogs or prostamides, alpha agonists and carbonic anhydrase inhibitors. Eye drops are the first line of treatment for lowering the IOP.

1.5.2 Surgical treatment methods

If medications fail to control eye pressure, or if they create intolerable side effects to patients, performing surgical procedure may be necessary. In this type of treatment, surgical procedure is performed using surgical tools to reach the aqueous humor by dissecting through the layers and sub-layers of the tissues (creation of fistula) to improve the evacuation of the liquid out of the eye. Approximately, 12,000 to 15,000 surgical procedures are performed each year in France [3]. Depending on the type and seriousness of the disease, the ophthalmologist may perform one of the following surgical procedures to treat glaucoma: trabeculectomy (filtration surgery), canaloplasty, non-penetrating deep sclerectomy (NPDS), and iridectomy. The first three surgeries are used for treating open-angle glaucoma and the last one (iridectomy) is for closed-angle glaucoma treatment.

1.5.2.1 Trabeculectomy
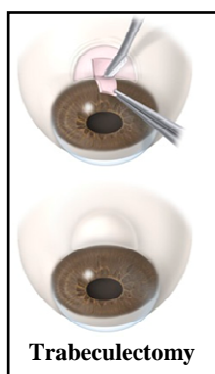
Trabeculectomy

Trabeculectomy (also called filtration surgery) is the most common technique of glaucoma surgery. The procedure involves opening the full thickness of the drainage area by removing part of the eye's trabecular meshwork and the adjacent structure in order to allow the drainage of aqueous humor from within the eye to underneath the conjunctiva where it is absorbed (see the figure on the left [12, 13]). During a trabeculectomy, the patient's eye is held open with a speculum. The surgeon then creates

a sclerectomy, a passage in the sclera for draining excess eye fluid. A flap is created that allows fluid to escape without deflating the eyeball. Finally the scleral flap and the conjunctiva is closed and sutured. A small bubble called a bleb nearly always forms over the opening, which is a sign that fluid is draining out.

1.5.2.2 *Canaloplasty*

It is a less-invasive surgical alternative of lowering the IOP. In this procedure, a new aqueous humor discharge channel is not opened as in previous trabeculectomy, but rather attempts are made to restore the existing, natural drainage mechanism available to the eye. Canaloplasty uses a microcatheter technology whereby an incision is made into the limbus to get access to Schlemm's canal. Schlemm's canal is then cut and a microcatheter is inserted in one side and is gently pushed until it appears on the other side of the cut. Finally a thin suture follows the microcatheter in the circular path through the channel, which is tightened after removal of the catheter to stretch the channel and keep it permanently open thereby relieving the pressure inside the eye (see Figure 1.7).
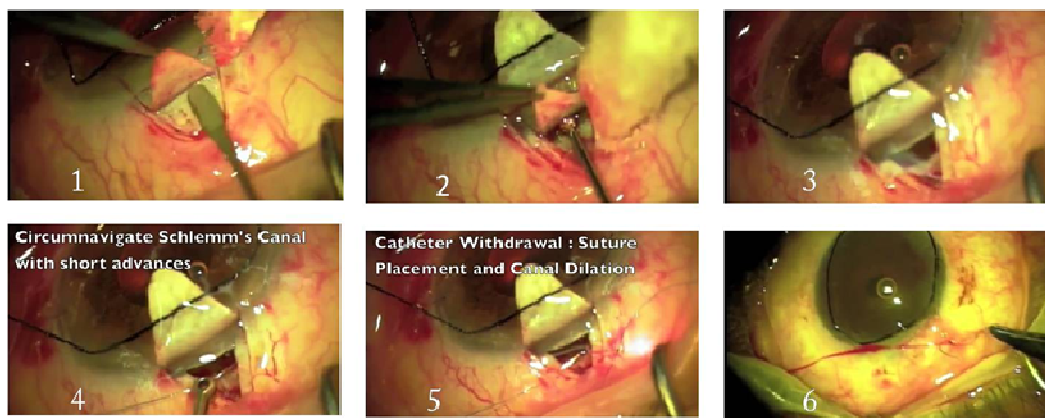
Figure 1.7 Photography showing the different steps of canaloplasty [14].
(1) Creation of the outer flap, (2) Creation of inner flap, (3) Removing the inner flap, (4) Catherization and dialation, (5) Suture placement and tensioning, (6) Closure of the outer flap.

1.5.2.3 *Non-penetrating deep sclerectomy (NPDS)*

It is a less invasive technique than trabeculectomy (filtering surgery). Deep sclerectomy minimizes the risk of over filtration and avoids serious complications; however NPDS techniques do not lower IOP as much as trabeculectomy does. In NDPS, the surgeon creates a flap in the outer part of the sclera and then removes a deep piece of the sclera underneath without perforating the eye. NPDS leaves the anterior chamber intact and avoids creation of blebs. This procedure was developed in an attempt to avoid many of the postoperative complications of trabeculectomy associated with over filtration. The major advantage of

NPDS is that it precludes the sudden hypotony (sudden drop in IOP ≤ 5 mm of Hg) that occurs after trabeculectomy by creating progressive filtration of aqueous humor from the anterior chamber to the sub-conjunctival space, without perforating the eye.

In general, NDPS procedures have fewer post surgery complications than standard trabeculectomy; however they require excellent surgical skill. The residual membrane in a nicely done NDPS procedure should be no more than $10 - 15$ µm. A thinner residual membrane would otherwise lead to a risk of perforation similar to those in trabeculectomy, and thicker membrane would on the other hand make the fluid removal inefficient.

1.5.2.4   Iridectomy

Iridectomy is performed in cases of closed-angle glaucoma. It involves surgical removal of portion of the iris tissue. The iridectomy can be done in several ways:

 ➢ Basal iridectomy: removing iris tissue from the far periphery, near the iris root or base
 ➢ Peripheral iridectomy: removing iris tissue close to the periphery
 ➢ Sector iridectomy: removing a wedge-shaped section of iris that extends from the pupil margin to the iris root.

In peripheral iridectomy, for example, the procedure starts by outlining the clear cornea incision. Then a 2-3 mm corneal incision is made and the anterior chamber is entered without injuring the iris. The iris is gently grasped and exteriorized. The required iridectomy is then performed by cutting out the grasped part of the iris. Finally the procedure ends by closing the cornea. Figure 1.8 shows the summary of peripheral surgical iridectomy. Opening the eye's globe for surgical iridectomy in a patient with high IOP greatly increases the risk of suprachoroidal hemorrhage[7], with potential for associated explosive hemorrhage.
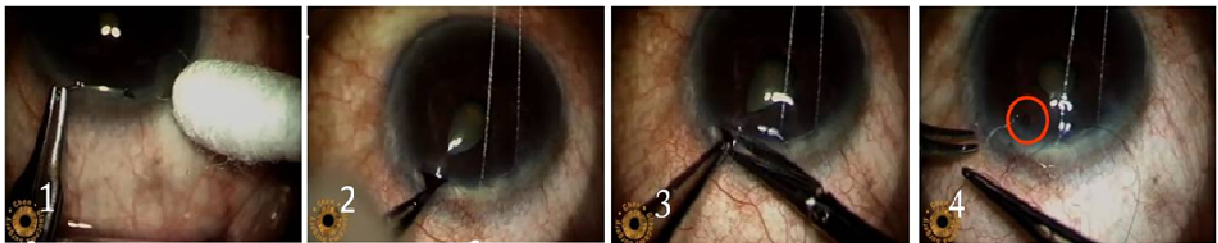
Figure 1.8 Steps in surgical iridectomy.
(1) Corneal incision is made and the anterior chamber is entered without injuring the iris (2) The iris is gently grasped and exteriorized (3) The required iridectomy is then performed by cutting out the grasped part of the iris (4) Finally the procedure ends by closing the cornea [15].

---

[7] Suprachoroidal hemorrhage is defined as accumulation of blood between the choroid and the sclera.

1.5.3 Laser surgery

While medication is the first choice of glaucoma treatment in controlling further damage of the optic nerve, the fact that eyedrops are often prescribed to be applied several times a day, and in some cases, for entire life, makes it harder for patients to strictly follow the prescription. However, the success of medical treatment highly depends on the rigorous monitoring of prescription, hence poor compliance with medications and follow-up visits is one major problem related to medication. A 2003 study of glaucoma patients in an HMO (health maintenance organization - USA) found that half failed to fill their prescriptions the first time, and one-fourth failed to refill their prescription second time. Skipping even a few doses can greatly increase the risk of visual loss. In addition, eyedrops have many side effects too. Affording the price of one's entire life medication is another reason for poor compliance. Eyedrops do also have side effects, and some of them can cause adverse consequences and may not be tolerated any more by the patient. In such situation, the patient will be recommended to undergo eye surgery.

Depending on the type and seriousness of glaucoma, different surgical procedures are available. For open-angle glaucoma treatment, for example, trabeculectomy is the golden surgical standard. However, because of the complete opening, trabeculectomy has potential risks of complications such as infection, leakage, irritation, hypotony (IOP ≤ 5 mm of Hg), choroidal detachment, scarring and development of cataract over time. Generally, due to post-surgical complications, such conventional surgical methods of glaucoma treatment have low success rate globally (60%).

The availability of compact lasers and their ability to make safe surgery has opened a third alternative method of glaucoma treatment. The value of laser therapy lies in reducing medication and postponing or avoiding undergoing risky surgical procedures like filtration surgery. Laser therapy is very useful especially for those (but not limited to) glaucoma patients who cannot tolerate eyedrops due to medical complications but do not want (or are in dilemma) to undergo traditional surgical procedure. Laser treatment procedures often do not produce scarring and can be repeated later on. Several laser techniques can be used, which ultimately increase the drainage of the aqueous humor from the eye by improving the eye's natural drainage system.

1.5.3.1 Laser trabeculoplasty

A trabeculoplasty is a modification of the trabecular meshwork (TM). Laser trabeculoplasty (LTP) involves sending a visible laser beam through the cornea to burn areas of the TM base (uveal meshwork), located close to the base of the iris, in order to decrease its resistance. LTP increases outflow and has no influence upon aqueous secretion. The value of trabeculoplasty lies in reducing medical therapy and postponing or avoiding the risks of filtration surgery. LTP is used in the treatment of various open-angle glaucomas. The two types of LTP are argon laser[8] trabeculoplasty (ALT) and selective laser trabeculoplasty (SLT) (see Figure 1.9).
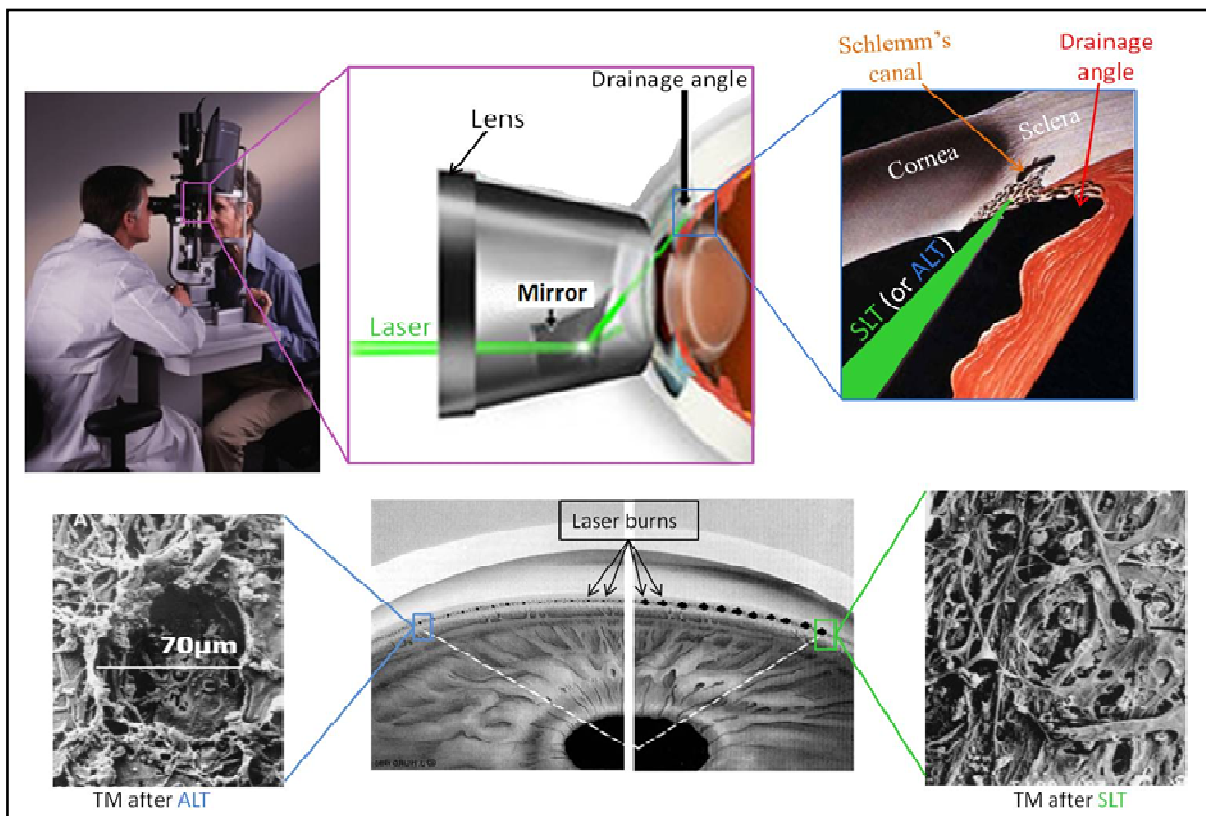
Figure 1.9 Laser trabeculoplasty (LTP) for treating open-angle glaucoma [16, 17].
The laser is sent through clear cornea and is focused on the base of TM to burn holes and increase the rate of aqueous humor. Selective Laser Trabeculoplasty (SLT) selectively targets pigmented cells while preserving the surrounding tissues and causes less collateral damage than Argon Laser Trabeculoplasty (ALT).

As the name implies, ALT uses argon laser to create several tiny burns (each ~ 50 µm in diameter) on the TM. This consists of spacing 100 (may be more) non-perforating laser burns 360 degrees around the TM to shrink the collagen in the tissues of the trabecular ring. This reduces the circumference and therefore the diameter of the trabecular ring, pulling the trabecular layers apart with reopening of the inter-trabecular spaces and of Schlemm's canal

---

[8] Argon laser is family of ion lasers that uses the noble gas argon as its active medium.

[17]. SLT is a recently introduced glaucoma treatment method that selectively targets pigmented trabecular cells without causing thermal damage to non-pigmented structures. In this treatment, a frequency doubled, Q-switched Nd:YAG laser[9] with pulse duration of 3 ns and spot size of 400 µm is used. The 532 nm wavelength is highly absorbed by melanin and can selectively target pigmented cells while preserving surrounding tissue.

Histological studies evaluating SLT have shown that unlike ALT, there is no scarring of TM. ALT causes thermal injury and coagulative damage to TM, making repeat treatment difficult. The selectivity of SLT, added to its relatively much lower power, protects TM against thermal or coagulative effects, thus SLT may be theoretically repeated and result in additional reduction in IOP greater than that with ALT. Hence SLT is effective and safe as primary treatment for patients with ocular hypertension and open-angle glaucoma [18].

1.5.3.2 Laser iridotomy

Laser iridotomy is the laser equivalent of surgical iridectomy and is used for treatment of closed-angle glaucoma. In this case a focused laser beam (either argon laser or Nd:YAG laser) is used, instead of sharp tools employed in surgical iridectomy, to burn a hole through the iris without damaging and opening the overlaying cornea tissue (see Figure 1.10). This new opening allows fluid (aqueous humor) to flow from the posterior chamber to the anterior chamber. Compared to the traditional surgical iridectomy, laser iridotomy is much safer.
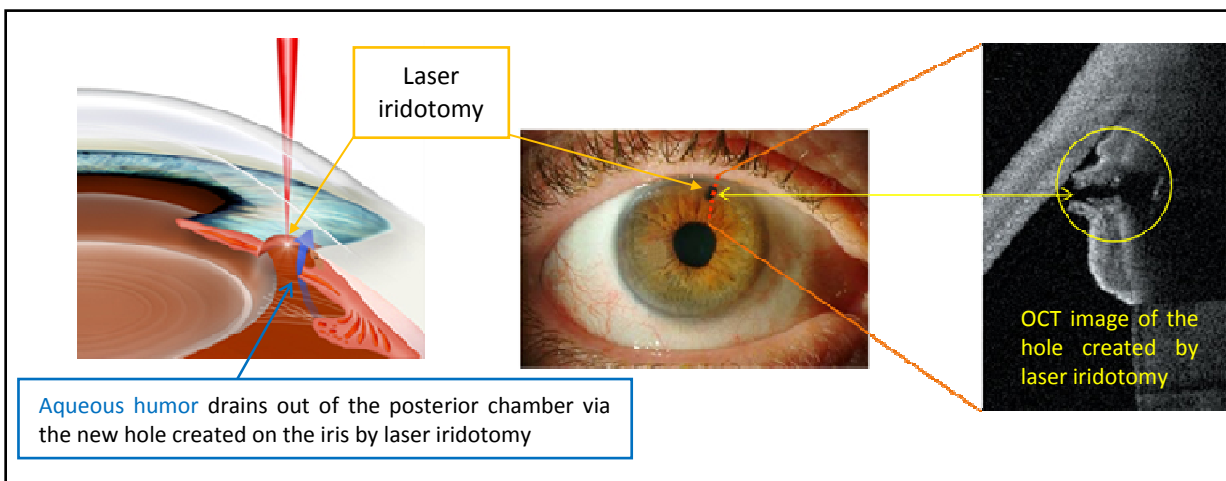
Figure 1.10 Laser iridotomy for treating closed-angle glaucoma, images taken from [8, 19].
Note that, as shown by the OCT image, laser surgery enables to make a hole on the iris without opening the cornea.

---

[9] Nd:YAG laser is a solid-state laser that uses neodymium-doped yttrium aluminum garnet (Nd:Y3Al5O12) crystal as a lasing medium.

1.5.4 New approach for laser glaucoma surgery and monitoring

The current laser treatments of both open-angle and closed-angle glaucomas make use of the clear cornea window to perform the procedure. For closed-angle glaucoma treatment, laser is directly focused on the iris after passing through the cornea. For closed angle-glaucoma treatment, a special scanning system is employed to send the laser beam at a specific angle through the cornea towards the base of the TM. Moreover, both procedures use a white light microscope for monitoring the laser intervention, which again depends on the transparency of cornea to image the under-laying anterior segment. Hence opacity of the cornea may limit the use of such a procedure. If a glaucoma patient already has corneal edema, visible laser light will be strongly scattered and fail to properly induce holes on the required target in the anterior chamber. Scattering will also inhibit the use of white light microscopy to monitor the intervention.

For open-angle glaucoma treatment, corneal opacity is not the only limitation of laser trabeculoplasty. The other drawback of this procedure is related to the fact that while most of the resistance to the aqueous outflow is in the outer most portion of TM (see Figure 1.11), ALT or SLT targets the base (inner most portion) of the TM, the *uveal meshwork*, which does not offer much resistance. Moreover, early investigations on chronic open-angle glaucoma cases showed that malfunctioning of TM (like plaque formation) that leads to blockage of the drainage system often starts in the *cribriform meshwork*, which itself is located in the outer most part of the TM.

A schematic representation of the different layers of TM from inner to the outer most portion is shown in Figure 1.11. The inner most portion of TM (see Figure 1.11) that lies next to the anterior chamber is the uveal meshwork. It is formed by prolongations of connective tissue arising from the iris and ciliary body stromas totally covered by endothelial cells. The intercellular spaces in this region are large (25 - 70 µm) [5] and put less resistance to the aqueous humor outflow. The next layer, the corneoscleral meshwork, is characterized by the presence of lamella[10]. The higher organization of the corneoscleral meshwork and their narrower intercellular spaces (5 - 50 µm) [5] are responsible for the increase in flow resistance. The third layer, which is in direct contact with the inner wall of endothelial cells from the Schlemm's canal, is the cribriform meshwork. The last barrier that aqueous humor

---

[10] A lamella is a thin plate-like structure, often one amongst many lamellae (pl.) very close to one another, with open space in between.

has to cross before exiting the eye is the inner endothelial wall of the Schlemm's canal. As cells in cribriform are embedded in a dense extracellular matrix and due to the high density of pores across the inner endothelia wall, the outer most portion of the TM is responsible for the majority of the tissue resistance to aqueous outflow. However, the target of current laser trabeculoplasty is rather on the inner most portion of TM where the intracellular spaces are already wide enough to permit outflow.
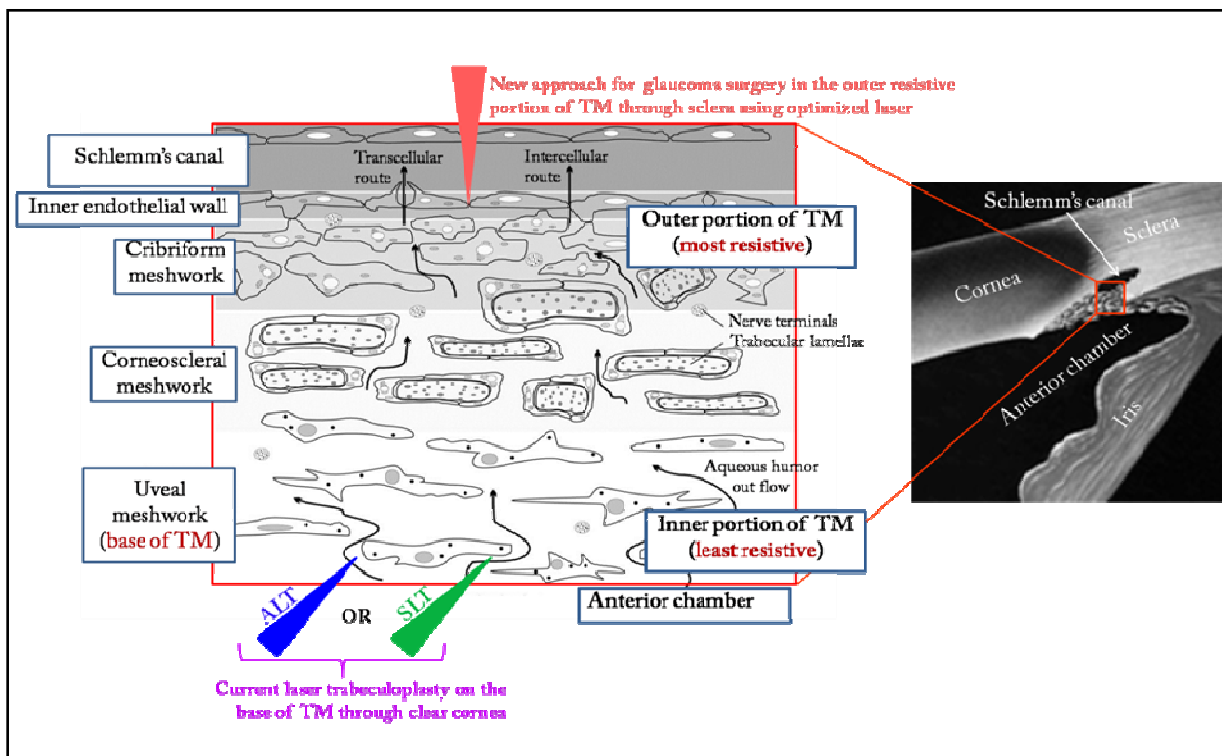
Figure 1.11 Schematic diagram of the trabecular meshwork (TM) adapted from [20], showing the new surgery approach .The black arrows indicate the direction of the aqueous humor outflow from the anterior chamber towards Schlemm's canal through the intercellular spaces of the different regions of the TM: from the least resistive uveal meshwork to the most resistive inner wall of Schlemm's canal.

In addition, for patients with chronic open-angle glaucoma, Rohen and Witmer [21] described for the first time that *malfunctioning of TM (like plaque formation)*, which blocks the intercellular spaces and causes additional elevation of the resistance of TM, often starts in cribriform meshwork. It was later noticed by Tripathy [21] that the vacuolated cells within the endothelial lining of the Schlemm's canal, which are responsible for allowing the fluid to enter the Schlemm's canal, were almost lacking in case of open-angle glaucoma, being replaced by plaques that block the flow of the aqueous humor (see Figure 1.12).

(a)   **(b)**
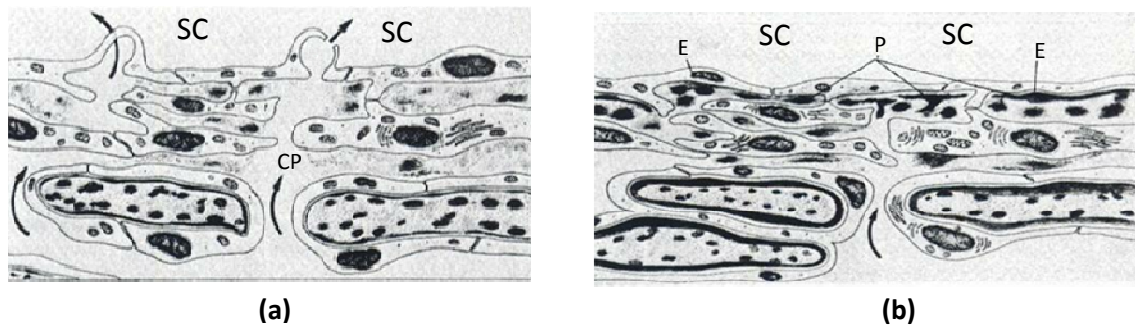
Figure 1.12 Schematic drawing of cribriform meshwork in normal (a) and glaucomatous (b) eyes. Notice that the cribriform pathways (CP) are directed to the vacuolated inner wall cells in normal eye (a); and the plaque-material (P) is located within the cribriform meshwork in case of chronic simple glaucoma (b).E: Endothelium of Schlemm's canal; SC: Schlemm's canal; CP: cribriform pathway; V: Vacuoles

Because of this anatomical reason of TM and as visible lasers cannot penetrate TM to reach this high resistive part, the current SLT (or ALT) procedure targets the less resistive part of TM that is accessible to visible laser light. Hence this procedure is inefficient for controlling the IOP in the long run. For the time being, it can only help reduce medication and prolong conventional filtrating surgery. An ideal solution for laser treatment of open-angle glaucomas would require the delivery of surgery laser light to this highly resistive outer most portion of the TM, around the Schlemm's canal, directly through the sclera. However, as sclera scatters visible and even near-infrared light, it will not be possible to penetrate deep enough to reach the Schlemm's canal ($\sim 800\ \mu m$ depth) using conventional lasers.

One of the solutions to overcome scattering is to increase the wavelength of the laser beam. The development of glaucoma laser surgery tool has to account for the attenuation of light due to the strongly scattering tissues of sclera and edematous cornea. Both the surgical laser and the imaging system used to monitor the surgery are concerned by this problem.

The idea of the NOUGAT project, to which this PhD contributed, has been developing a new tool that uses an optimized ultrashort pulse laser to make the glaucoma surgery and an imaging system based on optical coherence tomography (OCT) to monitor the intervention in real-time. LOA has worked on the femtosecond laser optimization and has carried out experiments on sclera and pathological cornea. They have demonstrated that the incision depth of femtosecond laser in highly scattering sclera and pathological cornea can be enhanced by using an optimized femtosecond laser source at $1.65\ \mu m$ central wavelength.

My work in this project has mainly been focused on the development and utilization of high-resolution and fast Fourier-domain OCT (FD-OCT) for visualization of the Schlemm's canal directly through the highly scattering tissues sclera and edematous cornea. In collaboration

with LOA, we have also worked on the coupling of the OCT imaging system operating at 1.30 µm center wavelength with the laser surgery system optimized at 1.65 µm center wavelength. We demonstrated the use of OCT for real-time imaging of the laser surgery in human cornea. The preliminary results demonstrate the potential of OCT in monitoring glaucoma laser treatment.

Before describing the experimental work accomplished in this PhD work, a general overview of the OCT technology is presented in the next chapter.

Chapter 2 - Optical coherence tomography: principles and techniques

2.1 Introduction

Proposed in the early 1990's by Huang *et al* [22] *optical coherence tomography* (OCT) is an imaging technique that uses *optical* radiation to perform non-invasive *tomographic* imaging of internal microstructures of biological tissues and semitransparent materials up to few millimeters of depth using the *coherence* property of light. The principle of coherence-gating and its ability to make high-resolution cross-sectional imaging in scattering media are explained in the appendix (section A.3.3).

Tomography, derived from the Greek tomos ("part" or "section") and graphein ("to write"), refers to the use of a penetrating wave and a computer algorithm to reconstruct the cross-sectional image of a three dimensional object in order to obtain a slice image of the internal structures as shown in Figure 2.1. Depending on the type of the penetrating wave used, the various types of tomographic imaging techniques widely used in medical applications can be mentioned:

Figure 2.1 Schematic diagram of tomography

- ✓ Ultrasound (uses high frequency sound waves)
- ✓ Computed tomography (uses X-ray radiation)
- ✓ Magnetic resonance imaging (uses magnetic field)
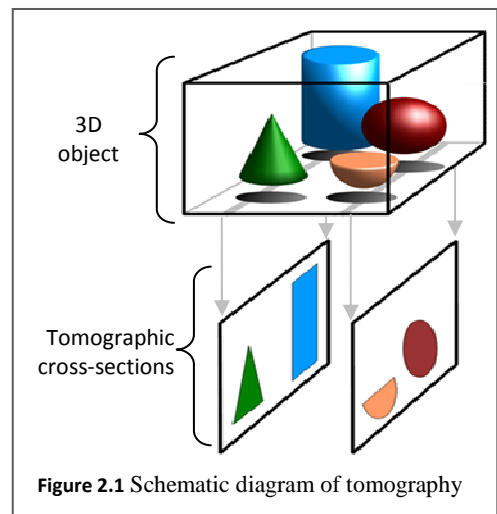
OCT is a relatively new tomographic imaging method that uses optical waves. By measuring the echoes of backscattered light in a way similar to ultrasonic pulse-echo imaging, OCT acquires high-resolution tomographic cross-sections of internal structures of semi-transparent samples. As OCT is based on the coherence-gating technique, the high-resolution sectioning is achieved by exploiting the short temporal coherence length of a low-coherence broadband light source.

2.2 Comparison of OCT with other tomographic imaging modalities

In general, optical imaging techniques are of particular importance in the medical field, because these techniques promise to be safe and relatively cheaper and, in addition, offer a therapeutic potential. Considering different imaging parameters such as resolution, imaging depth, acquisition time, system complexity and sample intrusiveness, OCT can be compared with other tomographic imaging techniques: confocal microscopy, ultrasound, computed tomography (CT) and magnetic resonance imaging (MRI). Figure 2.2 shows a summary of the comparison based on imaging depth and resolution, where the length of the pendulum represents the imaging depth and the size of the sphere represents the resolution [23].
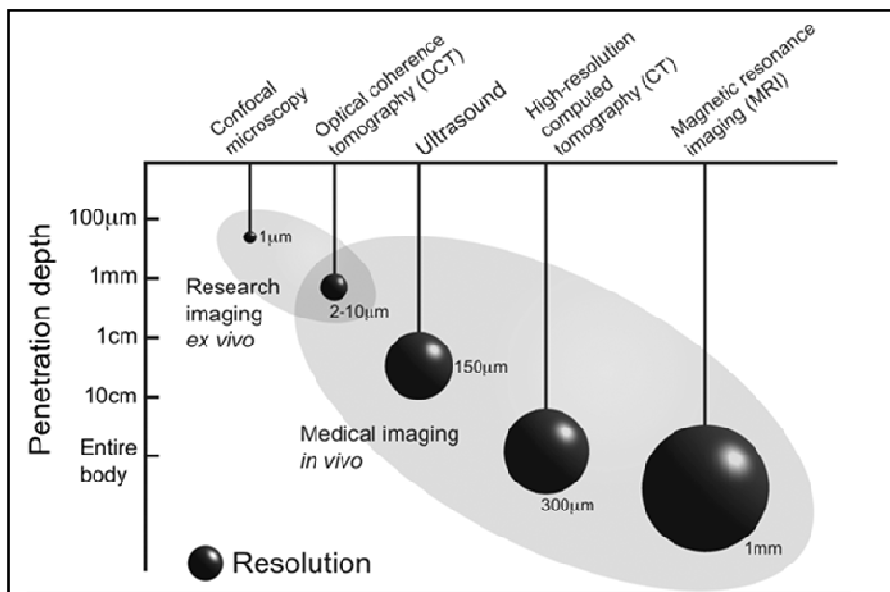
Figure 2.2 Comparison of OCT resolution and imaging depth to those of alternative techniques. The "pendulum" length represents the accessible imaging depth; the "sphere" size represents the imaging axial resolution [23].

Clinical ultrasound uses acoustic waves with frequencies ranging between 3-40 MHz and gives a resolution of 0.1-1 mm [24, 25]. The comparatively long wavelengths of ultrasound are not attenuated significantly by biological tissues, thereby offering deep imaging of the body. Using high frequency ultrasound (~ 100 MHz), imaging resolutions of 15 to 20 µm have been developed for research and clinical applications. However such high frequency sound waves are strongly attenuated in biological tissues, and imaging depths are limited to only few millimeters [26]. On the other hand, confocal microscopy has high resolution, approaching 1 µm; however optical scattering degrades image signal and contrast, and the typical imaging depth of confocal microscopy in most biological tissues is limited to few hundreds of microns [26]. In terms of resolution and imaging depth, OCT fills the gap between confocal microscopy and ultrasound. With the current OCT technology, an axial

image resolution of 1-15 µm and a penetration depth of 2-3 mm can be achieved. As OCT itself is an optical imaging technique, its imaging depth, though better than that of confocal microscopy, is ultimately limited by the effects of absorption and scattering within the biological samples. Unlike confocal microscopy, the axial resolution of OCT is determined by the bandwidth of the light source; the broader the source bandwidth, the better the axial resolution.

With the current OCT technology, the acquisition time of OCT has been brought at a level where video rate imaging is possible like ultrasound, making it more tolerant to sample motion than either CT or MRI [23]. Unlike ultrasound imaging which needs a contact of the probe with the sample for coupling and propagation of sound waves, OCT is a non-contact imaging technique. Moreover, OCT uses non-ionizing radiation at biologically safe levels, allowing for long exposure times, and its level of complexity is closer to ultrasound than to CT or MRI, allowing for the realization of low-cost portable scanners. The point-scanning nature of OCT technology allows it to be implemented in fiber optics, which makes endoscopic and catheter-based imaging possible.

This combination makes OCT be a great technique for *in-vivo* and *in-situ* imaging of epithelial structures, and could possibly replace excisional biopsy as a non-invasive alternative. Since its invention, OCT has got a wide range of applications. It has been employed for *in situ* and *in vivo* biomedical imaging [27] as well as material characterization [28]. Since the eye provides an optically transparent window, OCT has been the most competitive technique for non-invasive and cross-sectional imaging of the internal structures of the eye with high resolution. Hence, the most significant impact of OCT has been in ophthalmology for retinal imaging [29, 30] and measurement of the dimensions of the anterior segment of the eye [31, 32].

2.3 General principle of OCT

Generally speaking, the basic working principle of OCT is analogous to ultrasound but OCT uses light instead of sound. As the wavelength of light wave is by far shorter than that of ultrasound, using light instead of ultrasound significantly improves image resolution. Ultrasound and OCT are analogous in a sense that when a beam of sound or light is sent to a biological tissue, it is backreflected or backscattered differently from structures that have varying acoustic or optical properties, as well as from boundaries between structures. The

dimensions of these structures can be determined by measuring the "echo" time it takes for the sound or light wave to return from various axial distances. In ultrasound, such axial measurement of distance or depth is called A-mode scanning, while cross-sectional imaging is called B-mode scanning [26]. These terms are also used in OCT in a similar fashion (see Figure 2.3).
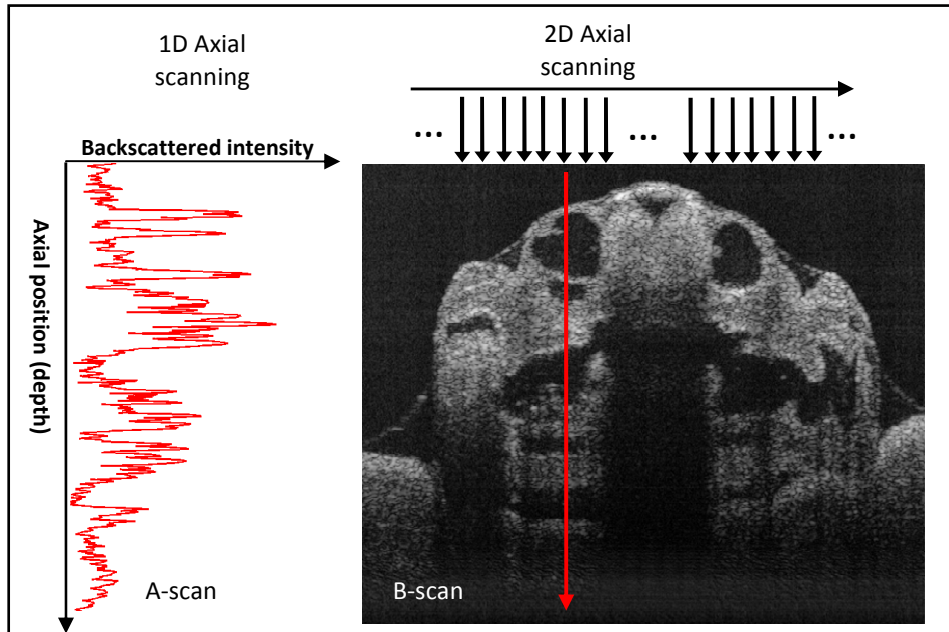
Figure 2.3 OCT generates cross-sectional images by measuring the magnitude and echo time delay of backscattered light. Axial scans (A-scans) measure backscattered intensity versus depth. By performing series of A-scans at different transverse positions, a two dimensional data set (B-scan) is generated. The data set will be processed and an intensity-based cross-sectional OCT image of the sample will be displayed either in a grey scale or false color image.

The main technical difference between ultrasound and OCT comes from the fact that the speed of light is much faster than sound. The speeds of sound and light waves in tissue are $\sim 1.5{\times}10^3$ m/s and $\sim 1.5{\times}10^8$ m/s, respectively. Using sound wave, the measurement of distances with a 150 µm resolution, typical resolution of ultrasound, requires a time resolution of $\sim$ 100 ns, which is well within the limits of electronic detection. Unlike ultrasound, due to the extremely high speed of light, the detection of echo time delays of light waves with 15 µm resolution, typical OCT resolution, requires a times resolution of $\sim$ 50 femtoseconds (1 fs = 10^{-15} second). This time is extremely short and direct electronic detection is impossible on this time scale. In OCT, such small scale echo time delay measurement is achieved by using *low-coherence interferometry* (**LCI**). OCT is therefore an interferometric-based imaging technique. Interferometry is a powerful technique for measuring the amplitude and the echo time delay of backscattered light with high sensitivity.

In LCI, an interferometer illuminated by a low-coherence light source is used to perform correlation or interference between light that is backscattered from tissue with light that has travelled a known distance or time delay through a reference path. LCI was first developed for measuring reflections in fiber optics and optoelectronic devices [33-35]. The first applications of low-coherence interferometry in biomedicine were in ophthalmology to perform precision measurements of the axial eye length and corneal thickness [36, 37].

2.4 Low-coherence interferometry (LCI)

The most commonly used interferometer in LCI is the Michelson interferometer [38]. The configuration of the Michelson interferometer with a light source and a light detector is shown in Figure 2.4. Light from the source is directed into the beamsplitter. The beamsplitter (often with a 50:50 splitting ratio) splits the light between the two arms of the interferometer: the reference arm and sample arm. One of the beams is incident onto the sample to be imaged, while the second beam travels a reference path with a variable path length. Light waves backscattered and/or backreflected from sample of arm length z_S are made to recombine at the beam splitter with light waves reflected back from a reference mirror located at a distance of z_R from the beamsplitter. If interference conditions are fulfilled, the superposed waves can produce interference patterns that can be detected with a photodetector at the interferometer output, creating a data that will be analyzed.
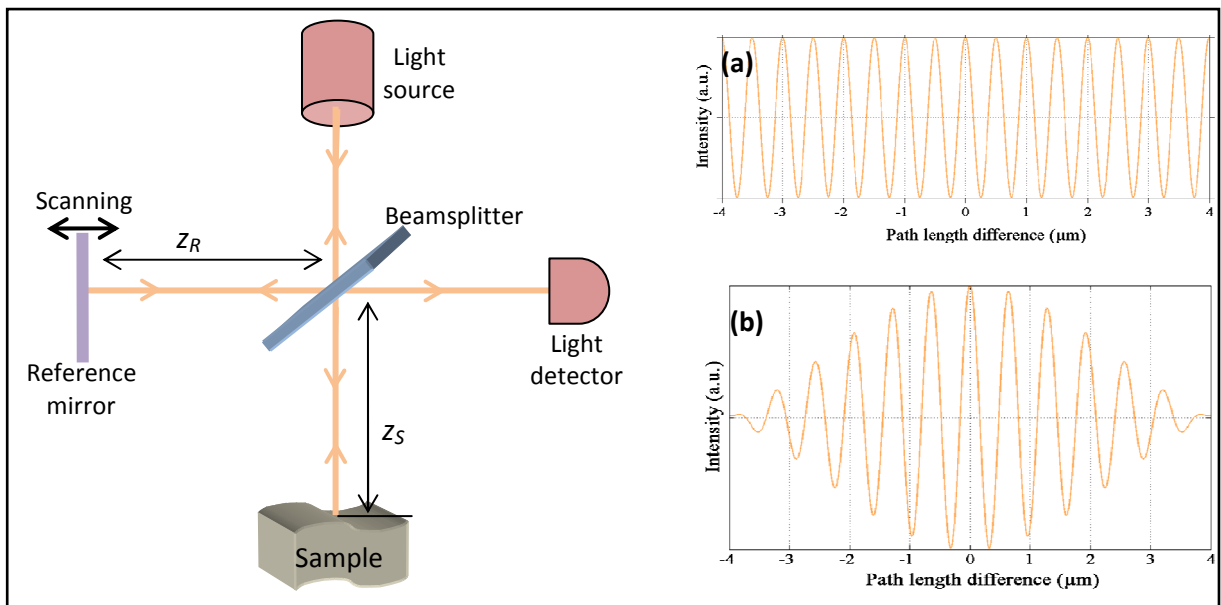
Figure 2.4 Michelson interferometer, the basic building block of OCT.
If the light source is coherent (i.e. monochromatic), interference fringes will always be observed as the path length difference is varied **(a)**, however, if low-coherence light is used, interference occurs only when path length difference is within the coherence length **(b)**.

2.4.1 The interference condition

For the two combined waves to interfere, they should be temporally coherent. This property of interference dictates that interference between the sample and reference beams occurs only if the optical path length difference between the two arms of the interferometer $\delta = 2(z_R - z_S)$ is within the temporal ***coherence length*** of the illuminating light.

The quantitative measure of how well a light wave interferes with a delayed version of itself is called temporal coherence. The time delay over which the phase or amplitude of the wave varies by a significant amount (and hence the correlation/interference decreases by a significant amount) is called coherence time τ_c. At delay time $t = 0$, the degree of coherence is perfect whereas at $t = \tau_c$, degree of coherence drops significantly. ***Coherence length*** L_c is defined as the distance the wave travels in time τ_c, and is given by $L_c = c \times \tau_c$, where c is the speed of light. Temporal coherence tells us how monochromatic a given light source is. The coherence length of monochromatic light is theoretically infinity. For example, the coherence length of a stabilized He-Ne laser ($\Delta\lambda = 10^{-6}$ nm at $\lambda = 632$ nm) is ≈ 400 m. Such light sources are called coherent sources. However, not all lasers have long coherence length. The coherence length of a Kerr-lens mode-locked Ti:sapphire laser (with $\Delta\lambda = 350$ nm at $\lambda = 800$ nm) [39] can be as short as $\sim 2\ \mu$m. Such light sources with short coherence length are called ***low-coherence*** or ***partially-coherence sources***.

If the light source in Figure 2.4 has a high coherence (i.e., long coherence length), interference between the sample beam and reference beam will be observed for a significant optical path length differences (OPD) between the two arms (see Figure 2.4 (a)). This is not what we want for OCT. On the other hand, if a low-coherence light (i.e., short coherence length) is used, interference fringes will only be observed within a limited OPD (see Figure 2.4 (b)). When the OPD between the two arms starts to be longer than the coherence length, interference fringes start to disappear. This means that any light coming out of the coherence zone will not contribute to interference signal. Such coherence-gating technique can be utilized to measure the reflectivity and relative location of a thin layer in a sample with an accuracy determined by the coherence length of the light source. From this, one can institutively tell that shortening the coherence length of the light source helps improve the accuracy of measurement. Such physical phenomenon has been used in the late 1980s to measure reflections in fiber optics and optoelectronic devices [40]. It is this coherence-gating

technique that gives OCT its capability to make high-resolution tomographic imaging of internal structures of biological tissues and materials in scattering media.

2.5   Mathematical formulation of two beam interference

In order to quantity the imaging parameters of OCT (such as axial resolution, sensitivity, imaging depth, etc), mathematical formulation of LCI is presented in this section. For the sake of simplicity, the interference of monochromatic light is introduced first.

2.5.1   Description of electric field and intensity of light wave

The electric field of a linearly polarized monochromatic plane light wave propagating in the z direction can be written as:

$$E = A\cos(\omega t - \varphi),$$ 2. 1

where A is the amplitude, $\varphi = kz$ the arbitrary phase, $k = 2\pi/\lambda$ the wavenumber, λ the wavelength, $\omega = 2\pi v$ the angular frequency, and v the optical frequency (see Figure 2.5).
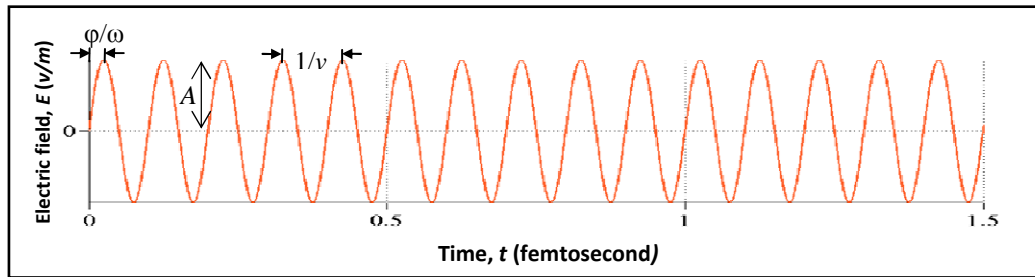
Figure 2.5 Electric field plot of a monochromatic light wave for $\lambda = 600$ nm, with oscillation period $T = 1/v = 2\times10^{-15}$ s.

For simplicity, the electric field in equation 2.1 can be expressed in a complex function as

$$\mathbf{E} = \mathbf{A}\exp\{i(\omega t - \varphi)\}.$$ 2. 2

Bold style letters represent complex values. The optical intensity of a light wave, defined as the optical power per unit area, is given by the time averaged value of modulus square of the complex electric field

$$I = \left\langle |\mathbf{E}|^2 \right\rangle = |\mathbf{A}|^2 = A^2.$$ 2. 3

2.5.2   Interference of monochromatic light

Now, let us illuminate a Michelson interferometer (shown in Figure 2.6 - mirrors on both arms) with a monochromatic plane wave whose complex electric

field $\mathbf{E}_o$ at the beamsplitter (where z = 0 is assumed) is given by

$$\mathbf{E}_o = \mathbf{A}_o \exp(i\omega t).$$ 2. 4

Considering a beamsplitter with 50:50 power splitting ratio, the light will be equally split (in power) between two arms of the interferometer and the amplitude of the corresponding electric field going to each arm will be $\dfrac{|\mathbf{A}_o|}{\sqrt{2}}$. The electric fields in each arm will then travel the corresponding lengths z_R and z_S, reflect back at the mirrors, travel back the same distances to the beamsplitter where they recombine.
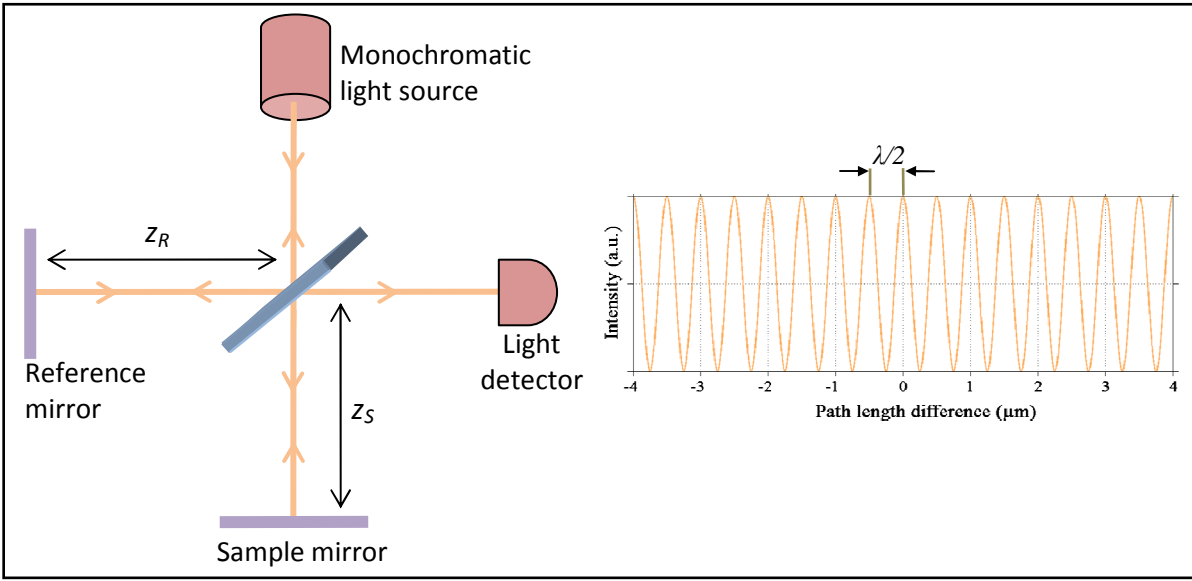
Figure 2.6 Michelson interferometer with monochromatic light source and identical mirrors on both arms. The detected signal by the light detector looks like the one shown on the right. A monochromatic light ($\lambda = 1$ µm) was used to plot the interference signal as a function of the path length difference between the two arms (expressed in equation 2.7). When monochromatic light is used, interference occurs for any path length difference.

Let $\mathbf{E}_R$ and $\mathbf{E}_S$ be the two electric fields that are reflected back from the reference and sample arms, respectively. At the beamsplitter, these fields can be defined as

$$\mathbf{E}_R = \mathbf{A}_R \exp\{i(wt - \varphi_R)\}; \quad \mathbf{A}_R = r_R \frac{1}{\sqrt{2}} \mathbf{A}_o$$

$$\mathbf{E}_S = \mathbf{A}_S \exp\{i(wt - \varphi_S)\}; \quad \mathbf{A}_S = r_S \frac{1}{\sqrt{2}} \mathbf{A}_o$$ 2. 5

where $\mathbf{A}_R$ and $\mathbf{A}_S$ represent the amplitudes of the complex electric field reflected from reference and sample arm with field reflectivities of r_R and r_S, respectively. φ_R and φ_S represent the corresponding phases accumulated during propagation in each arm. After recombination at the beamsplitter, half of the light power contained by the wave in each arm will go back to the source and the other half propagates to the detector. Hence the

34

superimposed complex electric field $\mathbf{E}_D$ arriving at the detector can be expressed as

$$\mathbf{E}_D = \frac{1}{\sqrt{2}}(\mathbf{E}_R + \mathbf{E}_S) = \frac{1}{\sqrt{2}}\left[\mathbf{A}_R \exp\{i(\omega t - \varphi_R)\} + \mathbf{A}_S \exp\{i(\omega t - \varphi_S)\}\right],$$ 2. 6

where the factor $1/\sqrt{2}$ shows that only half of the returning power from both arms goes to the detector.

According to equation 2.3, the intensity I_D that impinges on the detector, assuming that the photodetector captures all of the light from the reference and sample arms, is given by

$$I_D = \left\langle |\mathbf{E}_D|^2 \right\rangle = \frac{1}{2}\left[\left\langle |\mathbf{E}_R|^2 \right\rangle + \left\langle |\mathbf{E}_S|^2 \right\rangle + \left\langle \mathbf{E}_R.\mathbf{E}_S^* \right\rangle + \left\langle \mathbf{E}_R^*.\mathbf{E}_S \right\rangle \right]$$

Substituting the expressions of $\mathbf{E}_R$ and $\mathbf{E}_S$ from equation 2.5, we get the following expression for I_D

$$\boxed{I_D = \frac{1}{2}\left[I_R + I_S + 2\sqrt{I_R I_S}\, \cos(\Delta\varphi) \right]}$$ 2. 7

where $I_R = A_r^2$ and $I_S = A_s^2$ are reference and sample arm intensities, $\Delta\varphi = \varphi_R - \varphi_S = k \times 2z$ is the phase difference between the two arms of the interferometer with $k = 2\pi/\lambda$ where λ is the wavelength. $2z$ is the round-trip optical path length difference in air where $z = z_R - z_S$ the path length difference. The factor of 2 here is related to the double pass. The factor ½ in intensity tells us that only half of the total power returning from both arms goes to the detector. The other half goes back to the source, and hence lost. For laser sources, caution should be taken in handling this returning power as it may affect or damage the laser oscillator.

From equation 2.5, given r_R and r_S, as amplitude reflectivities of reference and sample mirrors, respectively, the detected intensity I_D of equation 2.7 can be expressed in terms of the corresponding power reflectivities, $R_R = r_R^2$ and $R_S = r_S^2$ as

$$\boxed{I_D = \frac{1}{4} I_o\left[R_R + R_S + 2\sqrt{R_R R_S}\, \cos(\Delta\varphi) \right]}, \text{ where } I_o = A_o^2.$$ 2. 8

Equation 2.8 can be decomposed into two terms: a DC term (I_{DC}) and an interference term Γ as

$$\boxed{I_{DC} = 0.25(R_R + R_S)I_o}...DC \text{ term}$$ 2. 9

$$\boxed{\Gamma = 0.5\sqrt{R_R R_S}\, I_o \cos(\Delta\varphi) = 0.5\sqrt{R_R R_S}\, I_o \cos\left(2\pi\frac{1}{\lambda} \times 2z \right)}...interference \text{ term}$$ 2. 10

The DC term does not vary as the phase $\Delta\varphi$ changes and is constant whereas the interference term Γ varies with $\Delta\varphi$ in a sinusoidal manner, with constructive interference occurring for $z = 2m\lambda/4$ and destructive interference for $z = (2m+1)\lambda/4$, for an integer $m = 0, \pm1, \pm2, \pm3$, etc. Note that $z = z_R - z_S$ is the path length difference.

Figure 2.7 shows the plots of Γ versus the path length difference z between two arms for the two different monochromatic light waves $\lambda_1 = 1\,\mu\text{m}$ and $\lambda_2 = 1.3\,\mu\text{m}$. For a given monochromatic light, interference continues indefinitely for any path length difference with a fringe period given by

$$T_{fringe} = \lambda/2.$$

2. 11

When the wavelength λ changes, the fringe period T_{fringe} and the corresponding values of z where constructive and destructive interferences occur change. This means that if the light source is polychromatic, composed of more than one wavelength, the resultant intensity profile will change as shown in Figure 2.7 (c).
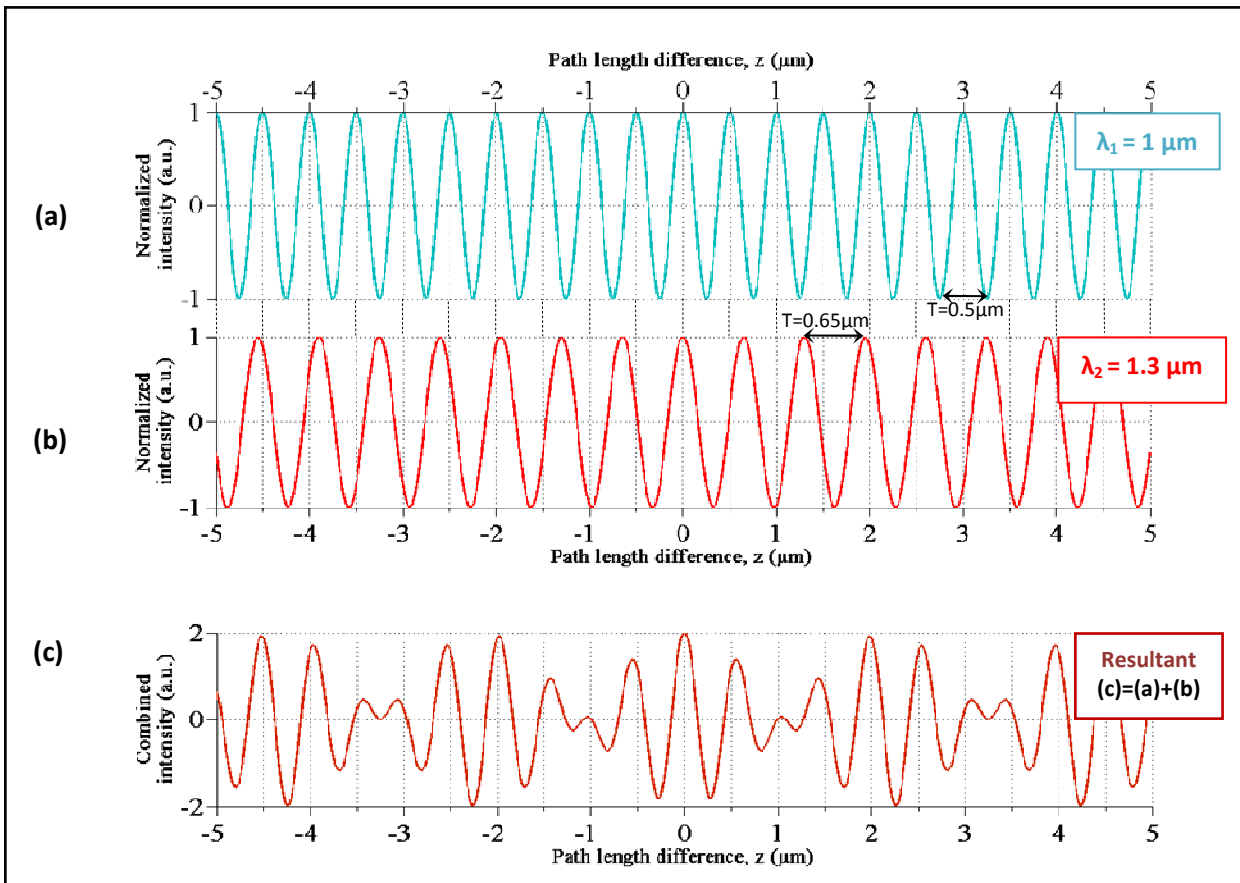
Figure 2.7 Plot of the interference term Γ of the detected intensity I_D versus path length difference z between the two arms of the Michelson interferometer for two monochromatic light waves of wavelengths $\lambda_1 = 1\,\mu\text{m}$ **(a)** and $\lambda_2 = 1.3\,\mu\text{m}$ **(b)**. Note that the fringe period $T_{fringe} = \lambda/2$ varies with wavelength. Plot **(c)** shows the resultant intensity profile of interference if the light source was composed of the two wavelengths.

2.5.3 Interference with polychromatic light

2.5.3.1 Interference with polychromatic light having discrete wavelengths

Now let us consider a polychromatic light wave, a wave with more than one wavelength, illuminating the Michelson interferometer (see Figure 2.8).
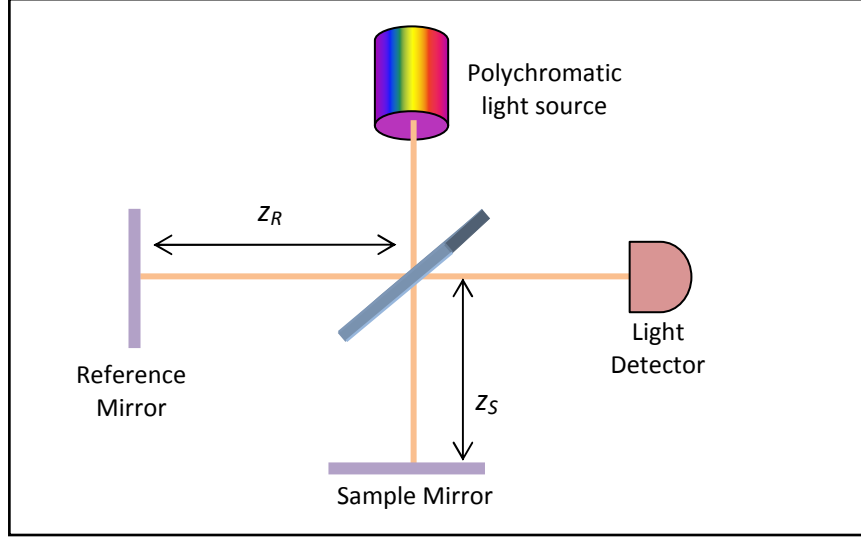
Figure 2.8 Michelson interferometer with polychromatic light source and identical mirrors in both arms.

Assuming that the polychromatic light wave is composed of N discrete monochromatic waves and that the reflectivity of both mirrors is independent of the wavelength, the DC and interference terms of equations 2.9 and 2.10 can be written as

$$I_{DC} = 0.25(R_R + R_S)\sum_{i=0}^{N} I_o(\lambda_i)$$

$$\Gamma(\lambda_i) = 0.5\sqrt{R_R R_S}\sum_{i=0}^{N}\left[I_o(\lambda_i)\cos\left(2\pi\frac{1}{\lambda_i}\times 2z\right)\right].$$

2. 12

Equation 2.12 implies that for a given path length difference z, the interference signal Γ will be determined by sum of all the interference signals corresponding to each wavelength.

Assuming a rectangular power spectrum (power carried by individual wavelength components is equal), i.e., $I_o(\lambda_1) = I_o(\lambda_2) = ... = I_o(\lambda_N) = I_o$, the interference given in equation 2.12 can be further simplified to

$$\Gamma(\lambda_i) = 0.5\sqrt{R_R R_S}\, I_o \sum_{i=0}^{N}\cos\left(2\pi\frac{1}{\lambda_i}\times 2z\right).$$

2. 13
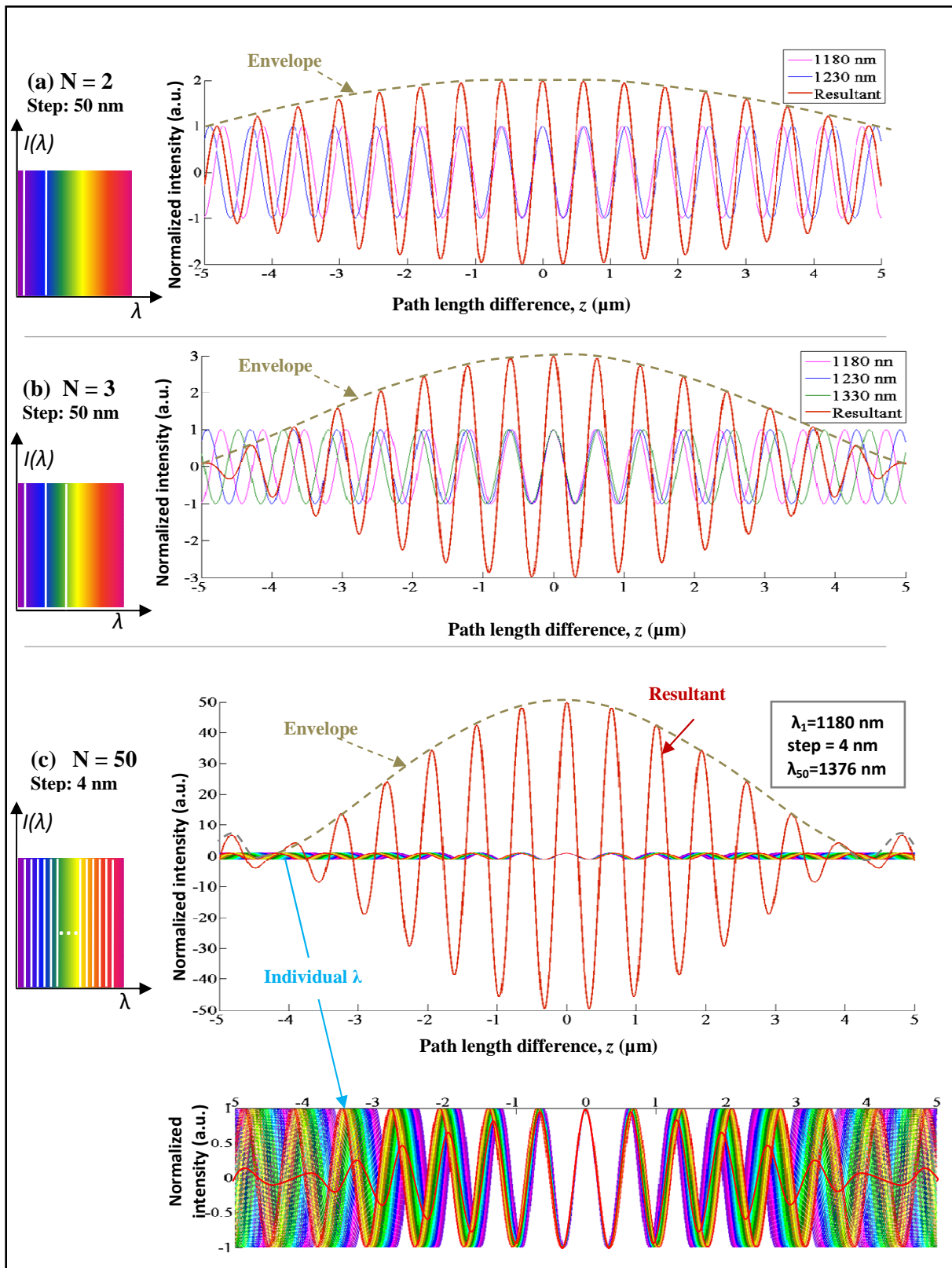
Figure 2.9 Interference with polychromatic light. N represents the number of wavelengths contained in interfering light. As N increases, the envelope width of the interference signal decreases, limiting interference to happen only around the zero path length difference z = 0 between the two arms of the interferometer. The signal power around z = 0 increases with N.

In Figure 2.9 (a), (b) and (c), the plots of individual monochromatic waves and the resultant interference term (Γ) for interference of polychromatic light wave with number of wavelengths N = 2, N = 3, and N = 50, respectively are given. From these plots, it can be concluded that as N increases, constructive interference becomes confined only around the zero path length difference, the maximum occurring at $z = 0$ and decaying as $|z|$ increases. For larger values of N, the decay rate is faster. This means that the envelop width of the interference signal is inversely proportional the number of wavelengths. Note also that the shape of envelope in Figure 2.9 (c) takes the shape of a sinuscardinal (*sinc*) function, which is related to the Fourier transform of the rectangular shape of the power spectrum.

2.5.3.2 *Interference with polychromatic light having continuous spectrum*

Light sources such as light emitting diodes or thermal light sources radiate polychromatic light energy with a continuous power spectrum (see Figure 2.10 (a)). The amplitude of the electric field, hence the power, corresponding to the individual spectral/wavelength components can also be different, giving rise to a specific shape of the spectrum, that defines the light source. The resultant electric field **E** of such polychromatic light wave with a given spectral shape (amplitude $\mathbf{A}(v)$ versus frequency v) can be written as a harmonic superposition of the individual electric fields (see equation 2.4) as

$$\mathbf{E}(t) = \int_{-\infty}^{\infty} \mathbf{A}(v)\exp(i2\pi vt)dv.$$ 2. 14

The spectral dependence of the source power on frequency, called the spectral power density (SPD), can be expressed the averaged square of the amplitude as

$$S(v) = \left\langle \left| \mathbf{A}(v) \right|^2 \right\rangle.$$ 2. 15

The plot of the resultant electric field $E(t)$ of a polychromatic light source is given in Figure 2.10 (b). The harmonic superposition of individual monochromatic waves with different frequencies gives rise to a resultant wave called wave packet (or wave train). Hence polychromatic light sources can be viewed as sources of streams of wave packets (see Figure 2.11, and note its difference with the plot of monochromatic wave given in Figure 2.5). The characteristic of wave packets is that a fixed phase relation exists only within individual wave packets. The length of an elementary wave packet where there is a definite phase relation is

called coherence length L_c, and the time it takes for the wave packet to pass a single point is called the coherence time τ_c, and $L_c = c/\tau_c$, where c is the speed of light.

Fourier transform pair

$$\mathbf{E}(t) = \int_{-\infty}^{\infty} \mathbf{A}(v)\exp(i2\pi vt)dv$$

$$\Delta\tau_c \cong \frac{1}{\Delta v}; \; v = \frac{c}{\lambda}$$

(a) Source spectrum (b) Elementary wave packet
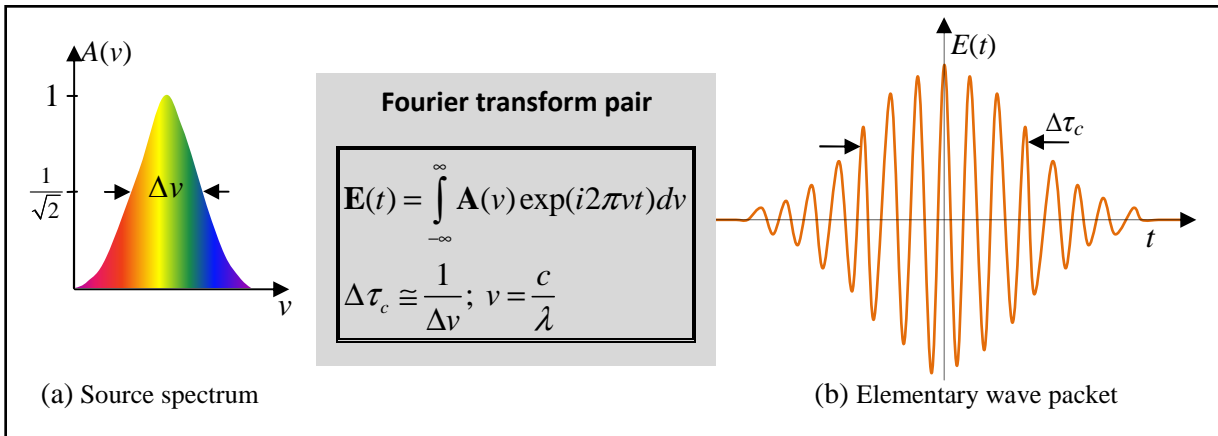
Figure 2.10 Polychromatic light sources emitting light with a continuous spectral bandwidth Δv. The harmonic superposition of individual frequencies gives rise to a resultant wave called wave packet. Fixed phase relation occurs only within individual packets. The time it takes for the wave packet to pass a single point is called coherence time. The Fourier transform relationship between Δv and $\Delta\tau_c$ implies that the broader the power spectrum, the shorter the coherence time.

The physical consequence behind having fixed phase relation only within individual wave packets is that two wave packets of the same origin (replica) can be made to interfere with a Michelson interferometer only if they are recombined in such a way that the optical path difference that each replica of the wave packet has travelled in each arm is within the coherence length of the wave packet. If the length mismatch is greater than the coherence length, no significant interference will be observed.
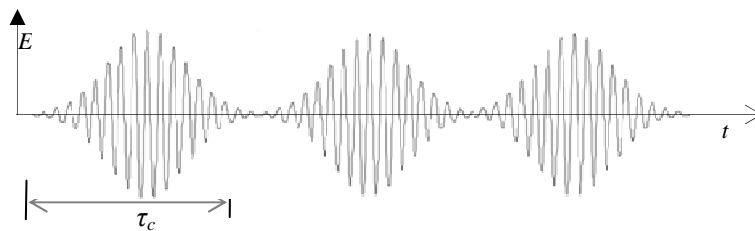
Figure 2.11 Low-coherence light comprised of wave packets emitted at a random time. Note its difference with the plot of monochromatic light wave given in **Figure 2.5**.

For a Michelson interferometer that is illuminated by a low-coherence light source having such a continuous spectral band as shown in Figure 2.10, the DC and interference terms of the intensity at the detector that was given in equation 2.12 can be expressed using integral as

$$\boxed{\begin{aligned} I_{DC} &= 0.25\left(R_R + R_S\right)\int_0^\infty S(\sigma)d\sigma \\ \Gamma &= 0.5\sqrt{R_R R_S}\int_0^\infty S(\sigma)\cos\left(2\pi\delta\sigma\right)d\sigma \end{aligned}} \quad , \text{where} \quad \delta = 2z, \ \sigma = \frac{1}{\lambda}. \qquad 2.16$$

Equation 2.16 shows a Fourier transform relation between the interference term Γ and the source spectrum $S(\sigma)$.

In modeling of low-coherence interferometry, a Gaussian-shaped light source spectrum is convenient to use because it approximates the spectral shape of most actual light sources. Moreover, a Gaussian function has a useful Fourier transform property: the Fourier transform of a Gaussian function is a Gaussian function as shown in equation 2.17

$$FT\left\{e^{-\left(\frac{x-b}{c}\right)^2}\right\} = c\sqrt{\pi}\times e^{-\pi^2 c^2 \xi^2}\times\cos\left(2\pi b\xi\right). \qquad 2.17.$$

Consider a low-coherence source with a Gaussian spectral power density $S(\sigma)$ given by

$$S(\sigma) = S_o e^{-4\ln 2\left(\frac{\sigma-\sigma_o}{\Delta\sigma}\right)^2}, \qquad 2.18$$

where $S_o = S(\sigma_o)$, $\Delta\sigma$ is the full-width-at-half-maximum (FWHM) and σ_o is central frequency and $\lambda_o = 1/\sigma_o$ is the central wavelength (see Figure 2.12 (b)).

The total intensity I_o of the low-coherence light will be the integral of SPD $S(\sigma)$ over all the frequency components

$$I_o = \int_{-\infty}^\infty S(\sigma)d\sigma = \int_{-\infty}^\infty S_o e^{-4\ln 2\left(\frac{\sigma-\sigma_o}{\Delta\sigma}\right)^2}d\sigma = \frac{\Delta\sigma}{2\sqrt{\ln 2}}\sqrt{\pi}\times S_o. \qquad 2.19$$

Hence the DC and interference terms of the detector light will be (see Figure 2.12 (c)).

$$\boxed{\begin{aligned} I_{DC} &= 0.25\left(R_R + R_S\right)I_o \\ \Gamma(\delta) &= 0.5\sqrt{R_R R_S}I_o \times e^{\frac{-\pi^2}{4\ln 2}\times\Delta\sigma^2\times\delta^2}\cos\left(2\pi\sigma_o\delta\right) \end{aligned}} \quad , \text{where} \quad \sigma_o = \frac{1}{\lambda_o}, \ \Delta\sigma = \frac{\Delta\lambda}{\lambda^2}, \ \delta = 2z. \qquad 2.20$$

The amplitude of Γ is called the coherence function $\gamma(\delta)$, and is given by

$$\gamma(\delta) = 0.5\sqrt{R_r R_s}I_o e^{\frac{-\pi^2}{4\ln 2}\times\Delta\sigma^2\times\delta^2} = 0.5\sqrt{R_r R_s}I_o \times e^{-4\ln 2\left(\frac{\delta}{L_c}\right)^2}, \qquad 2.21$$

where L_c refers to the FWHM of the coherence function as shown in Figure 2.12.
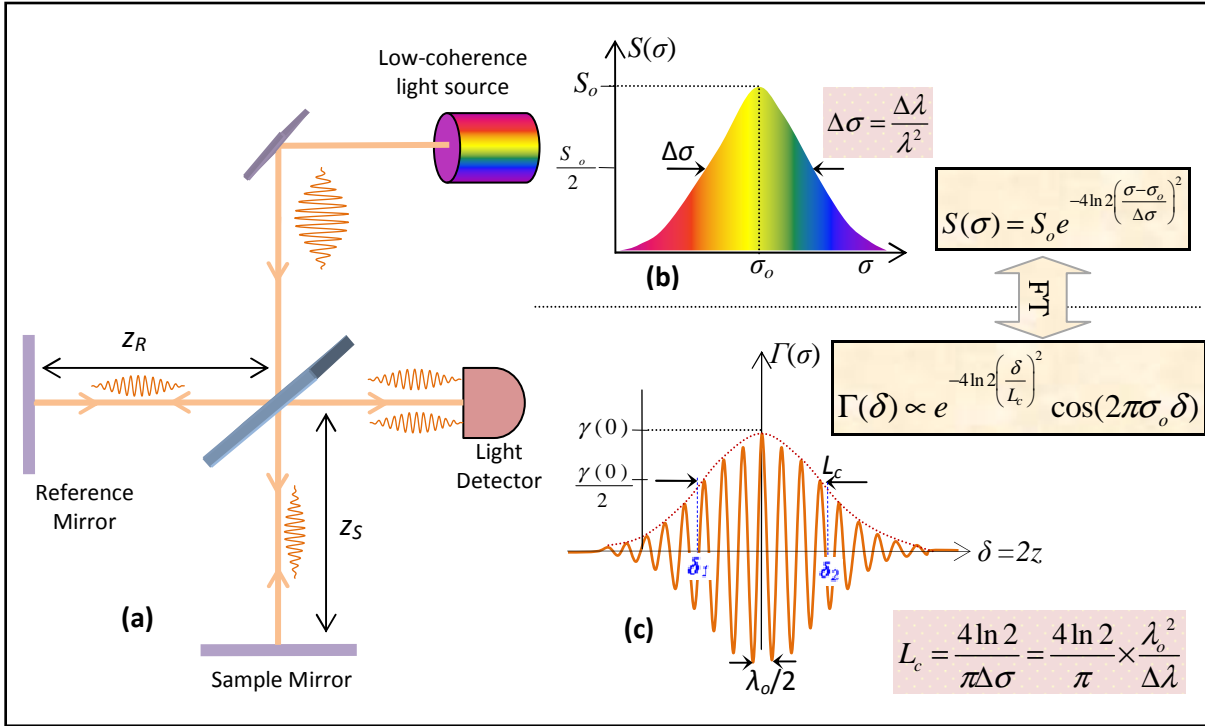
Figure 2.12 Interference of low-coherence light (a). Note that the envelope width Δδ of the interference term Γ shown in (c) is inversely proportional to the spectral width Δσ of the source spectrum $S_o(\sigma)$ shown in (b).

As it will be seen later, the coherence function determines the axial resolution of OCT. Hence this function is also called axial point spread function (PSF). It means that when low-coherence light is used, the coherence function determines the spread of the interference fringes corresponding to a planar reflector. As the coherence function is the envelope of the Fourier transform of the source spectrum, its shape and width entirely depend on the spectral shape and bandwidth Δσ of the emitted light. The coherence function is often characterized by the value of FWHM. This width is called coherence length, L_c. For Gaussian-shaped spectral power density considered above, the coherence length L_c (see equation 2.21) is given by

$$L_c = \delta_2 - \delta_1 = \frac{4\ln 2}{\pi\Delta\sigma},$$
2. 22

where $\delta_2 = 2z_2$ and $\delta_1 = 2z_1$ refer to the values of δ at which the coherence function attains half of its maximum value. Substituting $\Delta\sigma = \frac{\Delta\lambda}{\lambda_o^2}$, where $\Delta\lambda$ refers to the FWHM and λ_o the central wavelength of the spectrum , the coherence length is often expressed as

$$L_c = 2(z_2 - z_1) = 2\Delta z = \frac{4\ln 2}{\pi\Delta\sigma} = \frac{4\ln 2}{\pi} \times \frac{\lambda_o^2}{\Delta\lambda} .$$
2. 23

Comparing the interference of monochromatic light given equation 2.10 with that of low-coherence light wave given equation 2.20, a number of conclusions can be drawn:

a) In both cases, the fringe amplitude is proportional to the power reflectivity R_S of the sample, and the fringe period of low-coherence light interference is approximately equal to half of the center wavelength of the spectrum.

b) Unlike the constant fringe amplitude of monochromatic light interference, the envelope of fringe amplitude of low-coherence light interference depends on two parameters: the spectral bandwidth $\Delta\sigma$ of the low-coherence light and the round trip optical path difference (OPD) δ between the two arms.

c) For a given value of δ, the coherence function decays faster as $\Delta\sigma$ increases (as previously shown by simulation in Figure 2.9). This means that interference with broadband light occurs for relatively short OPD.

The actual shape of the coherence function is determined by the Fourier transform of the spectral power density of the light source (see Figure 2.13).

$$L_c = \frac{4\ln 2}{\pi} \times \frac{\lambda_o^2}{\Delta\lambda}$$
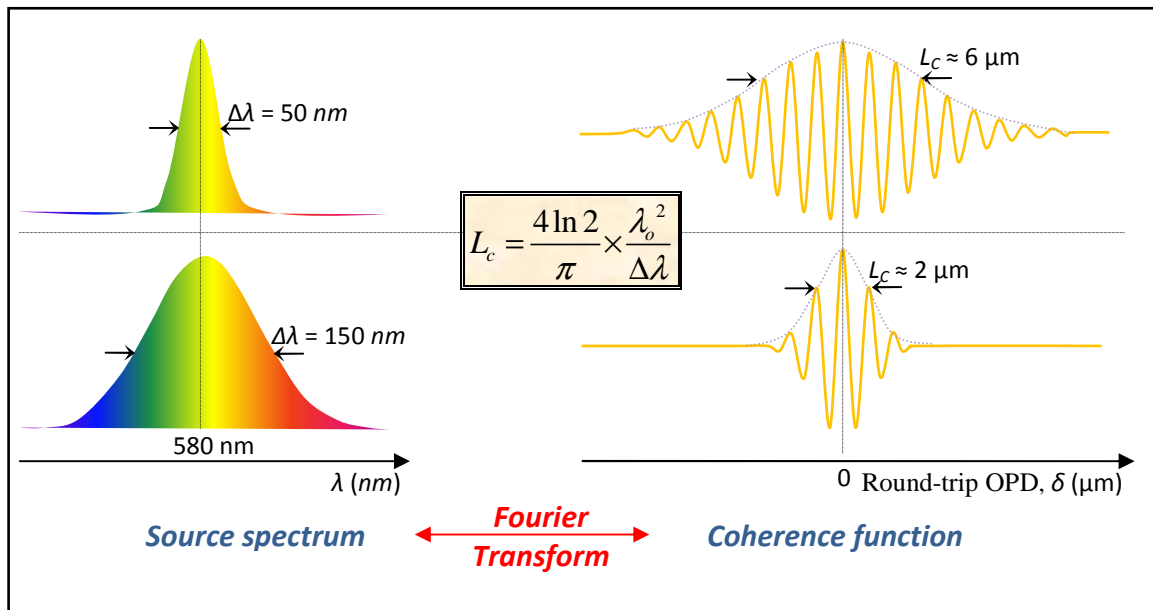
Figure 2.13 Illustration of Fourier transform relationship between spectral bandwidth $\Delta\lambda$ of the light source and the coherence length L_c of the coherence function. Note that when the width of the spectrum increases by a factor of three (from $\Delta\lambda = 50$nm to 150nm), the coherence length shortens by the same factor (from $L_c = 6\mu$m to 2μm)

For a Gaussian-shaped source, the shape of the coherence function is also Gaussian. If a rectangular-shaped source spectrum had been used, the coherence function would have been a "*sinc*" function. The FWHM of the coherence function, called coherence length, L_c, is directly proportional to the square of the center wavelength and inversely proportional to the spectral

bandwidth of the slight source: the broader the spectrum, the shorter the coherence length. It can be shown that a light source with Gaussian-shaped spectrum will give nearly a twice shorter coherence length than a rectangular-shaped source spectrum having a similar FWHM value of spectral bandwidth. Hence one should pay attention about the spectral shape of the source before using equation 2.23 to determine the coherence length of the source. A light source with a short coherence length provides good axial resolution for imaging.

2.5.4 Axial ranging using LCI

Let us now consider a sample (with a refractive index n) placed in the sample arm of the Michelson interferometer as shown in Figure 2.14. The reference mirror with a given reflectivity R_R is mounted on a translation stage at distance z_R from the beamsplitter. Assume that the sample is composed of three distinct partially light reflecting layers with power reflectivities $R_{S1} > R_{S3} > R_{S2}$ located from the beamsplitter at z_{S1}, z_{S2} and z_{S3}, respectively, with $z_{Sm} = z_R + nz_m$, where m = 1, 2, 3.

Figure 2.14 Axial profile measurement of a sample using LCI. By translating the reference mirror, the corresponding interference signal is captured. Applying the required signal processing gives information about the axial profile (reflectivity versus axial position) of the sample. The measurement accuracy, Δz, is limited to half of the coherence length.

As the reference mirror is translated, it changes the path length mismatch between the two arms of the interferometer. Let $\Delta\delta_1 = 2n(z_R - z_{S1})$, $\Delta\delta_2 = 2n(z_R - z_{S2})$ and $\Delta\delta_3 = 2n(z_R - z_{S3})$ be

the instantaneous round-trip optical path length differences corresponding to each sample reflector as the reference mirror is scanned. When $\Delta\delta_1 < L_c$, interference occurs between the backreflected light from the first reflecting layer of the sample and the light from the reference mirror. As the reference mirror keeps on translating, another interference between the reference mirror and the second layer, and later by the third layer, will be observed as soon as $\Delta\delta_2 < L_c$ and $\Delta\delta_3 < L_c$, respectively. The three separate interference fringes corresponding to the three different axial depths of the sample that are generated by translating the reference mirror are sequentially captured by a photodetector (see Figure 2.14(a)).

The amplitude of the interference fringe in each case is proportional to the intensity of the backreflected light from the each layer. In this typical illustration, the power reflectivity of the first layer is greater than the second and the third layers. Hence the amplitude of the interference fringes related to the first layer is proportionally greater than the amplitudes of the fringes related to the second and third layers, i.e., $R_{S1} > R_{S3} > R_{S2}$. This means that the sample reflectivity information is carried by the modulation amplitude of the high frequency interference fringe, often called the carrier signal. This useful information is extracted from the carrier term using demodulator electronics circuit (similar to AM radio receiver) as shown in Figure 2.14(b). The demodulated signal will be converted to digital signal by the analog-to-digital convertor (ADC) and stored in a personal computer (PC). Finally, the axial profile, plot of relative intensity versus depth, can be displayed as shown in Figure 2.14 (c). Hence in LCI, the amplitudes and echo time delays of sample reflections are measured by scanning reference mirror, and by simultaneously recording the amplitude of the interference signal.

Such technique of measuring short echo time delay and intensity of backreflected light from various layers of a sample using LCI has been applied in photonics in the late 1980s to measure optical echoes and backscattering in optical fibers and waveguide devices [40]. The first biological application of LCI was reported in 1988 by Fercher *et al* for the measurement of axial eye length [36].

2.5.5   Axial resolution of LCI

The axial resolution Δz of LCI refers to the minimum axial gap or distance between two axially oriented backreflecting layers that would still give rise to different interference peaks when using a low-coherence light wave with coherence length L_c. Consider the first and

second reflecting layers of the sample arm in Figure 2.14. Let $z' = z_{S2} - z_{S1}$ be the axial distance between the two layers. Assuming the sample has a refractive index of n, the corresponding the round-trip optical path difference will be $2nz'$. From the interference law of low-coherence light discussed in the previous section, if $2nz' < L_c$, the backreflected intensity from these two layers is added up together to give one big peak, looking like the existence of only one strong reflector. In this case, it will be impossible to know the presence of two individual structures. Hence for the two layers to be distinguishable, the round-trip optical path length difference between them should be greater than the coherence length, i.e., $2nz' \geq L_c$. This implies that $z' \geq L_c/2n$. Substituting the values of L_c from equation 2.23, the minimum resolvable axial separation Δz, simply called the axial resolution of LCI, is given by

$$\Delta z = \frac{L_c}{2n} = \frac{2\ln 2}{\pi n} \times \frac{\lambda_o^{\,2}}{\Delta\lambda} .$$

2. 24

Equation 2.24 shows that the axial resolution of LCI is directly proportional to the square of the center wavelength λ_o and inversely proportional to the spectral bandwidth $\Delta\lambda_o$ of the light source. An increase in $\Delta\lambda$ and/or a decrease in λ_o give rise to an improved axial resolution Δz. For example, if one uses a low-coherence light having a spectral bandwidth of $\Delta\lambda = 95$ nm centered at $\lambda = 800$ nm, the axial resolution will be $\Delta z = 3$ µm. It means that using such a light source, one can use LCI to measure an echo time delay down to 20 fs in air (≈ 13 fs in glass).

2.6 OCT techniques

The first OCT technique was first proposed by Huang *et al* in 1991 as an extension of LCI to tomographic imaging by incorporating a transversal beam scanning system [22]. In this type of standard OCT, two scans have to be performed: the depth (axial scan) and the transverse (lateral) scan. The OCT axial-scan uses time-domain LCI to detect axial positions of light re-emitting sites in the sample (producing A-scan). A series of A-sans at different transverse positions are performed using the transverse OCT beam scanner to addresses laterally adjacent sample positions in order to generate two-dimensional cross-sectional images (producing B-can). Performing multiple B-scans allows generating three-dimensional image of the sample. In order to increase the A-scan rate, a high-speed continuous-motion longitudinal (axial) scanning of the reference mirror is performed. A transverse beam scanning mechanism makes two dimensional imaging possible. Such type of OCT modality in which the depth profile in the sample is obtained sequentially in time by scanning the reference mirror with a constant speed is called Time-Domain OCT.

2.6.1 Time-domain OCT (D-OCT)

A schematic diagram of TD-OCT is shown in Figure 2.15 . It shows an example of an OCT system using a fiber optic Michelson-type interferometer. Fiber-based OCT is convenient for portable and endoscopic (catheter) imaging applications. Broadband light from the low-coherence light source is coupled into the Michelson interferometer using a single mode fiber. The interferometer contains a broadband 2×2 fiber coupler. Broadband fiber couplers are suitable for splitting or combining the broadband light. The beamsplitter in OCT usually has 50:50 splitting ratio; however practical OCT designs taking the advantage of unbalanced power splitting also exist [40].
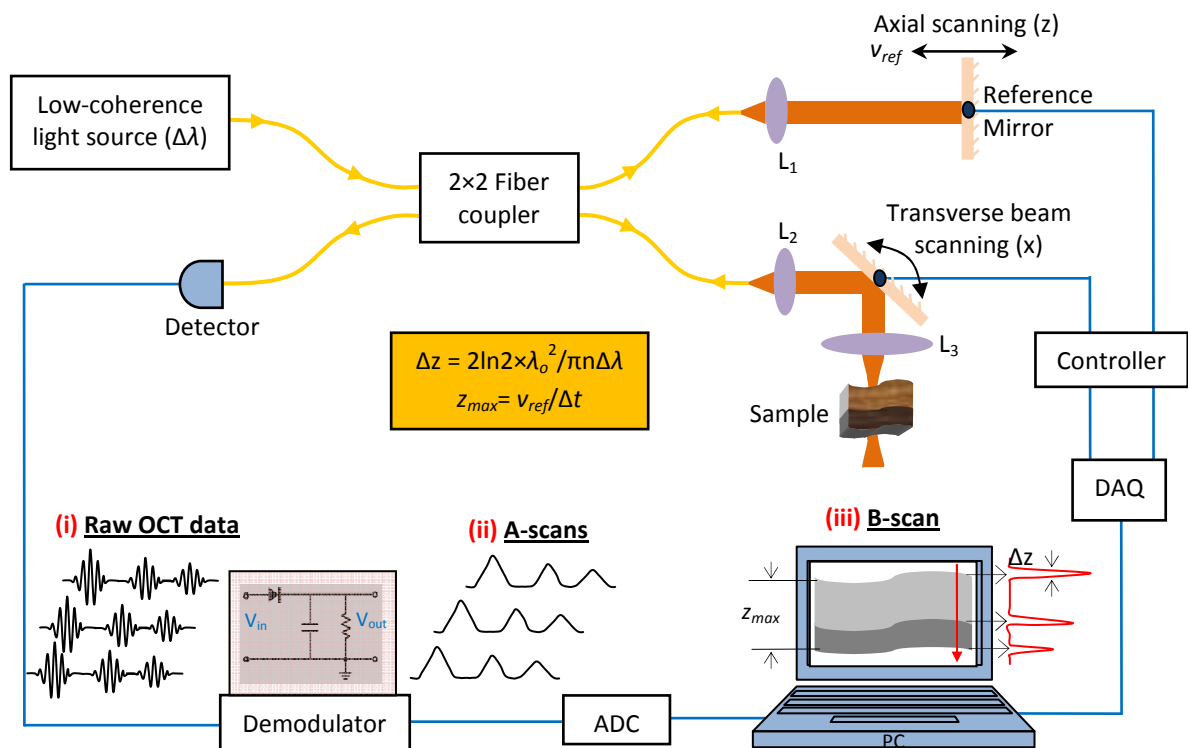
Figure 2.15 Schematic diagram of fiber-optic-based TD-OCT. The yellow solid line represents the single mode fiber-optic and the arrows indicate the direction of the light propagation. L_1, L_2 and L_3 refer to lenses. The red color represents the free space propagation of the broadband light. The blue line running from the light detector to the personal computer (PC) represents the flow path of the electronic signal. v_{ref} and Δt refer to the scanning speed and A-can acquisition time.

Light exiting the reference arm fiber is directed to the reference mirror that is mounted on a delay scanning mechanism. The reflected light from the mirror is redirected back into the same fiber. Light exiting the sample arm fiber is sent to a transverse beam scanning mechanism that scans the beam in one direction (x) or two directions (x-y). The scanned beam is focused on the sample using a scan lens L_3. The light backscattered or backreflected from the sample is redirected back through the same optical scanning system to the sample arm

fiber. After recombination in the fiber coupler, the returning reference and sample arm beams are then made to interfere on the light detector. The light detector converts interference fringes into electronic signals (voltage or current).

By continuously scanning the reference mirror (axial scan), the interference fringes corresponding to the different axial (longitudinal) profile of the sample are sequentially acquired by the detector, processed into A-scans and stored in a computer. After performing A-can for one transverse position, the same procedure is repeated for another transversal position of the beam on the sample. This is achieved by the transverse scanning system. A series of A-scans generated at different transverse positions are then stitched together to generate a two-dimensional (x-z, or y-z) cross-sectional images of the sample. In Figure 2.15, three raw A-scan data (i) corresponding to the three different transverse positions of the sample are shown. Each raw OCT signal has got three peaks corresponding to the three axial interfaces of the sample. Hence individual raw A-can OCT data carry the entire depth information of the sample along one line. Demodulating the raw data enables to reconstruct the depth dependent reflectivity (A-scan) shown in (ii). When multiple A-cans are combined together using appropriate image processing algorithm, an intensity-based two-dimensional image (B-scan) revealing the internal structural profile of the sample under investigation can be reconstructed (in grey scale or false color) as shown above (iii).

2.6.2   OCT parameters

The most important parameters often used to characterize an OCT imaging system are: imaging resolutions, sensitivity, imaging speed and imaging depth.

2.6.2.1 Image resolutions

Unlike conventional microscopy, the mechanisms that govern transversal and axial resolutions of OCT imaging system are decoupled from each other: transverse resolution depends on beam spot on the sample whereas axial resolution depends on the spectral width of the light source.

2.6.2.1.1   Transverse resolution

The transverse resolution refers to the resolution on a plane (x-y) that is orthogonal to the optical axis (z-axis). The transverse resolution, denoted by Δr, of images obtained from OCT systems, like other scanning imaging systems, is determined by the size of the focused beam spot on the sample. The spot size will be affected by the center wavelength λ_o of the light

source, the incident beam diameter D, and the effective focal length f' of the scan lens system. For a diffraction limited scan lens illuminated by a light beam having a Gaussian intensity profile, the transverse resolution Δr of OCT imaging is given by twice the beam waist w_o as

$$\Delta r = 2w_o = 2 \times \frac{\lambda_o}{\pi\alpha} = \frac{4\lambda_o}{\pi} \times \frac{f'}{D} \;. \qquad\qquad 2.\,25$$

where $\alpha = D/2f'$ is the spread angle of the focused Gaussian beam (see Figure 2.16).

Transverse Resolution

$$\Delta r = 2\frac{\lambda_o}{\pi\alpha} = \frac{4\lambda_o}{\pi} \times \frac{f'}{D}$$

Axial Resolution

$$\Delta z = \frac{2\ln 2}{\pi n} \times \frac{\lambda_o^2}{\Delta\lambda}$$

Transverse Field of View

$$FOV_{transverse} = 2f'\theta_{max}$$

Axial Field of View

$$FOV_{axial} = 2\frac{\lambda_o}{\pi\alpha^2} = \frac{\pi}{2\lambda_o}\Delta r^2$$
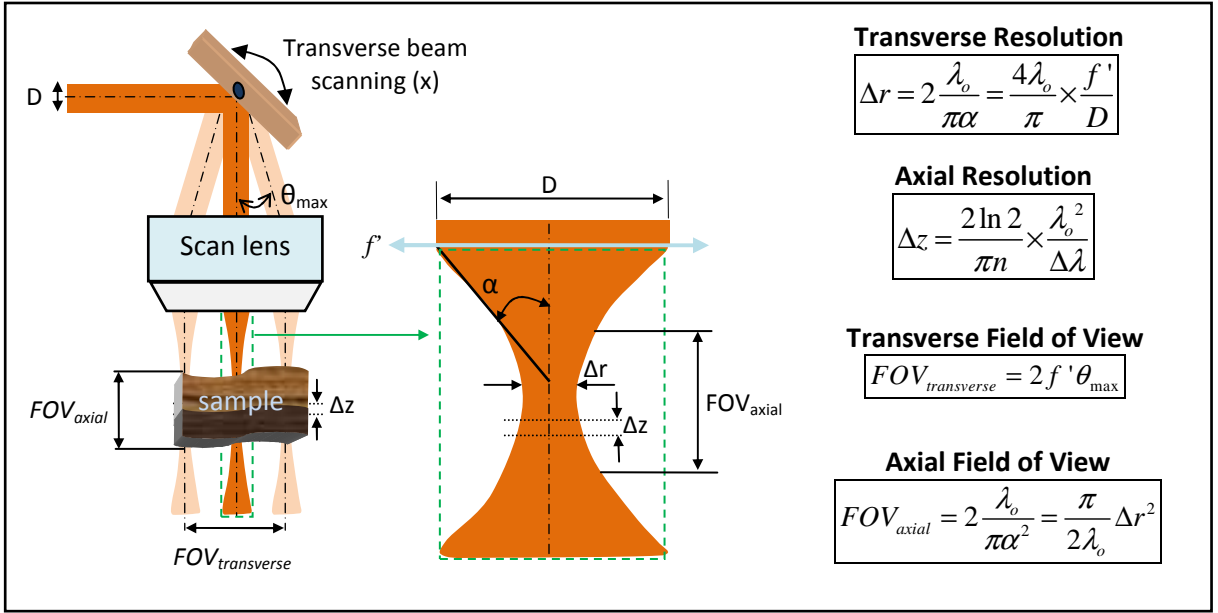
Figure 2.16 Schematic diagram of sample arm optics of OCT. The formula provided for $FOV_{transverse}$ is with the assumption of a simple f-theta scanning systems. The formulae given for Δz and FOV_{axial} are based on the assumption of a small diameter beam having a Gaussian intensity profile.

From equation 2.25, it is obvious that increasing the beam diameter D and/or using a scan lens with a shorter focal length f' improves the transverse resolution of OCT. However, the typical challenge of high-resolution OCT is the depth dependence of its transverse resolution. The stated resolution is valid only at the beam waist (often at the focal plane). However, if one moves away by distance z along the direction of beam propagation from the beam waist location, the depth dependent spot size $w(z)$ increases according to the following equation

$$w(z) = w_o\left[1+\left(\frac{\lambda_o z}{\pi w_o^2}\right)^2\right]^{1/2} = w_o\left[1+\left(\frac{z}{z_R}\right)^2\right]^{1/2}, \qquad\qquad 2.\,26$$

where $z_R = \pi w_o^2/\lambda_o$ is the Rayleigh range, the longitudinal distance from the beam waist to a point at which beam radius has increased by a factor of $\sqrt{2}$. Such an increase in the size of beam spot brings a depth dependent degradation of the transverse resolution, needing re-adjustment of the beam focus.

Figure 2.17 Effect of beam spot size on transverse resolution and axial Field of vew (FOV_{axial}). Note that large focused beam spot (a) gives long the a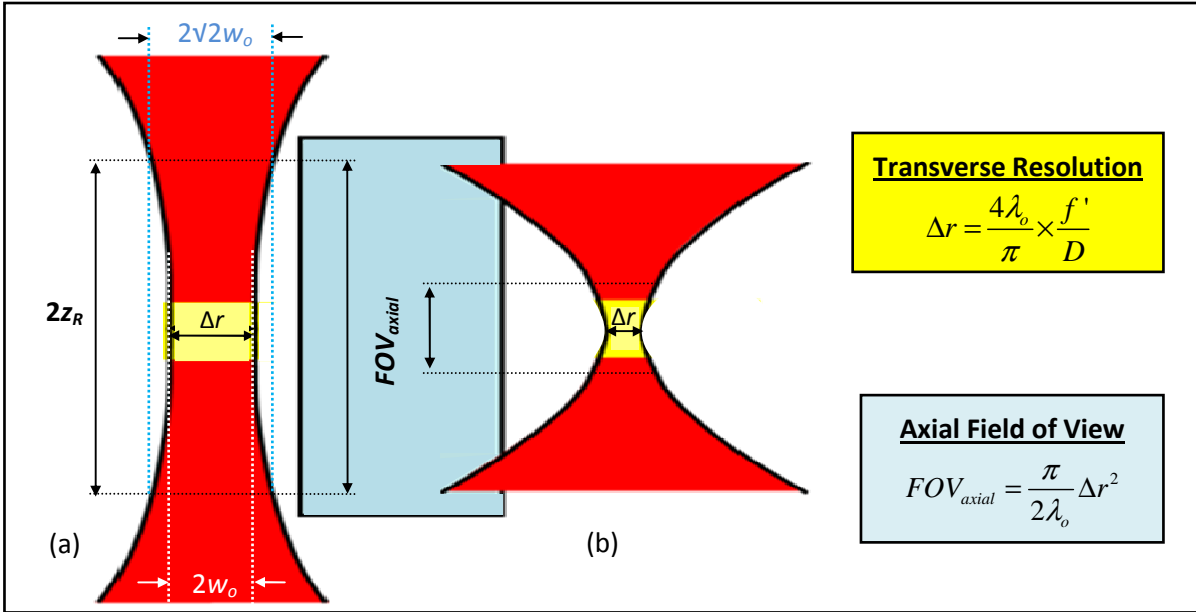xial field of view (FOV_{axial}) but bad transverse resolution, and vice versa when the focused beam size is small (b). The transverse resolution is given by the focus spot size and FOV_{axial} can be defined by twice the Rayleigh range/confocal parameter, adapted from [41].

The maximum axial extent of the sample that can be imaged without needing refocusing, often called depth of focus, or axial field of view (FOV_{axial}) in OCT, is defined by twice the Rayleigh range z_R as

$$FOV_{axial} = 2 \times z_R \simeq 2\frac{w_o}{\alpha} = 2\frac{\lambda_o}{\pi\alpha^2} = \frac{8\lambda_o}{\pi}\left(\frac{f'}{D}\right)^2 = \frac{\pi}{2\lambda_o}\Delta r^2 . \qquad 2.27$$

From equation 2.25 and 2.27, it can be easily understood that when the transverse resolution is improved by a given factor K either by decreasing f' and/or increasing D, the axial field of view will be reduced by a factor of K^2. As a result, OCT imaging with high transverse resolution over a significant depth range requires re-focusing of the beam in the sample [42], making the imaging system slower and more complicated.

2.6.2.1.2   Axial resolution

As OCT is based on LCI, its axial resolution Δz is mainly determined by the spectral properties of the light source, rather than the depth of focus as in microscopy (see section 2.5.5). Hence high axial resolution can be achieved with OCT even using low numerical aperture beam delivery optics.

From equation 2.24, we see that the axial resolution Δz is directly proportional to the square of the center wavelength λ_o and inversely proportional to the bandwidth $\Delta\lambda$ of the power

spectrum of the illuminating light. From this relation, one may intuitively conclude that one option to improve the axial resolution of OCT would be to use a light source that has a short center wavelength. However, as far as imaging biological tissues is concerned, the actual choice of the center wavelength depends on the attenuation of light due to absorption and scattering.

Optical absorption properties of tissues are dominated by the absorption of proteins, DNA, melanin, hemoglobin, and water as shown in Figure 2.18.
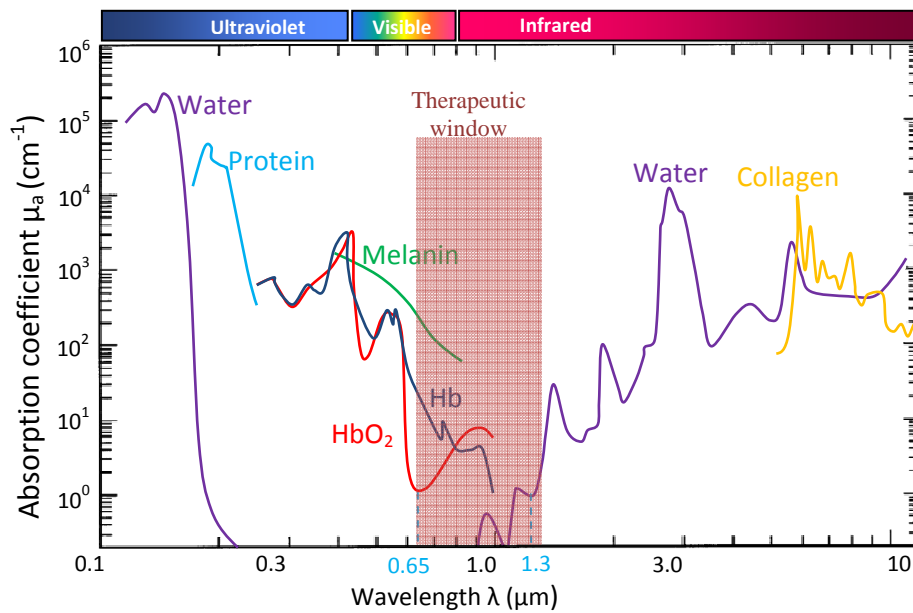
Figure 2.18 Optical absorption coefficients of principal tissue components (proteins, DNA, melanin, hemoglobin, and water) in the 0.1-12 µm spectral region (adapted from [43]).

Most biological soft tissues have relatively low light absorption property in the long visible and near infrared (NIR) spectral regions, especially between 650 nm and 1400 nm. This spectral range is known as "tissue optical window" or "therapeutic window". In this optical window, the absorption coefficient μ_a is relatively minimum and varies roughly between 0.1 - 1 mm^{-1}, whereas the scattering coefficient μ_s roughly varies between 10 mm^{-1} and 100 mm^{-1} [44], making scattering to be more prevalent than absorption. Outside of this region, light is greatly absorbed by tissue pigments (such as hemoglobin and melanin) in the visible spectral region and by tissue water content in the long wavelength NIR.

Within the therapeutic window, scattering is more prevalent than absorption. For imaging of low scattering such as the human retina, the short wavelength side of the therapeutic window around 800 nm is often used to achieve high axial resolution OCT images with a reasonable

bandwidth of light. For imaging of strongly scattering tissues such as skin, longer NIR wavelength is generally preferred because tissue scattering deceases nearly monotonically with wavelength. However above 1400 nm, absorption due to water becomes too high. In practice, wavelength around 1300 nm represents a good compromise between absorption and scattering, which enables to maximize the imaging penetration depth.

On the other hand, as the center wavelength increases, the axial resolution of OCT, according to equation 2.24, decreases. To keep the resolution high, one needs to significantly increase the source bandwidth. Figure 2.19 shows theoretical 'iso-resolution lines' for certain axial resolutions ranging from 0.25 µm to 24 µm. By moving along a given iso-resolution line, one can determine the spectral bandwidth of the light source required in order to maintain a given axial resolution for various center wavelengths. For any iso-resolution line, as the center wavelength become longer, the required bandwidth gets broader.
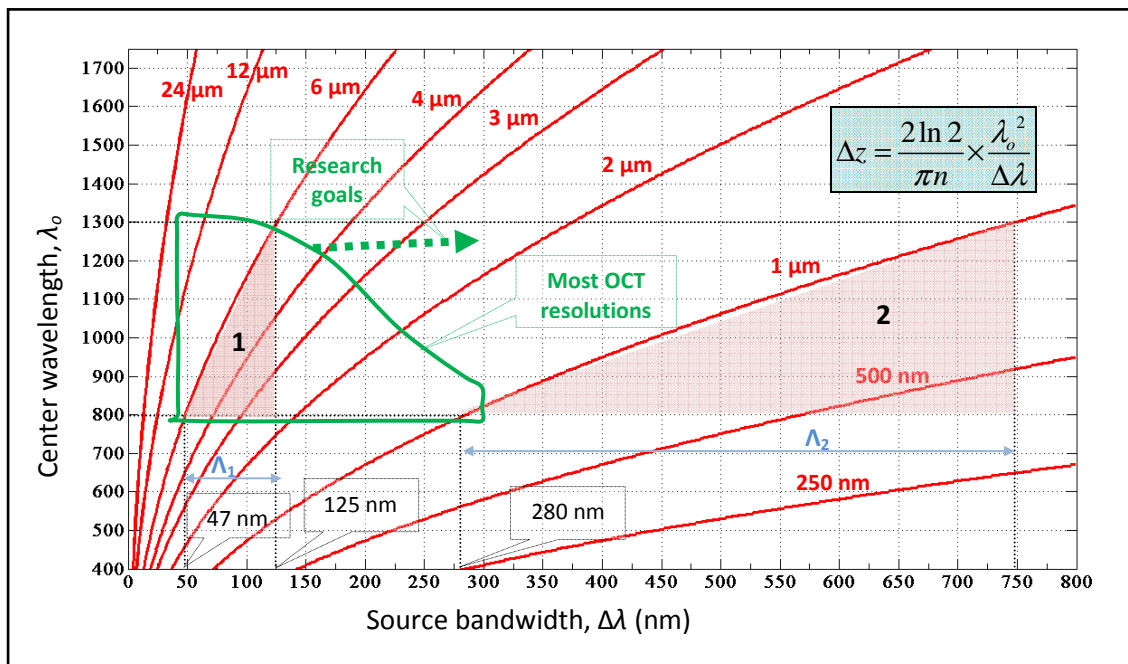
Figure 2.19 The red curves indicate 'iso-resolution' lines of few selected axial resolutions of OCT ranging from 0.25 µm to 24 µm, assuming a Gaussian light source spectrum. It shows the spectral bandwidth of the light source required in order to achieve a given axial resolution for various center wavelengths. The shaded regions (a) and (b) demonstrate that as we increase the center wavelength from 800 nm to 1300 nm, the additional bandwidth required to remain on the $\Delta z = 1$ µm iso-resolution line is 6 times of what is needed to stay on the $\Delta z = 6$ µm iso-line.

The two shaded regions (1) and (2) shown in Figure 2.19 explain that the additional bandwidth (the base of the shaded triangles) needed to stay in same iso-resolution line when increasing the center wavelength is smaller for low axial resolution than that for high-resolution. For example, for an axial resolution of $\Delta z_1 = 6$ µm, changing the center

wavelength from $\lambda_{oa} = 800$ nm to $\lambda_{ob} = 1300$ nm requires an additional bandwidth of $\Lambda_1 = 78$ nm ($\Lambda_1 = \Delta\lambda_{1b} - \Delta\lambda_{1a} = 125 - 47 = 78$ nm). Whereas, for an axial resolution $\Delta z_2 = 1$ µm, going from $\lambda_{oa} = 800$ nm to $\lambda_{ob} = 1300$ nm requires an additional bandwidth of $\Lambda_2 = 470$ nm ($\Lambda_2 = \Delta\lambda_{2b} - \Delta\lambda_{2a} = 750 - 280 = 470$ nm); and $\Lambda_2/\Lambda_1 = 470/78 \approx 6$.

The higher the axial resolution Δz, the more additional bandwidth is needed to go from short to long wavelength while keeping the resolution constant. As a result, getting a broadband light source with good spectral quality has still continued to be the technological bottleneck of long wavelength high-resolution OCT systems. If dispersion is not managed properly, the use of very broadband source will not necessarily give better resolution. The green zone in Figure 2.19 shows the region in which the resolutions of most OCT systems reside, and the goal of current research in OCT is to pull the green curve to the right.

2.6.2.2 Detection sensitivity

Another important parameter that characterizes OCT is its sensitivity. Detection sensitivity of OCT systems is a measure of the smallest sample reflectivity $R_{S,min}$ at which the signal-to-noise ratio (SNR) equals one. Sensitivity S can be defined as the ratio of the signal power generated by a perfectly reflecting mirror ($R = 1$) and that generated by $R_{S,min}$. Since these signal powers are proportional to the corresponding reflectivities, we have [44, 45]

$$S = \left. \frac{SNR}{R_{s,min}} \right|_{SNR=1} = \frac{1}{R_{s,min}} .$$

2. 28

The sensitivity is often expressed in decibel as $S[dB] = 10\times\log(1/R_{S,min})$. A high SNR is necessary for detection of the extremely low light intensities backscattered from turbid samples such as biological tissues. The SNR of any system is defined as the signal power divided by the variance of the noise

$$SNR = \frac{Signal_{Power}}{Noise_{Variance}} .$$

2. 29

The SNR analysis of TD-OCT systems can be followed directly from LCI presented in section 2.5.3.2. The analysis can be simplified by ignoring the autocorrelation (interference within the sample) terms and by considering only a single sample reflector in the coherence volume with power reflectivity of R_S.

In TD-OCT, a single photodiode is used to detect the optical power. Such detector registers

the continuous photoelectron current as a function of time. The detected photoelectron current (or simply photocurrent) i_D is related to the optical power P by $i_D(t) = rP$, where $r = \eta q_e/h v_o$ is the photodiode responsivity [Ampere/Watt], η is the quantum efficiency, q_e the electronic charge (1.602×10^{-19} C), h the Planck's constant (6.626×10^{-34} Js) and v_o the center frequency [Hz] of the low-coherence illuminating light. For $\lambda = 800$ nm, $\eta \approx 0.85$ and $r \approx 0.5 \, Ampere/Watt$.

From equation 2.20, the photocurrent $i_D(\delta)$ generated by interference term while scanning the reference mirror with a speed v_{ref} is given by

$$i_D(\delta) = r\frac{P_o}{4}\left[R_R + R_S + 2\sqrt{R_R R_S} \times e^{\frac{-\pi^2}{4\ln 2} \times \Delta\sigma^2 \times \delta^2} \cos\left(2\pi\sigma_o\delta\right) \right].$$ 2. 30

$P_o = \int_A I_o(r,\delta)dA$ is the instantaneous optical source power corresponding to the optical intensity I_o. Considering an ideal 50:50 beamsplitter, the instantaneous power incident on the sample and reference mirror will be each $P_o/2$. Depending on the application, this power is limited by the safety standards. From equation 2.30, the desired OCT signal $i_{D,signal}$ is given by

$$i_{D,Signal} = r\frac{P_o}{2}\sqrt{R_R R_S} \times e^{\frac{-\pi^2}{4\ln 2} \times \Delta\sigma^2 \times \delta^2} \cos\left(2\pi\sigma_o\delta\right).$$ 2. 31

The signal power is proportional to the square of the root-mean-square (RMS) of the signal current given in equation 2.31. At patch matched condition ($\delta = 0$), signal power is given by

$$Signal_{Power} = \left\langle i_D{}^2 \right\rangle_{Signal} = r^2 \frac{P_o{}^2}{8} R_R R_S . \quad \text{[in Ampere}^2\text{]}$$ 2. 32

In an optical detection system, several sources of noise are involved. They all cause random fluctuation in the detected electronic signal. If σ_i is the root mean square (RMS) current fluctuation, the power of the noise will be given by $\sigma_i{}^2$ [in Ampere^2]. The three dominating noise sources in a photodetector are receiver (dark + read out) noise $\sigma_{re}{}^2$, shot (Poisson) noise $\sigma_{sh}{}^2$ and excess intensity noise $\sigma_{ex}{}^2$. Receiver noise and excess noise dominate at low and high light conditions, respectively, and shot noise dominates in the intermediate regime [40]. In OCT, light detectors are usually operated close to saturation and the dominating source of noise in this condition is then shot noise. Shot noise is a Poisson process that is related to the random arrival of photons from the light source. The resultant photocurrent variance is the

shot noise and is given by [38, 44]

$$Noise_{Power} = \sigma_{sh}^{2} = 2q_{e}B\langle i_{D}\rangle, \text{ [in Ampere}^{2}] \qquad\qquad 2.33$$

where B is the electronic detection bandwidth and $<i_D>$ the mean detected current.

Assuming that the intensity of light backscattered from the sample is much smaller than that reflected from the reference mirror, the mean detector current is dominated by the reference arm power. Hence the mean value of the detected current (see equation 2.30) is given by

$$\langle i_{D}\rangle = r\frac{P_{o}}{4}R_{R}. \text{ [in Ampere]} \qquad\qquad 2.34$$

In TD-OCT, where the reference mirror is scanned over a maximum depth z_{max} during an A-scan acquisition time of Δt with at a constant scanning velocity of $v_{ref} = z_{max}/\Delta t$, the reference light frequency is Doppler shifted by $f_D = 2v_{ref}/\lambda_o = 2\sigma_o \times z_{max}/\Delta t$, and the resulting FWHM signal power bandwidth is $\Delta f_D = 2\Delta\sigma \times z_{max}/\Delta t$. The optimum detection bandwidth should be approximately twice the signal bandwidth. A larger bandwidth decreases the sensitivity and a smaller bandwidth decreases the axial resolution [46]. Hence the detection bandwidth B of TD-OCT is given by

$$B = 2\Delta f_{D} = 4\Delta\sigma v_{ref} = \frac{8\ln 2}{\pi}\times\frac{1}{\Delta z}\frac{z_{max}}{\Delta t} = 4\times\frac{\Delta\lambda}{\lambda_{o}^{2}}\frac{z_{max}}{\Delta t}. \qquad\qquad 2.35$$

Equation 2.35 shows that, in order to accommodate either an increased image depth z_{max} for a given resolution Δz, or an increased resolution for a given scan depth, the detection bandwidth B has to be increased. Increasing B has a negative impact on the SNR according to the expression given as

$$SNR = \frac{\langle i_{D}^{2}\rangle_{Signal}}{\sigma_{sh}^{2}} = \frac{r^{2}P_{o}^{2}R_{R}R_{S}/8}{2q_{e}B(rP_{o}R_{R}/4)} = r\frac{P_{o}R_{S}/4}{q_{e}B} = \frac{\eta}{hv_{o}}\frac{P_{S}}{B}. \qquad\qquad 2.36$$

Equation 2.36 shows that increasing the detection bandwidth decrease the SNR. $P_S = P_oR_S/4$ is the sample power returned to the detector out of $P_o/2$ incident on the sample.

Combing equations 2.28 and 2.36 for SNR = 1, the sensitivity S can be readily expressed as

$$S = \frac{1}{R_{s,min}} = \frac{r}{4}\times\frac{P_{o}}{q_{e}}\frac{1}{B} = \frac{\eta\pi}{32\ln 2}\times\frac{P_{o}\Delta t}{hv_{o}}\frac{\Delta z}{z_{max}}. \qquad\qquad 2.37$$

Equation 2.37 expresses that the shot noise limited sensitivity of TD-OCT is directly proportional to the source power and inversely proportional to the electronic bandwidth. Within the shot noise dominated range, S depends linearly on the source power. This regime is usually realized in OCT systems and can be regarded as optimum. This is because, at lower power, receiver noise would limit sensitivity, and at higher power, no additional sensitivity can be gained due to excess noise.

As it is based on interferometry, OCT is in general a high sensitive imaging technology. To have an idea about the order of sensitivity that can be obtained from OCT, let us insert typical numerical values: quantum efficiency $\eta = 0.85$, A-scan rate $1/\Delta t = 1$ KHz, axial resolution $\Delta z = 10$ µm and maximum imaging depth $z_{max} = 2$ mm. Substituting these values in equation 2.37 gives a sensitivity of $S = 2.4 \times 10^{11}$ with a source power $P_o = 1$ mW (0.5 mW on the sample). This means that a reflecting feature in the sample whose power reflectivity is as small as $R_{S,min} = 1/S = 4 \times 10^{-12}$ can be detected using TD-OCT at an acquisition rate of 0.35 MHz by sending an incident power on the sample of 0.5 mW. Any reflection below this value will be masked by the noise floor. Experimentally, in the shot noise limited regime, sensitivities of $S = 10^{11}$ and higher have been reported [44, 47].

2.6.2.3 Drawbacks of TD-OCT

If one wants to make two dimensional imaging at 10 frames per second using TD-OCT with 500 A-scan per image, the A-san rate has to be 5 KHz. Performing such fast mechanical scanning of the reference mirror is the first challenge of TD-OCT. The most common implementation of the reference arm delay line is a galvanometer-based translating retroreflector system [46]. The maximum scan rate of such type of scanner is approximately 0.1 KHz. Though faster scanning systems may be done with further system complications [40], the A-scan rate will be ultimately limited by the trade-off between signal bandwidth and detection sensitivity because for a given fixed optical power incident on the sample, the signal bandwidth is directly proportional to the reference mirror scanning speed (see equation 2.35) and inversely proportional to the sensitivity (see equation 2.37).

Hence the other drawback of TD-OCT imaging system is that the sensitivity, the optical power, resolution, imaging depth and A-scan rate are coupled together. Note from equation 2.35 that for a given A-san rate $1/\Delta t$, increasing the imaging depth z_{max} for a fixed axial resolution Δz, or increasing Δz for a fixed z_{max} requires increasing the detection bandwidth B, i.e., the signal acquisition rate must be increased. Since the maximum permissible power that

can be sent to biological sample is limited by the safety standards, increasing B will ultimately decrease the sensitivity according to equation 2.37.

For imaging of biological tissue, high sensitivity is generally needed with a limited incident optical power. Depending on the responsivity of the detector, this decides the maximum detection bandwidth. The maximum axial resolution will be determined by the light source bandwidth when choosing the source. This leaves the remaining two parameters, the A-scan rate and the maximum depth, to compete each other. If speed is the priority, one has to reduce the maximum imaging depth, or vice versa.

For example, consider that one is interested to perform TD-OCT imaging of a sample with a sensitivity $S = 95$ dB using a light source with output power P_o of 10 mW (with 5 mW on the sample) and spectral bandwidth $\Delta\lambda = 30$ nm centered at $\lambda_o = 840$ nm. If a camera having quantum efficiency $\eta = 85\%$ is used, equation 2.37 fixes the required maximum detection bandwidth to $B = 100$ KHz (i.e., electronic sampling period $T = 10$ µs). Knowing B fixes the maximum scanning speed v_{ref} of the reference arm according to equation 2.35 as

$$v_{ref,max} = z_{max}(1/\Delta t) = \frac{1}{4} \times \frac{\lambda_o^2}{\Delta\lambda} B \simeq 0.6 \, m/s \, .$$

The product between the maximum depth z_{max} and the A-scan rate $(1/\Delta t)_{max}$ becomes fixed, and increasing one will proportionally decrease the other. If one targets a maximum imaging depth of $z_{max} = 1.5$ mm, then the corresponding maximum A-scan rate is $(1/\Delta t)_{max} = 0.4$ KHz. Scanning the reference mirror faster than 0.6 m/s will make the axial resolution worse than 10 µm (which is determined by the source bandwidth). And if P_o is reduced from 10 mW to 1 mW, B should be reduced from 100 KHz to 10 KHz in order to maintain the same sensitivity. The scanning speed of the reference arm should also be reduced from 0.6 m/s to 0.06 m/s. Such trade-off between imaging parameters is the fundamental limit of TD-OCT for high-speed and high-resolution imaging requirements.

A relatively recent OCT technique where the sensitivity is no more a function of the scanning speed of the reference mirror is called Fourier-Domain OCT (FD-OCT). In FD-OCT, there is no need of scanning the reference mirror, hence it is faster. In this technique, the sensitivity of FD-OCT does not depend on the axial resolution (or source bandwidth).

2.7 Fourier-Domain OCT (FD-OCT)

In FD-OCT techniques, the depth information of a given sample which is illuminated by a multi-wavelength (low-coherence) light is obtained by measuring the spectral interferogram. The entire depth profile of the sample is retrieved, without scanning the reference mirror, by Fourier transforming the acquired spectral interferogram. Hence, the first obvious advantage of FD-OCT over TD-OCT is the imaging speed [48]. With comparable sensitivity, A-scan rate of FD-OCT which is ~ 60 times faster than that of TD-OCT has been experimentally demonstrated [49], enabling near real-time 3-D imaging [50, 51]. The other advantage of FD-OCT compared to TD-OCT is its improved sensitivity [52]. Sensitivity improvement of FD-OCT more than two orders of magnitude (21.7 dB) over TD-OCT has been experimentally demonstrated [53].

In FD-OCT, the mechanical A-san of TD-OCT is replaced by spectroscopic measurements achieved either by a spectrometer (spectral-domain OCT, SD-OCT) or by using a swept source (swept-source OCT, SS-OCT). The term FD-OCT is sometimes used to refer to SD-OCT only but in this dissertation, FD-OCT will be used to refer to both SD-OCT and SS-OCT.

2.7.1 Spectral-Domain OCT (SD-OCT)

In SD-OCT, the combination of reference mirror scanning and single photodetector of TD-OCT (see Figure 2.15) is replaced by a spectrometer as shown in Figure 2.20). The reference mirror in SD-OCT is immobile. The backreflected and backscattered light from reference and sample arms is recombined at the beamsplitter. Light backscattered from different depths in a sample, which correspond to various optical delays, interferes with light reflected back from a reference mirror located at a fixed position.

At the output of the interferometer, the recombined light beam is dispersed by a diffraction grating. When we look at the interference as a function of wavelength, for a given optical path difference between the backscattering feature in the sample and the reference mirror, destructive and constructive interference occurs depending on the wavelength component. This results in a modulated power spectrum, often called spectral spectrogram. The modulation frequency of the spectral interferogram is related to the optical path difference associated with the depth location of the backscattering feature within the sample, whereas the modulation amplitude is proportional to the intensity of the backscattered light.
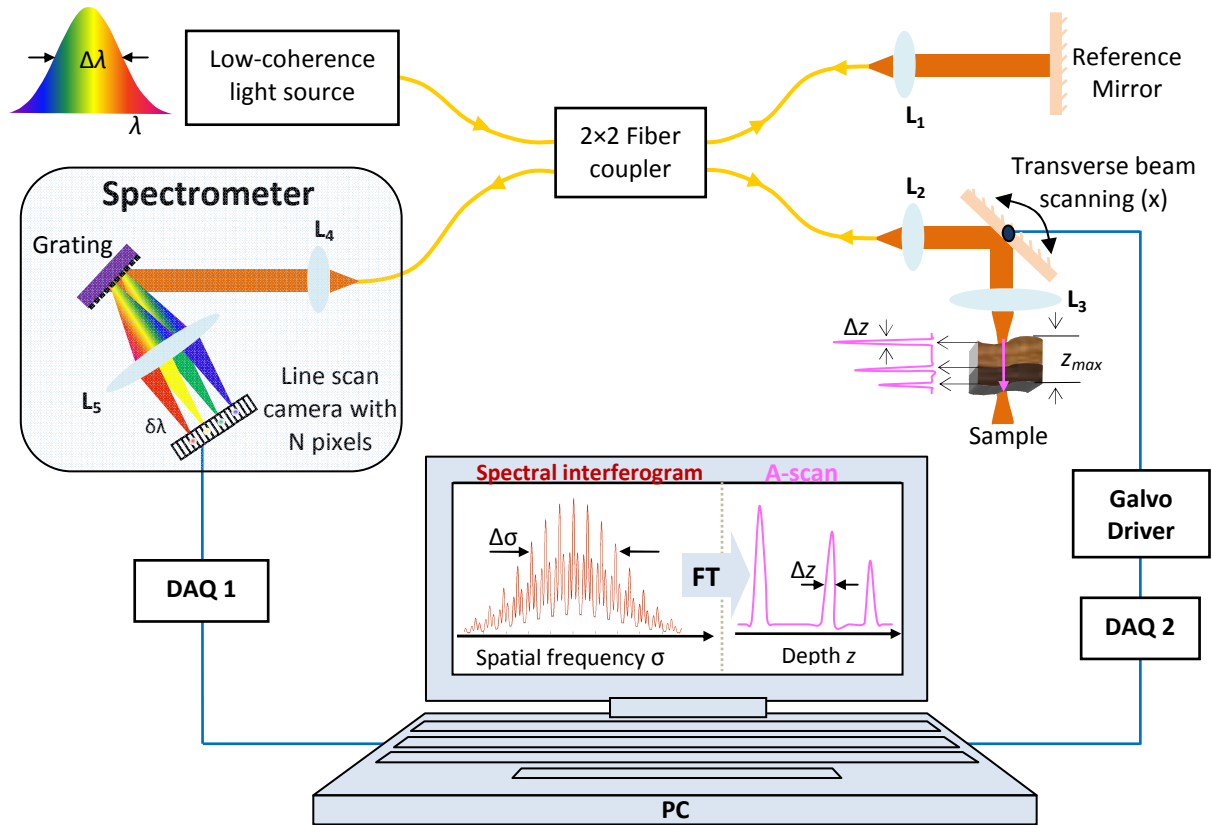
Figure 2.20 Schematic diagram of fiber-based SD-OCT.
The diffraction grating at the output of the Michelson interferometer disperses light, producing a spectral interferogram, which will be acquired in parallel by the line scan camera. Transverse beam scanning is still performed in SD-OCT. DAQ1 and DAQ1 are data acquisition boards.

The dispersed spectral interferogram is collected by a line-scan camera. Each pixel of the line-scan camera detects a spectral linewidth $\delta\lambda$ of the spectral interferogram. Therefore, $\delta\lambda$ refers to the sampling resolution of the spectrometer. The intensity-based depth profile of the sample is then reconstructed from a single-acquired spectral interferogram by performing the Fourier transform. The sampling resolution $\delta\lambda$ determines the imaging depth of SD-OCT: the finer $\delta\lambda$, the better the sampling resolution, and the deeper the imaging depth. The increased SNR in SD-OCT compared with that of TD-OCT is due to the significant reduction of the shot noise obtained by replacement of the single-element detector of TD-OCT with a multi-element array detector (to be discussed in chapter 3, section 3.2.4).

2.7.2 Swept-Source OCT (SS-OCT)

Another approach of realizing FD-OCT is by using a combination of a broadband tunable laser source and a single-element detector (see Figure 2.21). Such a configuration is called SS-OCT [53].
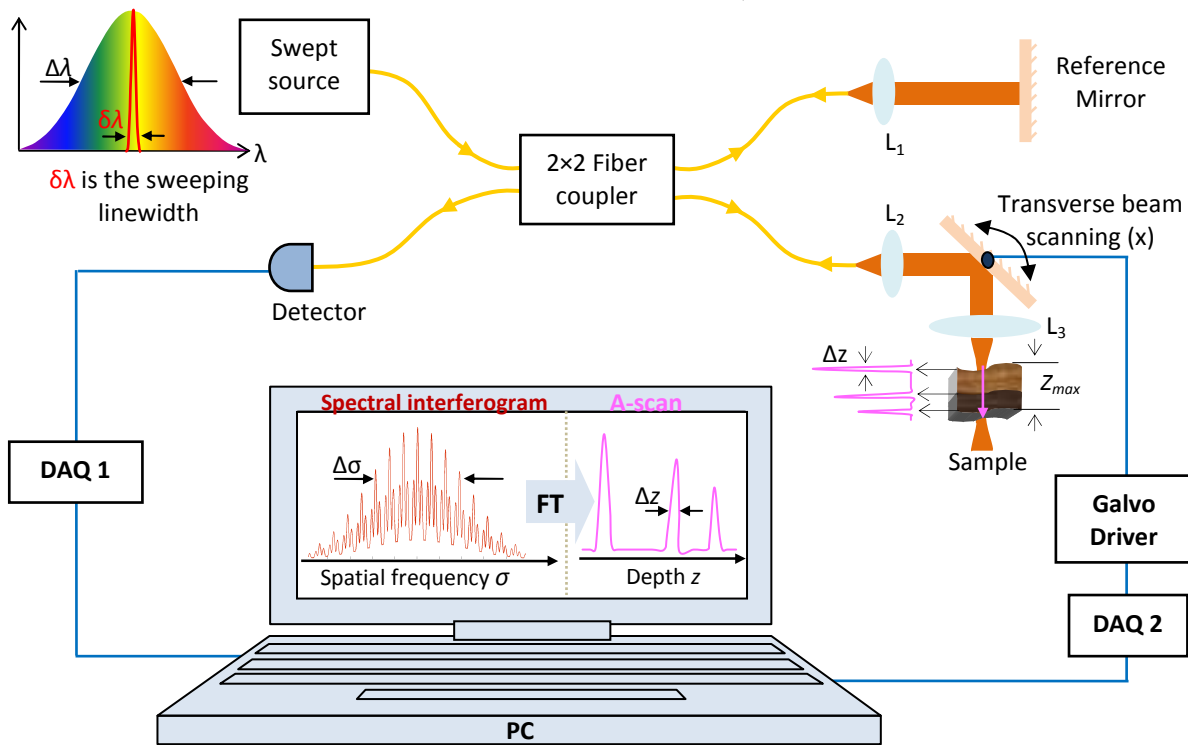
Figure 2.21 Schematic diagram of fiber-based SS-OCT.
In SS-OCT, the reference mirror scanning of TD-OCT (see **Figure 2.15**) is replaced by the use of a broadband swept source. By sweeping a narrow linewidth δλ across a broadband tunable laser source, the instantaneous interferogram is recorded by a single photodetector as a function of time.

As the emission wavelength of a narrow linewidth δλ is rapidly swept across the available bandwidth of the light source, the instantaneous interferometric signal is recorded using a single photodetector as a function of time. Once δλ is scanned across the entire source power spectrum, the recorded interferogram by SS-OCT resembles that of SD-OCT. Fourier transforming the recorded interferogram gives the A-san. The transverse scanning helps perform B-scan by acquiring multiple A-scans at different transverse positions of the sample.

2.8   Conclusion

OCT is a modern optical imaging technology that can perform cross-sectional imaging of biological tissues and semi-transparent materials at micrometer-scale resolution with few millimeters of imaging depth. Comparing OCT with other imaging systems, we see that OCT fills the gap between ultrasound imaging and confocal microcopy. As OCT is based on low-coherence interferometry, its axial resolution is determined by the coherence length of the light source: the broader the spectrum of the light source, the better the axial imaging resolution. The transverse imaging resolution of OCT, like any other scanning microscopes, is determined by the size of the focused beam spot on the sample.

Depending on the A-scan reconstruction technique, two main OCT modalities exist: TD-OCT and FD-OCT. For our application, a high-resolution OCT system capable of imaging the Schlemm's canal in real-time is required. As TD-OCT generates A-scans by mechanically scanning the reference mirror, high-speed scanning is one of the challenges of performing fast imaging using this modality. The other drawback of TD-OCT is that the detection sensitivity is inversely proportional to the axial resolution. For a given A-scan rate, high-resolution TD-OCT is realized at the expense of its sensitivity. If one wants to increase the sensitivity of high-resolution TD-OCT, then the A-scan rate (i.e., the imaging speed) has to be reduced. Hence TD-OCT is not appropriate for our application.

On the other hand, in FD-OCT, the A-scan is computationally reconstructed from the measured spectral interferogram without any reference mirror scanning. The sensitivity of FD-OCT does not depend on the axial resolution. As FD-OCT is faster and more sensitive than TD-OCT, it has been chosen for our project. FD-OCT itself can be realized either using a swept laser source (SS-OCT) or using a spectrometer (SD-OCT). For our project, a low-resolution commercial SS-OCT and a high-resolution SD-OCT developed in the laboratory both working at 1.3 µm center wavelength have been investigated.

Unlike the conventional OCT systems working around 0.8 µm, the center wavelength around 1.3 µm has been chosen in order to reduce the effect of scattering in sclera and edematous cornea and enhance the OCT imaging depth. However, because of the $\lambda^2/\Delta\lambda$ dependence of the axial resolution, high-resolution OCT imaging at 1.3 µm center wavelength requires a light source with extremely broad spectral width. Finding a broadband tunable laser source is a technological challenge for developing high-resolution SS-OCT at this center wavelength. On the other hand, as it does not require a tunable laser source, high-resolution SD-OCT at 1.3 µm seemed to be easier to achieve. As a result, we have developed a high-resolution resolution SD-OCT system working at 1.3 µm center wavelength [54] using a relatively low-cost broadband superluminescent diode (SLD) light source.

Developing a high-resolution SD-OCT system at 1.3 µm requires designing a broadband spectrometer and dealing with the subsequent dispersion management issues. In the next two chapters the design, characterization, performance and demonstration of the high-resolution SD-OCT system that was developed are discussed.

Chapter 3 - Development of spectral-domain OCT

3.1   Introduction

The concept of one-dimensional length measurement of an object by measuring the intensity of backscattered light at various wavelengths using one direction of illumination was demonstrated by Fercher *et al* in 1995 [55]. This work was adapted from an earlier work by Wolf in 1969: the three-dimensional distribution of the scattering potential of a semi-transparent object can be computationally reconstructed from the distribution of amplitude and phase of the light scattered by the object [56]. The technique was first called "backscattering spectral interferometry" and was applied for one dimensional measurement of intraocular distances, and later with addition of transverse scanning it evolved as a new OCT modality and took the name Fourier-domain OCT (FD-OCT) from the fact that the depth information is obtained by applying Fourier transform.

In the previous chapter, it has been explained that unlike TD-OCT where the depth information of the sample is obtained sequentially in time by scanning the reference mirror, the depth information in FD-OCT is rather computationally reconstructed by Fourier transformation of the interferometric signal. Hence getting access to the spectral interferogram is therefore the key issue to FD-OCT design. The spectrum can be obtained by two techniques: either by employing a spectrometer or by using a broadband tunable laser source whose instantaneous emission wavelength can be swept rapidly. The spectrometer based FD-OCT is called spectral-domain OCT (SD-OCT) and the other based on swept-source is called swept-source OCT (SS-OCT). Compared to conventional TD-OCT, both FD-OCT techniques yield significantly better imaging speed and detection sensitivity [45, 48, 57], which is required for *in vivo* imaging of biological tissues. For our application, we also need high axial resolution in order to image the Schlemm's canal of human eye. As the resolution of SS-OCT is limited by the availability of a broadband tunable laser source which is still technologically challenging, we have developed an original high-resolution SD-OCT system. In this chapter, the principle and design process of our SD-OCT system is presented.

Before going into the details of the SD-OCT design issues, the principle of SD-OCT is first presented to answer the following two basic questions:

    i.   What type of raw OCT signal is acquired in SD-OCT?

ii.   How does Fourier transform reconstruct the whole depth profile (A-san) of the sample from a single acquired dataset?

3.2   Principle of SD-OCT

A simplified schematic diagram of SD-OCT is given in Figure 3.1. SD-OCT detects the wavelength-resolved interference signal by using a spectrometer consisting of a diffraction grating, focusing optics and a line camera.
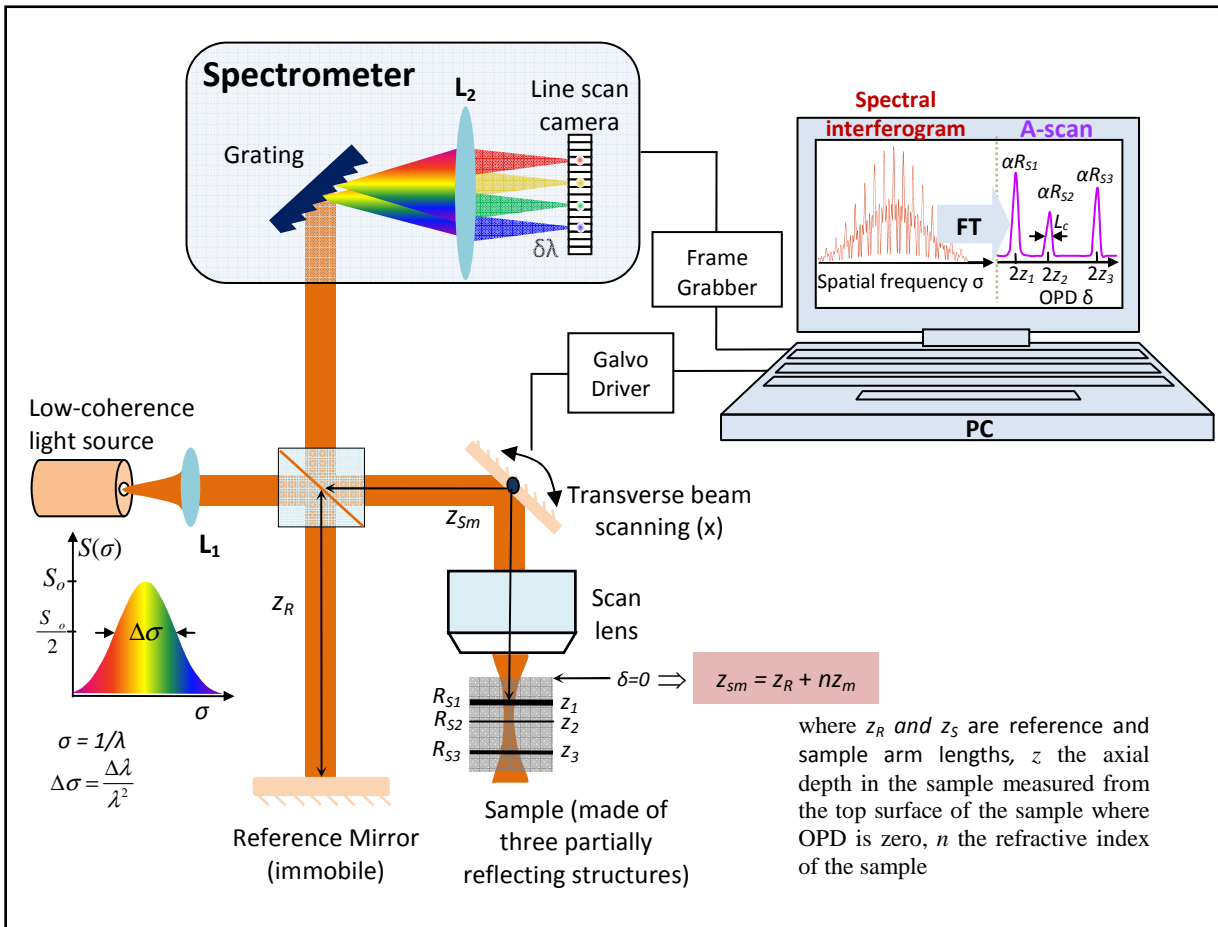

Figure 3.1 Schematic diagram of fiber-based SD-OCT

The grating at the output of the Michelson interferometer disperses the recombined light, producing a spectral interferogram, which will be acquired in parallel by the line scan camera that has N pixels. The axial profile of the sample (A-scan) is then reconstructed from the single spectral interferogram, which is acquired in one shot without scanning the reference mirror, just by applying Fourier transform. Transverse beams scanner is still present in SD-OCT. The axial resolution of SD-OCT, like that of TD-OCT and LCI, depends on the bandwidth of the light source.

The SD-OCT system shown above consists of a low-coherence light source that is directed into a Michelson interferometer. An broadband cube beamsplitter splits the incident broadband light with spectral power density $S(\sigma)$ into the reference and sample arms. Light backscattered by structures inside the sample located at different depths which correspond to

various optical delays, is recombined at the beamsplitter with the light reflected by the reference mirror (immobile). At the interferometer output, a spectrometer records the interference pattern as a function of wavelength. This is achieved by locally dispersing the recombined light beam by a grating, i.e., each wavelength component is spatially separated, producing the spectrum of the interference pattern (often called spectral interferogram). The dispersed light is focused on a one-dimensional CCD detector having an array of N pixels (often called line scan camera). Each pixel of the line CCD camera detects a given narrow spectral portion $\delta\lambda$ of the interference pattern, i.e., the spectral interferogram is sampled by the pixels of the line scan camera with a sampling resolution of $\delta\lambda$. The depth profile of the sample is then obtained by Fourier transforming the detected spectral interferogram.

3.2.1 Mathematical representation of the raw SD-OCT signal

Considering a sample with refractive index n composed of M discrete reflectors, the photocurrent i_D generated by a square-law detector can be expressed as a function of spatial frequency σ (or wavelength λ, $\sigma = 1/\lambda$) as [26]

$$
\begin{aligned}
i_D(\sigma) = &\frac{\rho}{4} S(\sigma) \left[R_R + \sum_{m=1}^{M} R_{sm} \right] \quad \text{DC component} \\
&+ \frac{\rho}{4} S(\sigma) \left[2 \sum_{m=1}^{M} \sqrt{R_R R_{Sm}} \cos(2\pi\delta_m \sigma) \right] \quad \text{Signal component} \\
&+ \frac{\rho}{4} S(\sigma) \left[2 \sum_{m \neq n=1}^{M} \sqrt{R_{Sm} R_{Sn}} \cos(2\pi\delta_{mn} \sigma) \right] \quad \text{Autocorrelation component}
\end{aligned}
\qquad 3.1
$$

$\rho = \eta_s \times r$, where η_s is the efficiency of the spectrometer and $r = \eta q_e / h v_o$ the responsivity of the line scan camera with η the quantum efficiency (≈ 0.85), q_e the electronic charge, h the Planck's constant and v_o the center frequency of the low-coherence light source. $\delta_m = 2(z_{Sm} - z_R) = 2nz_m$ is the round trip optical path difference (OPD) between the reference mirror and the mth sample reflector located at a distance of z_m from the top surface of the sample where the OPD is assumed to be zero. $\delta_{mn} = 2n(z_{Sm} - z_{Sn})$ is the round trip OPD between m^{th} and n^{th} sample reflectors.

Equation 3.1 contains three distinct components: DC term, signal term and autocorrelation term.

   i.   The first component is a constant offset (often called the DC term), and is independent of the OPD. It is basically the power spectrum of the source scaled by the power

reflectivities of the reference and sample arms. In SD-OCT, this is the largest undesired component of the detector current. It can be removed by simple subtraction. As sample power reflectivity is often small, the DC term is dominated by the power reflectivity of the reference mirror.

ii. The second component contains the cross-correlation between the reference arm and each reflector of the sample. The desired sample field reflectivity profile is embedded in this term. It is therefore the useful signal of OCT. As this signal is proportional to the sample field reflectivity $\sqrt{R_{Sm}}$, its magnitude is typically less than the DC term; however the fact that the signal term is amplified by the reference field reflectivity $\sqrt{R_R}$ represents an important gain factor compared to direct detection of sample reflections.

iii. The autocorrelation component represents the interference occurring between the different sample reflectors. The autocorrelation term linearly depends on the power reflectivity of the sample. For samples having strong reflectivities, this term appears as artifacts in OCT. The effect of the autocorrelation term can be reduced by an appropriate choice of reference arm reflectivity. For biological tissues, the autocorrelation term is generally negligible.

If we have only a single sample reflector ($m = 1$) in air ($n = 1$), equation 3.1 will be reduced to

$$i_{D1}(\sigma) = \frac{\rho}{4} S(\sigma) \left[R_R + R_{S1} \right] + \frac{\rho}{2} S(\sigma) \sqrt{R_R R_{S1}} \cos(2\pi\delta_1\sigma).$$ 3. 2

This gives a modulated spectrum or often called spectral interferogram, where the signal term rides on top of the DC term as shown in Figure 3.2. The signal term provides two pieces of information about the reflector:

i. *The magnitude of the field reflectivity, which is contained in the amplitude of the signal term*

ii. *The depth location of the reflector, which is contained in the phase term*

The amplitude of modulation is proportional to the field reflectivity $\sqrt{R_{S1}}$ of the reflector: the lower the reflectivity, the smaller the amplitude of the signal, or vice versa. The depth information z (the location of the reflector within the sample) is contained in the phase of the cosine oscillation. As shown in Figure 3.2, the period of modulation $\sigma_T = 1/\delta_1$ is inversely proportional to the OPD δ_1, where $\delta_1 = 2(z_{S1} - z_R) = 2z_1$.
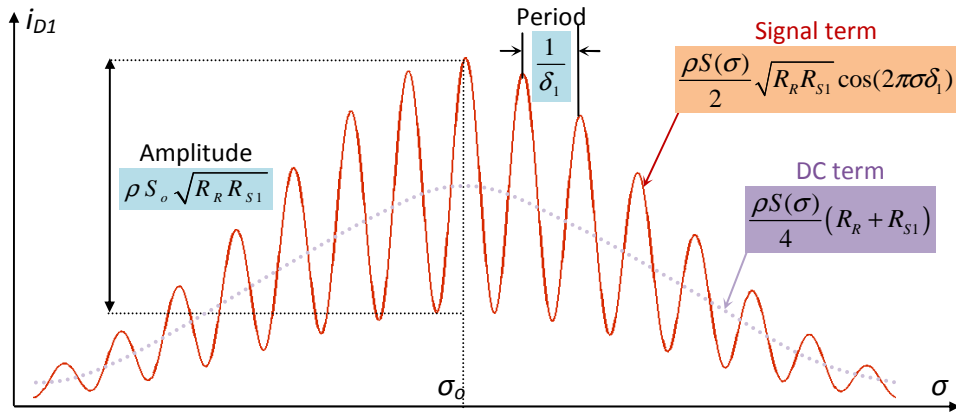
Figure 3.2 The detected current at the output of the spectrometer for a single reflector in air. The signal term of equation 3.2 with amplitude $\rho S(\sigma)\sqrt{(R_R R_{S1})}/2$ and frequency $\delta = 2(z_{S1} - z_R) = 2z_1$ of modulation rides on top of the DC term of magnitude $\rho S(\sigma)[R_R + R_{S1}]/4$.

In other words, the modulation frequency is directly proportional to the axial location z of the reflector. This means that as the optical path length mismatch δ increases, the modulation frequency increases. As the reference mirror in SD-OCT is immobile, increasing δ corresponds to increasing z. As a result, sample reflectors located at shallow depths give rise to low modulation frequencies, whereas reflectors located large depths correspond to high modulation frequencies (see Figure 3.3).
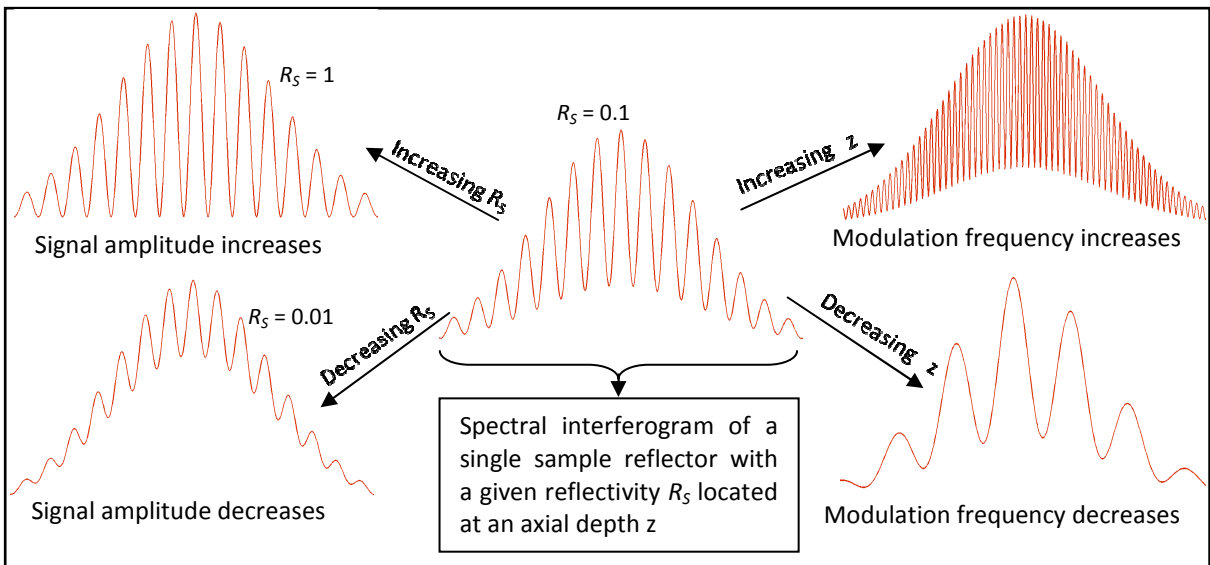
Figure 3.3 Illustration of how the spectral interferogram varies with sample reflectivity R_S and axial position z of a reflector. R_S is embedded in the amplitude of modulation whereas z is embedded in the frequency of modulation of the spectral interferogram. For all cases, $R_R = 1$.

If we have multiple reflectors at different depths, the signal term will be the superposition of the spectral interferograms related to the individual reflectors. Figure 3.4 shows the schematic of the resultant spectral interferogram corresponding to three partial light reflectors in air with power reflectivities $R_{S1} = 0.6$, $R_{S2} = 0.05$ and $R_{S3} = 0.2$ located at z_1, z_2 and z_3, respectively.

Distances are measured from the surface of the sample. In this case, the signal term is no more a single cosine function. However, the resultant spectral interferogram is still periodic, and can be decomposed into individual cosine functions having different modulation frequencies. The field reflectivity and frequency of modulation of each reflector can be reconstructed from the resultant spectral interferogram using the Fourier transform principle.
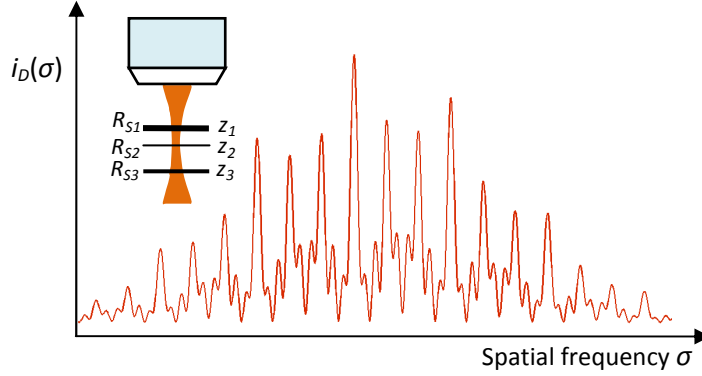

Figure 3.4 Illustration of the spectral interferogram corresponding to multiple sample reflectors with various reflectivities R_{S1}, R_{S2} and R_{S3} located at different axial positions z_1, z_2 and z_3. The signal term is the superposition of the spectral interferograms related to the individual reflectors.

3.2.2 A-scan reconstruction by Fourier transform

The A-scan (reflectivity versus the depth location) is extracted from the spectral interferogram by performing Fourier transformation. If we apply the Fourier transform to equation 3.1, we get the following expression

$$
\begin{aligned}
i_D(\delta) &= \frac{\rho}{4}\gamma(\delta)\otimes\left[\left(R_R dirac(0) + \sum_{n=1}^{M} R_{Sm} dirac(0)\right) + \sum_{m=1}^{M}\sqrt{R_R R_{Sm}}\, dirac\left(\delta\pm\delta_m\right) + \sum_{m\neq n=1}^{M}\sqrt{R_{Sm} R_{Sn}}\, dirac\left(\delta\pm\delta_{mn}\right)\right] \\
&= \frac{\rho}{4}\left[R_R + \sum_{m=1}^{M} R_{Sm}\right]\gamma(0) + \frac{\rho}{4}\sum_{m=1}^{M}\sqrt{R_R R_{Sm}}\times\gamma\left(\delta\pm\delta_n\right) + \frac{\rho}{4}\sum_{m\neq n=1}^{M}\sqrt{R_{Sm} R_{Sn}}\times\gamma\left(\delta\pm\delta_{mn}\right)
\end{aligned}
$$
3. 3

where $\gamma(\delta) = FT\{S(\sigma)\}$ is the coherence function and *dirac* is the dirac delta function often denoted by δ but here we preferred to use the word *dirac* not to confuse with the OPD δ.

Equation 3.3 shows that performing the Fourier transform leads to the convolution of the *dirac* terms with the coherence function. As a result, the best axial resolution that can be achieved with SD-OCT, like TD-OCT, is limited by the width of the coherence function. The illustration is given in Figure 3.5.
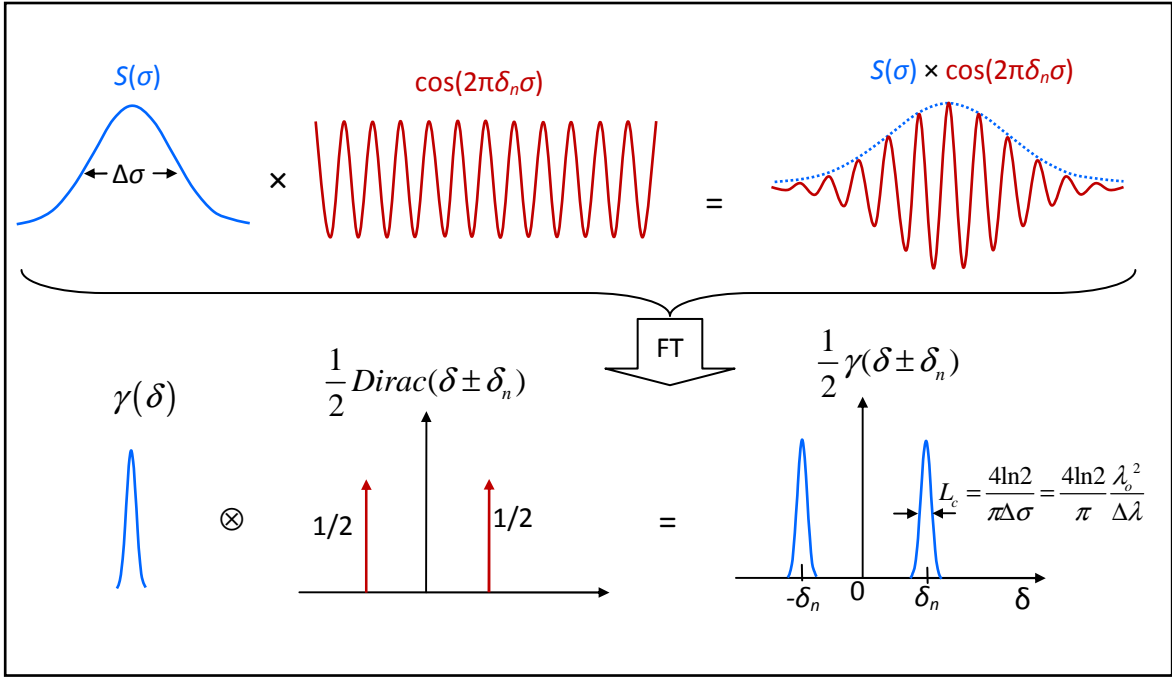
Figure 3.5 SD-OCT signal reconstruction via Fourier transform

If a Gaussian-shaped power spectrum is considered, the coherence function will be

$$\gamma(\delta) = FT\{S(\sigma)\} = \frac{\Delta\sigma}{2\sqrt{\ln 2}}\sqrt{\pi} \times S_o e^{\frac{-\pi^2}{4\ln 2}\times\Delta\sigma^2\times\delta^2} \; . \tag{3.4}$$

The FWHM of $\gamma(\delta)$, defined as the coherence length L_c in chapter 2 under equation 2.23, is given by

$$L_c = \frac{4\ln 2}{\pi\Delta\sigma} = \frac{4\ln 2}{\pi}\times\frac{\lambda_o^{\,2}}{\Delta\lambda} \; . \tag{3.5}$$

Considering the round trip propagation of light in both arms of the interferometer, half of the coherence length represents the axial resolution Δz of SD-OCT

$$\Delta z = \frac{L_c}{2n} = \frac{2\ln 2}{\pi n}\times\frac{\lambda_o^{\,2}}{\Delta\lambda} \; . \tag{3.6}$$

The results of equation 3.1 and equation 3.3 are plotted in Figure 3.6 for the case of a single and multiple reflectors by considering a light source with a Gaussian spectrum. Three cases of single reflectors are considered by changing both the reflectivity and the depth location of the reflectors. The reflectivity of each reflector $R_{S1} = 0.6$, $R_{S2} = 0.05$ and $R_{S3} = 0.02$ is deliberately chosen to be large in order to see the effect of the autocorrelation term when they all appear together in a single sample in (d).
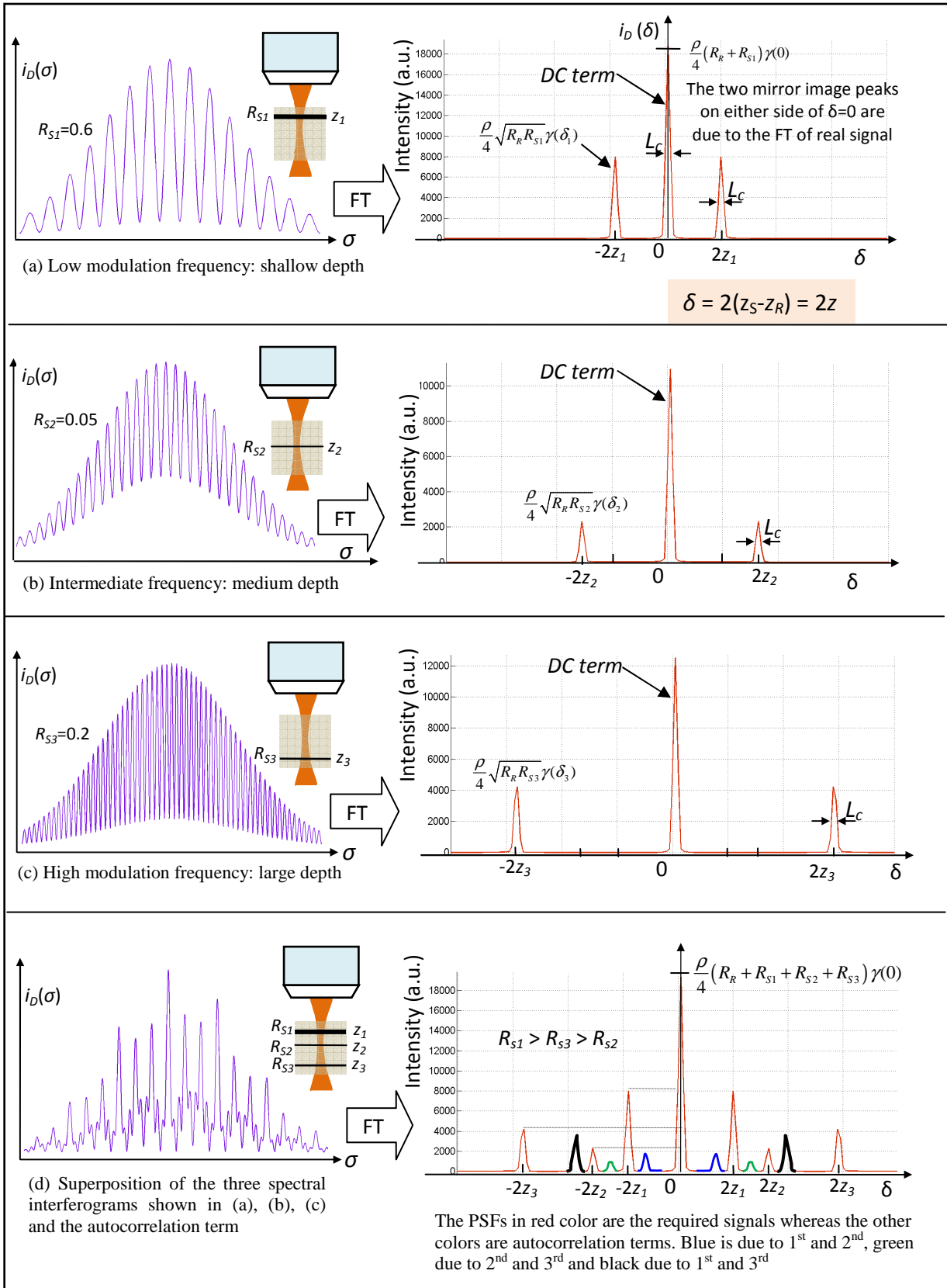
Figure 3.6 Illustration of A-san reconstructions from spectral interferograms using Fourier transformation. (a), (b) and (c) show a single reflector with different reflectivities located at different axial depths. By applying the Fourier transform, one is able to determine the reflectivity and axial location of the reflector. As expected, high modulation frequency σ gives rise to large OPD δ, and hence large reflector depth z. (d) shows the resultant interferogram for three reflectors. Fourier transforming this spectrum gives not only the signal peaks at their corresponding depths but also the autocorrelation peaks (blue, green, black).

3.2.2.1 The signal component

Plots of the Fourier transform of the signal term corresponding to single reflectors with different values of reflectivities and depth locations are shown in Figure 3.6 (a), (b) and (c). As explained above, (a) illustrates that a low modulation frequency in the σ-domain appears as a signal peak around $\delta = 0$ in the δ-domain, whereas a spectral interferogram with high modulation frequency, as shown in (c), gives a signal peak relatively further away from $\delta = 0$. Note also that each signal peak in δ-domain is the result of convolution of the dirac function with the coherence function, i.e., the dirac reflectivity profile corresponding to a plane reflector is spread axially according to the nature of the coherence function. Though the reflector is a plane perpendicular to the optical axis, not a point, this function is often called axial point-spread function (PSF), and the FWHM of each axial PSF is given by coherence length L_c of the light source.

The Fourier transform of each spectral interferogram gives two identical axial PSFs on either side of $\delta = 0$. This is due to the fact that as the detected interferometric spectrum is real, its Fourier transform must be Hermitian symmetric, i.e., its positive and negative distance are complex conjugates of each other. In FD-OCT, this is termed as the complex conjugate artifact. This artifact can be easily removed by keeping the sample on one side of the zero path length and displaying only the positive or negative distances. If the sample strays beyond the zero path length border, it begins to overlap with its mirror image.

3.2.2.2 The artifact components

In SD-OCT, the DC and the autocorrelation terms both appear as artifacts and obscure or degrade the quality of the image.

In Figure 3.6, the DC term appears as a large artifactual signal centered at the zero path length difference ($\delta = 0$). The FWHM value of the DC artifact is only one coherence length wide; however, its amplitude is so much larger than the amplitude of the useful signal terms that the side lobe this strong Dc term can overwhelm the useful signal components much further away. Since the main contributor of the DC term is the reference mirror, a simple method to remove the DC component is to record the amplitude of the spectrum with the sample arm blocked, and then to subtract this value from each subsequent spectral interferograms before performing the Fourier transform.

The other artifact of SD-OCT system comes from the autocorrelation component. When the sample is composed of multiple reflectors as shown in Figure 3.6 (d), the Fourier transform of the spectral interferogram reveals the signal terms as well as the autocorrelation peaks. Axial PSFs in red are signal terms, and those shown in blue, green and black are autocorrelation artifact terms. For M discrete sample reflectors, the total number of autocorrelation terms N_{AC} that appear in the δ domain after Fourier transform can be expressed as a statistical combination $N_{AC} = \dfrac{M!}{4(M-2)!}$.

Figure 3.6 (d), $M = 3$, $N_{AC} = 3$. We see three autocorrelation peaks: blue, green and black. The blue one is due to the interference between the 1st and 2nd reflectors, the green between the 2nd and 3rd reflectors, and finally the black between the 1st and 3rd reflectors. In this typical example, we see that for strong sample reflectors, the autocorrelation term can be as strong as or even stronger than the useful signal amplitude. The practical implication is that if a real sample has at least one strong light reflecting layer somewhere in its axial field of view, it behaves as a reference mirror, and light coming from this layer interferes with all other reflections from the sample, yielding an artifact image. This may significantly obscure the true sample structure that is given by the cross-correlation term. For such types of samples, sophisticated phase-shifting methods can be used to remove the autocorrelation term [58, 59]. However, such techniques increase the complexity of the system and the data acquisition time. In practice, since the typical distance between the sample reflectors is much smaller than the distances between the sample reflectors and the reference mirror, the autocorrelation artifact appears at shallow depths in OCT images. It is customary to displace the reference mirror so that the surface of the sample shows at a location beyond the autocorrelation structures, and then the shallow depth range is numerically zeroed in the image.

The typical sample reflectivity measured by an OCT system is roughly in the range of 10^{-4} to 10^{-11}. Therefore the easier method to reduce the effect of the autocorrelation artifact is to ensure that the reference reflectivity is sufficient so that the amplitude of the autocorrelation term becomes negligibly small compared to the cross-correlation signal term. However, if the reference arm power is too high, the SNR of the system will drop [38, 45] and optimal design is needed to have an appropriate reflectivity value of the reference mirror.

3.2.3 Maximum imaging depth of SD-OCT

SD-OCT images, like TD-OCT images, are computationally reconstructed by stitching or combining adjacent A-scans next to each other while performing transverse beam scanning on the sample. Each A-scan contains the depth reflectivity profile for each transverse sample location. In SD-OCT, individual A-sans are reconstructed from the acquired spectral interferogram by performing Fourier transform. In the previous sections and figures (see Figure 3.3 and Figure 3.6), it has been explained that because of the Fourier relationship between the cosine modulation of the spectrum and the depth location of the reflector, the modulation frequency δ_m of the spectral interferogram increases as the depth location of the reflector z_m increases according to the relation $\delta_m = 2nz_m$ (equation 3.1), where n is the refractive index of the sample and z_m the depth location of the mth reflector. As predicted, there will be a depth limit where the reflector can no longer be detected.

Excluding signal attenuation of the sample due to absorption and scattering, the maximum imaging depth z_{max} of SD-OCT is determined by the spectral sampling resolution $\delta\sigma$ of the spectrometer. $\delta\sigma$ refers to the spectral extent or spectral width that is detected (or sampled) by a single pixel of the line scan camera. If the FWHM $\Delta\sigma$ of the light source is dispersed across N/m pixels out of the total N line-scan CCD pixels, where $m \geq 1$, the sampling resolution $\delta\sigma$ of the spectrometer will be

$$\delta\sigma = \frac{\Delta\sigma}{N/m}, \text{ where } \sigma = \frac{1}{\lambda}; \ \ \delta\sigma = \frac{\delta\lambda}{\lambda_o^2}.$$ 3. 7

According to the Nyquist sampling criterion, for any modulation frequency δ_m to be resolved by the spectrometer that has a spectral sampling resolution (period) $\delta\sigma$, the signal frequency δ_m should not exceed half of the sampling frequency $\dfrac{1}{\delta\sigma}$, i.e.,

$$\delta_m \leq \frac{1}{2} \times \frac{1}{\delta\sigma}.$$ 3. 8

As $\delta_{max} = 2nz_{max}$, by combining equations 3.7 and 3.8, the maximum theoretical depth z_{max} that can be imaged using SD-OCT is given by

$$z_{max} = \frac{1}{2n} \times \delta_{max} = \frac{1}{4n} \times \frac{1}{\delta\sigma} = \frac{1}{4n} \times \frac{\lambda_o^2}{\delta\lambda}.$$ 3. 9

If $z_m > z_{max}$, the modulation frequency of the spectrum (i.e., the signal frequency) δ_m becomes greater than half of the sampling frequency, and the Nyquist criterion presented in equation

3.8 will no more be valid, causing aliasing. When this happens, the peaks corresponding to the Fourier transform of the aliased signals roll back into incorrect positions, thereby inducing artifacts and increasing the noise level.

To illustrate this point, we consider a Gaussian light source having a spectral bandwidth $\Delta\lambda = 80$ nm centered at $\lambda_o = 1300$ nm wavelength.
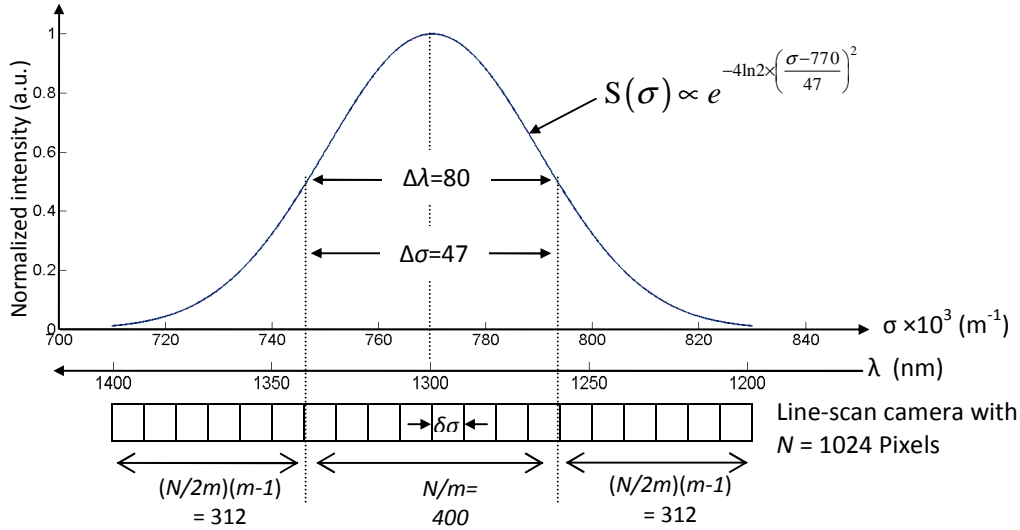

Figure 3.7 The FWHM of the source spectrum is spread over N/m pixels of the line scan camera where $m \geq 1$

Consider also a spectrometer equipped with a line scan camera having $N = 1024$ detector pixels. If the recombined light at the output of the interferometer is spread by the grating in such a way that the FWHM of the light source covers $N/m = 400$ of the camera pixels, the spectral sampling resolution will be (see Figure 3.7)

$$\delta\lambda = \frac{\Delta\lambda}{N/m} = \frac{80\,nm}{400} = 0.2\,nm \quad \text{or} \quad \delta\sigma = \frac{\delta\lambda}{\lambda_o^2} = 0.1\,\text{mm}^{-1}$$

This corresponds to a maximum imaging depth of $z_{\max} = \frac{1}{4} \times \frac{\lambda_o^2}{\delta\lambda} = 2.1\,mm$. Any reflector located deeper than $z = 2.1$ mm will therefore roll back and induce artifact. Let us now consider a single reflector and acquire three spectral interferograms at three axial positions $z_1 = 0.5$ mm, $z_2 = 1$ mm and $z_3 = 3$ by translating the reflector. When we perform the Fourier transform of the acquired spectral interferograms, the reflector at $z_3 = 3$ creates a signal peak at an incorrect depth of $z = 2 \times z_{max} - 3$ mm $= (2 \times 2.1 - 3)$ mm ≈ 1.2 mm (see Figure 3.8).
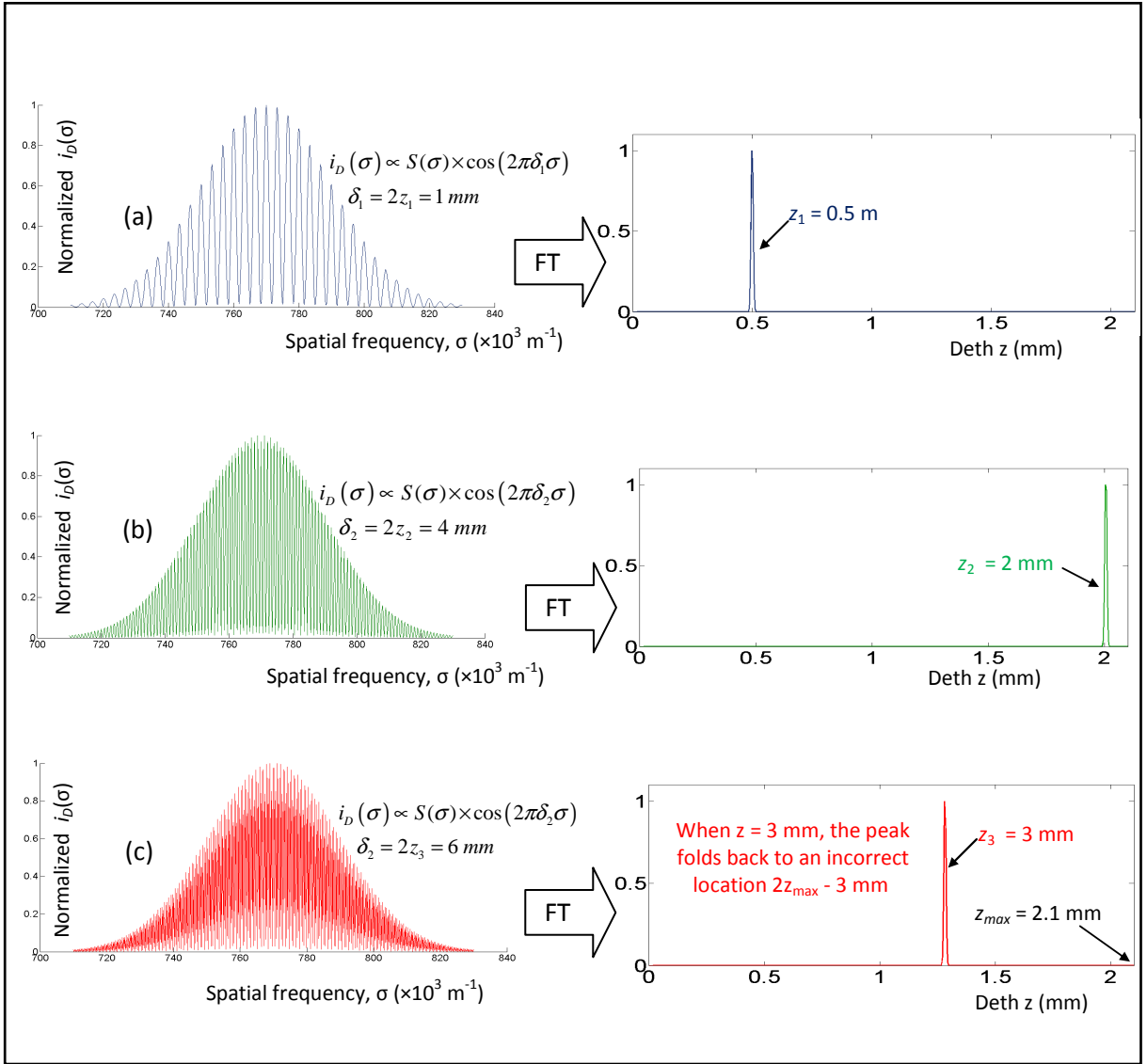
Figure 3.8 Illustration of imaging range limit of SD-OCT.
Note that when the depth of a reflector exceeds the maximum imaging depth, (c), it folds back and appears at a false location, creating an artifact and noise to the system. In this example, $z_{max} = 2.1$ mm. The imaging depth can be increased either by increasing the spectral sampling resolution, which in turn requires either increasing the number of detectors or decreasing the axial resolution.

3.2.4 Sensitivity of SD-OCT

The increased SNR of SD-OCT compared to that of TD-OCT is based on the significant reduction of shot noise obtained by replacement of the single-element detector of TD-OCT with a multi-element array detector in SD-OCT. In chapter 2 (from equations 2.33 – 2.35), it has been presented that for shot noise limited detection, the shot noise variance σ_{sh}^2 of TD-OCT is directly proportional to the detection bandwidth B and the DC optical power returned to the detector. For a given source optical power P_o, assuming that the DC power is dominated by the reference arm power $P_R = P_o R_R/4$ (assuming ideal balanced beamsplitter), the photocurrent signal power $\langle i_D^2 \rangle$ and the shot noise variance σ_{sh}^2 have been expressed as

$$\left\langle i_D{}^2 \right\rangle = 2 \times \left(\frac{\eta q_e}{h v_o} \right)^2 \mathrm{P}_R \mathrm{P}_S \quad [\mathrm{Ampere}^2] \quad \text{and} \quad \sigma_{sh}{}^2 = 2 \times \frac{\eta q_e{}^2}{h v_o} \mathrm{P}_R B \quad [\mathrm{Ampere}^2]. \qquad 3.\,10$$

The SNR_{TD} and sensitivity S_{TD} of TD-OCT read as

$$SNR_{TD} = \frac{\eta}{h v_o} \frac{P_S}{B} \quad \text{and} \quad S_{TD} = \frac{\eta}{h v_o} \frac{P_o / 4}{B}, \qquad 3.\,11$$

where η is the detector quantum efficiency, q_e the electronic charge, h the Planck constant, v_o the center frequency of the light source spectrum, and $P_S = P_o R_S / 4$ the sample power returned to the detector for a given source power P_o (assuming ideal balanced beamsplitter). The detection bandwidth B is in turn directly proportional to the spectral bandwidth $\Delta\sigma$ of the light collected by the single-element detector: the narrower the spectral bandwidth, the lower the required detection bandwidth (see equation 2.35).

Now consider that the recombined detection arm power is spectrally spread over N separate photodetecors and each detector receives $1/N$ of the source spectrum. If the detected signals are bandpass filtered before coherence summation, the required detection bandwidth at each detector will be approximately reduced by a factor of N. The sum of shot noise for such N detector elements, where each detector element receives $1/N$ of the total reference power P_R, is given by [57]

$$\sigma_{sh}{}^2 = 2 \times \frac{\eta q_e{}^2}{h v_o} \mathrm{P}_R \frac{B}{N}. \qquad 3.\,12$$

When coherently combined, the signal remains the same and the SNR for such kind of hybrid TD-OCT system will be (see equation 2.36)

$$SNR = \frac{\eta}{h v_o} P_S \frac{N}{B}, \qquad 3.\,13$$

where $P_S = P_o R_S / 4$ is the sample power returned to the detector for a given source power P_o (assuming ideal balanced beamsplitter). Equation 3.13 shows that spectrally dispersing the detection arm light offers a significant SNR improvement advantage.

In SD-OCT, an integrating detector such as a CCD can be used. In this case, optical energy is measured rather than optical power. This is due to the fact that CCD detectors collect photoelectron charges during the exposure time τ whereas PIN detectors register the continuous photoelectron current. The total number of photoelectron n_e collected during the

exposure time τ of in incident light having an optical power P is given by [45]

$$n_e = \eta \frac{Energy_{Optical}}{Energy_{Photon}} = \eta \frac{P\tau}{hv_o} \quad [electrons] \, . \tag{3.14}$$

For SD-OCT using such detectors with an integrating time τ, by the use of the Nyquist theorem, the bandwidth per detector element B/N given in equation 3.12 is replaced by $1/(2\tau)$. Considering that SD-OCT measures only the real part of the complex cross-spectral density, the signal is reduced by a factor of 2, and the photoelectron signal power $<n_e^2>$ and shot noise variance σ_{sh}^2 of SD-OCT read [53]

$$\left\langle n_e^2 \right\rangle = \left(\frac{\eta}{hv_o} \right)^2 P_R P_S \tau^2 \quad \text{and} \quad \sigma_{sh}^2 = \frac{\eta P_R \tau}{hv_o} \, . \tag{3.15}$$

Comparing equation 3.10 and equation 3.15, the photocurrent noise variance of TD-OCT, σ_{TD}^2, and the photoelectron shot noise variances of SD-OCT, σ_{SD}^2, can be related via [45]

$$\sigma_{TD}^2 = \sigma_{SD}^2 \left(q_e / \tau \right)^2 , \tag{3.16}$$

where the electronic bandwidth B is related to the exposure time τ by $B = 1/(2\tau)$.

The SNR_{SD} and sensitivity S_{SD} of a shot noise limited SD-OCT system will be

$$SNR_{SD} = \frac{\eta}{hv_o} P_S \tau \quad \text{and} \quad S_{SD} = \frac{\eta}{hv_o} \frac{P_0}{4} \tau \tag{3.17}$$

Taking the ratio between S_{SD} (equation 3.17) and S_{TD} (equation 3.11), we get

$$\frac{S_{SD}}{S_{TD}} = B\tau \, . \tag{3.18}$$

In order to properly compare the sensitivities of both techniques, the optimal bandwidth B of TD-OCT and the exposure time τ of SD-OCT should be linked. From equation 2.35, substituting τ for Δt, we get

$$B = 4 \times \frac{\Delta\lambda}{\lambda_o^2} \frac{z_{max}}{\tau}$$

$$\Rightarrow B\tau = 4 \times \frac{\Delta\lambda}{\lambda_o^2} \frac{\lambda_o^2}{4\delta\lambda} = \frac{\Delta\lambda}{\delta\lambda} = \frac{\Delta\sigma}{\delta\sigma} = \frac{N}{m} \tag{3.19}$$

where $\delta\sigma = \dfrac{\Delta\sigma}{N/m}$ (see equation 3.7). *N/m* refers to the number of pixels of line scan camera on which the FWHM of the source bandwidth $\Delta\lambda$ is dispersed (see Figure 3.7). The sensitivity of SD-OCT is approximately *N/m* times that of TD-OCT. The actual value depends on source spectral density and spectral bandwidth per detector.

For example, if we have an array of 1024 CCD pixels with *N/m* = 400, the sensitivity ratio in dB will be

$$10\times\log\left(\frac{S_{SD}}{S_{TD}}\right)=10\times\log\left(S_{SD}\right)-10\times\log\left(S_{TD}\right)=10\log\left(B\tau\right)=10\log\left(400\right)=26\,dB. \qquad 3.20$$

Equation 3.20 shows that for the same A-scan rate, the sensitivity of SD-OCT is 26 dB above that of TD-OCT. Experimental sensitivity comparison of both domains in retinal imaging demonstrated that SD-OCT was 21.7 dB more sensitive than TD-OCT [53].

The superior sensitivity of SD-OCT over TD-OCT is highly sensitive to the imaging depth. As the imaging depth increases, the sensitivity of SD-OCT drops significantly. Such depth dependent sensitivity fall-off effect is related to the limited resolution of the spectrometer. This is one of the drawbacks of SD-OCT. In SD-OCT, as the spectral interferogram has to be sampled by array detectors, physical parameters related to the size of the beam spot on each detector, the physical size of each detector and the total number of detectors in the array all contribute to depth dependent sensitivity fall-off effect of SD-OCT. Moreover, the sensitivity fall-off depends on the faithfulness of the image reconstruction algorithm utilized. Such and other practical considerations of SD-OCT design are addressed in the following sections of the manuscript.

3.3 Design of high-resolution SD-OCT: hardware and software aspects

As explained in the introduction part of this chapter, our objective was to develop a high-resolution SD-OCT that can properly resolve the Schlemm's canal of the human eye. As the axial resolution of OCT is determined by the bandwidth of the light source, designing a high-resolution OCT requires a light source with broad spectral width. Hence, getting a broadband light source and dealing with the subsequent dispersion issues is one of the challenges of high-resolution OCT.

The other challenge of high-resolution OCT when realized in the SD-OCT modality is the

design of a broadband spectrometer. If one wants to achieve a source-limited high axial resolution, the spectral range $\Delta\Lambda$ of the spectrometer needs to be broad enough to collect the required broad spectral width of the light source. On the other hand, given the finite number of detector pixels, increasing $\Delta\Lambda$ will decrease the spectral sampling resolution $\delta\lambda$. This will in turn have a negative impact on the maximum imaging depth that can be reached. Moreover, the depth dependent sensitivity fall-off effect of SD-OCT is directly related to the design parameters of the spectrometer. Hence having an optimal spectrometer is the other main task of high-resolution SD-OCT development.

In this section, the broadband light source used for the development of our high-resolution SD-OCT is presented. The design of a broadband spectrometer and its calibration method are discussed. At the end, the main SD-OCT image processing steps are explained.

3.3.1   The light source

OCT imaging parameters such as axial resolution and imaging depth are directly related to the spectral properties of the illumination light source. Depending on the application, choosing the right light source is therefore an important step in any OCT design. In our case, we are interested in designing a high-resolution SD-OCT capable of resolving Schlemm's canal. As the canal is found in a highly scattering corneoscleral junction (limbus) at a depth of ~ 0.8 mm (chapter 1, section 1.3.1), the centre wavelength of light should be chosen in such a way that attenuation of light is reduced and imaging depth is maximized.

Generally most biological soft tissues have relatively low light absorption in the long visible and NIR spectral regions, especially between 650 nm and 1400 nm (often called therapeutic window). Within this window, scattering is more prevalent than absorption. Dual-band experiments in scattering biological samples have demonstrated the superiority of OCT systems operating at 1.3 µm center wavelength compared to those operating at 0.8 µm in terms of imaging depth [60, 61]. Using a low resolution commercial SS-OCT working at 1.3 µm center wavelength, we have also demonstrated that the imaging depth at this wavelength in sclera is indeed deep enough to reach Schlemm's canal. For this reason, 1.3 µm center wavelength has been chosen for our high-resolution SD-OCT system. However, because of the $\lambda^2/\Delta\lambda$ dependence of the axial resolution, high-resolution SD-OCT imaging at 1.3 µm center wavelength requires extremely broad bandwidth.

According to equation 3.6, the spectral bandwidth $\Delta\lambda$ the light source needed for high-

resolution imaging at $\lambda_o = 1.3$ µm needs to be 2.6 times larger than the one at $\lambda_o = 0.8$ µm to maintain the same axial resolution. As a result, getting a broadband light source with good spectral quality has still continued to be the technological bottleneck of long wavelength high-resolution OCT systems. Remember also that if dispersion is not properly managed, the use of very broadband source will not necessarily give better resolution. As it will be seen in the next section, increasing the source has additional undesirable consequence on the imaging depth of SD-OCT.

Until recently, high-resolution OCT has been based on femtosecond solid-state lasers [39] and continuum generation-based light sources [62]. However, such light sources are bulky, expensive and sensitive to misalignment. In comparison, superluminescent diode (SLD) sources are compact, robust, easy to operate and cost-effective. Since the emission spectrum of a single SLD is not broad enough for high-resolution OCT imaging, wavelength-division multiplexing of several spectrally shifted SLDs can be done to broaden the spectrum and provide higher axial resolution than currently possible with one SLD alone [63].

The illuminating light source for our SD-OCT consists of a combination of two spectrally shifted broadband SLDs. The emission spectrum of each SLD, as specified in the manufacturer's manual, is shown in Figure 3.9 (dotted curves). SLD A emits light at a center wavelength of 1233 nm with a spectral bandwidth (FWHM) of 80 nm, while SLD B emits light having a spectral bandwidth of 110 nm centered at 1335 nm. The combination of the two SLDs results in a broadband light source that has a spectral bandwidth of 200 nm (see Figure 3.9, solid curve).
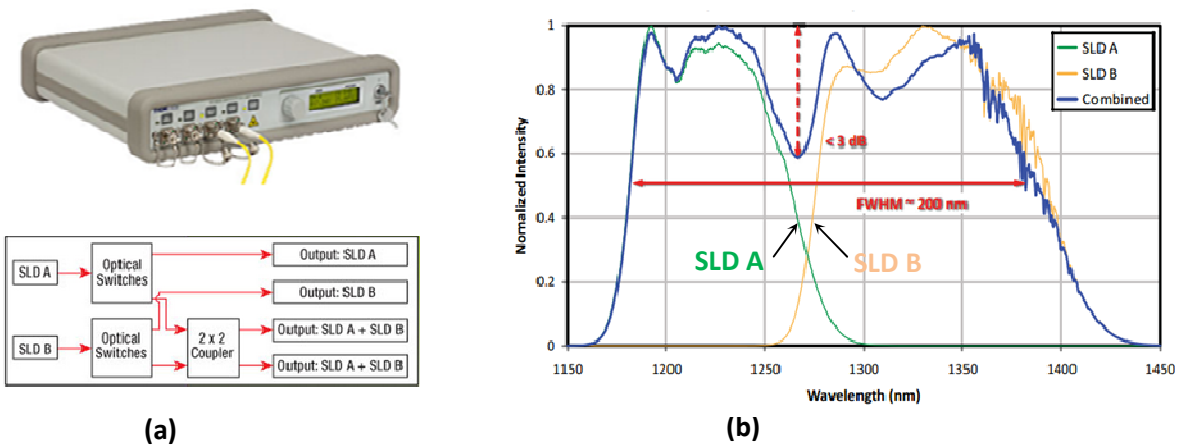

(a)   **(b)**

Figure 3.9 (a) Compact SLD broadband light source (Thorlabs, LS2000B), (b) typical mission power spectra: SLD A (green curve) and SLD B (yellow curve) and the spectrum of the combined shown in blue. An Effective spectral bandwidth ~ 200 nm at FWHM can be achieved.

The combined broadband SLD light source provides shorter coherence length and better axial resolution than we could get with one SLD alone. The emission spectrum of the combined SLD light source is centered at 1300 nm wavelength, and the maximum output power is 10 mW. The actual spectral bandwidth, the emission spectral shape and the output power of the combined SLD light source can be controlled to a certain extent by independently changing the current drive and the temperature control of each SLD.

The next main task of high-resolution SD-OCT development is designing a broadband spectrometer capable of collecting such a broadband light. If the spectral range of the spectrometer is narrower, all of the source spectrum will not be collected and the axial resolution will be inferior to the theoretically predicted value. On the other hand if the spectrometer is broader than required, imaging range of SD-OCT will be reduced without further improving the axial resolution.

3.3.2   Design of the OCT spectrometer

The schematic diagram of the SD-OCT spectrometer is given in Figure 3.10.
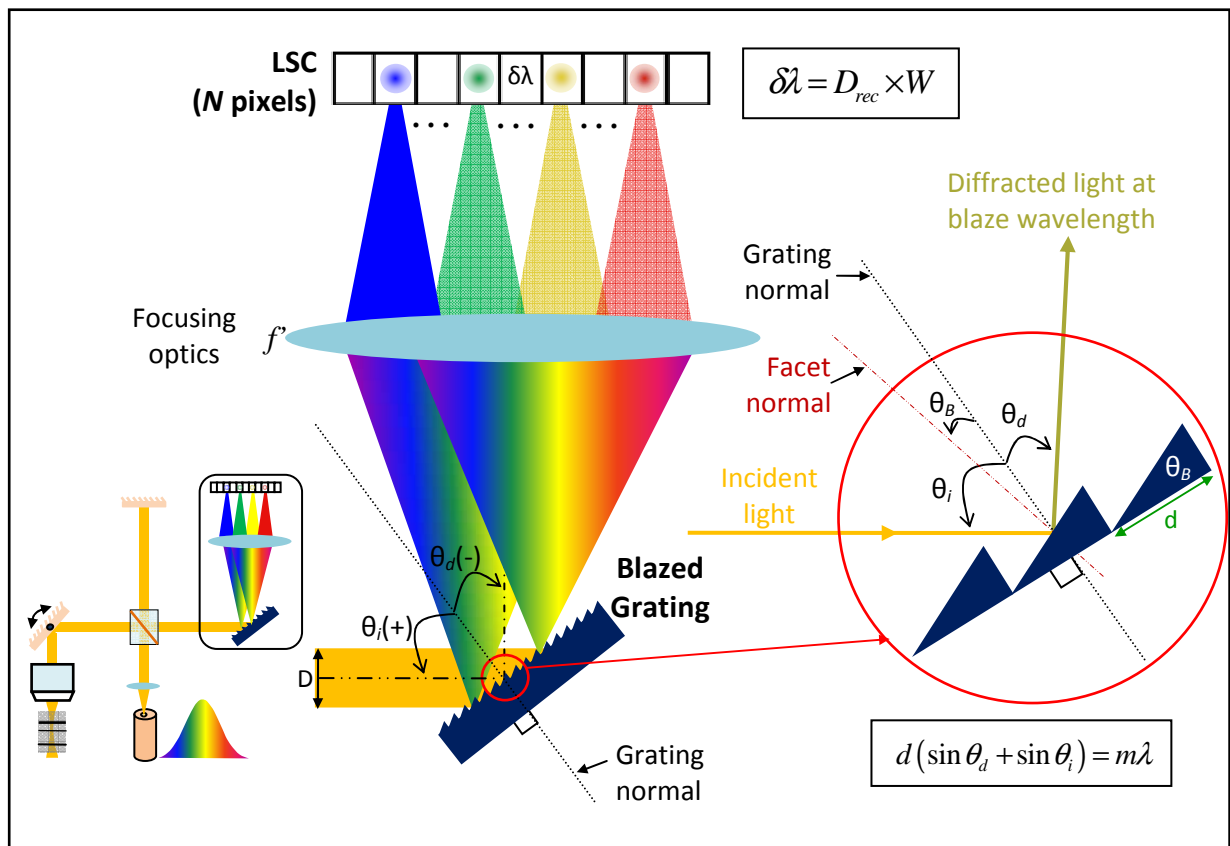

Figure 3.10 Schematic diagram of OCT spectrometer: a grating, a focusing optics and a line-scan camera (LSC).

The spectrometer consists of a diffraction grating, a focusing optics and a line-scan camera (LSC). The recombined beam at the output of the interferometer is incident on the diffraction grating with an angle θ_i with respect to the normal to the grating, and the first order beam diffracts at an angle θ_d from the normal according to the grating equation, thereby spatially separating each wavelength component. The center wavelength of the light source is designed to match the blaze wavelength of the grating. Focusing optics focuses the diverging beam back onto the LSC, with each pixel of the LSC detecting $\delta\lambda$ of the spectrum.

3.3.2.1 Diffraction grating

Diffraction gratings, in transmissive or reflective mode, can spatially separate a polychromatic incident light into different wavelengths using a repetitive structure embedded within the grating. The structure affects the amplitude and/or phase of the incident wave, modifying the distribution of light at its output. Depending on the application, various grating patterns are available. The type of grating we used in our SD-OCT design is a blazed (ruled) grating because such a grating with sawtooth pattern exhibits high diffraction efficiency for certain orders and wavelengths. The efficiency of blazed grating is greater than the efficiency of prisms and holographic gratings. A blazed grating is made by creating repeatable patterns (grooves) whose surface is inclined at an angle θ_B (blaze angle) with respect to the surface of the grating (see Figure 3.11). The normals to the facet surface of the groove and grating surface are called facet normal and grating normal, respectively.
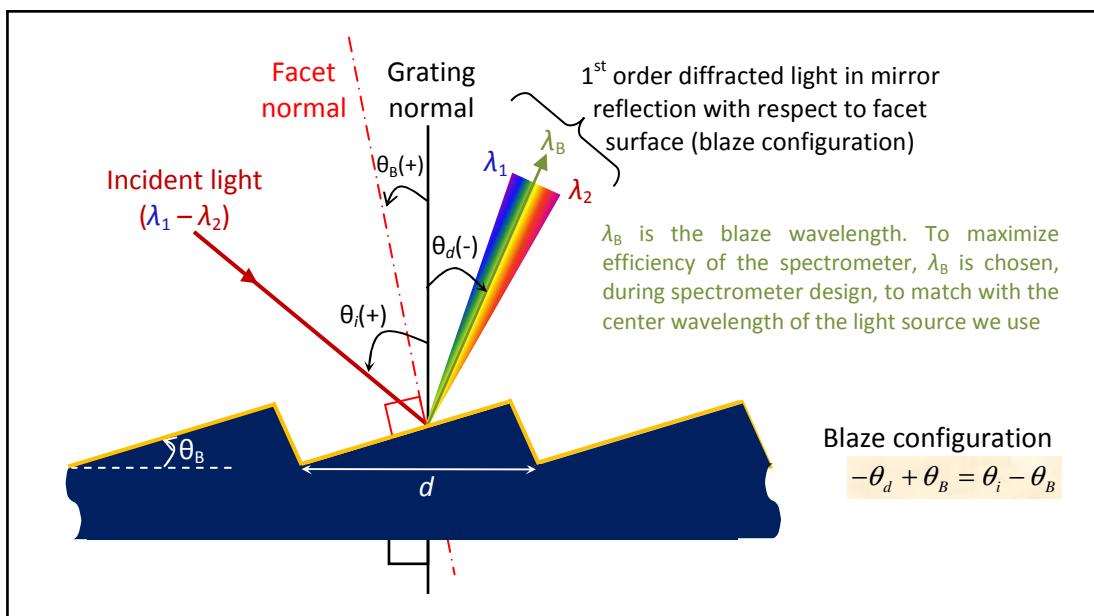

Figure 3.11 Blazed grating where the first order diffraction beam is at blaze configuration to maximize efficiency.

When light composed of different wavelengths is incident at an angle θ_i on a blazed reflective grating with grating period d, light of wavelength λ is diffracted at angle θ_d. Both θ_i and θ_d are measured from the surface normal. Considering counterclockwise direction as positive, the relation between θ_i, θ_d, λ and d is given by the well-known grating equation as

$$\sin\theta_d + \sin\theta_i = m\frac{\lambda}{d},$$ 3. 21

where $m = 0, \pm1, \pm2, \pm3$, etc is the diffraction order.

For a given diffraction order, equation 3.21 shows that different wavelengths exit the grating at different diffraction angles, giving rise to spatial separation of light into its components. For blazed grating, when the relationship between the incident light and the mth order diffracted light describes mirror reflection with respect to the facet surface of the grooves, most of the energy is concentrated into the mth order diffracted light. At this condition, the relation between θ_B, θ_i and θ_d satisfies the following condition

$$\theta_d = 2\theta_B - \theta_i.$$ 3. 22

The corresponding wavelength at this specific diffraction angle is called blaze wavelength, denoted by λ_B. Combining equations 3.21 and 3.22, the blaze wavelength is given by:

$$\lambda_B = \frac{2d}{m}\Big[\sin\theta_B \cos\left(\theta_i - \theta_B\right)\Big].$$ 3. 23

When $\theta_i = \theta_B$, the incident light is coming along the facet normal, and the 1st order diffracted beam returns in the same path as the incident light. This configuration, called Littrow mounting, is used to represent the blazing characteristics of gratings. The corresponding blaze wavelength $\lambda_{B(Litt)}$, called Littrow wavelength, is given by

$$\lambda_{B(Litt)} = 2d\sin\theta_B.$$ 3. 24

θ_B and $\lambda_{B(Litt)}$ characterize the blazed gratings and are given in the catalog of grating manufacturers. The blaze wavelength at any other configuration than the Littrow mounting is therefore given by

$$\lambda_B = \frac{\lambda_{B(Litt)}}{m}\cos\left(\theta_i - \theta_B\right).$$ 3. 25

The blaze wavelength varies with the blaze angle and the incident angle. It can be shown (see section 3.3.2.3) that both the wavelength dependent angular separation of wavelength

components and the resolving power of the grating increase as the diffracted order increases. However, for blazed gratings, both efficiency and free spectral range (FSR) decrease as the diffraction order increases. As the actual resolution of the spectrometer is limited by the aberration and imperfection of the optical components and the size of the detector, 1st order blaze configuration has been used in our SD-OCT design in order to concentrate the most of the diffracted energy in this order. Fixing the blaze wavelength λ_B to be the center wavelength of the light source λ_o, i.e., $\lambda_B = \lambda_o$, one can choose a blazed grating from the manufacturers datasheet whose $\lambda_{B(Litt)}$ is around (if possible greater than) λ_B , and by adjusting the incident angle, a blaze wavelength around the center wavelength can be achieved according to equation 3.25.

The center wavelength λ_o of our light source used for SD-OCT system is 1.3 µm. From Thorlabs catalog, the options available at the time of purchase were two gratings with the characteristics given in table 3.1

Table 3.1 Two blazed gratings from Thorlab's catalog whose $\lambda_{B(Litt)}$ lie around the value of 1.3 µm

Item #	g (grooves/mm)	θ_B	dλ/dθ_d (nm/mrad)	$\lambda_{B(Litt)}$(µm)
GR25-0616	600	28° 41'	1.46	1.60
GR25-0613	600	22° 1'	1.55	1.25

According to equation 3.25, if one chooses the first grating (GR25-0616) ($\lambda_{B(Litt)}$ = 1.60 µm), the required incident angle θ_i to get a blaze wavelength λ_B = 1.3 µm will be $\theta_i \approx 64°$. However, looking at the diffraction efficiency curves of the two gratings shown in Figure 3.12, the grating with $\lambda_{B(Litt)}$ = 1.60 µm has a dip in efficiency within the spectral range of our interest.
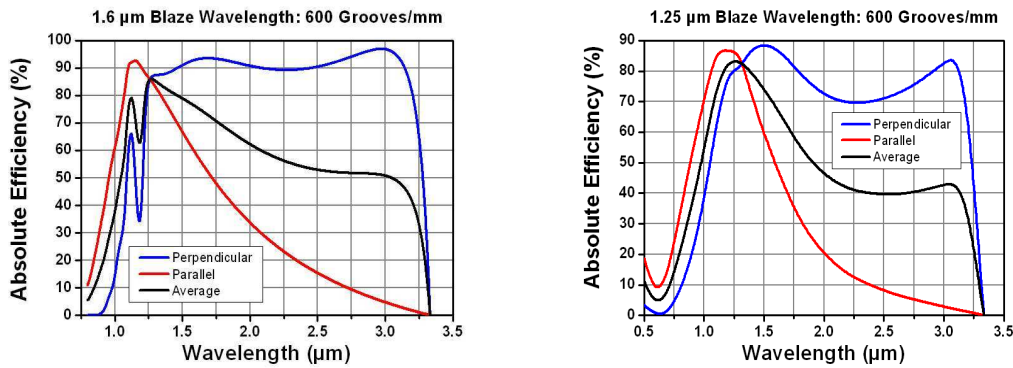

Figure 3.12 Diffraction efficiency for two blazed gratings designed at $\lambda_{B(Litt)}$ = 1.60 µm and $\lambda_{B(Litt)}$ = 1.25 µm. Both gratings utilize an Aluminum (Al) reflective coating and are measured in the Littrow mounting configuration. The parallel polarization is parallel to the grating grooves, plots taken from Thorlabs catalog.

On the contrary, the second grating (GR25-0613) ($\lambda_{B(Litt)} = 1.25\,\mu m$) shows a better efficiency around 1.3 µm at Littrow configuration but equation 3.25 yields a blaze wavelength that is always less than or equal to 1.25 µm. However, if the grating is mounted to work close to Littrow configuration, the overall effective diffraction efficiency of the second grating will give better performance. Hence for our spectrometer design, we have used this grating (GR25-0613).

3.3.2.2 Line-Scan Camera

The other important element of the spectrometer is the line-scan camera (LSC). For the development of SD-OCT working around 1.3 µm, a LSC with high quantum efficiency and high line rate is required. In the past, one of the challenges of the development of fast SD-OCT around 1.3 µm has been related to the availability of a high speed LSC with high responsivity in the long wavelength range. The fastest commercially available InGaAs camera at the time of our purchase was the *SUI[TM] SU-LDH Linear Digital High Speed InGaAs Camera* from GOODRICH. The detailed electro-optic performance of the camera is given in table 3.2.

Table 3.2 Electro-optical performance of the line-scan camera used in our SD-OCT, taken from camera manual.

Sensor format[1]	1024 pixels on 25 µm pitch with 4 readout ADCs					
Optical aperture (pixel height)[1]	500 µm or 25 µm					
Peak quantum efficiency [1]	> 70%					
Gain capacitor setting	0.1 pF		1 pF		10 pF	
	Typical	Specification	Typical	Specification	Typical	Specification
Net full well capacity (Me-)[2]	1.6	> 1.1	15.9	> 9.2	150	> 110
Gain (e-/cnt)[1, 3]	107		1000		9600	
Temporal noise (rms counts)[1,2]	8	< 10.5	3.5	< 10.5	2.5	< 10.5
Dynamic range [1, 2, 4]	2000:1	> 1500:1	4500:1	> 3500:1	5300:1	> 4500:1
Differential non-linearity [1, 2]	± 1 %	< ± 2 %	± 1 %	< ± 2%	± 0.8 %	<± 2 %
Bad pixel specification	White, dark, noisy or pixels exceeding +/- 10 of the mean value when illuminated at 50% of full well Number of bad pixels limited to a maximum of 1% of array total; no bad neighbors within 5 pixels					
Digital output format	14-bit base Camera Link compatible					
Exposure time [1, 3]	0.007 ms to 907 ms in corrected preset modes or user programmed in camera clock cycles to > 1 s					
Trigger modes [3]	Free run, Single line per trigger , programmable exposure , or gated burst					
Sync output	Digital signal, high during integration					
External trigger [3]	Three modes via CC1 or BNC					
External variable ET	User set by the duration of trigger signal (minimum ET pulse: 10 µs)					
External trigger jitter	1 clock cycle: nominally 80 ns					
Pixel rate	50×10^{6}pixel/s					
Readout mode	Integrate while read, differential double sampling					
Corrections (preset OPR)	Factory calibrated gain, offset, and bad pixel replace					

[1]Actual formats and performance governed by user selected SUI linear array purchased with camera (dark current may limit longest usable ET)
[2] Camera readout noise limited until exposure time for 500 µm pixels exceeds 50 ms in low gain, 10 ms in medium, and ½ ms in high gain mode
[3] User selectable by command over Camera Link ® serial lines
[4] Dynamic range limited to maximum values shown when camera operated at exposure times shorter than 28 µs

This camera can acquire A-scans at rate of up to 46 KHz. The quantum efficiency (QE) of the camera within our region of interest, i.e., around 1.3 µm, is more than 80 % (see Figure 3.13). The camera has 1024 pixels. When operated at maximum capacitor setting, the specified net full-well capacity (FWC) of the camera is ~ 1.1×10^8 electrons, yielding a dynamic range of ~ 73 dB.
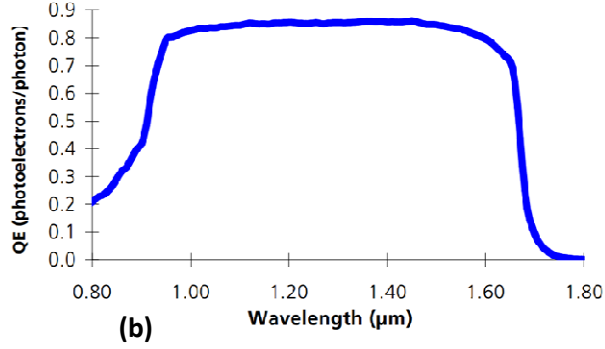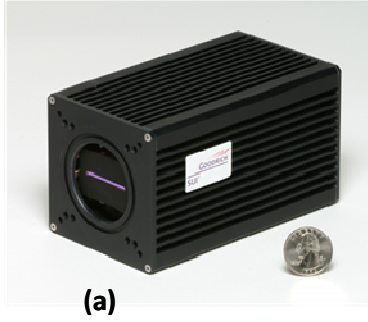

Figure 3.13 The line-scan camera (*SUI^{TM} SU-LDH,* GOODRICH) used in our SD-OCT **(a)** and its typical quantum efficiency, taken from camera manual **(b)**

Depending on the pixel size of the camera, there were two options available: the first option has been with square pixels (25 µm × 25 µm) and the other rectangular pixels with width (pitch) of 25 µm and height (aperture) of 500 µm. As the camera with larger aperture is relatively easier for optical alignment without affecting the resolution of the spectrometer, we bought the camera with rectangular pixels, i.e. 25 µm × 500 µm.

3.3.2.3 Sampling resolution of the spectrometer

The sampling resolution $\delta\lambda$ (or $\delta\sigma$) is an important parameter of the spectrometer because it determines the imaging depth (section 3.2.3) and affects sensitivity fall-off (section 3.3.4). The sampling resolution depends on the dispersion of the grating, the effective focal length f' of the focusing optics and the pitch size W of the detector pixel. The expression of the sampling resolution can be written as

$$\delta\lambda = W \times D_{rec},$$ 3. 26

where $D_{rec} = \mathrm{d}\lambda/\mathrm{d}x$ is reciprocal of linear dispersion and represents the difference in wavelength per unit length on the surface of the digital detector.

If the incident angle is regarded as a constant, differentiating both sides of equation 3.21 with respect to λ gives the angular dispersion D_{ang}:

$$D_{ang} = \frac{d\theta_d}{d\lambda} = \frac{g}{\cos\theta_d}, \; m = 1; \qquad\qquad 3.\,27$$

where $g = 1/d$ is the groove density [grooves/mm]. By inverting equation 3.27, multiplying by the effective focal length f' of the focusing optics and considering $dx = f' \times d\theta_d$ (see Figure 3.14), one gets

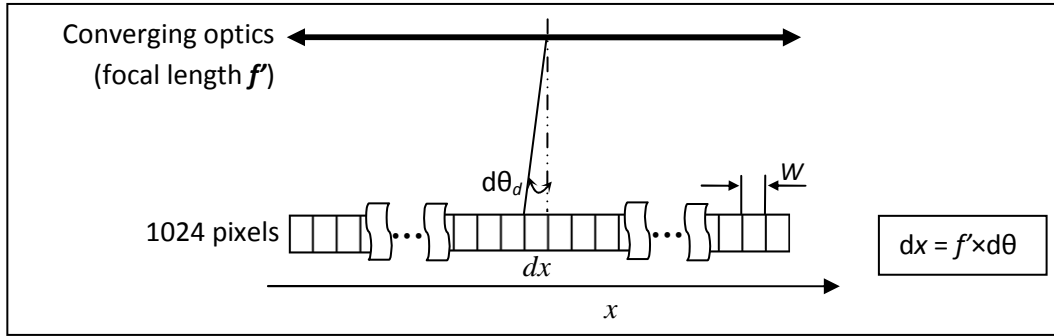$$D_{rec} = \frac{d\lambda}{dx} = \frac{\cos\theta_d}{gf'}. \qquad\qquad 3.\,28$$

Figure 3.14 Part of the spectrum contained within $d\theta_d$ will be translated by f' into dx

Combining equations 3.26 and 3.28, the expression of the the spectral sampling resolution $\delta\lambda$ will be

$$\delta\lambda = W \times D_{rec} = W \times \frac{d\lambda}{dx} = \frac{W}{gf'}\cos\theta_d. \qquad\qquad 3.\,29$$

Pixel pitch W and groove density g will be fixed once the camera and the grating are selected, and θ_d is also determined from the experimental setup. For $\theta_i = 30°$, the diffraction angle θ_d of the blaze wavelength will be $\theta_d = 2\theta_B - \theta_i = 2\times22°-30° = 14°$. However the focal length f' remains to be determined: one can target to achieve either a given imaging depth by compromising the axial resolution, or the other way round. We will see later (see section 3.3.3) that in SD-OCT, there is a trade-off between imaging depth and axial resolution. If one targets to achieve a given maximum imaging depth z_{max}, then $\delta\lambda$ and f' can be calculated from equations 3.9 and 3.29, respectively.

In our project, as our target was to improve the axial resolution Δz of the commercial SS-OCT system (which was $\Delta z = 12$ µm in air) by at least a factor of two, i.e., $\Delta z_{required} \leq 6$ µm, so as to properly view the Schlemm's canal, getting a high axial resolution with optimal imaging depth was our design priority. On the other hand, Schlemm's canal is found at a depth of ~ 0.8 mm (with diameter of 0.25 mm) inside the limbus (corneoscleral junction). Considering

a corneal refractive index of 1.38, the imaging depth of the SD-OCT should at least be 1.45 mm in air. Hence f' should be chosen in such a way that $\Delta z \leq 6\ \mu m$ and $z_{max} \geq 1.45$ mm (in air).

In order to resolve two reflections that are separated by Δz, the pixel spacing Δp in the axial domain (z-domain) should be at least $\Delta p = \Delta z/2$ [64]. As Fourier transform of real data gives redundant information, only $N/2$ the Fourier bins in the z-domain contain distinct information. This implies that the maximum imaging depth z_{max} will be

$$z_{max} = \frac{N}{2} \times \frac{\Delta z}{2}.$$ 3. 30

If the total spectral range of the spectrum collected by N pixels of the line camera is $\Delta\Lambda$, then $\delta\lambda$ can be easily calculated by $\delta\lambda = \Delta\Lambda/N$, and from equation 3.9, z_{max} can be expressed as

$$z_{max} = \frac{1}{4}\frac{\lambda_o^2}{\delta\lambda} = \frac{1}{4}\frac{\lambda_o^2}{\Delta\Lambda/N}; \quad \delta\lambda = \frac{\Delta\Lambda}{N} = \lambda_o^2 \times \delta\sigma.$$ 3. 31

Taking the ratio between equation 3.30 and 3.31 and substituting $\Delta z = (2\ln2/\pi)\times(\lambda_o^2/\Delta\lambda)$, the relation between the required spectral range $\Delta\Lambda$ of the spectrometer and the spectral bandwidth $\Delta\lambda$ (FWHM) of a Gaussian light source can be expressed as

$$\Delta\Lambda = \frac{\pi}{2\ln 2} \times \Delta\lambda.$$ 3. 32

An axial resolution of 6 µm at 1.3 µm center wavelength can be theoretically achieved by employing a Gaussian-shaped light source with spectral bandwidth $\Delta\lambda = 124$ µm (FWHM). This requires a spectrometer with $\Delta\Lambda = 281$ nm. Spreading 281 nm over 1024 camera pixels gives a spectral sampling resolution $\delta\lambda = 0.27$ nm can be achieved. The maximum imaging depth at $\delta\lambda = 0.27$ nm is $z_{max} = 1.56$ mm, which is well above the required imaging depth needed to view the Schlemm's canal.

Using equation 3.29, and substituting all the values, the required effective focal length f' of the focusing optics will be

$$f' = \frac{W}{g \times \delta\lambda}\cos\theta_d = \frac{25\times10^{-6}}{600\times0.27\times10^{-9}}\times\cos(14°)\ mm = 154\ mm.$$ 3. 33

If f' is too long, the spectral range collected by the spectrometer will be narrower than 281 nm, giving rise to an axial resolution that is inferior to the value limited by the light source. On the other hand, shorter f' will collect broader spectral range than 281 nm and lower

the spectral sampling resolution. This will reduce the imaging depth without further improving the axial resolution.

Note that the above analysis assumes a Gaussian light source and can only give us a rough approximation of the spectrometer parameters because the actual light source we have used is not Gaussian. If the spectral shape of light source is, for example, rectangular, it can be shown that the FWHM bandwidth $\Delta\lambda_{rect}$ of the rectangular light source needed to get $\Delta z \leq 6\,\mu\text{m}$ is almost twice of that FWHM $\Delta\lambda_{gaus}$ of Gaussian spectrum, i.e., $\Delta\lambda_{rect} = 2\times\Delta\lambda_{gaus}$. In this particular case, by going through the same steps, one can show that $\Delta\Lambda_{rect} \approx \Delta\lambda_{rect} = 2\times\Delta\lambda_{gaus} = 248$ nm, which is logical because the width of a rectangle does not change. The spectral sampling resolution and the focal length corresponding to $\Delta\Lambda_{rect} = 248$ nm are $\delta\lambda_{rect} = 0.24$ nm, $f' = 135$ mm. The new value of $\delta\lambda_{rect}$ changes the maximal depth range to $z_{max} \approx 1.8$ mm. As the spectrum of light we used is neither Gaussian nor rectangular, the actual experimental value the imaging depth will be in between the two theoretical cases, i.e. 1.56 mm $\leq z_{max} \leq 1.8$ mm.

3.3.3 Trade-off between axial resolution and imaging depth

One of the drawbacks of practical SD-OCT system is that its axial resolution and the imaging depth range are inversely related. If one wants to achieve an axial resolution Δz that is limited by the bandwidth $\Delta\lambda$ of the light source, the minimum spectral range $\Delta\Lambda$ (assuming Gaussian-shaped spectrum) that the spectrometer has to collect is expressed by equation 3.32. From a practical point of view, the number of detector pixels N of the spectrometer is finite (often 5012 or 1024). Spreading $\Delta\Lambda$ over N will make the spectral sampling resolution $\delta\lambda$ finite (equation 3.31).

Combining these design parameters in one equation, we get

$$\Delta z = \frac{2\ln 2}{n\pi}\times\frac{\lambda_o^{\,2}}{\Delta\lambda} = \frac{\lambda_o^{\,2}}{n\Delta\Lambda} = \frac{\lambda_o^{\,2}}{n\delta\lambda\times N} = \frac{\lambda_o^{\,2}}{4n\delta\lambda}\times\frac{4}{N} = \frac{4}{N}\,z_{\max}\,. \qquad 3.\,34$$

Equation 3.34 states the experimental trade-off between axial resolution Δz and maximum imaging depth z_{max} of SD-OCT. Increasing N would allow us to increase both the resolution and imaging depth, but N cannot be infinitely increased for practical reason. As a consequence, high-resolution SD-OCT systems are realized at the expense of reduced imaging depth, or vice versa. In our SD-OCT design, though the target has been improving the axial resolution, we also considered the fact that the depth range of the system should be large enough to view the Schlemm's canal.

3.3.4 Sensitivity fall-off

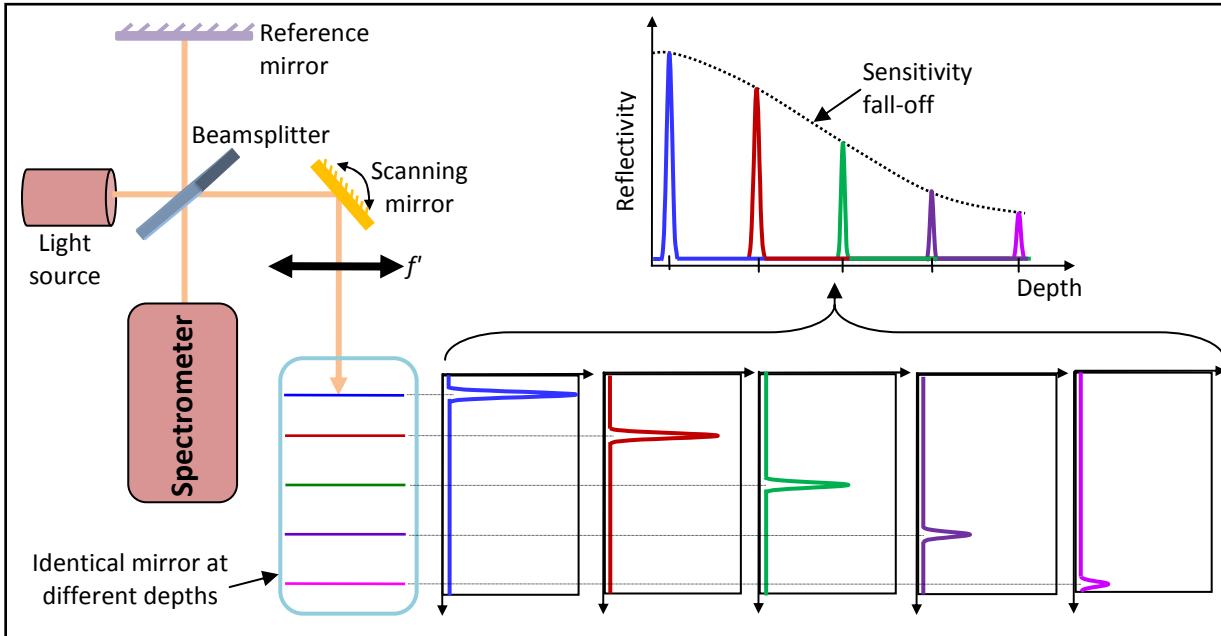The other main drawback of SD-OCT is its depth dependent sensitivity fall-off (see Figure 3.15).

Figure 3.15 Illustration of depth dependent sensitivity fall-off of SD-OCT. The plots show that the magnitude of the axial PSF corresponding to the same mirror decreases as its depth increases. This is due to the wash out of the fringe visibility, which is dependent on the spectral resolution of the spectrometer and the spectral sampling resolution.

In section 3.2.1, we have discussed that the signal magnitude of SD-OCT depends on the amplitude of the spectral modulation of the acquired spectrum. This amplitude, as shown in equation 3.1, is independent of the frequency of the spectral modulation. However, experimental results show that the same reflector at different depths gives rise to different magnitude of reflectivity, i.e. though the intensity of light reflected back from the sample remains the same, the magnitude of reflectivity decreases as the reflector's depth increases.

In other words, as the modulation frequency increases, the fringe visibility decreases. This leads to a decrease in sensitivity to waves reflected from deeper locations within the sample. Such dependent sensitivity fall-off of SD-OCT is due to the washout of the high frequency spectral fringes, and is mainly dependent on two factors: the resolution of the spectrometer and the resolution of spectral sampling achieved by the CCD pixels.

3.3.4.1 Qualitative explanation

Let us qualitatively explain this phenomenon by considering a spectral modulation corresponding to a single reflector. The modulated spectrum, as explained above, is measured

by spectrally separating the various wavelength components in a spatially defined way. After focused by the focusing optics, the CCD then samples the cosine oscillation by a finite number of pixels. This process can be thought at passing the light into two systems with different impulse responses:

> First, the focusing lens spreads a point into a finite Gaussian spot due to the diffraction limit of the optical system

> Second, the CCD pixel then integrates the intensity of light over its pixel area, which can be thought as imposing a rectangular function "*Rect*" on each Gaussian spot.

As the frequency of the cosine modulation increases, the fringe spacing becomes progressively narrower, i.e. the spatial separation of two neighboring fringe maxima/minima on the detector decreases. Due to the limited spot size of the individual maxima, the response of the line detector to different modulation frequencies will be different. The spectrometer, in this case, can be considered as a low pass filter, i.e., the amplitudes of fringes with high modulation frequencies are more attenuated than those with low frequencies (see Figure 3.16). In other words, the fringe visibility (contrast) decreases with increasing modulation frequency (or imaging depth). As the Fourier transformed signal strength of SD-OCT depends on the fringe contrast, high frequency terms will eventually appear as low light reflecting sample structures, though the reflector has not been physically changed.
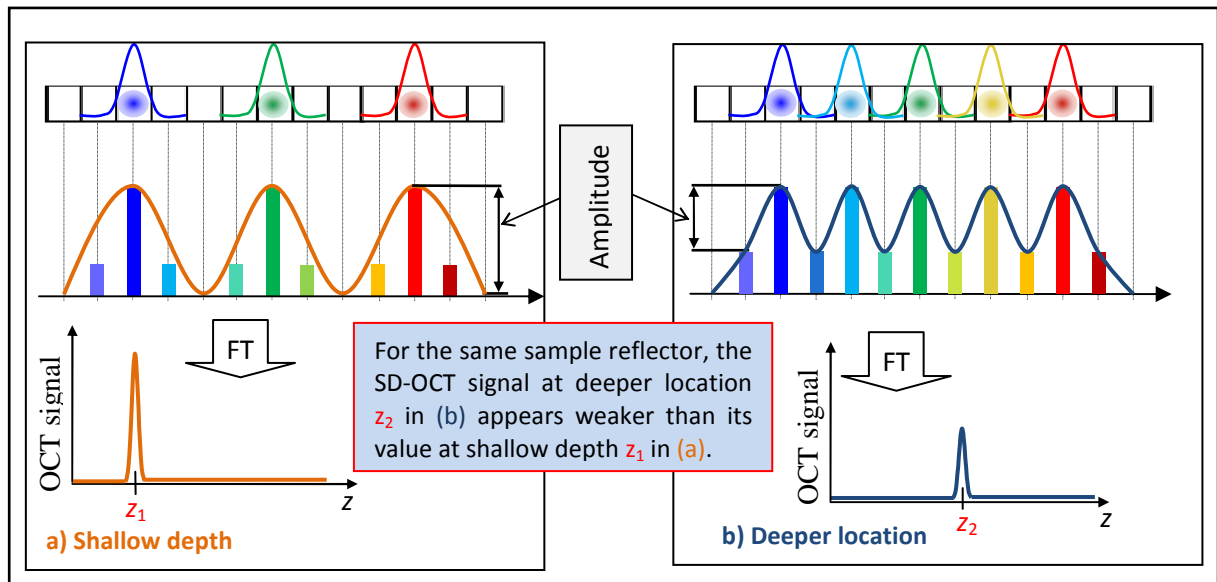

For the same sample reflector, the SD-OCT signal at deeper location z_2 in (b) appears weaker than its value at shallow depth z_1 in (a).

a) Shallow depth

b) Deeper location

Figure 3.16 Illustration of the impact of increasing depth on fall of SD-OCT signal: the same reflector when translated to deeper position appears to have a lower reflectivity. For a given beam spot size, an increase in the modulation frequency (due to an increases in the reflector's depth) decreases the fringe amplitude (or fringe contrast). As SD-OCT signal magnitude (reflectivity) after The Fourier transform is directly proportional to the amplitude of modulation, a reflector at shallow depth z_1 (a) gives rise to stronger signal than the same reflector at a deep location z_2 (b) in the sample.

This phenomenon becomes more significant when the spot size of the beam on the CCD increases as shown in Figure 3.17. This is because, as the beam spot size increases (b), the tail of the Gaussian-shaped beam profile extends to neighboring pixels, thereby further decreasing the fringe contrast.
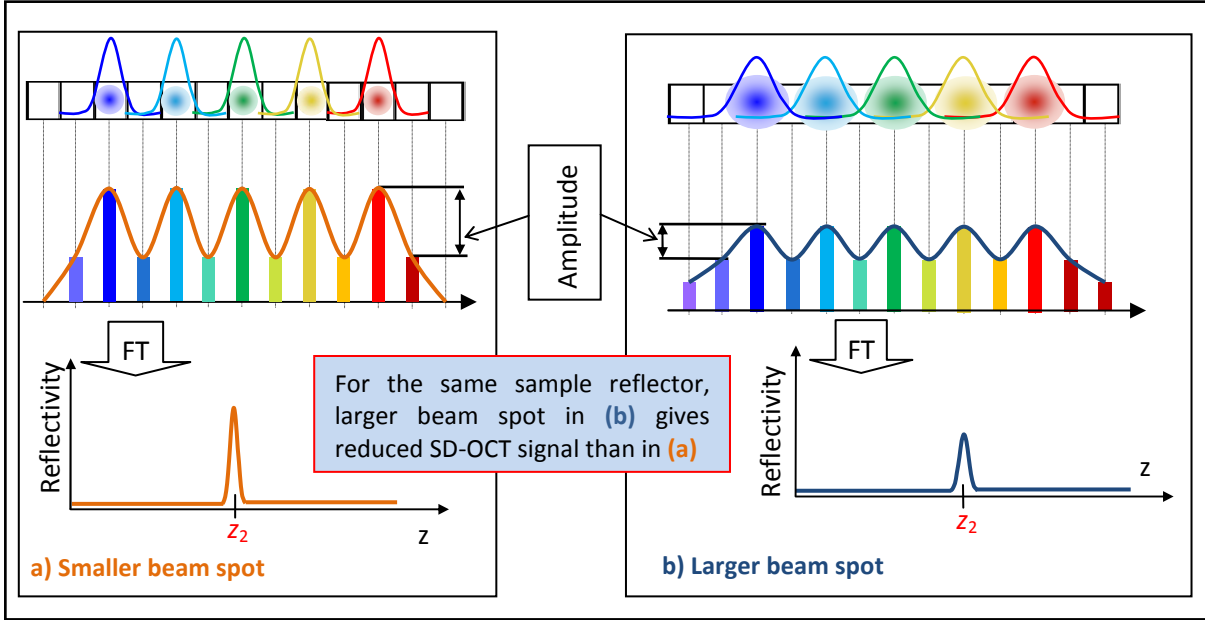

Figure 3.17 Illustration of the impact of increasing beam spot on fall of SD-OCT signal. For a given reflector at depth z_2, larger beam spot (b) allows the Gaussian beam to extend to neighboring pixels, thereby decreasing the fringe contrast and the SD-OCT signal than smaller beam spot (a). The situation gets worse at deep sample locations than shallow ones.

3.3.4.2 *Quantifying the sensitivity fall-off effect*

The actual spectrometer's spectral resolution depends on the size of the beam spot in the focal plane. Assuming a Gaussian beam profile, if *d* is the FWHM of the beam spot on the CCD, the FWHM of the actual spectral resolution δσ' is given by

$$\delta\sigma' = d \times \frac{d\sigma}{dx} = d \times \frac{1}{\lambda_o^2}\frac{d\lambda}{dx} = \frac{1}{\lambda_o^2}d \times D_{rec}. \qquad 3.35$$

Assuming that the spectrum is linear with respect to spatial frequency *σ*, the rectangular-shaped CCD pixels integrate the spectrum over its receiver area, which can be thought as imposing a rectangular function *"Rect"* on each Gaussian beam spot. If the physical pixel width is *W*, then the sampling resolution δσ by the rectangular CCD pixels will be

$$\delta\sigma = W \times \frac{d\sigma}{dx} = W \times \frac{1}{\lambda_o^2}\frac{d\lambda}{dx} = \frac{1}{\lambda_o^2}W \times D_{rec}. \qquad 3.36$$

And the *Rect* function is given by

$$Rect\left(\frac{\sigma}{\delta\sigma}\right) = \begin{cases} 0 & for \; |\sigma| > \dfrac{\delta\sigma}{2} \\[2mm] \dfrac{1}{2} & for \; |\sigma| = \dfrac{\delta\sigma}{2} \\[2mm] 1 & for \; |\sigma| < \dfrac{\delta\sigma}{2} \end{cases} \qquad 3.\,37$$

The graphical illustration of sensitivity fall-off effect due to the limited sizes of beam spot and pixel CCD pixels is given in Figure 3.18.
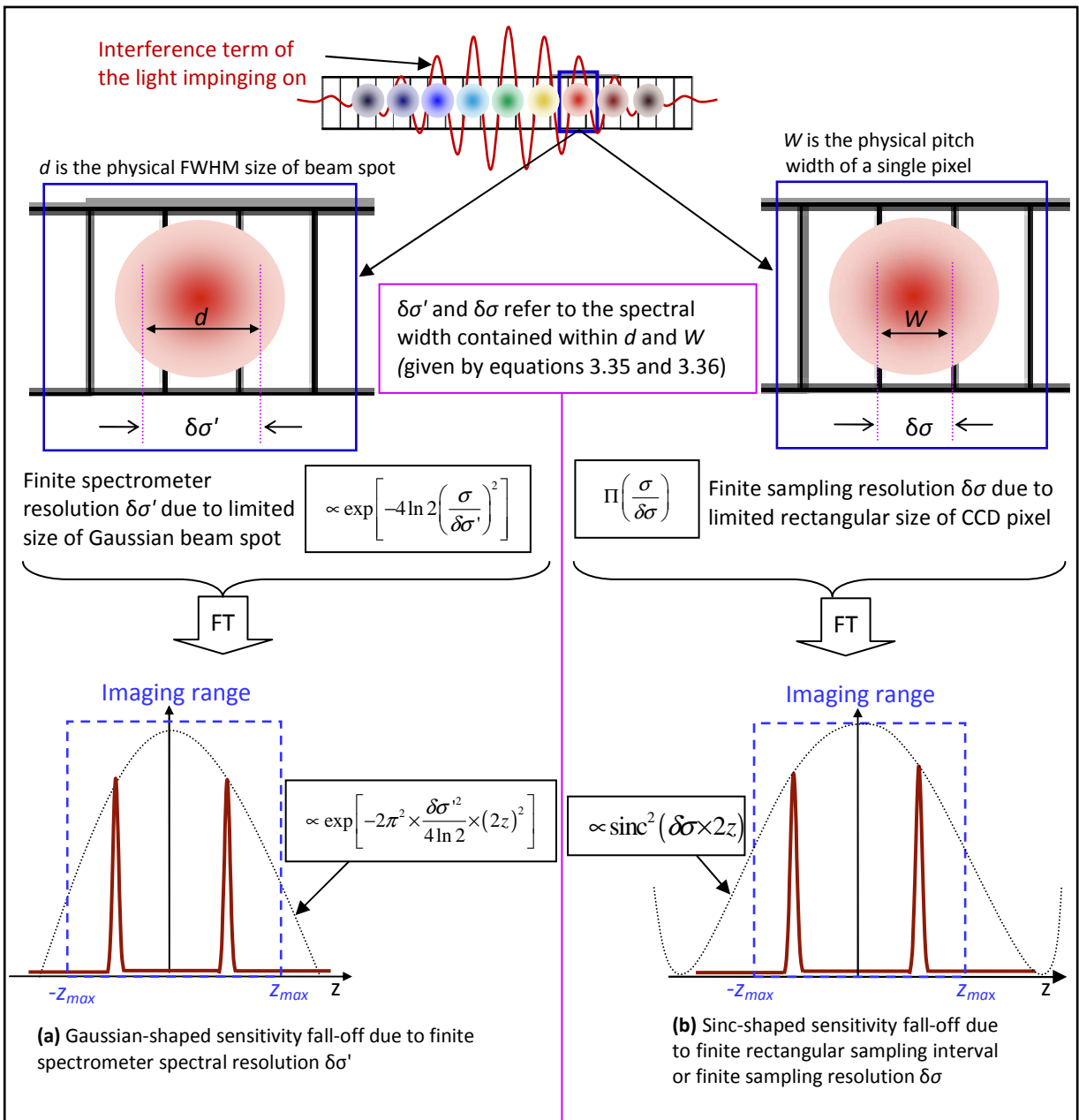

Figure 3.18 Illustration of sensitivity fall-off effect due to **(a)** the finite spectral resolution of the spectrometer (related to the limited beam spot size) and **(b)** the finite sampling interval of the spectrum (related to the physical size of the detector pixels).

The convolution of the finite Gaussian beam spot with the finite rectangular sampling interval becomes a multiplication after the Fourier transform, and the sensitivity reduction R as a function of imaging depth z can be easily derived from equations 3.35 and 3.36 as [48]

$$
\begin{aligned}
R(z) &= \left[\frac{\sin\left(\pi \times \delta\sigma \times 2z\right)}{\pi \times \delta\sigma \times 2z} \right]^2 \times \left[\exp\left(-\pi^2 \times \frac{\delta\sigma'^2}{4\ln 2} \times (2z)^2 \right) \right]^2 \\
&\Rightarrow R(z) = \operatorname{sinc}^2\left(\frac{1}{2} \times \frac{z}{z_{\max}} \right) \times \exp\left[-\pi^2 \times \frac{w^2}{8\ln 2} \times \left(\frac{z}{z_{\max}} \right)^2 \right]
\end{aligned}
$$

3. 38

where $w = \dfrac{\delta\sigma'}{\delta\sigma} = \dfrac{d}{W}$ is the ratio of the spectral resolution (FWHM) to the sampling interval.

By analyzing equation 3.38, the dependence of sensitivity fall-off on each parameter can be extracted and separately analyzed.

3.3.4.2.1 *Sensitivity fall-off due to finite sampling interval*

Considering the "*sinc*" function part of equation 3.38, its argument varies with respect to the sampling interval or spectral sampling resolution $\delta\sigma$, which in turn depends on the pixel width W and the reciprocal linear dispersion D_{rec} (see equation 3.36). If W *or* D_{rec} decreases, the sensitivity falls slowly with respect to z. However, if one wants to achieve a source limited axial resolution Δz using a given limited number N of detector pixels, decreasing W requires increasing D_{rec}. When we fix the axial resolution, we are also fixing the spectral range $\Delta\Lambda$ of the spectrometer (see equation 3.32), which in turn fixes the spectral sampling resolution $\delta\sigma$ according to equation 3.31. Once $\delta\sigma$ is fixed, as far as equation 3.36 is maintained, one can choose any pixel size W without affecting the "*sinc*" factor of sensitivity fall-off. Hence based on the availability of the camera, the right spectrometer that matches the pixel size can be designed.

If D_{rec} of the spectrometer is designed in such a way that the line scan camera with 1024 pixels having a pitch $W = 25$ µm collects the source spectrum of spectral range $\Delta\Lambda = 245$ nm centered at 1300 nm, the spectral sampling interval and the maximum imaging depth will be

$$
\delta\sigma = \frac{(245\,\text{nm}/104)}{(1300\,\text{nm})^2} = 0.14 \ \text{mm}^{-1} \quad \text{and} \quad z_{\max} = \frac{1}{4 \times 0.14}\,mm \approx 1.8\,mm \ .
$$

For such experimental configuration, the theoretical plot of sensitivity fall-off due to the "*sinc*" function is given in Figure 3.19. Note that at z = z_{max} = 1.8 mm, sensitivity falls nearly by 4 dB.
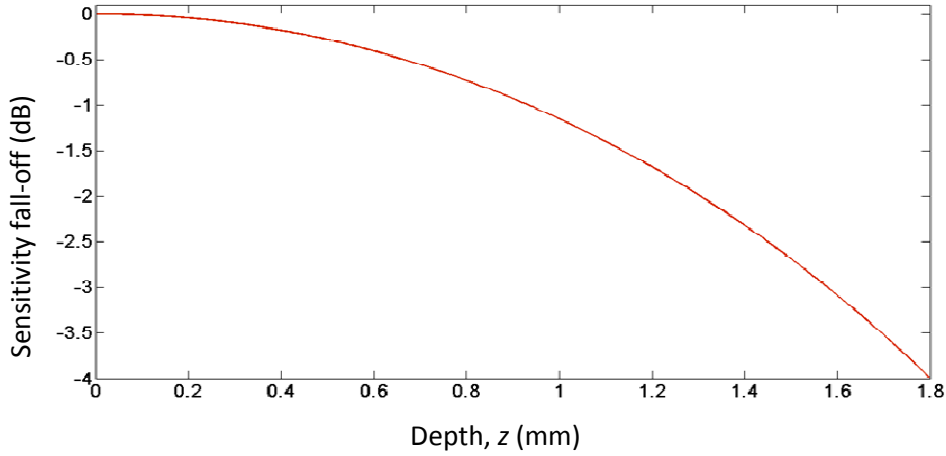

Figure 3.19 SD-OCT sensitivity fall-off effect due to finite sampling interval of a spectrometer that collects a spectral range of 245 nm using 1024 CCD pixels each having a pitch width of 25 µm. This corresponds to a theoretical sensitivity fall of ~ 4 dB at the end of the depth range, z_{max} = 1.8 mm.

3.3.4.2.2   *Sensitivity fall-off due to finite spectral resolution*

The Gaussian function part of equation 3.38 refers to the sensitivity reduction due to the finite spectral resolution $\delta\sigma'$ of the spectrometer. A spectrometer with high spectral resolution (smaller value of $\delta\sigma'$) yields a slowly falling sensitivity. $\delta\sigma'$ depends on the average beam spot size d (FWHM) on the detector plane and the reciprocal linear dispersion D_{rec} (see equation 3.35). The larger the beam spot, the lower the spectrometer resolution and the faster the sensitivity fall-off with increasing the imaging depth. Hence keeping the beam spot smaller helps reduce the fall-off. A focusing lens with short focal length can reduce the spot size. However, as the focal length f' is inversely proportional to D_{rec} (see equation 3.28), decreasing f' proportionally increases D_{rec}, ending up with the same value of $\delta\sigma'$. The beam spot size can independently be controlled by changing the beam diameter at the input of the spectrometer. D_{rec} can be decreased by choosing a spectrometer with high groove density g (see equation 3.28), but for a source limited resolution SD-OCT, the choice of D_{rec} is dictated by the required spectral range of the spectrometer.

Consider the above example where D_{rec} is designed in such a way that the line scan camera with 1024 pixels having a pitch $W = 25$ µm collects $\Delta\lambda = 245$ nm centered at 1300 nm, resulting in $z_{max} = 1.8$ mm. Figure 3.20 shows theoretical plots of sensitivity fall-off for different beam spot sizes, varied by changing the collimated beam diameter D at the input of

the interferometer. An optimum value of the beam spot size is when it is equal to the size of the CCD pixel pitch width *W*.
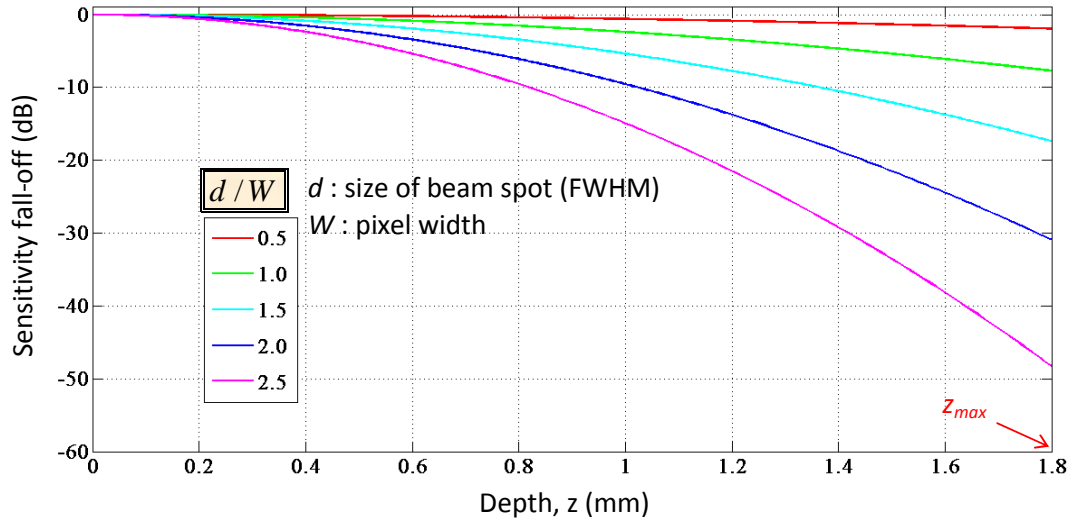

Figure 3.20 SD-OCT sensitivity fall-off effect due to finite spectral resolution of spectrometer that collects a spectral range of 245 nm using 1024 CCD pixels each having s pitch width of 25 µm. As shown in the legend, as the spot size to pixel width ratio increases, the sensitivity falls rapidly. When $d = W$, the sensitivity falls by ~ 8 dB, and when $d = 2W$, the sensitivity fall-off is about 32.7 dB.

The combined theoretical sensitivity fall-off at the end of the depth range due to finite spectral sampling interval and finite resolution of the spectrometer for a beam spot size that is equal to the width of the detector pixel is about 12 dB in our experimental configuration (see Figure 3.21).
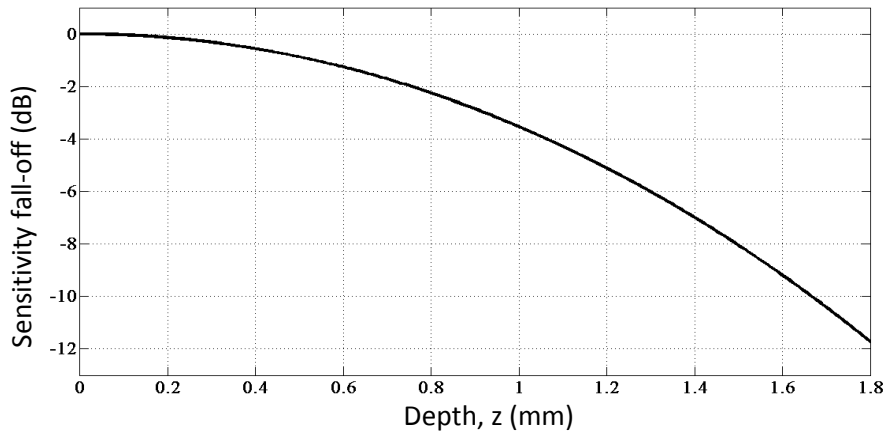

Figure 3.21 Combined sensitivity fall-off due to the two effects for a beam spot size that is equal to the size of the detector pixel. In our experimental configuration, a total of nearly 12 dB fall in sensitivity can be noted from the plot.

3.3.5 Spectral calibration

In the previous sections, we have seen that the A-scan in SD-OCT is computationally reconstructed from the acquired modulated spectrum by performing the Fourier transform

from spatial frequency σ to imaging depth z (see equation 3.1 and 3.3). As σ and z are conjugate variables, Fourier transform requires the data to be uniformly spaced in σ. However, the grating based spectrometer of SD-OCT operated at small diffraction angles disperses the light on the CCD pixels almost in a linear fashion with respect to wavelength, λ, and as σ and λ are inversely related, the spectrum will be non-uniformly sampled in σ. If one applies the Fourier transform directly on this non-uniformly sampled dataset, both axial resolution and sensitivity fall-off of SD-OCT will be much worse than the theoretically predicted values given by equations 3.6 and 3.38, where the spectrum has been assumed to be uniformly spaced in σ. As the acquired data by the spectrometer does not obey this assumption, the ultimate goal of spectral calibration, a very important step in SD-OCT design, is therefore to get a dataset that is uniformly spaced in σ.

Spectral calibration is the process of determining the wavelength-to-pixel mapping, i.e., the exact wavelength of the light falling on each CCD pixel is determined [65]. Once such wavelength-to-pixel mapping is done, using the relation $\sigma = 1/\lambda$, the dataset is interpolated at new values of λ to have equally spaced data in σ. After this, Fourier transform can be applied to reconstruct A-scans.

3.3.5.1 Hardware approach

Spectral calibration can be achieved with the use of one or more single wavelength lasers whose wavelengths lie within the spectral range of our interest. In theory, if all the geometrical parameters (light incident angle θ_i, groove density g, focusing optics focal length f and pixel width) of the spectrometer are known, then the knowledge of a single wavelength mapping on one of the detector pixels is sufficient to analytically deduce the corresponding wavelengths associated with all the other pixels. However, in practice, geometrical parameters such as the orientation of the grating and the incident angle of light hitting the grating are not precisely known. So the theoretical equation may not yield an accurate result. To overcome this issue, one can treat those parameters as unknown variables, register the pixel locations for as many known spectral lines as there are unknown parameters, solve the fitting equation for all those unknowns and deduce the wavelength-to-pixel mapping using the fully defined fitting equation.

As we are working in the spectral range of roughly 1300 nm ± 125 nm, the first challenge of such hardware-based spectral calibration method is finding multiple narrow linewidth calibration lasers within this spectral range. The second challenge is that once the calibration

is done, touching any translation stage or changing some optics in SD-OCT system requires re-doing the whole physical calibration process.

In our SD-OCT design, we have used a substantially different and convenient numerical calibration method without the use of calibration laser (s). This method does not involve wavelength-to-pixel mapping. It is rather based on extraction and linearization of the non-linear phase of the modulated spectral interferogram associated with arbitrary single reflector placed at any depth (within the depth range) in the sample arm.

3.3.5.2 Phase linearization method (Numerical approach)

Looking at the signal term of the acquired interferogram (see equation 3.1), the depth z_o and wavelength λ dependent phase φ is given by

$$\varphi = 2\pi\sigma \times \delta = \frac{4\pi}{\lambda} z_o \,.$$

3. 39

Equation 3.39 tells that for a given value of depth z_o, a linear variation of wavelength λ gives rise to a non-linear variation of the phase φ of the spectral interferogram.

Figure **3.22** (a) shows a simulation of this effect using the following parameters: $z_o = 10\,\mu$m and $\lambda_{min} = 1\,\mu$m, $\lambda_{max} = 2.023\,\mu$m, with uniform wavelength spacing of 1.0 nm. As we can see in Figure 3.22 , the fringe period is narrower in the left (shorter wavelength region) than on the right (longer wavelength region).
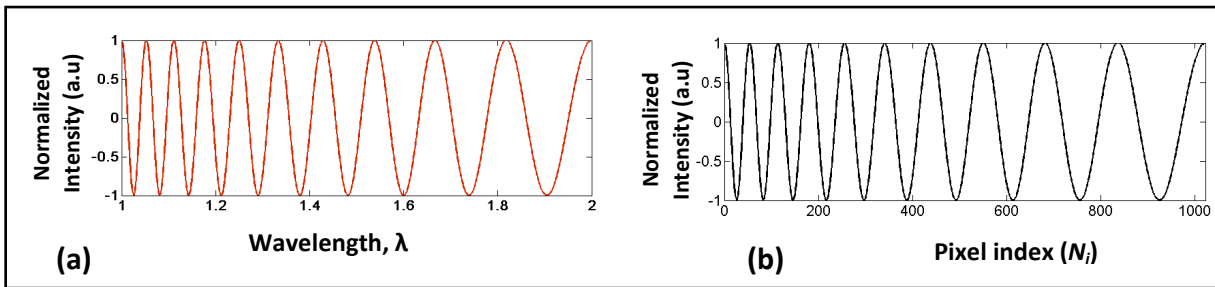

Figure 3.22 Simulation of a raw spectral interferogram acquired by the spectrometer plotted as a function of (a) wavelength λ and (b) pixel index N_i (b). The spectral fringe corresponds to a single sample reflector. When plotted with respect to λ (or N_i), the modulation is distorted. Spectral calibration is required to evenly sampled data in σ before applying the Fourier transform.

Figure 3.22 (b) shows a simulation this modulated spectrum acquired with a line camera that has 1024 pixels, each pixel detecting a spectral range of 1.0 nm. The x-axis in this case is pixel index, instead of wavelength. Comparing (a) and (b), we see that the two plots look similar except a change in x-axis. In both cases, the spectral modulation is distorted, indicating that the phase is non-linear.

The Fourier transform of this distorted spectral interferogram gives a broadened axial PSF. Had the spectrum been evenly sampled in σ domain, the single reflector would yield a raw SD-OCT signal having a linear phase. The phase linearization method of spectral calibration involves extraction and linearization of the non-linear phase associated with the distorted spectral modulation. The CCD pixel indices are then interpolated at those new values of the phase, giving new set of pixel indices (that may be non-integer) having non-uniform spacing. Finally the spectrum is interpolated at those new values of pixel indices to have non-distorted spectrum, which is uniformly spaced in σ (see Figure 3.23).
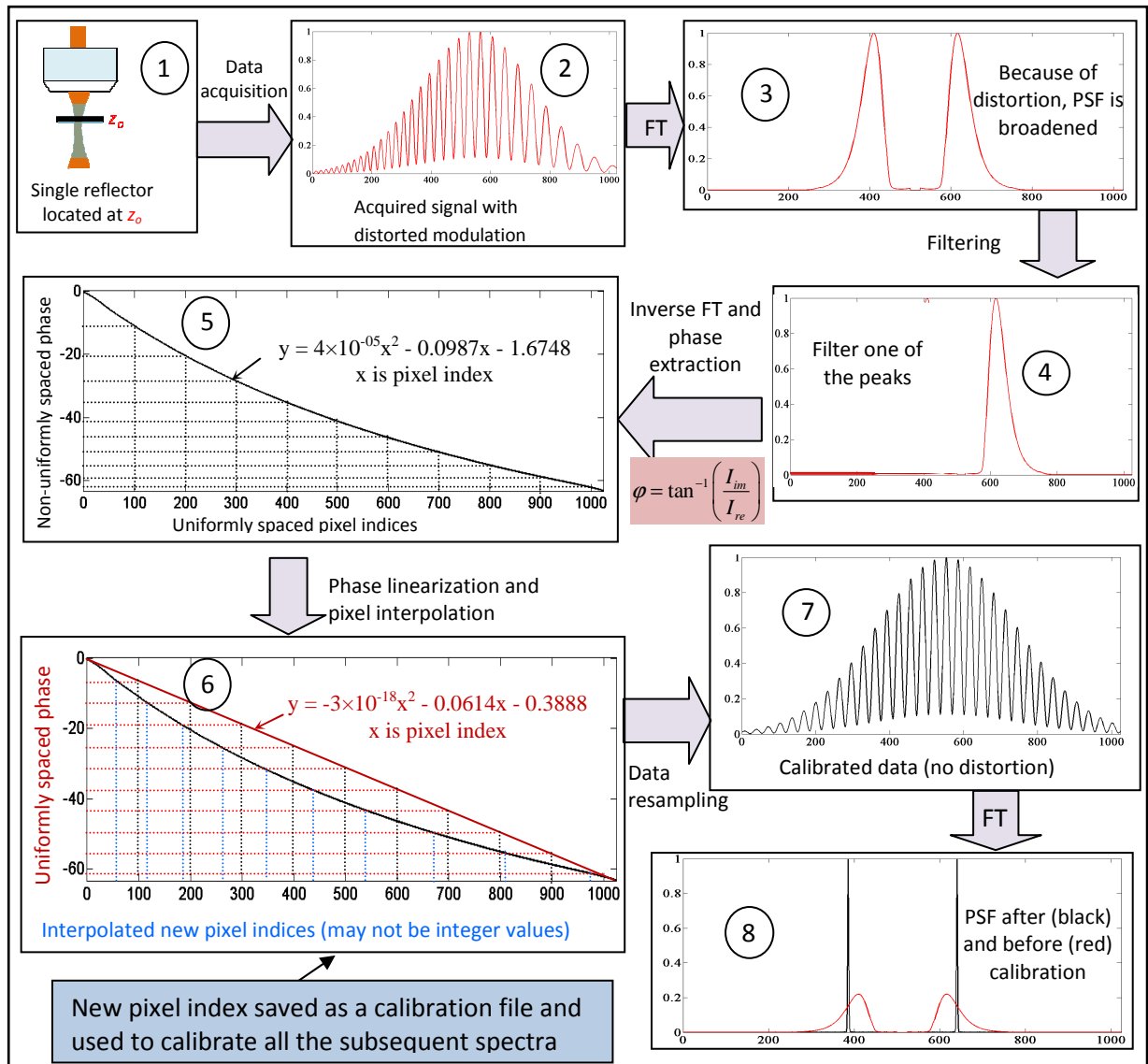

Figure 3.23 Numerical calibration procedure: starting with a distorted signal in panel 2 that is non-uniformly spaced in σ, a signal with uniformly spaced dataset is obtained in panel 7 via a numerical method of spectral calibration by extracting and linearizing the non-linear phase as explained in panel 3 to 6. After applying the Fourier transform, the corrected signal gives a narrow axial PSF (step 8) compared to the one shown in panel 3.

The phase is extracted by computing the inverse tangent of the ratio between the imaginary I_{im} and the real I_{re} part of the complex data that is obtained after applying inverse Fourier transformation on the filtered data (panels 3 and 4) [65]

$$\varphi = \tan^{-1}\left(\frac{I_{im}}{I_{re}}\right).$$

3. 40

When unfolded and plotted, the extracted phase shows a non-linear trend and non-uniform spacing with respect to uniform CCD pixels (step 5). The phase is then uniformly sampled with a constant step size given by

$$Phase_{step} = \frac{Phase_{\max} - Phase_{\min}}{N - 1},$$

3. 41

where N is the number of CCD pixels.

This uniformly spaced (linearized) phase is then used to interpolate the new pixel indices (step 6). Note that these newly generated pixel indices have non-integer values (and do not have physical significance).

Finally, the raw spectral interferogram is interpolated at the new pixel indices, and the plot of the signal (panel 7) does not show distortion in the modulation; and the Fourier transform will yield the proper depth profile, which is approximately a "delta" function located at depth z_o (panel 8). The pixel indices are saved as a calibration file which will be used to interpolate all the subsequently acquired raw SD-OCT data. This way, a spectral calibration is achieved numerically without using calibration lasers, and if some need arises to re-calibrate the system, all we need is a single reflector (mirror) and the procedure is repeated and a new calibration file is saved. Experimental results obtained using this method will be presented in the next chapter.

3.3.6 Image processing steps

Unlike conventional microscopy, SD-OCT requires several data processing steps (see Figure 3.24) before the final image is reconstructed. Image processing is therefore the most time consuming stage of SD-OCT. For real-time image display, image processing can become the bottleneck. Fast image processing requires the use of multiprocessor workstations, or specialized hardware such as digital signal processors. In our SD-OCT system, we have used a personal computer (HP workstation with E8400, 2GH processor and 2GB RAM).

The main SD-OCT image processing steps are summarized in Figure 3.24.

| Data Acquisition | $I(\lambda)$ → | Background subtraction | $I(\lambda)$ → | Spectral calibration | $I(\sigma)$ → | Fourier Transform | $I(z)$ → | Axial profile (A-scan) |

Figure 3.24 Main image processing steps of SD-OCT

At the start of the imaging experiment, the background signal is recorded by blocking both arms of the interferometer independently. The background signal includes the DC terms caused by the reference mirror, sample reflections, back-reflecting interfaces in the system, and ambient irrelevant signals (such as room or computer screen lights). This recorded background signal is automatically subtracted from each subsequent signal as the acquisition progresses. As the system is not perfectly stable, the background signal can be affected by any drift in the system. Practically, a new background image has to be acquired periodically.

The next step is spectral calibration. A numerical calibration method based on phase extraction has been employed to have uniformly spaced data points with respect to σ. The accuracy of interpolation can be improved by using zero padding technique. Zero padding is done after applying the Fourier transform, and then inverse Fourier transform is performed to increase the data points before interpolaton. Usually increasing the number of data points by a factor of two to four times is sufficient for this application. This certainly increases the image processing time. Finally the Fourier transform is performed on the resampled dataset to get the required A-scan with narrow axial PSF. As there is redundant information due to the Fourier transform of real signal, only half of the Fourier transformed data is kept. If the DC term has not been properly removed at the beginning, it will appear around the zero depth in the final image. As its presence prevents proper visualization of features located at deeper locations, it can also be removed at this stage by zeroing the zero depth region of the image.

3.4 Conclusion

In this chapter, we have discussed the principles and technical considerations of designing a high-resolution SD-OCT system for imaging the Schlemm's canal. We have shown that the cross-sectional image of an object can be computationally reconstructed by analyzing the spectrum of the interfering light at the output of the Michelson interferometer using a spectrometer. In the SD-OCT modality, the entire axial profile of the object is acquired in one shot without the need of scanning the reference arm. Both the acquisition speed and sensitivity of SD-OCT have been shown to be better than that of TD-OCT.

Looking at the optical properties (absorption and scattering) of biological tissues, the long wavelength range of the therapeutic window around 1.3 µm is preferred in order to image the Schlemm's canal in highly scattering sclera and edematous cornea. However, because of the $\lambda^2/\Delta\lambda$ dependence of the axial resolution, high-resolution SD-OCT imaging at 1.3 µm center wavelength requires a light source with extremely broad bandwidth. It has been shown that the spectral bandwidth of the light needed for imaging at 1.3 µm center wavelength needs to be 2.6 times larger than the one at 0.8 µm, in order to maintain the axial resolution. Finding such a broadband light source, dealing with the dispersion management and designing a broadband spectrometer are some of the challenges of high-resolution SD-OCT at longer wavelength.

If the spectrometer is not broad enough to collect the source spectrum, the actual axial resolution will eventually be limited by the spectrometer and will be inferior to the theoretically predicted value. On the other hand, if the spectral range of the spectrometer is broader than the spectral range of the light source, the spectral resolution of the spectrometer will be lowered. One of the drawbacks of SD-OCT is its depth dependent sensitivity fall-off. If the resolution of the spectrometer is too low, the sensitivity falls too fast with depth. Given the finite number and size of detector pixels, a low spectral resolution of the spectrometer is translated to a low sampling resolution, i.e., the spectral range that each detector receives gets broader that the spectrometer's resolutions decreases. Due to the Fourier transform operation, such low sampling resolution gives a reduced imaging depth. Hence the performance of SD-OCT system is directly dependent on the design of an optimum spectrometer.

The other important stage of SD-OCT development is spectral calibration. The A-scan reconstruction using Fourier transformation requires the acquired data to be uniformly sampled in spatial frequency σ. However, in a grating based interferometer, the acquired dataset is nearly uniformly sampled in wavelength λ, and as λ and σ are inversely related, the dataset has to be spectrally calibrated in order to uniformly sample it in σ. Otherwise both axial resolution and sensitivity of the system will be much worse than the theoretically predicted values. In this dissertation, a numerical method of spectral calibration based on phase extraction and linearization has been explained. As SD-OCT requires several data processing steps before the final image is reconstructed, image processing is the most time consuming stage of the SD-OCT system. In the next chapter, the characterization of the system performance and its demonstration will be presented.

Chapter 4 - System characterization and demonstration

4.1 Introduction

In the previous chapter, we have discussed the principles and technical considerations of SD-OCT design. We have shown that in SD-OCT, the main imaging parameters such as axial resolution, sensitivity and imaging depth range are directly affected by the design parameters of the spectrometer, and depending on what we want, the spectrometer can be specifically designed to meet our need. In our case, the goal has been the development of a high-resolution SD-OCT system in order to properly view the Schlemm's canal of the human eye that is located inside a highly scattering medium.

In this chapter, the experimental setup of the high-resolution SD-OCT developed for this application will be explained. Characterization of the system's performance will be presented and compared to the theoretically predicted values. The experimental results of depth dependent degradation of axial resolution and sensitivity will also be given. The importance of spectral calibration and zero padding for improving the sensitivity fall-off and axial resolution will be demonstrated. Finally, images of the Schlemm's canal and other samples will be given to demonstrate the performance of the system.

4.2 Experimental setup

The complete design of our high-resolution SD-OCT system, as reported in the journal *Optics Communications* [54], is shown in Figure 4.1. It mainly consists of a broadband superluminescent (SLD) light source, a Michelson interferometer with a transversal scanning system in the sample arm, a spectrometer and a personal computer (PC).

4.2.1 Materials

The illuminating light source, as presented in chapter 3, is composed of a combination of two spectrally shifted broadband SLDs. The combination of the two SLDs gives an extended broadband light source that provides shorter coherence length and better axial resolution than we could get with one SLD alone. The output power, spectral bandwidth and shape of the combined SLD light source can be controlled to a certain extent by independently changing the current drive and the temperature control of each SLD. The typical spectrum of the output

light we got has a bandwidth of 200 nm centered at 1.3 µm wavelength. The current I and temperature T of SLD A and SLD B have been set to $I_A = 398$ mA, $I_B = 469$ mA, $T_A = 14$ °C, $T_A = 28$ °C respectively.
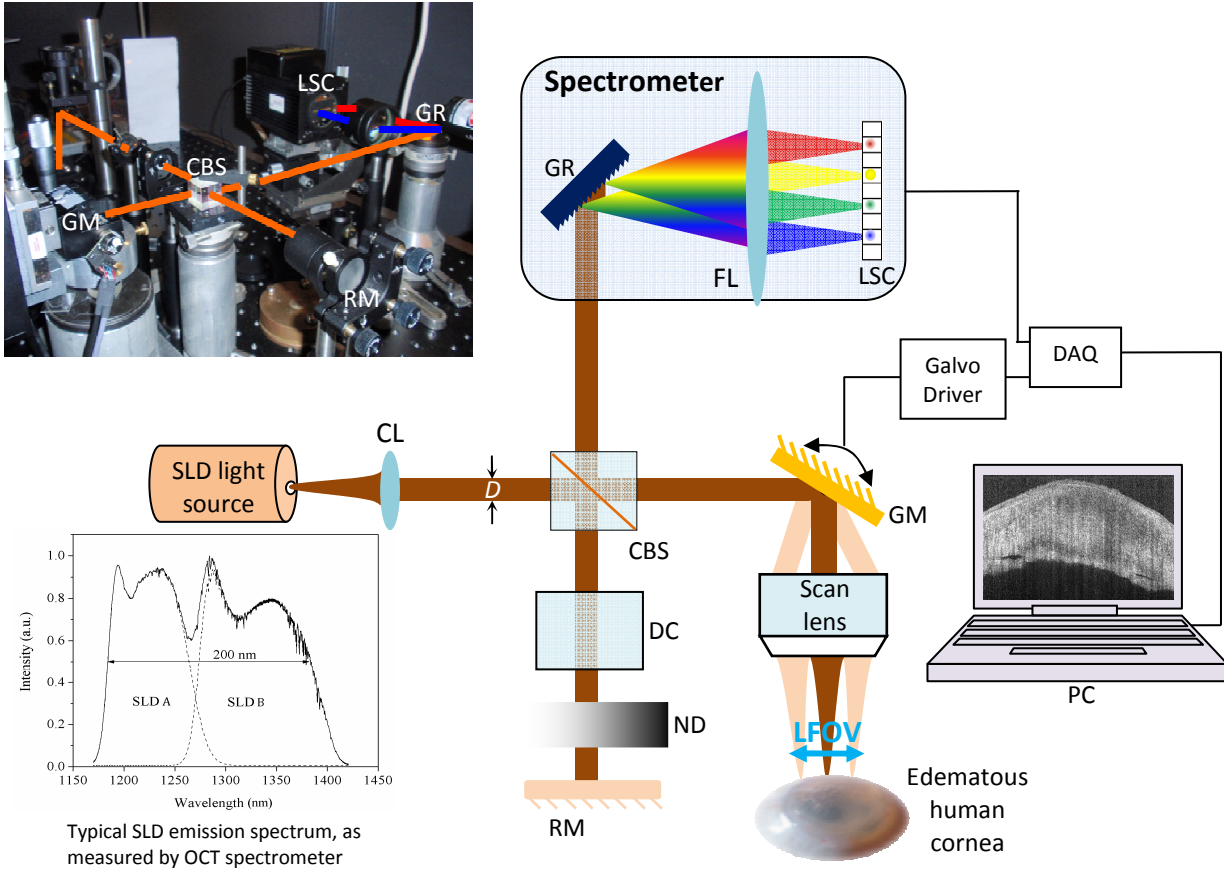

Figure 4.1 Experimental setup of high-resolution SD-OCT. CL: collimating lens, D: beam diameter, CBS: Cube beamsplitter, DC: dispersion compensator, ND: neutral density filter, RM: reference mirror, GM: galvanometric-mounted mirror, LFOV: lateral field of view, GR: grating, FL: focusing lens, LSC: line-scan camera, DAQ: data acquisition board, PC: personal computer.

Light from the SLD source is delivered by a single mode fiber (*P1-SMF28E-FC-1, Thorlabs*) and is collimated using a collimating optics (*F280APC-C, Thorlabs*). The measured diameter D of the collimated beam at the input of the interferometer is $D = 4.6$ mm. The light is then split between the sample arm and the reference arm by a balanced cube beamsplitter (*BS015, Thorlabs*). A continuously varying neutral density filter (*NDL-25C-2, Thorlabs*) with optical density between 0.04 and 2.0 is placed in front of a reference mirror (silver) in order to control the effective reference mirror reflectivity and optimize the sensitivity and autocorrelation terms of the system [66]. A galvanometer-mounted mirror in the sample arm (*6210H, Cambridge Technology*) enables transverse beam scanning on the sample. The voltage that derives the galvo-mirror is generated by a function generator (*33220A, Agilent*).

The function generator is connected to a computer via GPIB card. This allows us to control the shape, magnitude and frequency of the galvo drive voltage directly from the computer. For imaging non-moving samples with large transverse field of view, a motorized translation stage can also be used. A telecentric scan lens (*LSM02, Thorlabs*) focuses light onto the sample and collects the backscattered light. A dispersion compensator (*LSM02DC, Thorlabs*) in the reference arm is used to balance a dispersion mismatch in the interferometer introduced by the scan lens. A spectrometer, located at the output of the interferometer, consists of a diffraction grating (*GR25-0613, 600 lines/mm, Thorlabs*), an achromatic doublet (120 mm focal length) and an InGaAs linear array detector (*SU-LDH Digital Line Scan Camera, Goodrich*). The linear array camera acquires the spectral interferogram and transfers the 14-bit digital data to a personal computer (*HP workstation with E8400, 2GH processor, 2GB RAM*) equipped with an image acquisition card (*NI PCIe-1427, National Instruments*). The maximum line rate of the camera is 46 kHz.

4.2.2 Methods

An automated graphical user-friendly interface (GUI) for image processing and synchronization of the different hardware components (camera, galvo-driver, function generator, etc) has been developed using Labview. Matlab has also been used for doing the numerical spectral calibration. A screen shot of this interface is shown in Figure 4.2. In the GUI, the panels marked 1, 2 and 3 represent the different steps of image processing discussed at the end of chapter 4.

In panel 1, the program performs two processes and displays the result. The two processes are:

- ❖ Removing the DC background
- ❖ Performing spectral calibration

4.2.2.1 Removing the DC background

At the beginning of each experiment, it is important to save the strong background signal, mainly coming from the reference mirror. This is done by blocking the sample arm and clicking "Remove RL" button on the GUI. This saved value is then subtracted from the subsequent spectral interferograms that correspond to different transverse locations on the sample. This process also removes any other reflections from the optical setup, room light and/or computer screen light.

As we can see from the plot in panel 1, after removing this strong background signal, the interferometric signal is still riding over another relatively small DC term (~ 1% of the value at saturation) coming from the sample. Sample DC term can be removed either by:

➢ Saving the sample DC signal at the beginning of the experiment by blocking the reference arm and subtracting it from the subsequent raw SD-OCT signals like what we did for reference arm light or

➢ Zeroing the signal around the zero depth in the z-domain later after the Fourier transform (i.e., in panel 2) because DC terms generally appear around $z = 0$ in reconstructed A-scans.

Usually, the second method is preferred for our case because when we subtract the reference light, we also remove the inherent reflections and doing the same procedure for sample light may affect the effectiveness of background light removal.
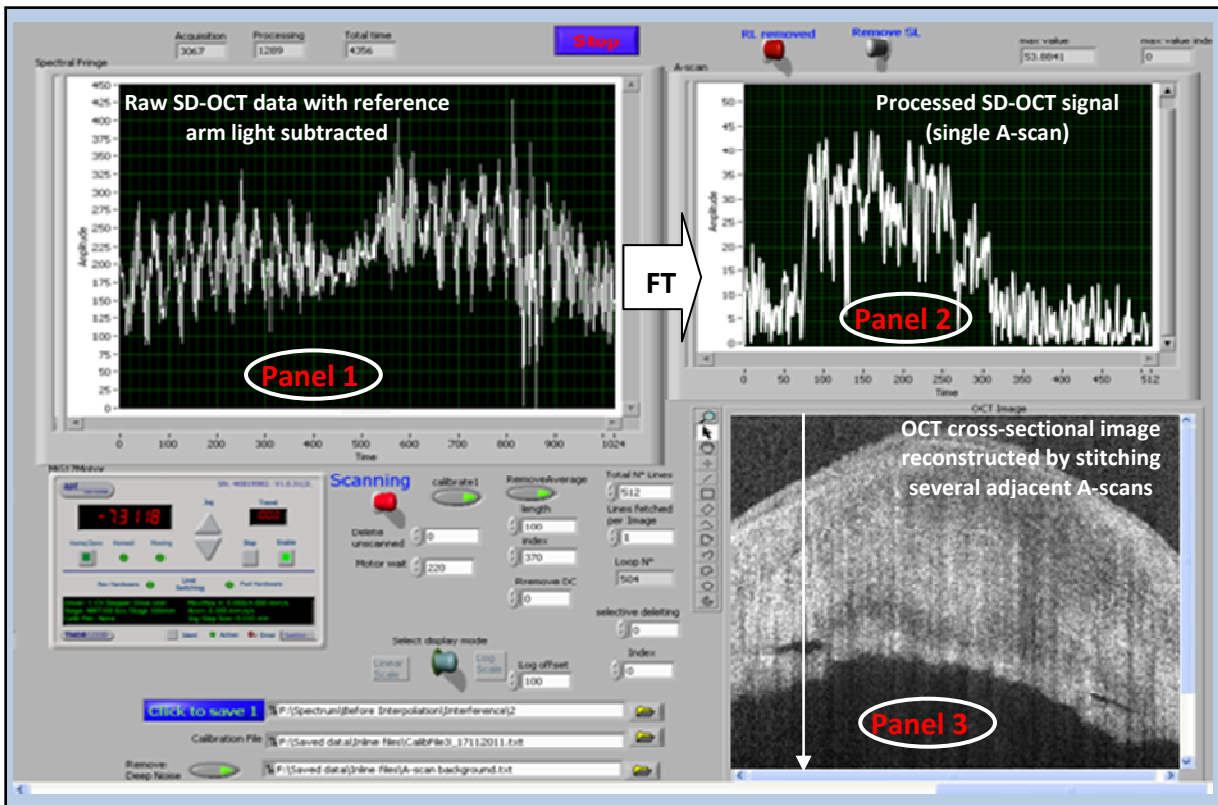

Figure 4.2 Screen shot of our home-made graphical user-friendly interface (GUI) for SD-OCT image processing and for synchronization of the different system hardwares (camera, transverse scanner, etc).

4.2.2.2 Spectral calibration

The other important process done in panel 1 of the above GUI is spectral calibration and data resampling. The ultimate goal need of spectral calibration, as discussed in chapter 3, is to

have a uniformly sampled data in σ because the data acquired by the spectrometer is non-uniformly sampled σ. If one omits spectral calibration step and directly applies the Fourier transform on the acquired spectral spectrogram to reconstruct A-scan, both axial resolution and sensitivity will be severely degraded. Figure 4.3 shows the axial PSF plot (without any calibration) of an attenuated mirror placed at nine different axial positions. The distance between each axial position of the mirror was ~ 200 µm.
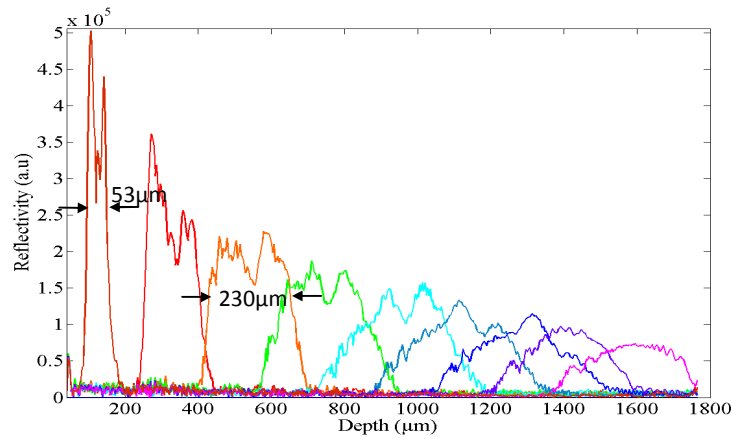
Figure 4.3 Uncalibrated experimental axial PSF corresponding to a single mirror at different axial positions. The mirror has been axially translated with a step of ~ 200 µm. Note that as the imaging depth increases, both the width and magnitude of the axial PSF significantly decreases, leading to depth dependent degradation of axial resolution and sensitivity fall-off.

From Figure 4.3, we note that as the imaging depth increases, both the FWHM and magnitude of the measured signal decrease significantly. This leads to a depth dependent degradation of axial resolution and sensitivity fall-off of the SD-OCT system. For example, when the mirror is placed at 120 µm from the zero path length difference ($z = 0$), the FWHM of the axial PSF, which defines the axial resolution, is $\Delta z = 53$ µm. And for $z = 520$ µm, $\Delta z = 230$ µm. As we keep on going away from $z = 0$, neighboring axial PSFs start to overlap. The theoretical axial resolution for $\Delta\lambda = 200$ nm and $\lambda_o = 1.3$ µm is $\Delta z = 3.7$ µm, assuming a light source with a Gaussian-shaped power spectrum. Such large difference between the theoretical and experimental values of axial resolution comes from the fact that the acquired spectral interferogram has been non-uniformly sampled in σ. The width of the axial PSF is further broadened by the effect of non-uniform sampling. To improve such a severe degradation, each acquired spectral interferogram has to be resampled by an appropriate calibration file before applying the Fourier transform.

A calibration file for our SD-OCT is generated by placing a single reflector (silver mirror) in the sample at an arbitrary depth ($z = 310$ µm in our case but not necessarily known). The acquired raw spectral interferogram is shown in Figure 4.4 (a) (left axis, in blue). The

horizontal axis, running from 0 to 1023 with uniform interval, corresponds to the pixel index. As wavelength is directly proportional to the pixel index, the wavelength also increases linearly with the pixel index.
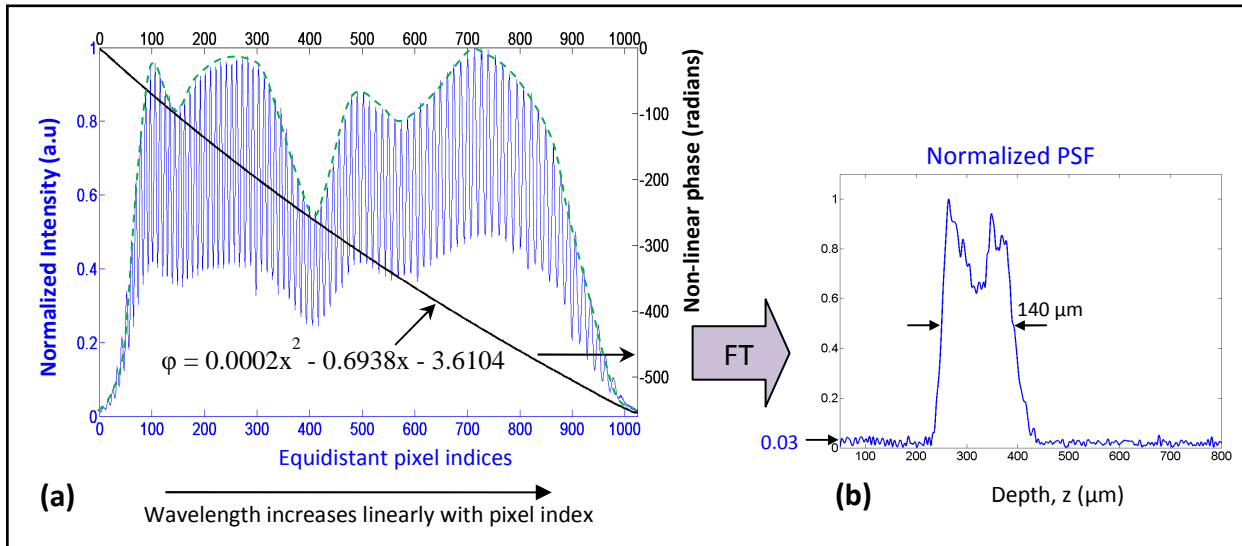

Figure 4.4 Acquired spectral interferogram ((a), left axis) and the non-linear phase (right axis). The period of modulation in the short wavelength region is narrower than the long wavelength region, giving rise to distorted modulation. Fourier transforming the distorted interferogram gives an axial PSF that is much wider compared to the theoretical value (3.7 µm).

The envelope of the modulated spectrum (represented by the dotted green curve) corresponds to the spectrum of the light source ($\Delta\lambda = 200$ nm, $\lambda_o = 1.3$ µm). The spectrometer is designed to achieve source-limited axial resolution, i.e, the whole spectral width of the light source is collected to maximize the axial resolution. This corresponds to a theoretical axial resolution of $\Delta z = 3.7$ µm.

Looking closely at the left and right side of the modulated spectrum, we observe that the modulation is a distorted one (fringe spacing narrower on the left than on the right). If the modulation frequency is too high, the left tail of the spectrum becomes under sampled and irretrievably lost while the right tail of the spectrum is within the Nyquist limit. This phenomenon is called partial aliasing [67] and contributes to the depth dependent signal fall-off.

Figure 4.4 (b) shows the plot of axial PSF when Fourier transform is directly applied to such distorted modulation without any calibration. Its FWHM is about 140 µm, which is very far from the theoretical value of axial resolution that is 3.7 µm. The non-linear phase associated with the distorted modulation is extracted and plotted in Figure 4.4 (a) (right axis). The second order non-linear coefficient is 0.0002.

The nonlinear phase is linearized and plotted Figure 4.5 (a), right axis. We see that the second order term of the linearized phase is very small (10^{-17}) compared to its value before linearization (0.002). When the pixel indices are interpolated at the new linear values of the phase, we get a new set of non-linear pixel indices (non-integer at this time). This new set of pixels is saved as a *calibration file* in the computer. The spectral interferogram is then interpolated at the new non-integer pixel indices. The resampled interferogram is shown in Figure 4.5 left axis, and is no more distorted.
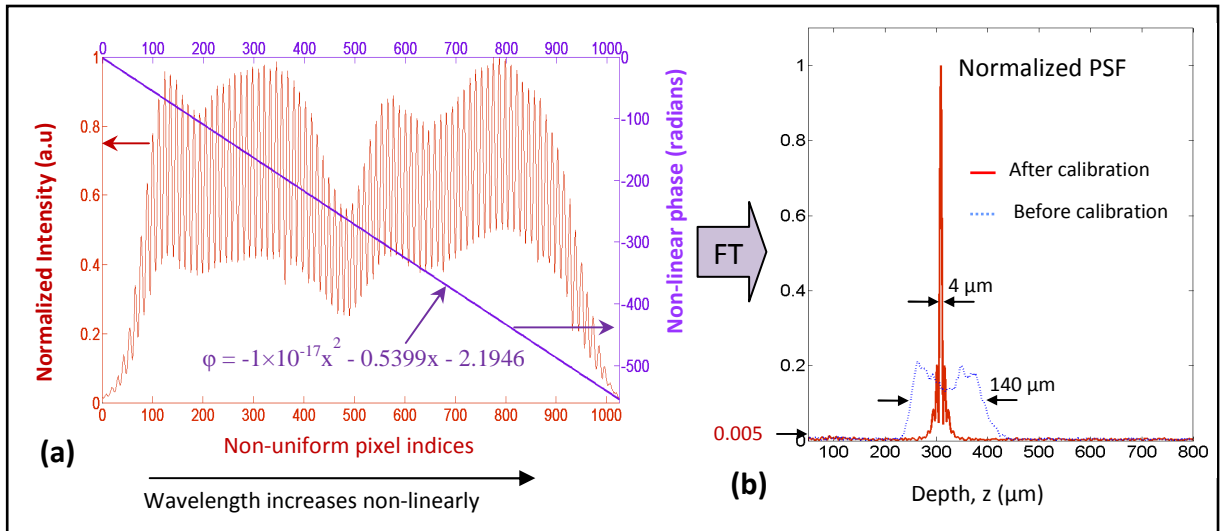

Figure 4.5 Linearized phase ((a), right axis) and uniformly sampled spectral interferogram ((a), left axis)). (b) in red shows the corresponding axial PSF after calibration and the axial PSF in blue before calibration. Calibration improves both axial resolution and SNR.

The Fourier transform of the resampled data, shown in Figure 4.5 (b) in red color gives an axial PSF that has ~ 4 µm width (FWHM), which is close to the theoretically predicted axial resolution (3.7 µm). The blue curve shows the axial PSF before calibration. Comparing the two axial PSFs, it is obvious that performing spectral calibration improves not only the axial resolution but also the SNR. In this specific example, the SNR has been improved more than 15 dB at this specific depth ($z = 310$ µm). Hence performing spectral calibration enables to significantly improve the accuracy and quality of the image.

Unless one translates the camera or some optics of the spectrometer, no further calibration is needed. The calibration file that is generated for one arbitrary depth is saved in the computer and used to interpolate all the subsequent spectrograms. Figure 4.6 shows the comparison of experimental axial PSF obtained before calibration (dotted curve) and after resampling (solid) of each spectrogram with the calibration file that is generated for a given spectrogram. From Figure 4.6, we see that spectral calibration significantly improves axial resolution and

sensitivity fall-off. However the sensitivity fall-off that is inherent to SD-OCT is still observed. This effect will be characterized in section 4.3.3.2
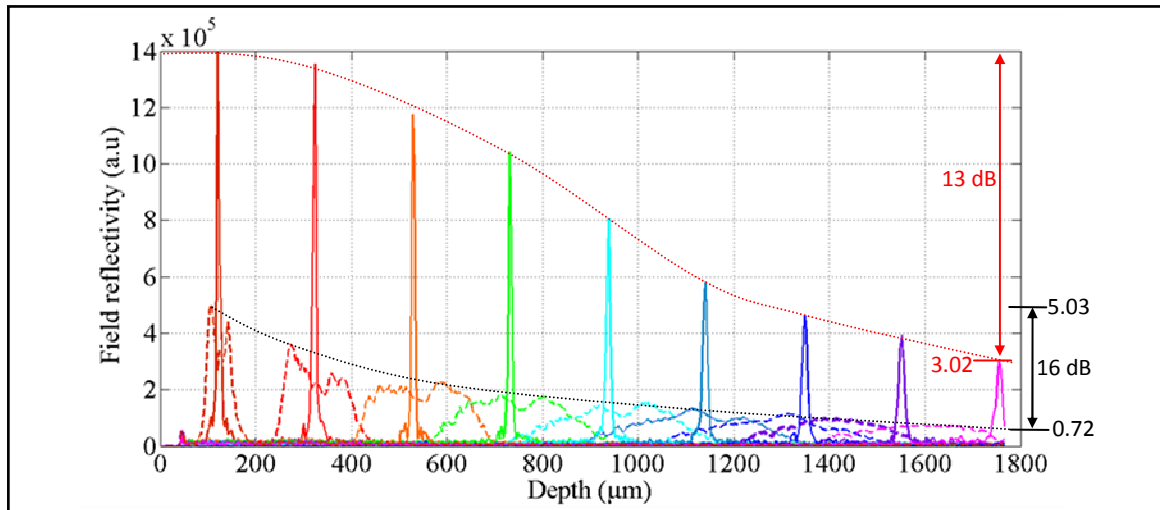

Figure 4.6 Axial PSF before calibration (doted curve) and after calibration (solid curve). We see that spectral calibration significantly improves axial resolution and sensitivity fall-off.

4.2.2.3   *Removing the complex conjugate and autocorrelation artifacts*

The complex artifact, autocorrelation and some remaining DC terms are removed in panel 2 of Figure 4.2. In chapter 3, section 3.2.2, we have shown that Fourier transformed signal gives identical images (complex conjugate artifact) on both sides of $z = 0$, leading to confusion in image interpretation. The complex conjugate artifact is removed by keeping the sample on one side of the zero path length and displaying only the positive or negative distances. Hence out of 1024 Fourier bins, only 512 of them have useful and distinct information, the other 512 bins contain copy of the same information. The other artifact that is removed in this panel is the autocorrelation term that results from the mutual interference between reflections within the sample. Usually this term appears at a shallow depth around $z = 0$. It is customary to displace the reference mirror by 150 µm to 200 µm from $z = 0$ position so that the surface of the sample shows at a location beyond the autocorrelation structures, and then the shallow depth range is numerically zeroed in the image. This procedure also gets rid of any DC term that was not properly removed in panel 1.

Finally, in panel 3, adjacent A-scans that correspond to adjacent transverse sample positions are stitched together numerically to give cross-sectional OCT image. From the GUI, the user can choose the number of A-scans (or lateral pixels) and the image processing system will automatically translate them into the corresponding size of lateral field of view (LFOV) that needs to be acquired and displayed. The relation between the LFOV and the drive voltage to

the galvanometric-mounted mirror that scans the beam on the sample has been calibrated and incorporated into the program.

4.3 System characterization

4.3.1 Spatial resolutions

4.3.1.1 Transverse resolution

The transverse resolution of images obtained from our SD-OCT systems, like other scanning imaging systems, is determined by the size of the focused beam spot on the sample (see Figure 4.7).
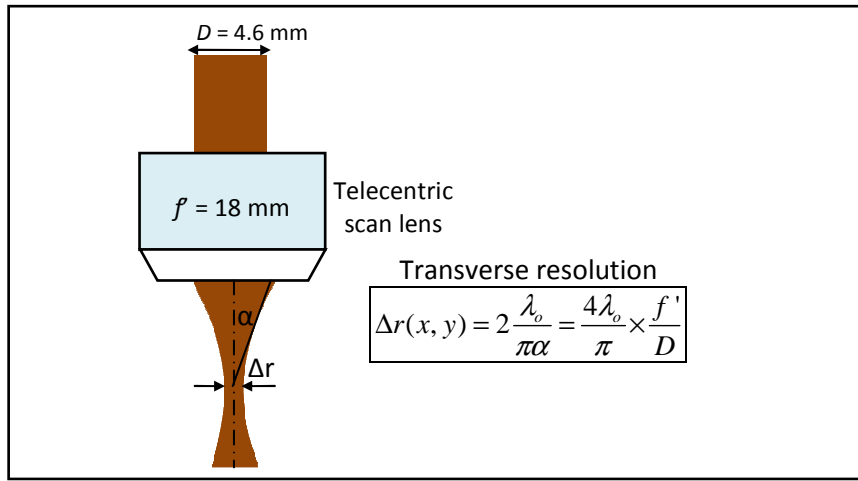

$D = 4.6$ mm

$f = 18$ mm

Telecentric scan lens

α

Δr

Transverse resolution

$$\Delta r(x, y) = 2\frac{\lambda_o}{\pi\alpha} = \frac{4\lambda_o}{\pi} \times \frac{f'}{D}$$

Figure 4.7 Schematic diagram of sample arm optics of SD-OCT.

The beam focus size depends on the focusing optics and the wavelength of the illuminating light. With a collimated Gaussian beam profile having a measured beam diameter of $D = 4.6$ mm and a telecentric scan lens with an effective focal length of 18 mm, the transverse resolution Δr of our SD-OCT is $\Delta r = 6.5$ µm. This is almost 4 times better than the transverse resolution of the commercially available FD-OCT (OCS1300SS, Thorlabs).

4.3.1.2 Axial resolution

The axial resolution of our SD-OCT, as explained before, is determined by the spectral shape, bandwidth $\Delta\lambda$ and center wavelength λ_o of the light source that is used for illumination. The spectrum of the light source, as measured by the OCT spectrometer, is given in Figure 4.8 (a) (solid curve). By comparing with a commercial spectrometer, we found that the typical emission spectrum collected by the spectrometer had a bandwidth of $\Delta\lambda = 200$ nm (FWHM) centered at $\lambda_o = 1.3$ µm. The current drive and temperature settings of SLD A and SLD B were $I_A = 390$ mA, $T_A = 14\,°C$, $I_B = 469$ mA and $T_B = 28\,°C$, respectively. Changing the

current and temperature settings changes the output power, bandwidth and center wavelength of the emitted light.
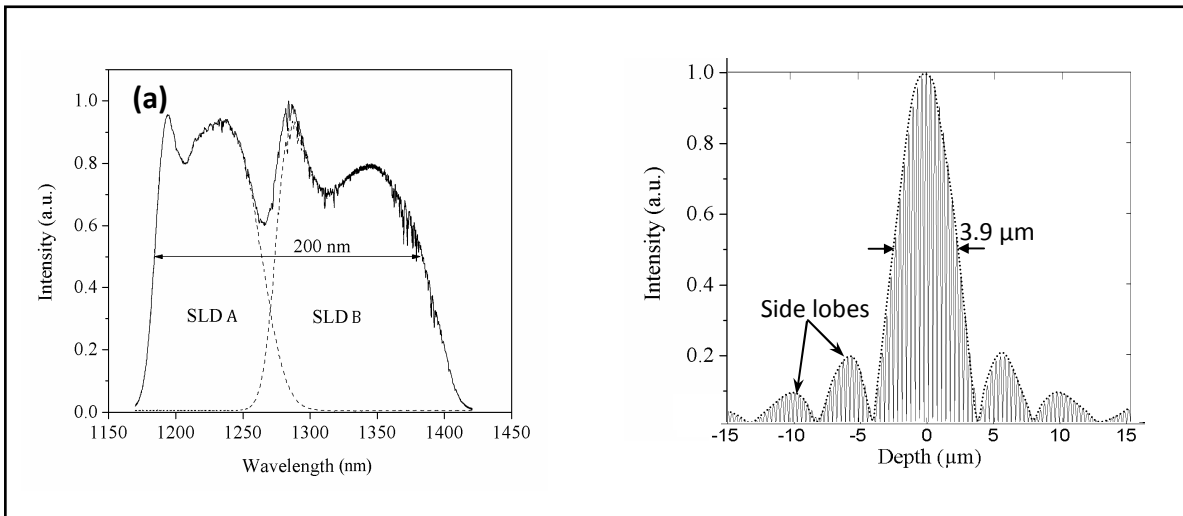

Figure 4.8 (a) Emission power spectrum of the light source (solid curve) that is collected by the spectrometer. SLD A and SLD B (dotted curves representing the emission spectra of each diode) are combined to increase the spectral bandwidth of the illumination light source. The effective spectral bandwidth after combination is 200 nm at FWHM centered at 1.3 µm. **(b)** The corresponding axial PSF obtained with simulation by considering the actual detected spectral shape and spectral range.

If the spectral shape of the light source is assumed to have a Gaussian shape, the theoretical axial resolution Δz in air will be

$$\Delta z = \frac{2\ln 2}{\pi} \times \frac{\lambda_o{}^2}{\Delta\lambda} = 3.7\,\mu m$$

However, the actual spectral shape is not Gaussian. The plot of the axial PSF obtained with simulation by taking the actual non-Gaussian shape of the spectrum into consideration is given in Figure 4.8 (b). As we can see, the FWHM of the axial PSF, which is 3.9 µm, is a little bit broader than 3.7 µm which is obtained by assuming Gaussian spectrum. However, the main difference between the simulated and theoretical axial PSF is rather the shape of the axial PSF. Gaussian-shaped axial PSF does not have side lobes, whereas the simulated axial PSF shown above does have side lobes. Side lobes have undesirable effects because side lobes from a strongly reflecting layer in a sample can mask the central PSF signal of low light reflecting layers that may be located immediately above or below it. In SD-OCT, as we have access to the spectral property of the light source, additional imaging processing algorithm can be employed to reduce the undesired effect of the side lobes.

The experimental axial resolution is determined by measuring the FWHM of the PSF that is obtained in panel 2 of Figure 4.5. Fourier transform of the acquired spectrum, after resampling, gives the PSF as a function of Fourier bins (pixel indices after the Fourier

transform become Fourier bins in z-domain). To convert bins into actual depths, depth calibration is required. This is achieved by translating the single reflector by a known step and noting the number of bins the PSF peak has shifted from its original location. The experimental axial PSF determined this way is plotted in Figure 4.9, and its FWHM is 4 µm, which is close to the theoretical value.
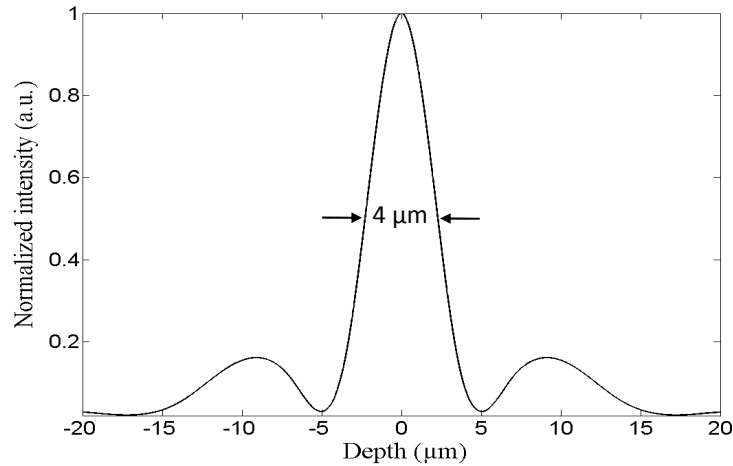

Figure 4.9 Experimental axial PSF measured as FWHM.

4.3.1.3 Degradation of axial resolution with depth

The experimental axial PSF given in Figure 4.9 corresponds to a sample depth $z = 0$. In free space, the same axial resolution is expected within the depth range of SD-OCT. However, experimental results indicated that the axial resolution is degraded with an increase in imaging depth. Using a single reflector as a sample, we determined the FWHM axial PSF (i.e., axial resolution) for various axial locations. The result is plotted Figure 4.10.
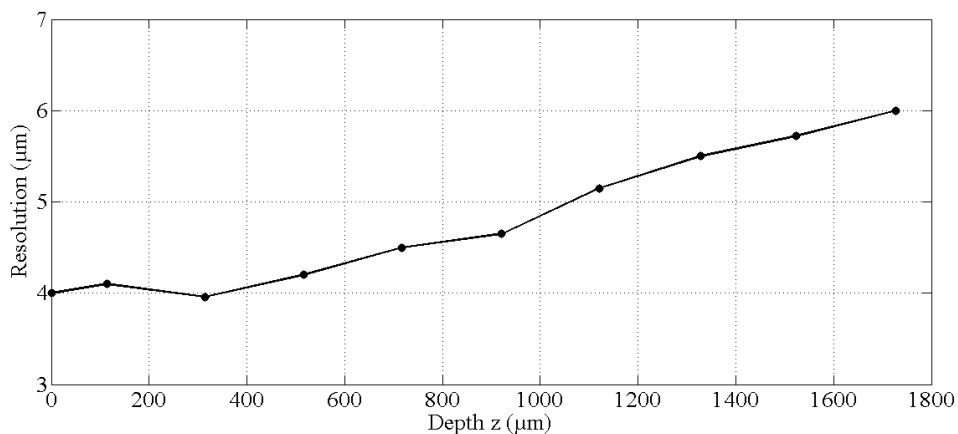

Figure 4.10 Evolution of axial resolution (measured at FWHM) with imaging depth. The FWHM of the axial PSF of a single reflector is measured at 10 different axial positions.

At depths smaller than 600 µm, the free space axial resolution was measured to be

approximately 4.0 µm, which is close to the theoretical value calculated from the source bandwidth. At the end of the depth range, the axial resolution is around 6 µm.

This degradation is due to the interpolation error of high frequency fringes. The interpolation accuracy of high frequency fringes that correspond to larger depths can be improved by zero padding technique, i.e., the number of data points is first increased before interpolation. This is achieved by performing the Fourier transform, zero padding, performing the inverse Fourier transform and then finally interpolation (see Figure 4.11).
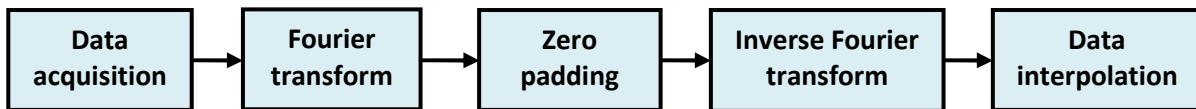
| Data acquisition | → | Fourier transform | → | Zero padding | → | Inverse Fourier transform | → | Data interpolation |

Figure 4.11 Steps of improving the accuracy of data interpolation using zero padding.

Increasing the numbers of padded zeros improves the accuracy of interpolation at the cost of increasing the data processing time. When we increase the data points of the acquired data by 4 times (i.e., 3072 zeros are padded), the degradation of axial resolution at the end of the depth range has been improved by 1 µm. (see Figure 4.12.)
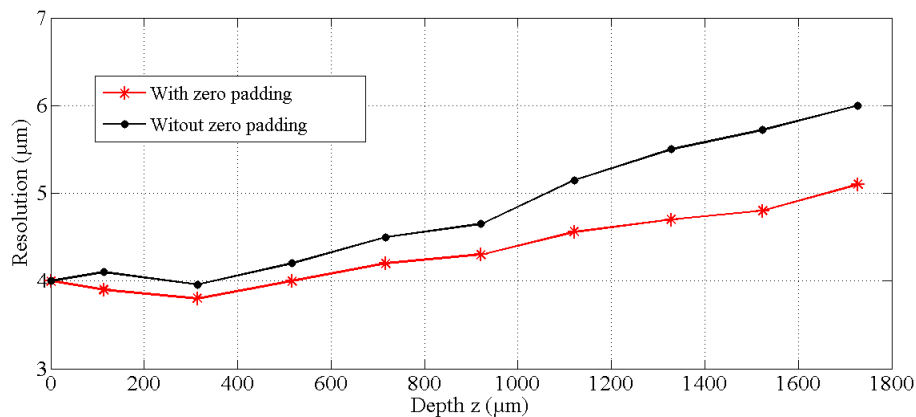

Figure 4.12 Evolution of axial resolution with imaging depth without (black color) and with (red color) zero padding. Zero padding minimizes the degradation of axial resolution but it also increases the computation time. In this specific case, the number of data points has been increased by a factor of 4. The purpose of increasing the data points is to reduce the interpolation error during re-sampling of the spectrum to have equally spaced dataset with respect to spatial frequency σ.

4.3.2 Sensitivity and dynamic range

Sensitivity and dynamic range are sometimes used interchangeably in the OCT literature [68]. However in this dissertation, sensitivity refers to the measure of the lowest sample reflectivity $R_{S,min}$ that can be measured [45], whereas dynamic range is the ratio between the highest and the lowest measurable signals that the OCT system can measure in a particular scene or image

without saturating the detector [69]. In practice, no TD-OCT or SD-OCT system realizes a dynamic that is equal to the sensitivity, which can be well above 100 dB.

4.3.2.1 Sensitivity

In chapter 3, we have given the definition of OCT sensitivity as a measure of the smallest sample reflectivity $R_{S,min}$ at which the signal-to-noise ratio (SNR) equals one. Sensitivity is given by the ratio of the signal power generated by a perfectly reflecting mirror ($R = 1$) and that generated by $R_{S,min}$. Since these signal powers are proportional to the corresponding reflectivities, sensitivity S in decibels is given by [44, 45]

$$S[dB] = 10 \times \log\left(\frac{1}{R_{s,min}}\right).$$
4. 1

We have experimentally characterized the sensitivity of our SD-OCT system by using a silver mirror as a sample and by placing a neutral density (ND) filter with a density value $ND = 2$ in front of the mirror. Considering a double pass through the ND filter, the combination of the mirror and the ND filter corresponds to an equivalent sample reflectivity of 10^{-4}. A typical axial PSF obtained in this configuration at a depth of 150 µm, after performing the required spectral re-sampling (see section 4.2.2.2) and the Fourier transform, is shown in Figure 4.13.

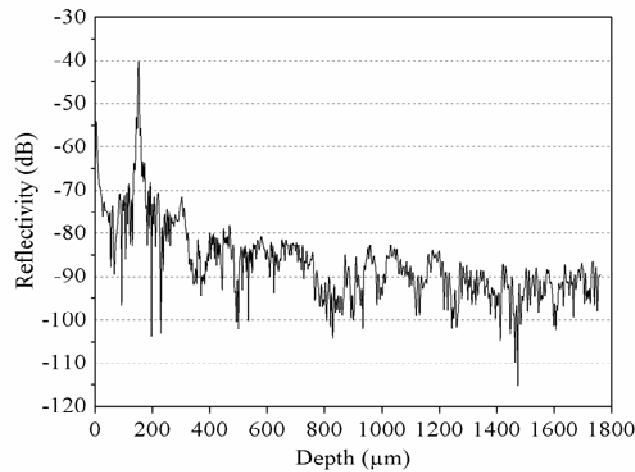**Figure 4.13** Sensitivity measurement of SD-OCT.A single A-scan corresponding to a mirror with neutral density filter of ND = 2 placed in the sample arm. The mirror is 150 µm away from the optical path match condition which is $z = 0$.

The vertical axis in Figure 4.13 gives the reflectivity expressed in decibels (- 40 dB corresponds to a reflectivity of 10^{-4}). For SNR = 1, $R_{S,min}$ ~ - 95 dB = 3.16×10^{-10}. This gives a sensitivity of S = 95 dB. A variable attenuator in the reference arm helps to optimize the

sensitivity and to match the experimental conditions during system characterization and imaging of actual samples.

4.3.2.2 Dynamic range

For shot-noise limited detection, the dynamic range (DR) is proportional to the full-well capacity of the camera [69]. A DR of 70 dB can be reached with our InGaAs line camera, depending on the gain capacitor setting. The 14-bit digitization of the camera guarantees that the analog-to-digital convertor (ADC) faithfully renders all the levels of the captured analog signal into a useable digital output for further digital processing. A higher gain capacitor improves the dynamic range at the cost of increasing the readout noise. However, a DR that is as high as sensitivity is not necessary, because tissue reflectivity is at least 4 orders of magnitude smaller than a perfect reflector. In that case, a system with DR of 40 – 60 dB suffices in most cases [26].

In TD-OCT, a 60 dB DR would require at least a 10 bit (6 dB per bit) ADC. An advantage of TD-OCT systems is that the low frequency strong DC background can be filtered out and only the interference signal can be sent to the ADC. In SD-OCT, the CCD detectors do not easily permit removal of a DC component, and considerations similar to that for TD-OCT system suggest that for an SD-OCT system, the ADC bit depth needed to capture the interference modulation that is riding on top of the strong DC component, with sufficient bit resolution to provide 40 – 60 dB DR, would require an ADC resolution significantly exceeding that of TD-OCT system. Fortunately, the required bit resolution capturing the interference modulation to achieve 40 – 60 dB DR turns out to be much smaller. This is because, in SD-OCT, the reflectivity (in z-domain) is proportional to the product of the magnitude of the modulation depth of the spectrum and the number of illuminated pixels N of the camera (which is on the order of ~ 1000). Thus a relatively small magnitude of modulation depth of the spectrum (on the order of few bits) gets amplified by N, easily providing a DR in z-domain exceeding 40 – 60 dB.

4.3.3 Depth range and sensitivity fall-off

Depth range and sensitivity fall-off are the two SD-OCT parameters that entirely depend on the quality of the spectrometer. A spectrometer that has high spectral resolution and high sampling resolution provides larger imaging depth and slower sensitivity fall-off than a low resolution spectrometer.

4.3.3.1 Depth range

In our SD-OCT system, a total spectral width of $\Delta\Lambda = 245$ nm centered at $\lambda_o = 1.3$ µm wavelength is collected by the spectrometer equipped with a linear detector having $N = 1024$ pixels, resulting in a spectral sampling resolution of $\delta\lambda = \Delta\Lambda/N = 0.24$ nm. The theoretical depth range (or maximum imaging depth) $z_{\max}$ was calculated to be $z_{\max} = \dfrac{1}{4n} \times \dfrac{\lambda_o^{2}}{\delta\lambda} = 1.8\, mm$ in air (~ 1.3 mm in tissue), and is in agreement with the imaging depth observed experimentally.

Experimentally, the depth range has been determined by axially translating a single reflector in the sample arm with a known distance. The depth at which the axial PSF peak rolls back gives the maximum imaging depth of the SD-OCT system. As explained in chapter 3, section 3.2.3, when the maximum imaging depth is reached, the axial PSF peak starts to fold back into an incorrect position. This value is experimentally observed to be 1.76 mm. Hence excluding signal attenuation by the sample (due to absorption and scattering), the experimental depth range z_{max} of our SD-OCT, as determined by the spectral sampling resolution $\delta\lambda$ of the spectrometer, is $z_{max} = 1.76$ mm. This useful imaging depth of SD-OCT is also limited by the depth dependent sensitivity fall-off effect given below.

4.3.3.2 Sensitivity fall-off

SD-OCT suffers from a depth dependent sensitivity fall-off, even in the absence of absorption or scattering from the sample. This is mainly due to the washout of spectral fringe visibility of high frequency spectral fringes that correspond to large depths primarily caused by the limited spectral resolution and finite spectral sampling resolution of the spectrometer [68, 70]. Another factor that contributes to the depth dependent signal fall-off, which becomes even worse for high-resolution SD-OCT, is partial aliasing [67]. Due to the non-uniform sampling of the spectrum in spatial frequency σ, high frequencies of the spectral fringes are aliased and irretrievably lost in the part of the spectrum while the rest of the signal can remain within the Nyquist limit.

To characterize the depth dependent sensitivity fall-off of our SD-OCT system, we repeated the sensitivity characterization experiment (see section 4.3.2.1) for different axial positions of the same reflector that is used as a sample. The plot of depth dependent experimental sensitivity fall-off is given in Figure 4.14.
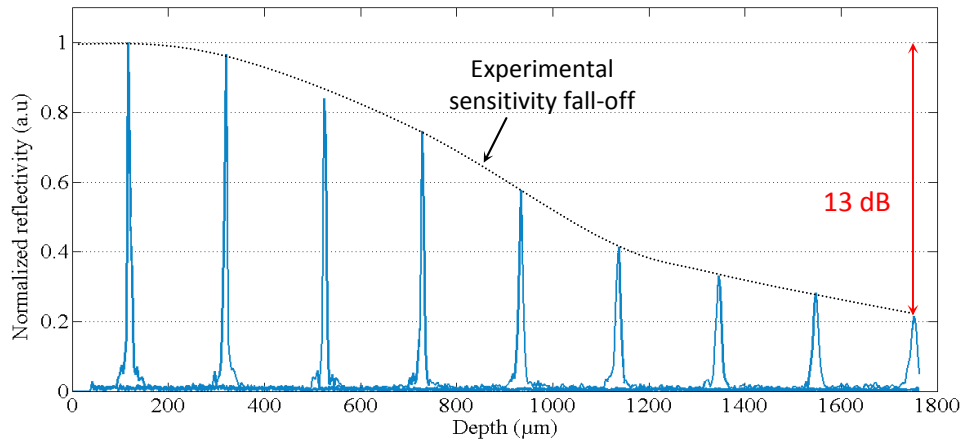
Figure 4.14 Reflectivity of an attenuated silver mirror plotted for various depth locations. For the same amount of reflected power, the magnitude of the reflectivity decreases as the imaging depth increases due to wash out high frequency interference fringes. Once characterized, sensitivity fall-off effect can be numerically compensated.

From the plot given in Figure 4.14, we can see that for the same amount of reflected signal power, the magnitude of the reflectivity decreases as the imaging depth increases. The actual sensitivity fall-off depends on the accuracy of interpolation. Accurate interpolation gives a relatively improved signal fall. With zero padding technique that increases the data points by 4 times, we have obtained a sensitivity fall-off 13 dB at the end of the depth range compared to the 18 dB fall measured without zero padding. The theoretical drop in sensitivity is around 12 dB (see chapter 3, section 3.3.4.2.2).

The comparison between the experimental and theoretical sensitivity fall-off is given in Figure 4.15. It shows that though zero padding increases data processing time, it helps improve the signal fall-off. Compared to the signal peak value in the proximity of zero path length difference, the sensitivity falls by less than 6 dB at a depth of 1 mm.
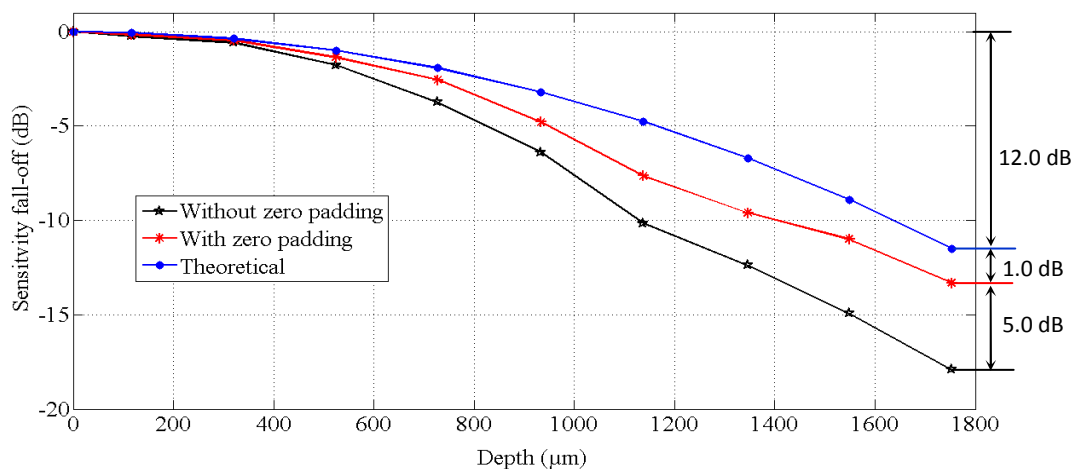

Figure 4.15 SD-OCT sensitivity fall-off. Without zero padding, the experimental sensitivity falls by 18 dB (6.5 dB below the theoretical value) at the end of the depth range. When the dataset is 4 times increased by zero padding before interpolation, the sensitivity fall-off is improved by nearly 5 dB. Hence zero padding improves both axial resolution and sensitivity fall-off.

Various hardware modifications [67, 71, 72] and advanced image reconstruction methods [70] have been reported to achieve a sensitivity fall-off that is close to the theoretical limit but at the cost of more hardware complexity and/or increased image acquisition and processing time.

Experimental studies of tissue absorption and scattering have shown that the number of ballistic photons used to image biological tissues using OCT decreases exponentially as a function of depth [73]. Tissue attenuation is therefore the ultimate limit of large depth imaging in biological tissues.

4.4 Illustration of imaging capabilities

4.4.1 Imaging a test sample

Our FD-OCT system was compared in terms of image resolution with a commercially available SS-OCT (OCS1300SS, Thorlabs), another FD-OCT modality. The commercial system is based on swept source technology. It operates at the same center wavelength of emission (1.3 µm). The axial and transverse resolutions (in air) of the system are 12 µm, and 25 µm, respectively. The schematic representation of the SS-OCT is given in Figure 4.16.
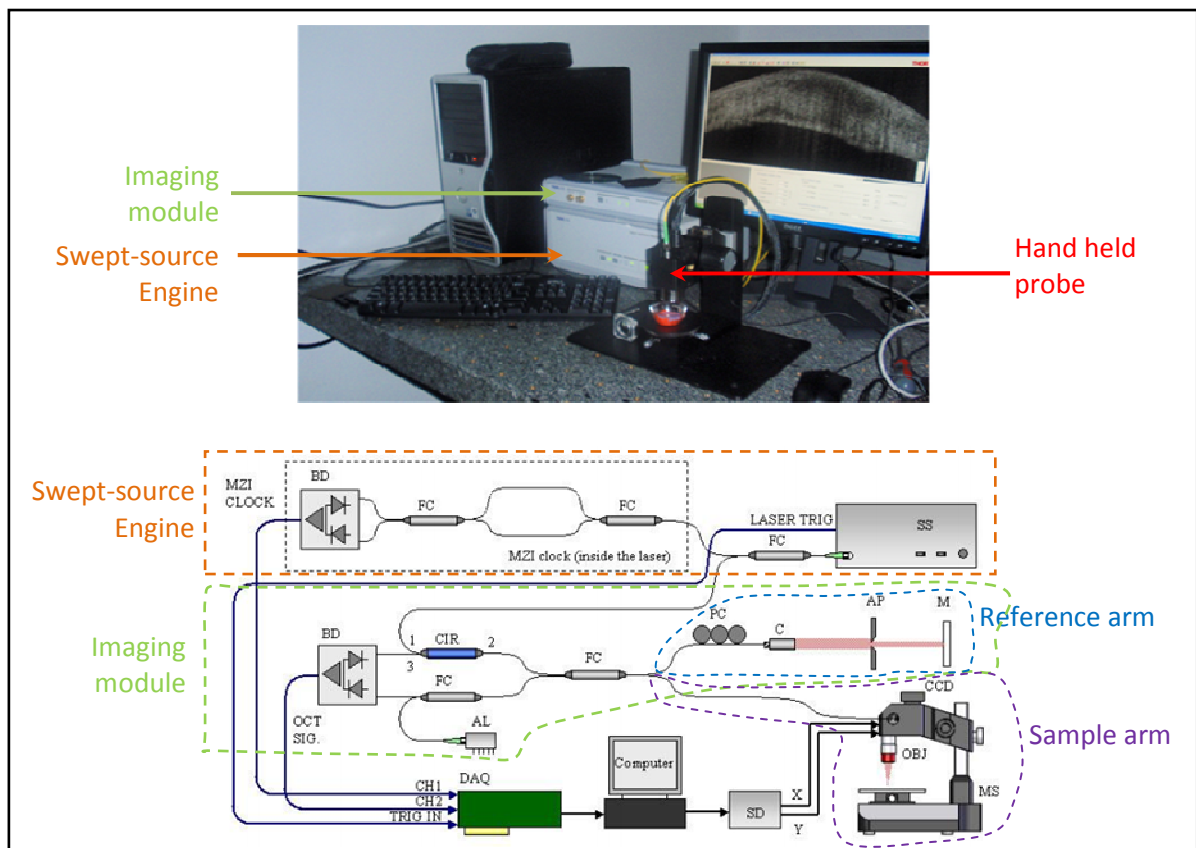

Figure 4.16 Photo of commercial SS-OCT (top) and its schematic (below) [74], SS: swept laser source, FC: fiber coupler, PC: polarization controller, CIR, circulator, C: collimator, AP: adjustable pinhole variable attenuator, M: mirror.

An infrared viewing card (VRC5, Thorlabs) was used as a test sample for the comparison between the SD-OCT developed in the laboratory and the commercial SS-OCT. The cross-sectional OCT images shown in Figure 4.17 (a) and (b) were obtained using the commercial SS-OCT system and the SD-OCT system, respectively.
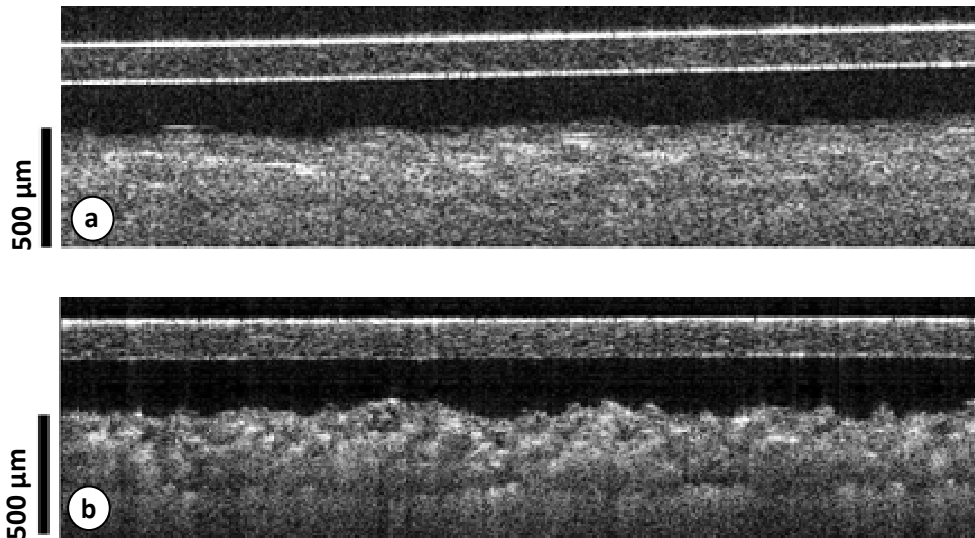

Figure 4.17 Image comparison two FD-OCT imaging systems. Cross-sectional image of an infra-red viewing card by SS-OCT (a) and SD-OCT (b). As can be seen, the high-resolution SD-OCT image provides detailed internal structures of the viewing card better than what can be obtained with SS-OCT system working at the same center wavelength.

The images reveal the internal structures of the card. Three distinct layers can be distinguished. The upper layer corresponds to plastic material with a thickness of 170 µm. A random distribution of scattering structures is revealed inside this polymer material. The bottom layer is very inhomogeneous and corresponds to the photosensitive material. The middle layer, in contrast, is very homogeneous since no scattered light is detected from this region. This layer is assumed to be the glue used for bonding the photosensitive material to the plastic layer.

As can be seen from Figure 4.17, the high-resolution SD-OCT image of the infra-red viewing card given in (b) provides detailed internal structures better than what can be seen with SS-OCT system given in (a) working at the same center wavelength, i.e. 1.3 µm.

4.4.2 Imaging the Schlemm's canal

As part of a collaborative project on glaucoma surgery, we imaged samples of excised human corneas to see if our SD-OCT can resolve Schlemm's canal (SC). SC has been our target for OCT imaging because it plays an important role in the treatment of glaucoma. It is believed to be the principal site for the outflow resistance of the aqueous humor in glaucomatous eye

[75]. Being able to image the canal non-invasively would allow for glaucoma diagnosis and monitoring of any possible intervention.

SC is situated at the depth of ~ 0.8 mm inside a highly scattering corneal limbus, 2 to 3 mm wide ring at the interface between cornea and sclera (see Figure 4.18).
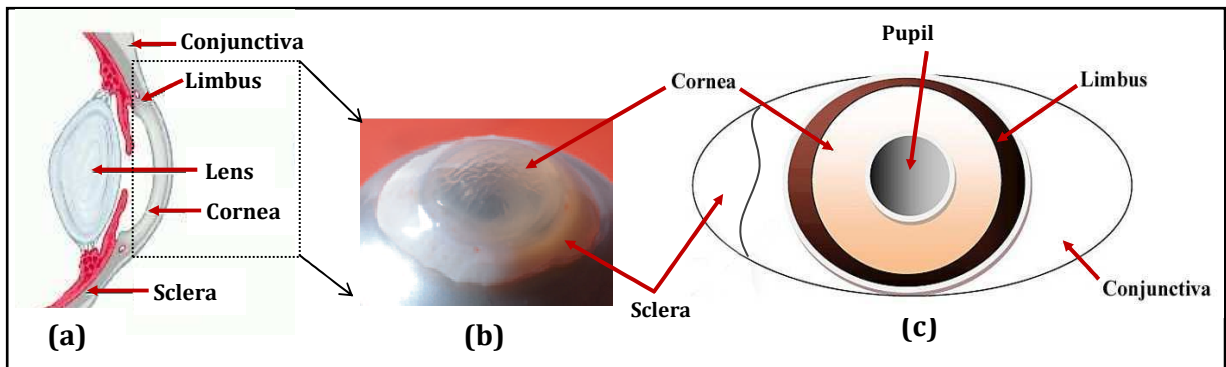

Figure 4.18 (a) Segittal view of the anterior segment of human eye, (b) Photo of human cornea with rim of sclera, (c) Front view of ocular surface showing the limbus. Limbus is a 2 to 3 mm ring that surrounds the cornea. Conjunctiva is the surface layer overlying the white portion of the eye (sclera).

Cornea from a person with glaucoma scatters more light than a healthy cornea. This is partly because of the fact that glaucoma and corneal edema often co-exist [76]. It has been observed that there is a high incidence of endothelial dystrophies among patients with glaucoma [77]; and one of the clinical manifestations of endothelial dystrophies is corneal edema [78]. Moreover, the persistent elevated IOP, which is often the case of glaucoma, creates high pressure gradient against stroma that drives the aqueous humor from the anterior chamber across endothelium into stroma, affecting corneal hydration and hence corneal edema [79, 80]. Unlike transparent fibers in a healthy cornea, limbus and sclera are made up of less organized and opaque fibers that strongly scatter light. Moreover, sclera is covered by conjunctiva - a multilayer tissue that influences the beam propagation differs significantly.

To minimize the attenuation of light due to scattering, we have used an SLD light source centered at 1.3 µm. This is because generally tissue scattering decreases nearly monotonically with increasing wavelength and corneal absorption is still reasonably low around 1.3 µm. Above 1400 nm, corneal absorption (mainly due to water) becomes significant (see Figure 4.19). Increasing the wavelength further enables to have another window around 1.65 µm where local absorption is again minimum but availability of a broadband light source and optical components limits the development of high-resolution OCT in this long wavelength range.
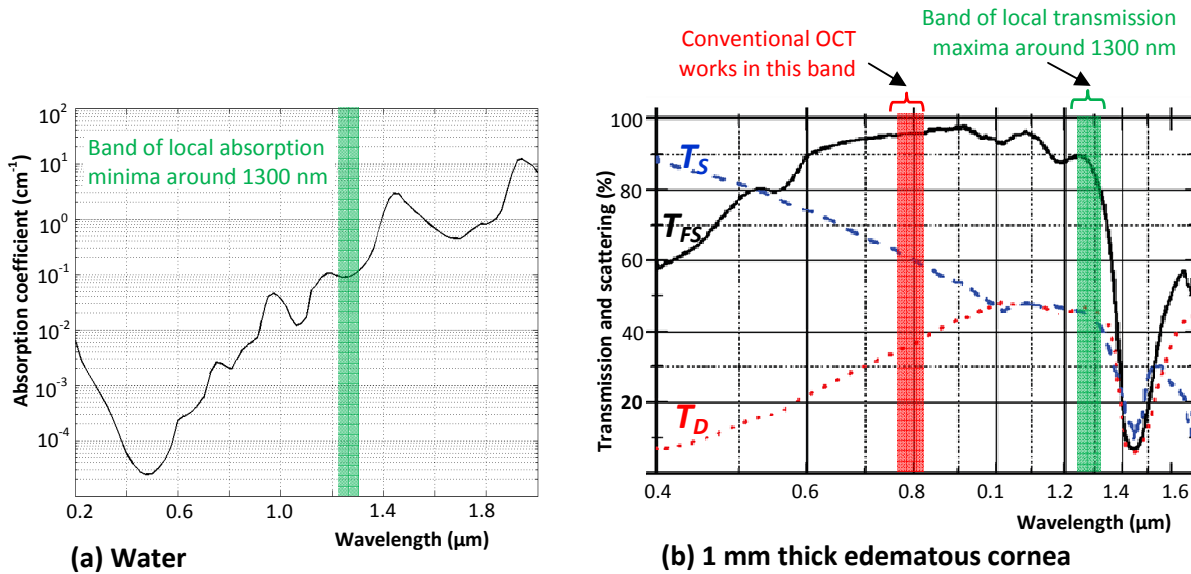
(a) Water **(b) 1 mm thick edematous cornea**

Figure 4.19 a) Absorption of water, taken from [81], **(b)** optical characteristics of an approximately 1 mm thick edematous cornea [82]: forward scattered light T_{FS}, unscattered light T_D, and percentage of scattered light T_S. From (a) and (b), we see that spectral band around 1.3 µm corresponds to a local absorption minimum.

For our experiment, human corneas not suitable for transplantation mostly because of their insufficient endothelial quality (< 2000 cells/mm^2) [83] were obtained from the *Banque Française des Yeux* (French Eye Bank, Paris, France). The study was conducted according to the tenets of the Declaration of Helsinki and the French legislation for scientific use of human corneas. The OCT cross-sectional image of excised cornea with a sclera rim of human eye suffering from glaucoma is shown in Figure 4.20.

When we scan in the sclera, the OCT image shows only the scalera (see Figure 4.20 (a)). When we scan on the border between the sclera and cornea, the Schlemm's canal (SC) appears as a line in the OCT image (b). When the scanning beam traverses the limbus two times, the SC appears as two holes in the OCT image (as indicated by the two arrows) (c). In principle, the two holes have the same size. However, on the OCT image, hole 1 (on the left) is wider than the hole 2 (on the right). This may be due to the collapse of one side of the channel while working ex-vivo. The location and the size of the canal obtained using OCT is shown in red and its histological data in blue. The exact depth location and size of SC varies from person to person. The width of SC obtained with OCT was 20 µm, and is almost half of the histological value (50 µm). One possible explanation may be due to fact the channel may collapse while working *ex-vivo*.
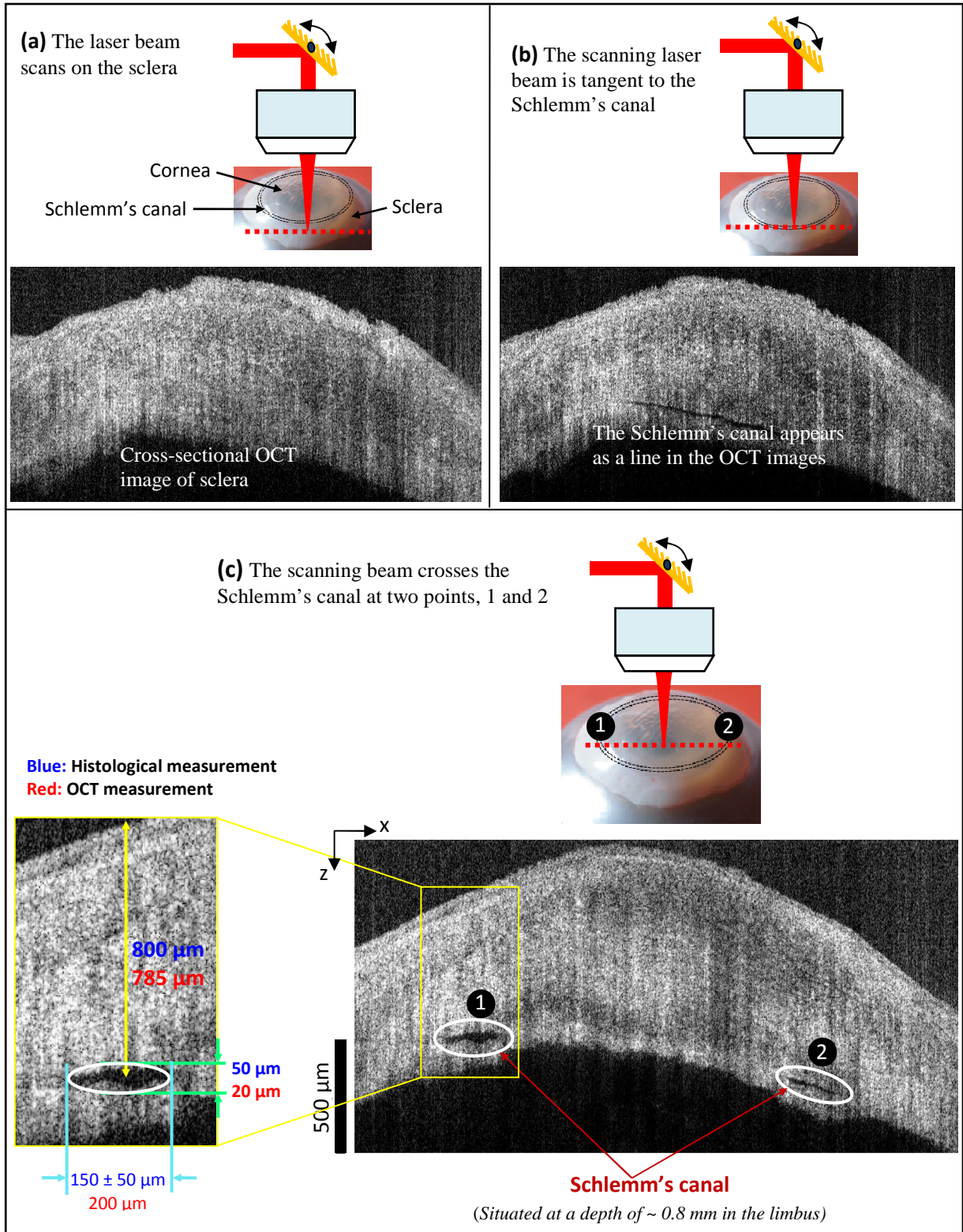
Figure 4.20 Cross-sectional OCT images of an excised corneosclera. Note that when he scanning laser beam traverses the limbus two times, the Schlemm's canal appears as two holes (indicated by arrows **(c)**) in the cross-sectional OCT image . Hole (1) on the left is wider than the hole (2) on the right. This may be due to the collapse of one side of the channel while working *ex-vivo*.

The enhanced resolution of our system enables us to properly visualize the SC. To the best of our knowledge, it is the first time that SC can be observed with OCT. This result has been

published in *Optics Communications* [54] and orally presented in *Photonics Europe Conference* 2012 [84]. Being able to resolve the SC helps to use OCT tm monitor a laser incision in the limbus around SC in order to increase the outflow rate of aqueous humor so as to lower the IOP and treat glaucoma. Glaucoma usually develops as a result of elevated IOP of the eye above the normal physiological range. If not treated on time, glaucoma can permanently damage vision and lead to total blindness.

4.4.3 Image of other samples

The system has also been used to image other samples. such as an orange (a) and an onion (b) of Figure 4.21. In both images, the internal structures can be visualized up to a depth of more than 1 mm
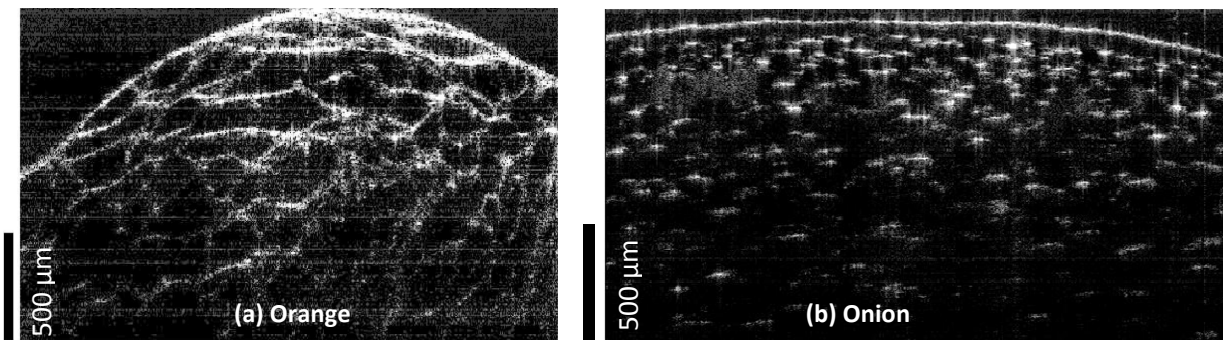

Figure 4.21 Cross-section OCT image of orange (edible part)

4.5 Conclusion

In this chapter, we have reported the characterization of a high-resolution SD-OCT imaging system developed for imaging the Schlemm's canal. This system employs a relatively low-cost broadband SLD light source centered at $1.3\,\mu$m. The light source consists of a combination of two multiplexed SLDs with shifted spectral properties. The spectral region around this center wavelength is optimal for its reduced absorption and relatively low tissue scattering. The experimental setup and the different optical and electrical components that we have used during the development of the system have been explained. A user-friendly GUI that automates all the hardware components of SD-OCT has been developed. The GUI also includes all the images processing steps needed to reconstruct the SD-OCT.

In SD-OCT, imaging parameters such as axial resolution, imaging depth and sensitivity fall-off all depend on the spectrometer. The transverse and axial resolutions of the system (in air) are $6.5\,\mu$m and $4.0\,\mu$m, respectively. In SD-OCT, the axial resolution decreases, even in air, as the imaging depth increases. This is mainly due to the interpolation error of data

resampling. By using a zero padding technique, we have reduced the data resampling error and improved the resolution degradation of the system. The system has a measured depth range of 1.76 mm and sensitivity of ∼ 95 dB. This sensitivity refers to the value around a shallow depth. However, as one goes deeper, the sensitivity of SD-OCT falls significantly, mainly due to the limited resolution of the spectrometer. Both the finite spot size of the beam on the CCD and the limited sampling resolution of the spectrum by the size of the CCD pixels lead to this sensitivity fall-off. The accuracy of the spectral calibration also affects the sensitivity at large depths. The measured value of sensitivity at the end of the depth range (∼ 1.8 mm) was found to be 13 dB less than the value around the zero depth. The maximum line rate of the system is 46 kHz.

Images of different samples were shown to illustrate the performance of the system. In particular, we have demonstrated for the first time the possibility of imaging the Schlemm's canal that is situated at a relatively large depth inside the highly scattering limbus of a human eye suffering from glaucoma. As Schlemm's canal plays a predominate role in controlling the IOP, we believe that high-resolution OCT imaging systems optimized at 1.3 µm may be used for guiding glaucoma laser surgery. To demonstrate this, we have coupled a laser incision system with the OCT imaging system, and we imaged the laser surgery in human cornea in real-time. The details of this demonstration will be presented in the next chapter.

Chapter 5 - Coupling OCT with the laser surgery

5.1 Introduction

Since the 1970s, lasers have been used for a variety of applications including, but not limited to, medical interventions. When a laser light is focused on biological tissues, a variety of laser-tissue interaction mechanisms may occur. Optical properties of tissues such as reflection, absorption and scattering determine the total transmission of tissues at a certain laser wavelength. Laser parameters such as wavelength, pulse duration, pulse energy, peak power and focusing conditions determine the kind of interaction mechanism. Thermal and mechanical properties of tissues also affect the dynamics of laser-tissue interaction.

The desired type of laser-tissue interaction depends on the type of medical application. For instance, thermal interaction may be the desired effect for applications involving laser coagulation but it is an undesired phenomenon in other applications that require precise incision as in refractive surgery. For a given medical application, appropriate choice of laser parameters therefore allows the enhancement of certain effects and the minimization of others [1]. In order to achieve the required laser-tissue interaction mechanism for the intended medical application, the choice of laser with appropriate parameters is therefore a crucial step. For our application, a precise subsurface surgery inside human corneosclera (in the vicinity of the Schlemm's canal) is required with minimal damage of the surrounding tissues.

To understand the importance of choosing the right laser parameter for our application, a short overview of laser-tissue interaction will be first introduced in this chapter. The specific interaction type of ultrashort pulse lasers that makes them unique for precise incision will be highlighted. To emphasize the need of laser wavelength optimization, histological sections and scanning electron microscope images of femtosecond laser incisions at various wavelengths performed on human sclera and edematous cornea and sclera will be presented.

In order to demonstrate the possibility of monitoring the ongoing laser surgery in real-time, we have coupled the OCT imaging system (Laboratoire Charles Fabry - Institut d'Optique) with the laser surgery system (Laboratoire d'Optique Appliquée (LOA) – ESNTA ParisTech, École polytechnique, CNRS UMR 7339)). The protocols/methods, experimental setups and the results obtained will be presented and discussed.

5.2 Laser-tissue interaction mechanisms

Among the laser parameters, laser pulse duration is a very crucial parameter worth considering when selecting a certain type of interaction because it controls the laser-tissue interaction time. Based on the exposure time and laser power density, mainly five categories of interaction types can be classified [85]. These are *photochemical interactions, thermal interactions, photoablation, plasma-induced ablation and photodisruption.*

Figure 5.1 shows the map of the laser-tissue interactions as a function of exposure time. The power density variation across these different interaction types is over 15 orders of magnitude, however, they all share a single common datum: the characteristics energy density ranges approximately from 1 to 1000 J/cm2 [85]. Thus, a single parameter that distinguishes and primarily controls these processes is the duration of laser exposure, which corresponds the laser pulse duration. The inverse relation between power density and exposure time clearly demonstrates that roughly the same energy density is required for any intended type of interaction. Thus, the exposure time appears to be the main parameter responsible for the variety of interaction mechanisms.
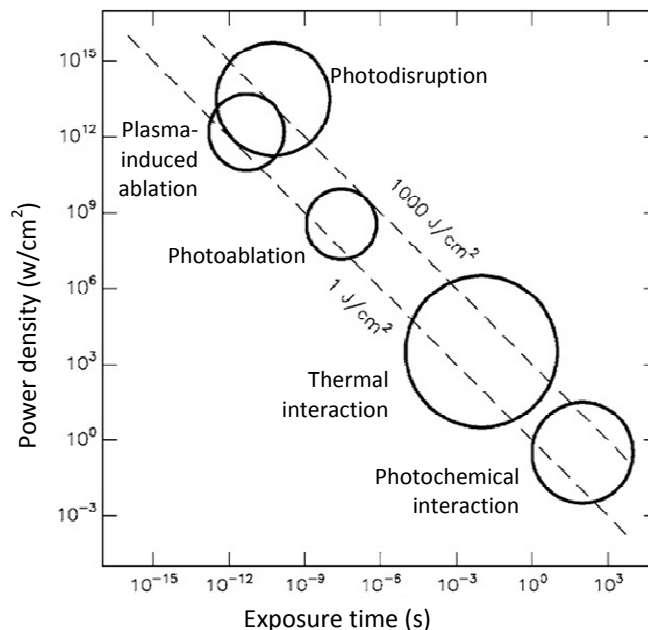

Figure 5.1 Map of laser-tissue interactions as a function of exposure time. The circles give only a rough estimate of the associated laser parameters, taken from [85]

Photochemical interactions take place at very low power densities (typically $1W/cm^2$) and long exposure times ranging from seconds to continuous wave. One of the applications of

photochemical effect in clinics is photodynamic therapy (PDT). In PDT, a non-toxic photosensitizer that acts as a catalyst is used. Tumor treatment is the principal, but not the only, application field of PDT. Typical lasers used red dye lasers and diode lasers.

Thermal interaction stands for a wide variety of laser-tissue interactions where rise in local temperature is the significant parameter that changes. While photochemical processes are often governed by a specific reaction pathway, thermal effects generally tend to be nonspecific. Observations of thermal effects include coagulation, vaporization, carbonization and melting. Typical lasers that can induce photothermal interactions include CO2 (10.6 µm), Er:YAG (2.94 µm), Ho:YAG (2.12 µm), Nd:YAG (1.064 µm), argon ion (0.514 µm) and diode lasers (~ 0.8 µm) and the typical power densities range from 10 to 10^6 W/cm^2.

Photoablation occurs due to dissociation of chemical bonds as a result of application high energy UV photons using UV lasers such as excimer lasers: ArF (193 nm), KrF (248 nm), XeCl (308 nm), XeF (351 nm) [85]. Typical pulse durations and power densities required to achieve photoablation are 10-100 ns and 10^7-10^{10} W/cm^2, respectively. Photoablation yields a precise ablation and is often used in refractive corneal surgery where precise etching of part of the cornea under the flap is required.

Plasma-induced interaction involves tissue ablation by ionization plasma formation. Typical laser pulse duration to induce plasma formation is in the range of 100 fs to 500 ps with typical power densities of 10^{11} to 10^{13} W/cm^2. When the intensity of the laser exceeds some threshold value, the external electric field of the laser light becomes strong enough to overcome atomic or intramolecular Coulomb electric fields, forcing ionization of molecules and atoms and causing optical breakdown. The physical effects associated with optical breakdown are plasma formation and shock wave generation. If breakdown occurs inside soft tissues or solids, cavitation and jet formation may additionally take place. The whole process of tissue ablation by optical breakdown is depicted in Figure 5.2.

Mechanisms for the generation of the initial free electrons for the ionization cascade are either thermionic emission by heating of linear absorbing chromophores in the target (in liquids these can be impurities), or multiphoton ionization [86]. Thermal ionization is supposed to dominate in Q-switched nanosecond pulses whereas in mod-locked pulses, multiphoton ionization may occur due to the high electric field induced by the intense laser pulse [85].
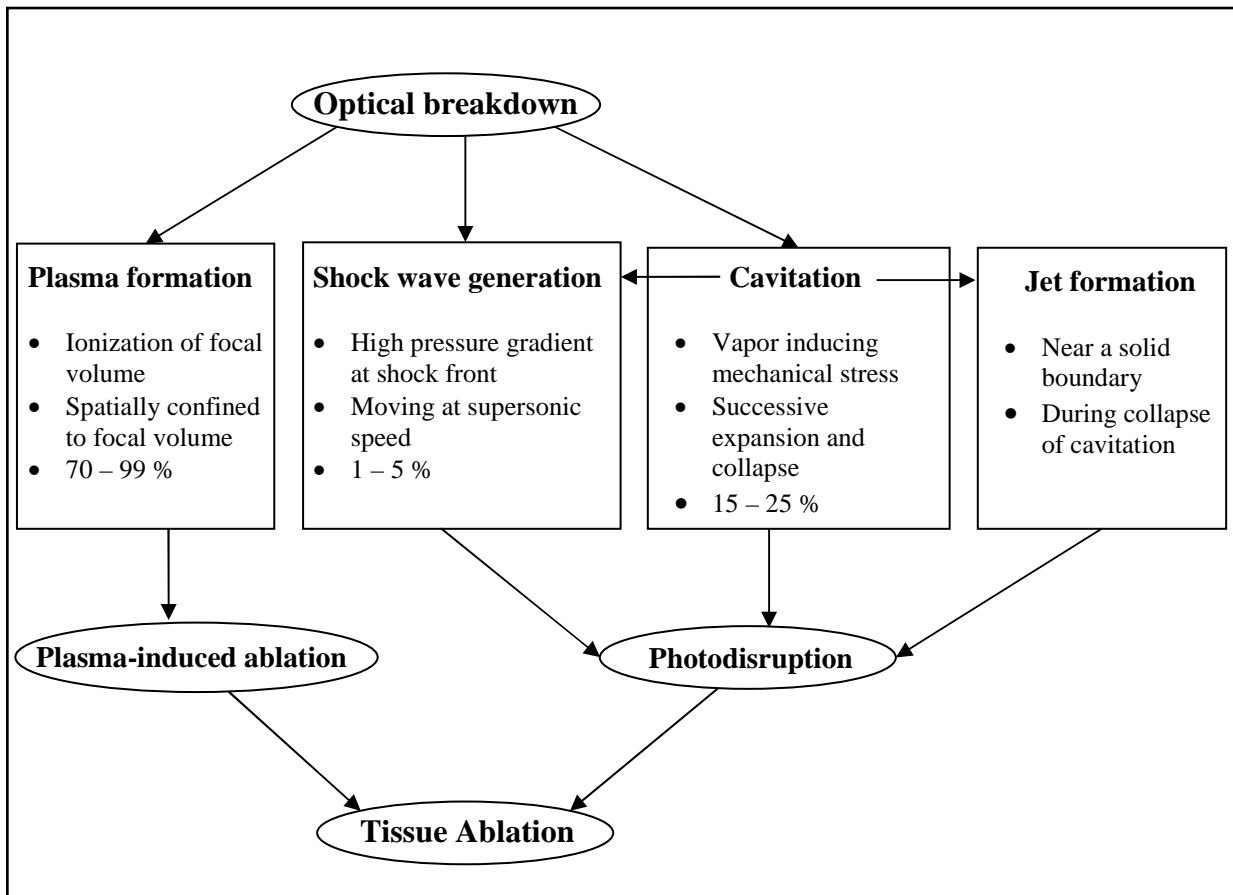
Figure 5.2 Scheme of the physical processes associated with optical breakdown that leads to tissue ablation. Percentages given are rough estimates of the approximate energy transferred to each effect (incident pulse energy: 100%). Cavitation occurs in soft tissues and fluids only. In fluids, part of the cavitation energy might be converted to jet formation, taken from [85].

The multiphoton ionization rate is proportional to I^k, where I is the intensity of the beam and k is the number of photons required for ionization [86]. Due to the requirement of coherence, multiphoton ionization is achievable only during high peak intensities as in femtosecond laser pulses. Typical lasers that cause ionization include Nd:YAG, Nd:YLF and Ti:Sapphire laser [85]. Generally, it has been observed that the threshold energy E_{th} for achieving optical breakdown increases with increasing the pulse duration τ of the laser in the form of $E_{th} \propto \sqrt{\tau}$, i.e., optical breakdown can be reached at lower energy threshold with femtosecond lasers than with nanosecond and picosecond lasers.

Increasing the laser pulse energy too much beyond the threshold value does not necessarily yield a good incision because at higher pulse energies – and thus higher plasma energies – shock waves and other mechanical side effects become more significant and might even determine the global incision effect upon the tissue. Primarily, this is due to the fact that mechanical effects scale linearly with the absorbed energy.

For nanosecond and picosecond laser pulse durations, the interaction process is complex and not very strongly localized as multiple ionization cycles, thermal effects and shock wave propagation contribute simultaneously to the disruption of the tissue, resulting in damage of surrounding tissues and scar formation [87]. For example, the zone of collateral tissue damage with the nanosecond Nd:YAG laser may be greater than 100 µm, which makes it impractical for applications that require precise incisions such as corneal surgery [1]. On the other hand, the interaction process with ultrashort pulse lasers occurs on timescales much shorter than those typical for heat conduction or propagation of acoustic shock waves: optical breakdown occurs while the energy is still confined to the focal volume. Hence because of the strongly localized interaction process, ultrashort pulse lasers are best candidates for precise subsurface incisions with minimal collateral damage of tissues [1].

5.3   Advantages of ultrashort pulse laser surgery

Ultrashort pulse lasers produce pulses in the sub-picosecond range ($<10^{-12}$ s), specifically in the femtosecond regime. Because of the high peak intensities of femtosecond pulses, the main free-electron generation process in laser-induced optical breakdown of biological tissues is said to be the multiphoton ionization of water [88]. If liquid water is treated as a lone-pair semiconductor [89], the band gap an electron has to exceed is 6.5 eV. Therefore, if we use femtosecond lasers at 780 nm (photon energy: 1.56 eV), roughly four-photon-processes are taking place in the focus region.

Compared to nanosecond and picosecond pulse lasers, the threshold energy needed for femtosecond lasers to achieve tissue optical breakdown is lowered by more than one order of magnitude [88]. Thus, the mechanical side effects, like shock waves or cavitation bubbles generated in the focus region, are expected to be reduced. Moreover, thermal damage to the surrounding tissue is minimized because of the very slow energy transfer of the excited electron plasma. The extremely short pulse duration allows ultrashort pulse lasers to become useful in a range of biomedical applications involving diagnostics and biomedical imaging.

Generally, advantages of ultrashort pulse laser surgery over conventional and other longer pulse laser surgery systems include [90]:

   i.   efficient ablation due to the small input of laser energy per ablated volume of tissue and the resulting decrease of energy density needed to ablate material

ii. minimal collateral mechanical damage due to the efficient ablation and the short duration of the stress impulse

iii. minimal collateral thermal damage due to the extremely short deposition time

iv. the ablation threshold and rate are less dependent on tissue type and condition

v. high precision in ablation depth is achievable because only a small amount of tissue is ablated per pulse

vi. low acoustical noise level (compared to the acoustical noise produced by other laser systems)

vii. minimized pain due to localization of energy deposition and damage

viii. precise spatial control: the intensity-dependent, multi-photon process self-ensures that tissue below or laterally shifted from the beam focus will not experience ablative interaction

ix. since ultrashort pulses interact strongly with all matter regardless of specific linear absorption characteristics, efficient processing of many tissue types is possible.

5.4 Need for femtosecond laser wavelength optimization

For interventions in clear cornea, commercially available solid state lasers are routinely used in ophthalmology. The most successful application of femtosecond laser is refractive error surgery on human cornea often called femto-LASIK (laser *in situ* Keratomileusis), where a femtosecond laser is used to create a precise corneal flap and then an excimer laser is used to perform laser corneal ablation for reshaping the cornea and correct the refractive error. Because of a greater accuracy in flap size, shape and thickness, the corneal flap created by femto-LASIK procedure is considered by many ophthalmologists as improvement over traditional LASIK procedure that uses microkeratome.

However in sclera and edematous cornea, the tissues lose their transparency, giving rise to wavefront distortion thereby decreasing the quality of femtosecond laser surgery inside such strongly scattering tissue [91]. That is exactly the situation for our application because for glaucoma treatment, in order to facilitate the drainage of the aqueous humor, one needs to make a precise surgery inside a strongly scattering corneal limbus at the depth of 0.8 mm around the Schlemm's canal.

5.4.1 Selecting the right laser wavelength

Generally, increasing the wavelength decreases the effects of scattering. However, for biological tissues, absorption should also be taken into consideration. For non-vascular tissues like cornea, absorption due to water plays the dominant role. From the spectral absorption characteristics of water shown in Figure 5.3 (a), we see that in the spectral region between 1.60 µm and 1.70 µm, there is a relative minimum in the water absorption spectrum.
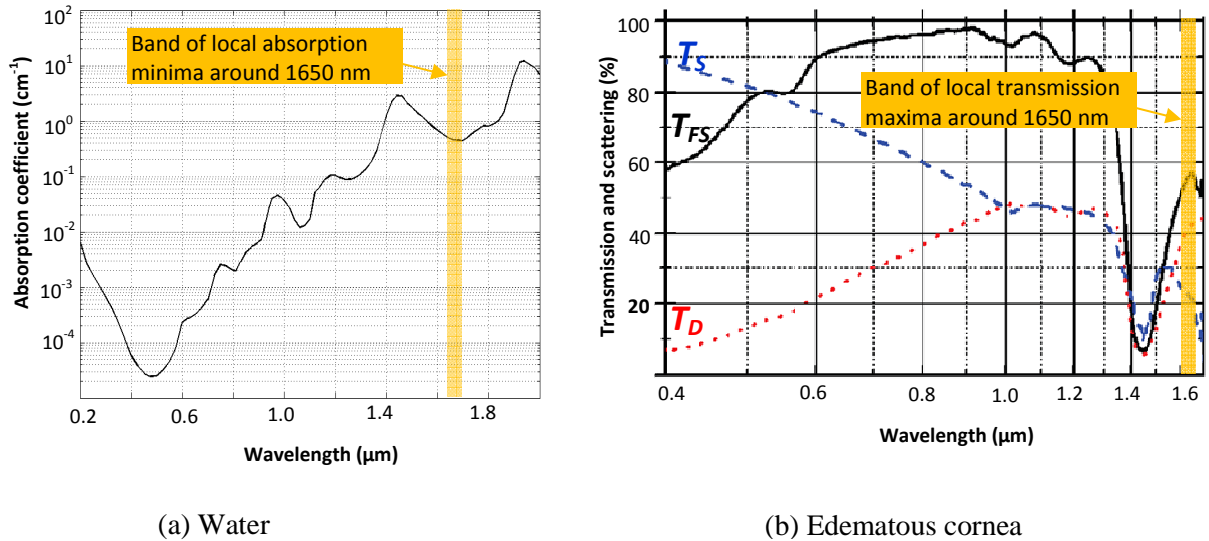

(a) Water   (b) Edematous cornea

Figure 5.3 (a) Absorption of water, taken from [81], **(b)** optical characteristics of an approximately 1 mm thick edematous cornea [82]: forward scattered light T_{FS}, unscattered light T_D, and percentage of scattered light T_S. From both plots, we see that spectral band around 1.65 µm corresponds to a local absorption minimum.

An optical setup to quantify the optical scattering in the edematous cornea has been developed in LOA [82]. The total transmitted light T_{FS} is measured with an integrating sphere whereas the unscattered part T_D of the transmitted light is measured with a confocal setup [82]. The measured optical properties of an approximately 1 mm thick edematous cornea are given in Figure 5.3 (b). It shows that the transmitted light with little or no scattering (shown in red dots) is maximum around 1650 nm. Between 1400 nm and 1500 nm, there is a local light absorption peak by cornea due to the presence of water. Hence using a laser near 1650 nm would enhance the laser incision depth. However, as commercially available femtosecond laser systems have a wavelength of emission around 1000 nm, development of a new femtosecond laser system around 1650 nm is required.

5.4.2 Generating femtosecond laser near 1650 nm

Nonlinear optical parametric processes are particularly interesting when no laser is available emitting at the wavelengths of interest or when wavelength tunability is required. To have access to the wavelength region near 1650 nm, a nonlinear wavelength conversion has been used to up-convert the wavelength of a commercial femtosecond laser emitting at 1030 nm (s-pulse HP system, Amplitude systèmes, Pessac, France). Such parametric processes depend on the optical phases of the waves involved. Efficient conversion requires phase matching or quasi-phase matching to get amplification of the wavelengths of interest. Phase matching conditions are verified when two or more photons travel at the same speed in the same direction [1]. This is only possible for two different wavelengths in birefringent media, i.e. which have an anisotropic refractive index. Two typical schemes of achieving nonlinear wavelength conversion, optical parametric amplification (OPA) and optical parametric generation (OPG), was developed in LOA by F. Deloison (PhD) and C. Crotti (PhD) under the supervision of Prof. K. Plamann [1, 3, 83]. This system was used in our project for performing incisions in cornea and sclera.

In OPA, a signal 'seed' beam and a pump beam of shorter wavelength interact in a nonlinear crystal, as shown schematically in Figure 5.4.
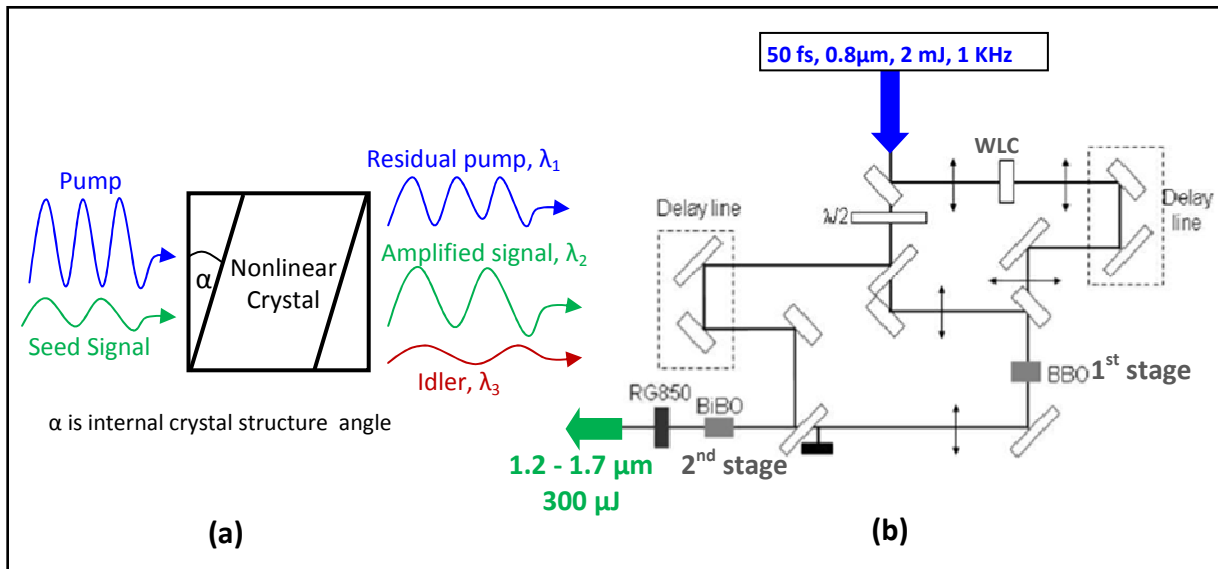

Figure 5.4 Principle (a) and schematic (b) of OPA [1, 3]

The signal seed beam can be obtained from a white light continuum (WLC) generated by a separate nonlinear process. The nonlinear interaction process in the OPA crystal converts photons from the pump beam into signal photons of lower energy. The same number of

complementary photons forming the 'idler' beam. The photon energy of the idler wave corresponds to the difference between the photon energies of the pump and signal waves. Crystals (such as β-barium borate-BBO, or lithium triBOrate-LBO) used for the OPA scheme are most of the time selective in the wavelengths they generate. In this case, tuning the output wavelengths may often be achieved simply by rotating the nonlinear crystal (changing the angle α as shown Figure 5.4). However, as the gain of such systems is very low, a second amplification stage that employs bismuth TriBOrate (BiBO) crystal has been used in order to reach an energy on the order of micro joule per pulse that is required for performing incision [1].

For low power requirements (few micro joules), a relatively simpler and efficient method of wavelength conversion can be achieved with an OPG (see Figure 5.6). Periodically poled lithium-niobate-doped magnesium (PPMLN[11]) crystal was used for efficient wavelength conversion of the 1030 nm wavelength emitted by the femtosecond laser to 1650 nm without requiring a seed beam by achieving quasi-phase matching. Wavelength tuning was achieved within a restricted range by changing the temperature of the crystal, thereby modifying the dimensions of its periodically poled structure.
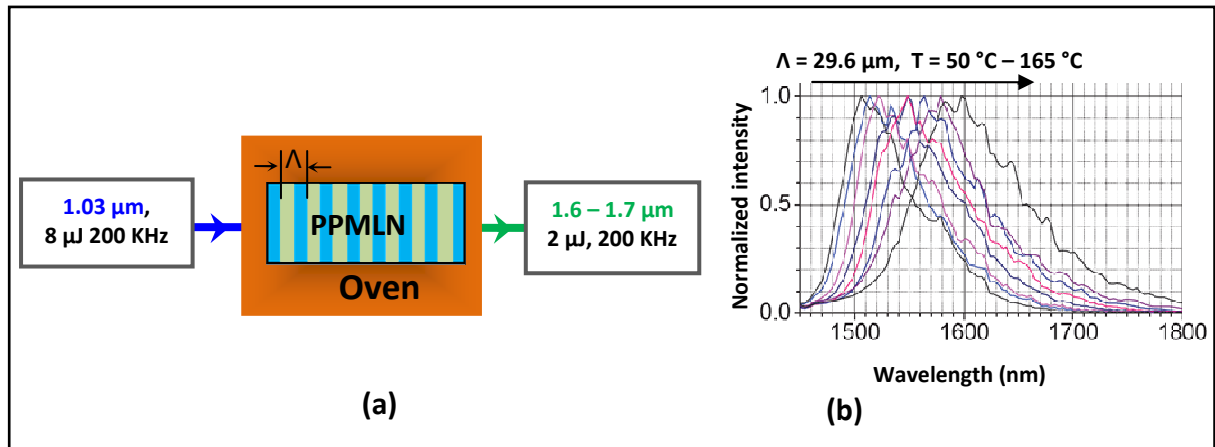

Figure 5.5 Schematic of OPG (a) and spectral evolution with oven temperature (b), realized with PPMLN crystal. Λ is the period of the poled structure in PPMLN crystal [1, 83]

OPAs require relatively complex optical set-ups and a strong pump laser. They are very versatile laboratory sources, but generally considered impractical for clinical applications. OPGs are conceptually more straightforward, more efficient and steadier but remain limited concerning input power [1].

---

[11] HC Photonics, Taiwan

5.5   Femtosecond laser surgery in edematous cornea and sclera

In order to make an incision in the tissue, the energy required is of the order of 1 µJ. For the reasons mentioned above, the pulse duration should be a few hundreds of femtosecond. The duration of the incision should not exceed a few minutes because the patient is anesthetized locally in order to avoid the maximum movements of the eye. Typically, the rate of the laser must be greater than or of the order of tens of kHz. On the other hand, this rate should not exceed a few MHz to avoid possible thermal effects on the fabric by heat buildup between the different pulses. If the rate is less than tens of MHz, the heat generated by a pulse has time to dissipate before the arrival of the next pulse [3].

5.5.1   Experimental setup and methods

The experimental setup used for doing laser surgeries in cornea and sclera is shown in Figure 5.6. The incision results presented in section were performed in LOA by F. Deloison (PhD) and C. Crotti (PhD) under the supervision of K. Plamann (Prof).
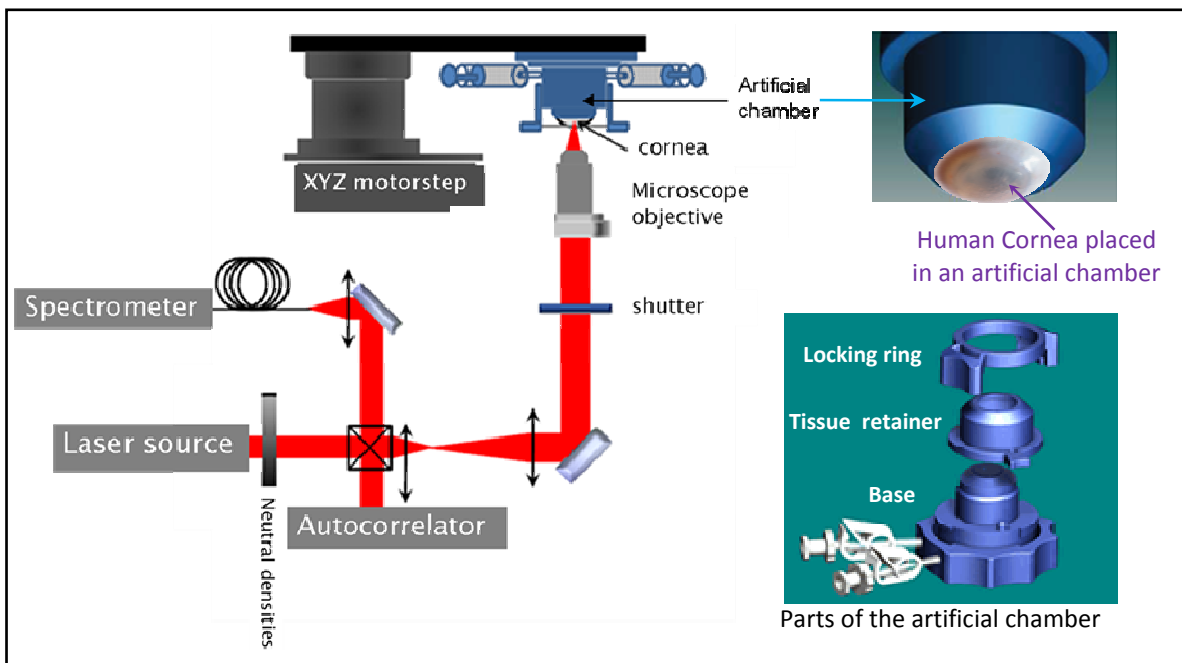

Figure 5.6 Schematic diagram of the experimental setup used for doing the femtosecond laser incisions in cornea and sclera in LOA [3, 83].

The setup mainly consists of a tunable laser source and an inverted microscope (Olympus, IX70) with a 3-axis stepper motor translation stage (Newport, XPS). The automated translation stage enables us to make different incision types: penetrating line, lamellar incision, incision in volume (or 3-D), etc, as shown in section 5.7, Figure 5.15. The system is

equipped with a spectrometer (OceanOptics, NirQuest 256) in order to verify the spectrum of the laser, and a variable neutral density to adjust the energy applied to the tissue.

The experiments were performed on human corneal grafts from the *Banque Française des Yeux* (French Eye Bank, Paris, France) which were unsuitable for transplantation and were made available for research purposes. The study has been conducted according to the tenets of the Declaration of Helsinki and the French legislation for scientific use of human corneas. As most of the corneas were rejected because of their insufficient endothelial quality (< 2000 cells/mm^2) [83], they typically present corneal edema of varying degree and therefore are quite representative for the tissular quality which laser surgery has to address in the patient's eye. The thickness and transparency of the cornea specimens may also be modified in the laboratory by a controlled chemical deturgescence treatment [1, 83].

An artificial chamber that holds the cornea is fixed with the motorized 3D translation stage. The purpose of the artificial chamber is to achieve incision conditions that are similar to clinical surgery. To reproduce the configuration of the anterior chamber and mimic the effect of the intraocular pressure, biological serum is filled into the artificial chamber. A glass slide with a thickness between 100 and 160 µm is placed over the cornea in order to flatten the surface [3].

5.5.2 Laser incision in cornea

To find the optimum wavelength of laser surgery for our application, seven different incisions have been made in an edematous cornea at seven different wavelengths (1030 nm, 1450 nm, 1500 nm, 1550 nm, 1600 nm, 1650 nm and 1700 nm). The laser energy for all incisions was 2 µJ. The histological section of incisions taken by Michèle Savoldelli (Hôpital Hôtel Dieu, Paris) are shown in Figure 5.7 [83].

From Figure 5.7, we see that when the laser wavelength is tuned to the local absorption maximum of water, i.e., between 1400 nm and 1500 nm, the incision depths become shallow. On the other hand, due to its relatively low absorption and reduced scattering, the laser light at the wavelength of 1650 nm allows us to achieve a relatively deep incision. An incision depth of more than 900 µm can be achieved at this wavelength, which is more than twice the incision depth achieved at 1030 nm. This agrees with the predicted value of the optimum wavelength that is deduced from the optical characteristics of edematous cornea (see Figure 5.3 (b)).
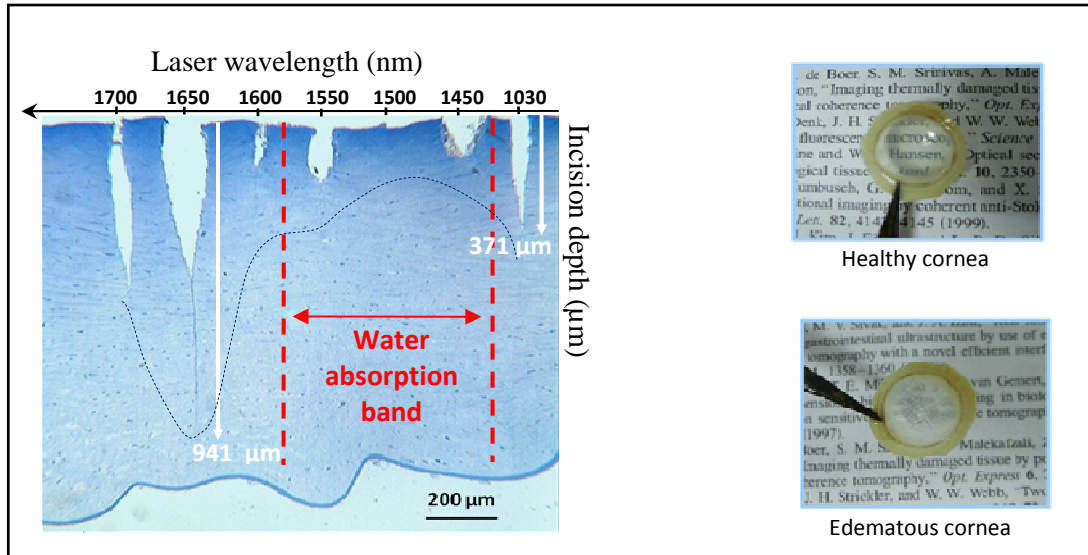
Figure 5.7 Comparison of histological section of femtosecond laser incisions in edematous cornea realized at different wavelengths using OPG laser source (2 µJ, 10 KHz, 700 fs) and focusing optics with numerical aperture NA = 0.56 [83].

Figure 5.8 shows scanning electron microscope (SEM)[12] images of another laser incision performed in an edematous cornea. The laser incision is lamellar, i.e., cutting in a horizontal plane. The laser beam optimized at the wavelength of 1.65 µm has been focused by microscope objective of 0.4 NA. The incision made at the depth of 200 µm s of high quality. On ca see that the collagen is well cut.
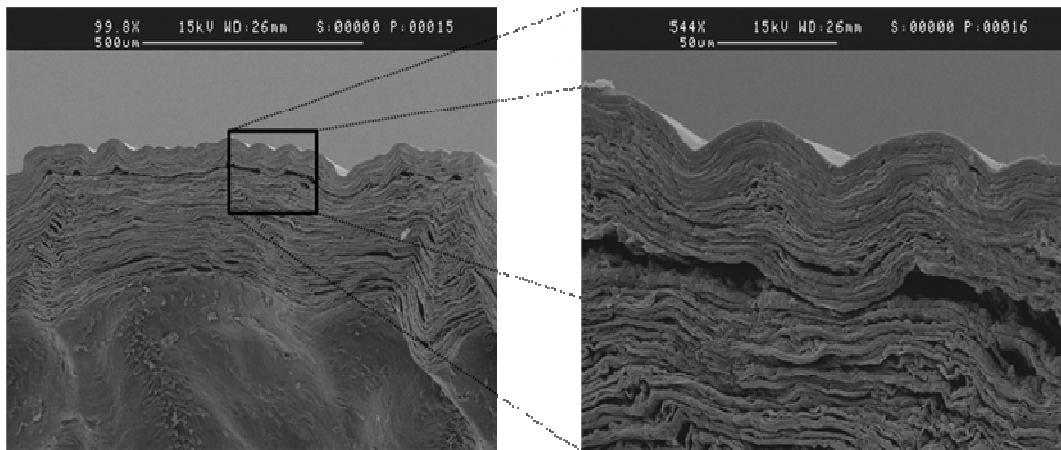

Figure 5.8 SEM (StereoScan 260, Cambridge Instruments – Leica), image of lamellar laser incision in cornea, realized by 0.4 NA focusing objective and femtosecond laser (2 µJ, 10 KHz, 700 fs) working at 1.65 µm wavelength, taken from [3].

5.5.3 Laser incision in the limbus and sclera

Limbus is the junction between sclera and cornea. Unlike cornea, limbus and sclera are made up of less organized and opaque fibers that strongly scatter light. Moreover, sclera is covered

---

[12] Virginie Garnier-Thibaud ; Service de Microscopie Electronique, Institut de Biologie Intégrative (IFR 83), Université Pierre et Marie Curie

by conjunctiva, a multilayer tissue that protects microbes from entering the eye, and also
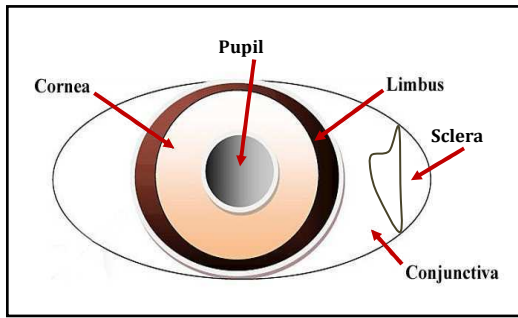
lubricates the eye by producing mucus and tears. Different histological sclera show that the conjunctiva is sometimes dense, sometimes loose, implying that according to its structure, its influence on the beam propagation differs significantly [3]. As a result, in order to perform a laser incision in the limbus (corneosclera junction) and sclera that is sufficiently deep enough to reach the location of the Schlemm's canal, a relatively higher energy is required.

Figure 5.9 shows laser incision performed in the corneal limbus with conjunctiva. The incision was made at two pulse energies 1.1 µJ and 2.2 µJ. We can see that when the laser energy is increased to 2.2 µJ, conjunctiva does not appear to be a problem and the laser cuts almost the whole depth of the limbus in both cases.
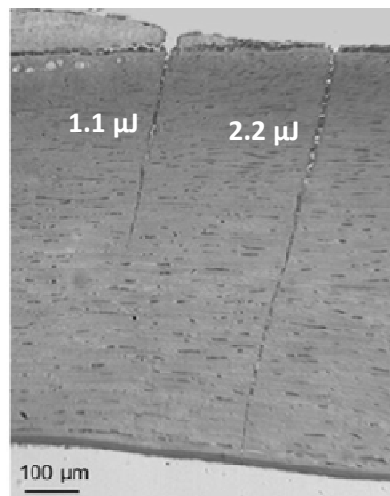
Figure 5.9 Histological section of incisions in the limbus. A laser wavelength at 1592 nm with energy of 1.1 µJ (incision on the left) and 2.2 µJ (incision right) has been used in both cases. Incision is realized under NA of 0.4. Note that when laser energy is 2.2 µJ, the effect of conjunctiva on the incision depth is no more visible [3].

In addition to the presence of conjunctiva, the fibers in sclera relatively less organized than that of corneal limbus. Hence incision in sclera requires even more laser energy. Figure 5.10 shows that to cut the entire depth of sclera, laser energy of up to 7 µJ was required.

Figure 5.10 Incision in sclera carried out by a laser (OPA) with energy of 7 µJ at the wavelength of 1600 nm using Cassegrain objective (NA = 0.28) [3].

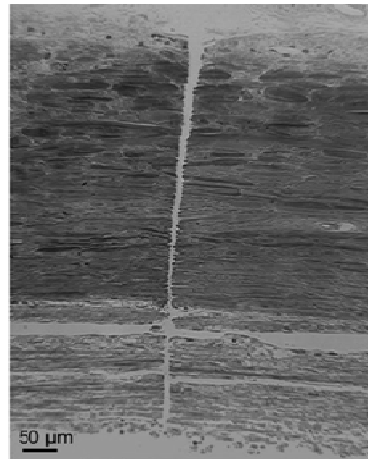Such enhanced incision depths achieved in the limbus and sclera with the optimized laser wavelength of 1650 nm enables us to reach the Schlemm's canal directly from the top surface of the sclera. This result is promising as a new glaucoma treatment method because the current laser treatment of glaucoma (trabeculoplasty: SLT or ALT, see chapter 1) is limited to the use of the clear cornea to send the laser beam to make surgery at the base of the trabecular meshwork (see Figure 5.11).

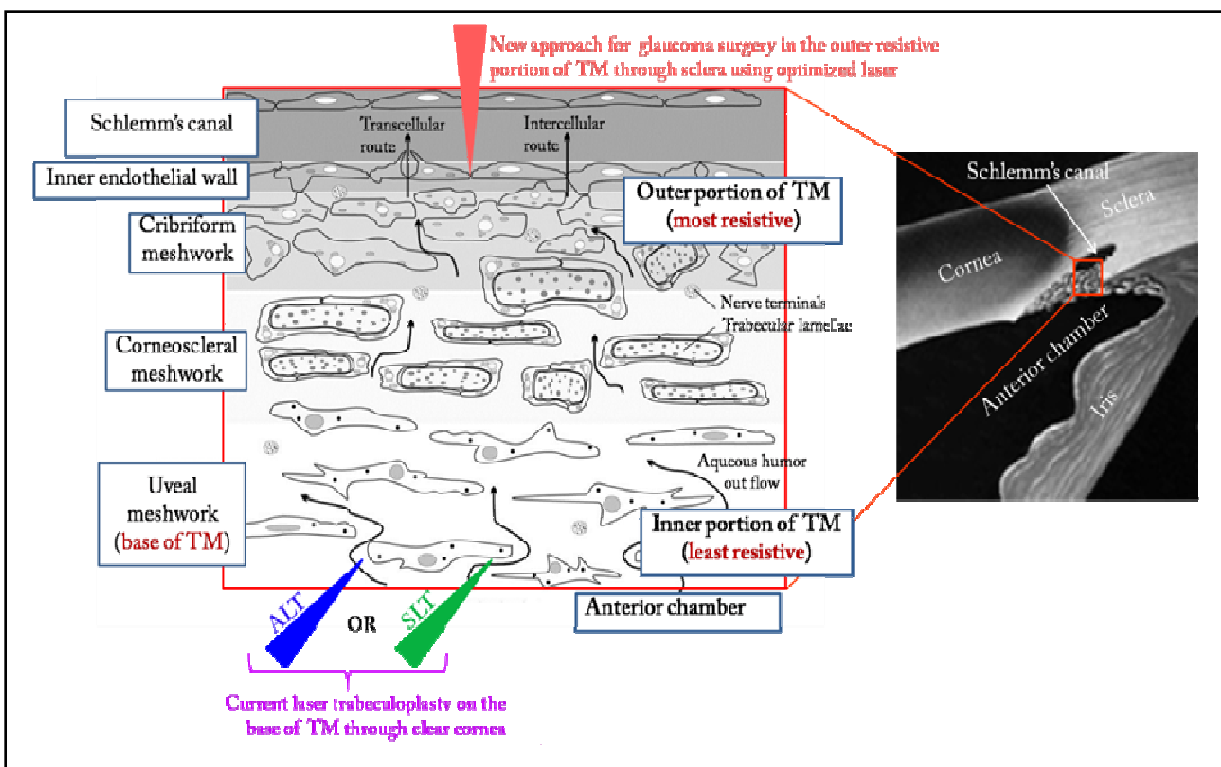**Figure 5.11** Schematic diagram of the current and the proposed methods of laser treatment of glaucoma. Both ALT and SLT use the clear cornea to send the laser beam into the base of the trabecular meshwork to make surgery. The proposed method targets the outer portion of the trabecular meshwork (where resistance to fluid drainage is high) by sending an optimized laser (wavelength at 1650 nm) directly through the sclera.

As we explained in chapter 1, such a method can be inefficient because of two reasons. Firstly, most of the resistance to the drainage of the aqueous humor in glaucomatous eye occurs not at the base of the trabecular meshwork but rather in the outer portion of the trabecular meshwork around the Schlemm's canal. Secondly, the procedure entirely depends on the transparency of the cornea. However glaucoma and corneal edema often co-exist [76] and this will ultimately limit the uses of the conventional trabeculoplasty.

With the optimized laser at 1650 nm, one can send the laser beam directly through the limbus in order to make the surgery at the right place around the Schlemm's canal where there is strong resistance to fluid outflow (see Figure 5.11).

5.6 OCT imaging of laser incisions

Though histology and SEM techniques are very important tools for basic research, they cannot be used for *in-situ* imaging. Once the laser incision procedure is performed, the cornea has to be taken out of the artificial chamber and undergo several post-surgery specimen preparation steps in order to analyze the incisions. The cornea needs to be treated with different solutions and this may take a few days before the sample is ready to be imaged. Moreover, the procedure is highly invasive: the incisied cornea should be cut in thin slices for sectional histology, and a deposition of thin gold layer a few nanometers thick may be required in order to obtain good resolution and good contrast when viewing the incision under the SEM [3].

For clinical application, however, a non-invasive imaging system capable of making *in-situ* imaging of laser incision in real-time would be ideal. Non-invasive cross-sectional imaging of biological tissues with few millimeters of imaging depth and with micrometer resolution is now possible using OCT. With OCT, no post-surgery specimen preparations like dehydration, dissection and staining are required. The incised cornea can be directly imaged with OCT right after the incision while the cornea is still in the artificial chamber.

Figure 5.12 shows a cross-sectional OCT image of a cornea where two laser incisions had been performed. Such lamellar incisions are easy to be viewed with OCT. The OCT image of the incised cornea was performed (in LOA with C. Crotti [3]) right after the laser incision without any sample preparation (the gas bubbles along the incision are visible and even help observation).
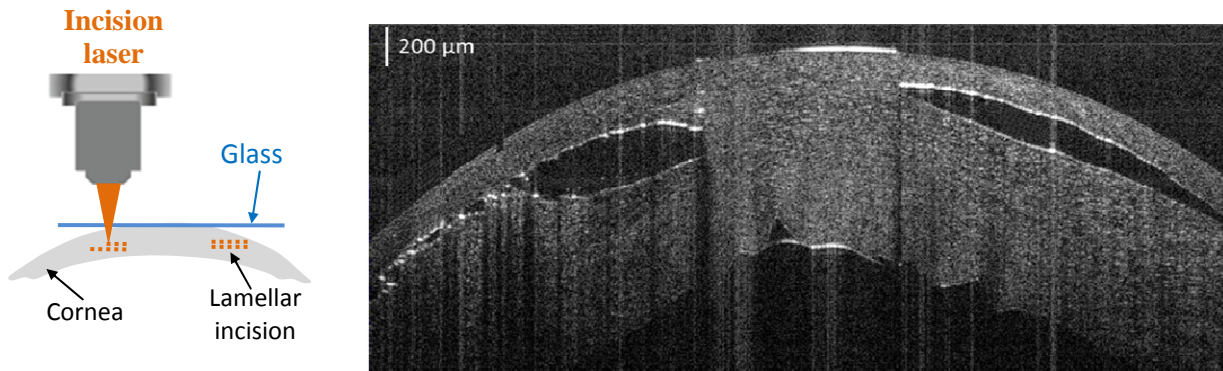
Figure 5.12 OCT image of two lamellar laser incisions in cornea realized by 0.4 NA objective and a laser pulse energy of around 2 µJ.

5.7   Coupling OCT imaging and laser surgery systems

The recent advances in OCT have also brought a dramatic increase in the imaging speed. Today, real-time cross-sectional imaging of tissues can be achieved with OCT. As a preliminary work, we have coupled the SS-OCT imaging system with the laser surgery setup, and have demonstrated the possibility of viewing the evolution of the corneal laser surgery in real-time. I have done this experiment in LOA with C.Crotti from LOA.

The schematic diagram of the coupling of the two systems is shown in Figure 5.13.

Figure 5.13 Schematic diagram of coupling between the OCT imaging and the laser incision systems. A pellicle beamsplitter has been used to minimize dispersion mismatch between two arms of OCT.

The OCT beam at a wavelength of 1.3 µm and the surgery beam optimized at 1.65 µm are superimposed by a very thin beamsplitter, and the two beams are simultaneously sent to the same location on the specimen. Such configuration allows us to image the ongoing laser incision in real-time.
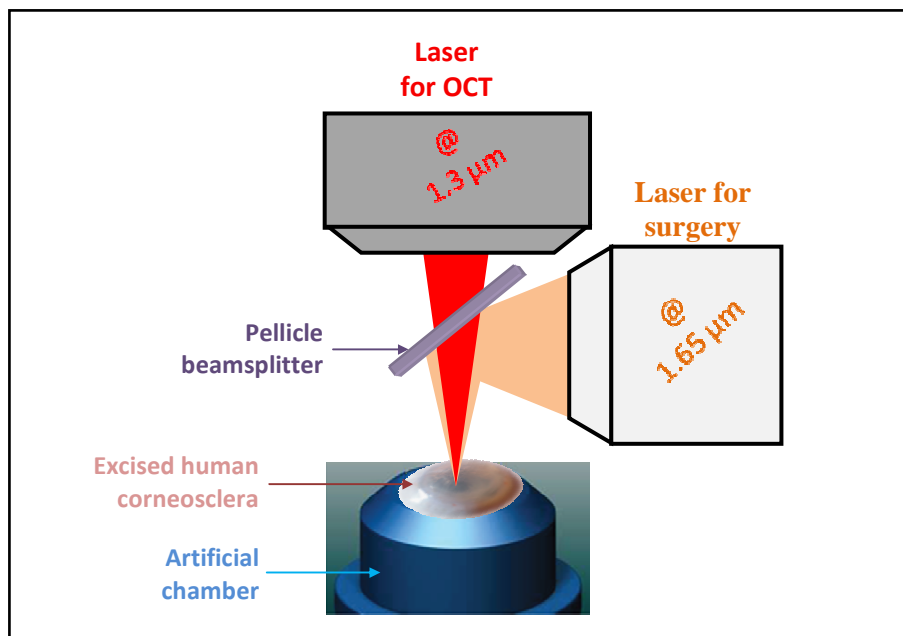
In this specific setup, the laser incision was achieved by the moving the 3-axis automated translating stage. Incisions can also be achieved by scanning the laser beam using galvanometric mirror scanners, just like the OCT beam scanners. However, as the laser incision requires a relatively small beam spot size in the tissue in order to induce the required nonlinear process, a microscope objective with a large pupil diameter is required.

In principle, for any amount of dispersion present in one arm of the OCT interferometer, similar amount of dispersion should be introduced in the other arm to cancel the dispersion mismatch. However, for the commercial OCT system, we do not have access to reference arm to do the compensation. Hence in order to minimize such dispersion mismatch between the two arms of the OCT interferometer, a thin beamsplitter has to be used instead of cubic beamsplitter. In our case, a pellicle beamsplitter (BP245B3, Thorlabs) that reflects 45 % and reflects 55 % has been used. As it is made of an extremely thin and fragile membrane (2 µm – 5 µm), it also eliminates ghosting and chromatic aberration with focused beams. Geometrical aberration and lateral deviation of the focused beam is also negligible.

To demonstrate real-time monitoring of laser surgery in cornea, we have launched the automated incision system from the computer in such a way that five different holes can be made at five different lateral and axial locations as shown in Figure 5.14, (a) and (b).
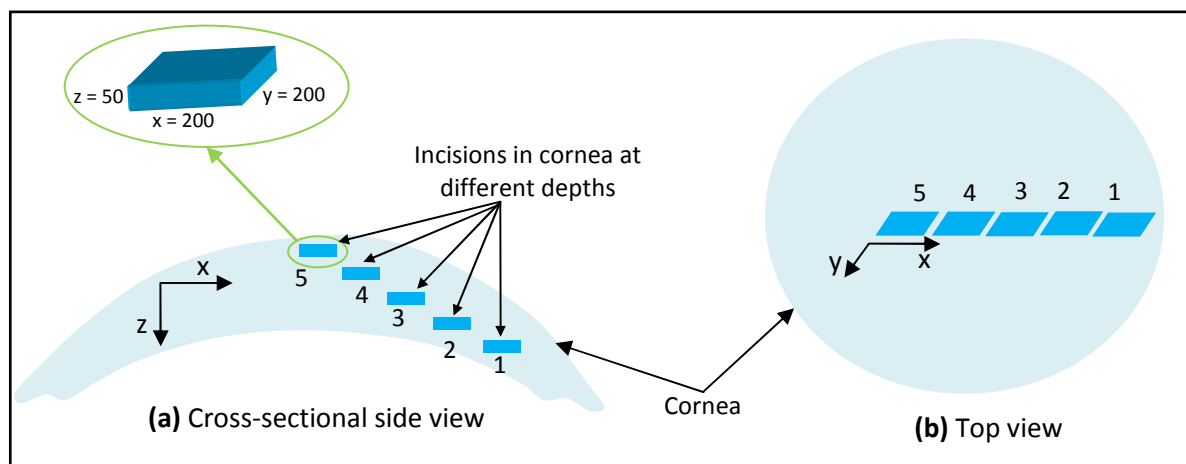

Figure 5.14 Schematic diagram showing the location of each laser incision in cornea from side view **(a)** and top view **(b)**. From bottom to top, the five locations where incision will made are indicated. The size of each incision is $200{\times}200{\times}50$ µm^3.

The size of each incision is approximately $200 \times 200 \times 50$ µm^3. To make a single hole of this size, multiple lamellar incisions are performed at different axial positions (see Figure 5.15, c). The axial separation between each successive lamellar incision was ~ 5 µm (of the order the focused beam spot size). Each lamellar incision was realized by performing multiple x-y line incisions that are close to each other (see Figure 5.15, b). To have a continuous lamellar cut, the separation between each line should also be of the order of the beam spot size. Each line incision was achieved by translating the stage along one direction only (see Figure 5.15, a).
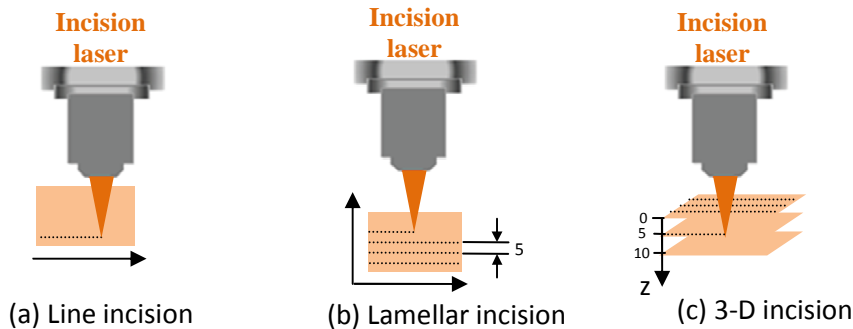

Figure 5.15 Schematic of laser incision configurations, the unit is in µm.

Since the lateral and axial fields of view of the OCT imaging are long enough (5 mm and 3 mm respectively), it was possible to visualize the progress of the laser incisions in real-time. The incision starts with the bottom of the cornea by making the first hole denoted as 1 in Figure 5.16. Then the incision progresses to making the 2nd, 3rd, 4th and 5th holes, respectively.

The OCT imaging system enables us to visualize the evolution of the laser incision in real-time, and the cross-sectional OCT images shown in Figure 5.16 demonstrate that OCT can indeed help monitor the ongoing laser surgery. These images were extracted from a video that was simultaneously recorded while the incision was progressing. The result has been communicated in Photonics Europe 2012 conference [84].

The experimental result demonstrates the possibility of using OCT for monitoring the glaucoma laser surgery - where only few holes are needed to be made around the Schlemm's canal. In the OCT image shown in Figure 5.16, the Schlemm's canal is not visible. One of the main reasons is related to the low axial resolution of this commercial SS-OCT system (12 µm in air) which was used for this proof of concept. Improving the resolution of OCT helps us properly visualize the canal, and that was the motivation for developing a high-resolution SD-OCT. The axial resolution has been improved by nearly a factor of three, from 12 µm to 4 µm (see chapter 4, section 4.3.1.2).
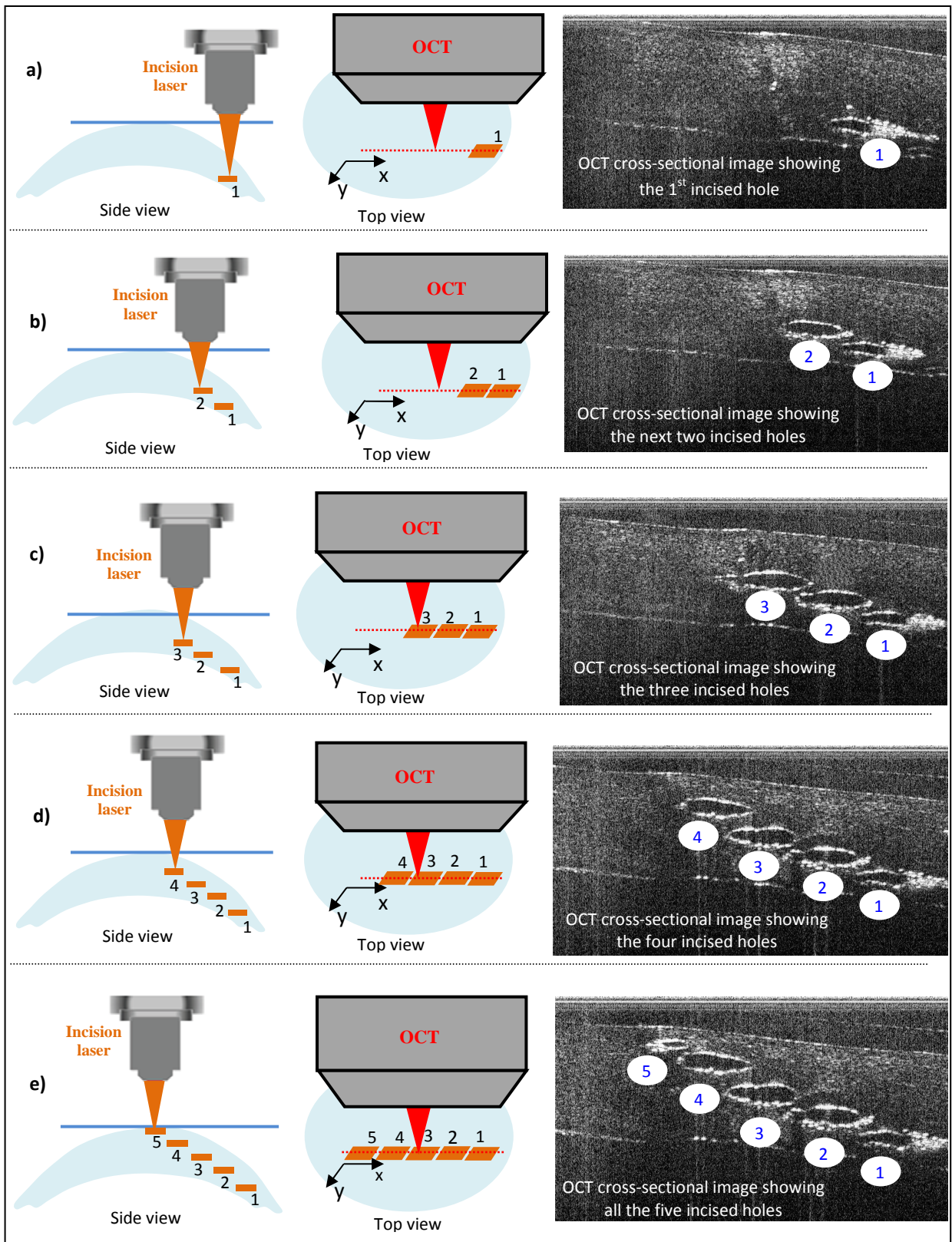
Figure 5.16 Schematic of laser incision configuration and typical cross-sectional OCT images of incision that are saved as the incision progresses from making the first hole (a) to making five holes (e). An automated system controlled from a computer is launched to make these holes at various depths. The result demonstrates the possibility of using OCT for monitoring the glaucoma laser surgery where only few holes are needed to be made around the Schlemm's canal.

5.8 Conclusion

The most important laser parameter that controls the type of laser-tissue interaction mechanism is the laser exposure time (laser pulse duration). The required type of interaction depends on the medical application. For our application where a precise subsurface surgery is required in the corneal limbus, ultrashort pulse lasers in the femtosecond regime have been used because the interaction process with femtosecond lasers occurs on timescales much shorter than those typical for heat conduction or propagation of acoustic shock waves. Such localized interaction enables us to achieve precise incision in tissues with minimum collateral damage. Another important laser parameter worth considering while performing incisions in a non-transparent medium is the laser wavelength. The laser incision results performed on sclera and edematous cornea suggest that the optimal wavelength for achieving high quality and deep incision inside such strongly scattering media is 1650 nm. At this wavelength, the whole thickness of corneal limbus can be incised. Such enhanced incision depth enables us reach Schlemm's to make the glaucoma surgery by sending the laser beam directly from the top surface of the sclera. As femtosecond lasers at this wavelength are not commercially available, nonlinear optical parametric processes (like optical parametric generation - OPG) have been used to up-convert the wavelength of a commercial femtosecond laser.

Once the incision is performed, the next challenge is the analysis of the image result. Though histology and scanning electron images provide a high-resolution images, both methods are limited for research because they require a very intensive, time consuming and highly invasive sample preparation steps (only for *ex-vivo* samples). Moreover, the laser incision is performed based on the predefined incision parameters set from a computer, without having any information about what might go wrong during incision. As far as clinical application is concerned, what would be best is to be able to visualize the laser surgery in real-time while it is progressing. To benefit the potentials of OCT as a non-invasive micrometer cross-sectional imaging technique, we have coupled the OCT imaging system with that of the laser incision system (see Figure 5.13), and we demonstrated imaging of the ongoing laser incision in real-time. We have made five laser incisions at five different depths in cornea and we managed to observe the evolution of the incision (as shown in Figure 5.16). This paves the way to using OCT imaging systems for monitoring the glaucoma laser surgery.

Chapter 6 - Conclusion and perspectives

6.1 Conclusion

Glaucoma and the Schlemm's canal

Glaucoma, an eye disorder characterized by the damage of the optic nerve, is one of the major causes of blindness in the world. Globally, approximately 110 million people are affected (~ 1 million in France) by glaucoma and as many as 6 million individuals are totally blind in both eyes due to this disease. The damage to the optic nerve is mainly caused by an elevation in the IOP due to the accumulation of excess aqueous humor. An increase in IOP happens when the rate of production of the aqueous humor exceeds its rate of removal. This may happen in many ways. However, the most common type of glaucoma, the open-angle glaucoma, occurs when *the conventional (trabecular) pathway* is clogged because this route contributes to the removal of more than 85 % of the aqueous humor. An important circular channel located in the conventional pathway that plays a predominant role in the regulation and stability of IOP is called the Schlemm's canal (SC). As mentioned in chapter 1, the principal site of the aqueous humor outflow resistance in glaucomatous eyes is related to the inner wall of the SC and the outer portion of the trabecular meshwork (TM) around the SC.

Conventional treatment methods and their drawbacks

The globally practiced method of glaucoma treatment involves lowering IOP, either by decreasing its rate of production or increasing its rate of removal. Eyedrops are in most cases the first choice of treatment. Even though the success of medical treatment highly depends on the rigorous monitoring of prescription, the fact that eyedrops are often prescribed to be applied several times a day, and in some cases, for entire life, makes it harder for patients to strictly follow the prescription. Hence, poor compliance with medications and follow-up visits is one major problem related to medication. Affording the price of one's entire life medication is another reason for poor compliance. Eyedrops also have side effects, and some of them may cause adverse consequences and may not be tolerated any more by the patient. Under such circumstances, the patient will be recommended to undergo surgical procedure. For open-angle glaucoma treatments, trabeculectomy is the golden surgical standard. However, because of the complete opening, trabeculectomy has potential risks of complications such as infection, leakage, irritation, hypotony (IOP ≤ 5 mm of Hg), choroidal detachment, scarring

and development of cataract over time. Generally, due to post-surgical complications, such conventional surgical methods of glaucoma treatment have low success rate globally (60%).

Current glaucoma laser treatments and their limitations

The availability of efficient lasers and their ability to make safe surgery has opened a third alternative method of glaucoma treatment. The most widely used laser treatment for open-angle glaucoma is laser trabeculoplasty, where a visible laser beam is sent through the cornea to burn specific areas -the *uveal meshwork* - at the base of the TM (see Figure 5.11). Burning the TM shrinks the collagen, thereby reopening the intertrabecuar spaces and allowing the flow of the aqueous humor. As trabeculoplasty involves burning (with a focal spot diameter that can reach 50 microns), it destroys the tissue and cannot be repeated frequently. The other drawback of this procedure is related to the fact that while most of the resistance to the aqueous outflow is in the outer most portion of TM (i.e., around the SC), trabeculoplasty targets the base of the trabecular meshwork, which does not offer much resistance. Corneal edema is another challenge that may limit the use of visible lasers to do trabeculoplasty to pass through the cornea. Hence, laser trabeculoplasty is inefficient for controlling the IOP in the long run. Generally, the value of trabeculoplasty lies in reducing medical therapy and postponing undergoing a surgical procedure.

New approach for the glaucoma laser treatment

A better approach for laser treatment of open-angle glaucomas would require the delivery of surgery laser to the outer portion of the TM around the Schlemm's canal, directly through the sclera. This would help perform the laser cut in the region where surgery is required. However, as sclera strongly scatters visible and near-infrared light, it is not possible to penetrate deep enough to reach the Schlemm's canal that is located at ~ 0.8 mm depth in the corneoscleral junction of the limbus using the conventional laser sources. One of the solutions to reduce scattering is to increase the wavelength of the surgery laser. For this reason, an optimized femtosecond laser source emitting at 1650 nm has been developed in LOA-ENSTA under the framework of the NOUGAT project. Laser incisions performed in human sclera and edematous cornea have shown that the laser at 1650 nm indeed helps enhance the incision depth.

A high-resolution non-invasive imaging system capable of resolving the Schlemm's canal is required in order to monitor the laser surgery that needs to be performed in the area of the Schlemm's canal. As OCT can perform cross-sectional imaging of biological tissues in real-

time with spatial resolution of a few micrometers and imaging depth of a few milimeters, this imaging technique was our choice for this purpose.

Development of OCT

Comparing OCT with other imaging systems, we can see that OCT fills the gap between ultrasound imaging (~ 150 µm resolution and few centimeters penetration) and confocal microscopy (~ 1 µm resolution and few hundreds of micrometers penetration). OCT can be used for *in-situ* and *in-vivo* imaging because it does not require sample preparation. As OCT is based on low-coherence interferometry, it exploits the temporal coherence property of light to perform high-resolution tomographic imaging. The axial resolution of OCT is determined by the coherence length of the light source: the broader the spectrum of the light source, the better the axial imaging resolution. The transverse imaging resolution of OCT, like any other scanning microscopes, is determined by the size of the focused beam spot on the sample.

Among the different OCT modalities, we have developed and utilized Fourier domain OCT (FD-OCT). The reason of our choice was because FD-OCT is faster and more sensitive than time-domain OCT (TD-OCT). FD-OCT itself can be realized either using a swept laser source (swept-source OCT, SS-OCT) or using a spectrometer (spectral-domain OCT, SD-OCT). For our project, we investigated both SS-OCT and SD-OCT. At the beginning of the project, a commercially available SS-OCT (OCS1300SS, Thorlabs) working at 1.3 µm center wavelength has been used to image the Schlemm's canal. Because of its low-axial resolution (12 µm in air), this SS-OCT system could not properly resolve the Schlemm's canal. The center wavelength of 1.3 µm has been chosen in order to reduce light attenuation due to scattering within biological tissues. However, because of the $\lambda^2/\Delta\lambda$ dependence of the axial resolution, high-resolution OCT imaging at 1.3 µm center wavelength requires a light source with extremely broad bandwidth. Finding a broadband tunable laser source is indeed a technological challenge of developing high-resolution SS-OCT at the center wavelength of 1.3 µm. High-resolution SD-OCT at 1.3 µm seemed to be easier to achieve since this technology does not require a tunable laser source. However, developing a high-resolution SD-OCT system requires designing a broadband spectrometer.

During this PhD work, we have developed an ultrahigh-resolution SD-OCT working at 1.3 µm center wavelength [54]. By combining two spectrally shifted SLDs, an axial resolution of ~ 4 µm (in air) was reached, which was the best resolution ever achieved with SD-OCT at this wavelength. The imaging system has a transverse resolution of 6.5 µm. The sensitivity

and the maximum line rate are 95 dB and 46 kHz respectively. Comparing our SD-OCT with the commercial SS-OCT system working at the same wavelength, we have improved the axial resolution by a factor of three and the transverse resolution by nearly a factor of four.

A numerical method of spectral calibration has been used to improve the detection sensitivity fall-off and the degradation of the axial resolution as the imaging depth increases. A detection sensitivity of 95 dB at the sample surface and 82 dB at a depth of ~ 1.8 mm was measured. We have demonstrated the possibility to produce high-resolution images of human cornea. The Schlemm's canal was properly imaged for the first time.

As our system was not fast enough for video rate imaging, the commercial SS-OCT system has been used to demonstrate the capability of OCT to monitor the laser incision in real-time. To achieve this, the OCT system and the laser incision system have been coupled together using a very thin beamsplitter (as shown in Figure 5.13). Using the incision laser, we made five separate holes at five different depths in a human cornea, *in-vitro*, and at the same time, we managed to observe the evolution of the laser incision in real-time using OCT. We believe that this demonstration paves the way to using OCT imaging systems for monitoring the glaucoma laser surgery.

6.2   Perspectives

The SD-OCT system developed during this PhD uses a standard personal computer (HP workstation, 2GH processor, 2GB RAM). As image processing is the main time consuming step of SD-OCT, a video rate imaging speed is not possible at the moment. But the performance of the system could be significantly enhanced by using a more powerful computer. Optimizing the signal processing algorithm would also improve the processing speed. A new camera that is twice faster than the one we have is also now commercially available. With these improvements, video rate imaging should then be possible.

In chapter 5, section 5.7, we have presented the coupling of the commercial SS-OCT system with the laser incision system. We have placed a pellicle beamsplitter in the sample arm of the interferometer in order to couple the two systems. This configuration requires enough space between the objective and the sample to accommodate the beamsplitter. As a result, only low NA objectives having a long working distance can be used. This was possible with the SS-OCT because it uses a low NA objective (LSM32, Thorlabs) with a working distance of 25 mm. For the same reason, a low NA objective was used for the incision setup. Moreover,

in this configuration, half of the OCT signal coming back from the sample was also lost at the pellicle beamsplitter.

For the SD-OCT developed in the laboratory, an objective (LSM02, Thorlabs) with higher NA was used to improve the transverse resolution. As a consequence, the working distance was only 7.5 mm. In this small space, putting a beamsplitter was not possible. So as a perspective, we propose to couple the incision laser with the SD-OCT system at the output of the SD-OCT interferometer using a dichroic mirror (DMSP1500, Thorlabs) that passes the short wavelength OCT beam and reflects the long wavelength incision beam (see Figure 6.1).
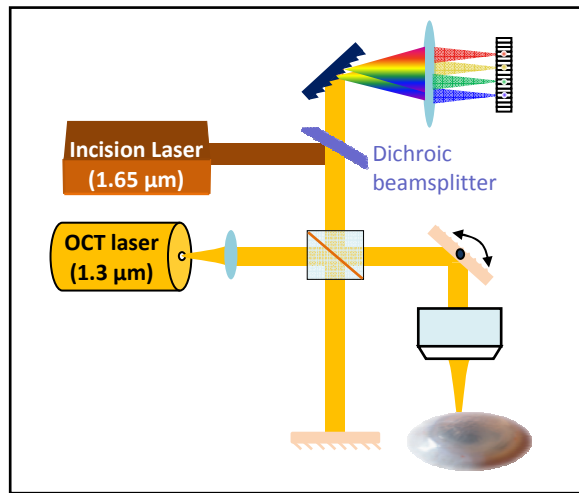
Figure 6.1 Schematic of coupling the laser surgery system with the high-resolution SD-OCT system.

A schematic of the prototype, with the surgical laser coupled to the high-resolution SD-OCT system, is shown in Figure 6. 2.
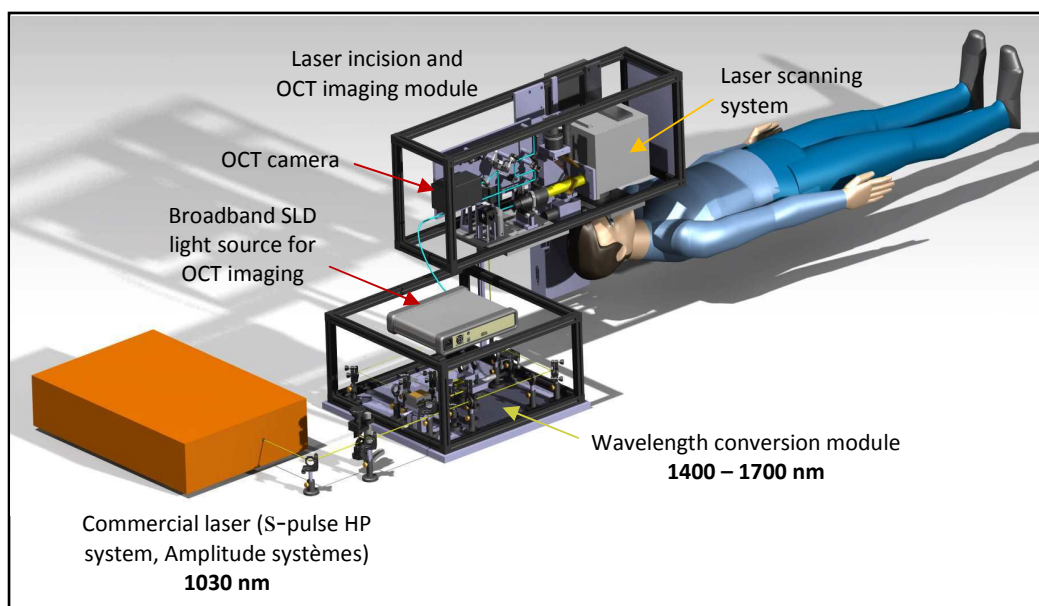
Figure 6. 2 Coupling prototype, light blue is the OCT beam and dark yellow is the surgery beam.

This modular approach of coupling the two systems reduces the overall size of the surgery tool and makes it convenient for clinical environment. With some more work to be done on the laser scanning system, in addition to the OCT imaging speed, such a system could become a powerful tool of great help in ophthalmology for the laser treatment of glaucoma.

Appendix - Optical imaging in attenuating media

Driven by the current need in optical biopsy, creating digital volumetric model of an object using optical tomography techniques becomes an active field of research in biomedical imaging. Turbid media like biological tissues attenuate light and put a fundamental limit on the maximum optical imaging depth that can be reached. In this appendix, the concept of light attenuation due to absorption and scattering, and its impact on the imaging depth in biological tissues are discussed. Various techniques for enhancing the imaging depth such as time-gating, spatial-gating and coherence-gating are presented. Optical coherence tomography is based on the coherence-gating technique.

A.1 Introduction

Since its birth in the late 16th century, optical (light) microscopy has played a major role to the discovery of worlds within worlds and has opened new doors to the understanding of biological tissues and materials down to sub-micron levels [92]. Today, the optical microscope becomes a standard medical tool and can be found in most (if not all) health institutions. While conventional light microscope is a powerful method to look at small objects on or very close to the top surface of samples with high (submicron) spatial resolution, its ability to achieve clear images of objects hidden inside or behind strongly scattering random media like biological tissues is limited. As a result, when some need arises to make optical tomography in order to look inside a living subject and examine, for instance, the presence of a disease, medical removal of tissues from the living subject (biopsy) becomes necessary. For example, when a cancer in human breast is suspected, the medical doctor may recommend performing biopsy from the suspected zone of the breast for further breast cancer diagnosis. Then the excised breast tissue is sliced into thin layers in order to examine it under a microscope. Hence cross-sectional tissue imaging by a conventional microscope is highly invasive and involves intensive sample preparation.

A biopsy destroys the site under study, and leaves a scar. Sometimes the best area to biopsy is difficult to ascertain. In clinical settings, the procedure can be time consuming and expensive because if biopsies are performed at incorrect sites, they must be repeated, for which patients must return to the clinic.

Moreover such *ex vivo* examinations of tissues could sometimes lead to over-interpretations and erroneous conclusions that may not match with the reality. In certain surgical settings, such as for Moh's procedure[13] for basal cell carcinomas, histology of excised tissue slices, to determine tumor margins, is performed in the operating room to guide the surgery. Typically, two to four slices are removed, and there is a waiting time for the surgeon of 15–45 min for each slice while it is being histologically processed [93].

Despite of its drawbacks, biopsy is still a widely used procedure in hospitals for diagnosis and treatment of several kinds of diseases. However, sometimes it may not be practical (if not impossible) to do biopsy for diagnosis of tissues located in the most sensitive organs like the eye, heart, brain, etc. In such circumstances, the ideal solution would be to have a high-resolution non-invasive cross-sectional imaging device that can image deep inside living organs without doing biopsy so that tissues can be examined while they are functioning (*in vivo*) in their own natural location (*in situ*). If light is employed to look at the inside part of tissues non-invasively, such technique is termed as optical biopsy.

Optical biopsy allows to make optical slicing or sectioning of tissues in any angle and examine the inside part of tissues from different directions non-invasively. Indeed, to do so, optical biopsy inevitably requires image acquisition through significant depths of biological tissues. Following the invention of the lasers in the 1960s, various techniques of extending the depth of optical imaging inside a scattering medium have been developed. Invented in the early 1990s, OCT is one of such techniques that can be used to acquire cross-sectional images of biological tissues [22]. Other high-resolution techniques include confocal microscopy, and non-linear microscopy.

A.2 Challenges of optical imaging in attenuating media

The development of high-resolution optical imaging techniques with significant imaging depth remains to be a major scientific challenge mainly due to attenuation and complex interaction of light with tissues. While functional biomedical imaging makes use of this light-tissue interaction, the strong attenuation of light due to absorption and scattering by various bulk tissue components has historically restricted optical imaging to thin histological tissue sections or to superficial tissues [94].

---

[13] Moh's procedure, created by a general surgeon Dr. Frederic Mohs, is a microscopically controlled surgery used to treat common types of skin cancer.

A.2.1 Absorption

Absorption of light by biological tissues extinguishes light and limits the maximum depth at which optical imaging can be done. The intensity of incident light I_o decays exponentially as it travels through the tissues. In general, the intensity of light I_t transmitted after it travels a distance l inside an absorbing medium with absorption coefficient μ_a is given by the Beer-Lambert law

$$I_t = I_o e^{-\mu_a l} .$$ A. 1

The inverse of the absorption coefficient (called absorption length) represents the mean distance that a photon can travel in the medium before it is absorbed. In other words it refers to the penetration depth.

In biological tissues, light absorbing is mainly dominated by the presence of water, melanin and hemoglobin (HbO_2) (see Figure A.1).
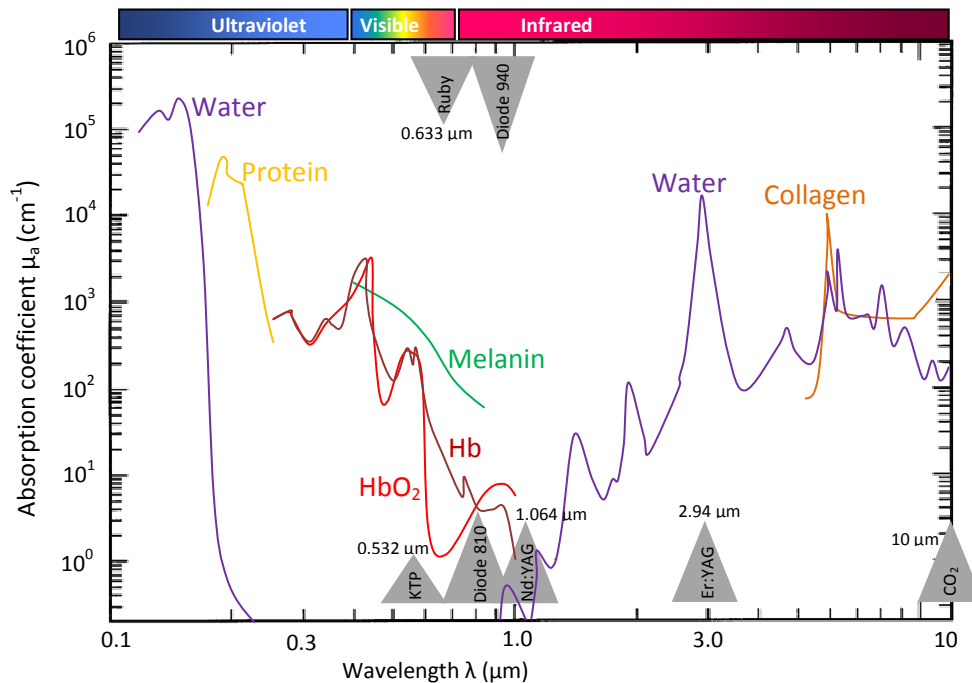
Figure A.1 Optical absorption coefficients of principal tissue components in the 0.1-12 µm spectral region (adapted from [43])

Looking at the absorption spectra shown in Figure A.1, tissue absorption is apparently low in the near infrared (NIR) from 650 nm to 1400 nm. Hence, to minimize light absorption by tissues and increase the imaging depth, most biomedical imaging techniques work in this optical window. The absorption coefficient μ_a in this window is relatively minimum and varies roughly between 0.1 – 1.0 mm^{-1} [44]. And the corresponding absorption length of a

photon will be of the order of few millimeters. One of the challenges of biomedical imaging research in the past was indeed the availability of NIR light sources that match this window. Today, owing to the advent of compact and convenient semiconductor and solid-state NIR laser technologies (see Figure A.1), biomedical optics becomes a very active research field and several optical techniques are moving from research laboratories to clinical applications.

A.2.2 Scattering

In general, diffraction-limited image resolution is achieved by the use of unscattered (or ballistic) light. When light travels through turbid medium, it experiences significant scattering and the intensity of the unscattered light decays exponentially as a function of the propagation distance. Scattering tends to destroy the localization of light and is the main factor that severely affects the quality and depth of imaging in turbid media. The problem of scattering while imaging an object in turbid media such as biological tissues is illustrated in Figure A.2.
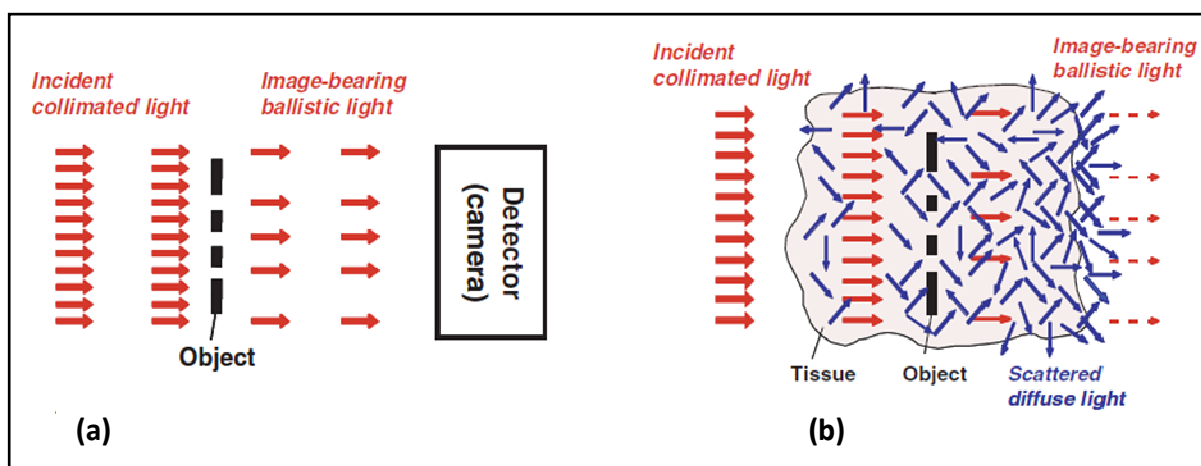
Figure A.2 (a) shows imaging in a non scattering medium and (b) illustrates how imaging performance is impacted when the object is located in a scattering medium such as biological tissue (taken from [94])

Figure A.2 (a) shows a conventional imaging configuration of an object with no scattering medium. Here the photons travel in straight lines and their intensity distribution is modified by the object and recorded by the detector such as a CCD camera. Figure A.2 shows how the situation is changed when the object is embedded in a scattering medium. In such condition, most photons undergo multiple scattering and only few photons will manage to travel straight. Such unscattered photons are called ballistic photons. The number of ballistic photons decreases exponentially with the propagation distance in the scattering medium.

In general, if I_o is the intensity of the incident light, the intensity of light I_t that is transmitted without scattering after it travels a distance l in a scattering medium with a given scattering coefficient μ_s is given by

$$I_t = I_o e^{(-\mu_s l)}.$$ <div align="right">A.2</div>

The inverse of scattering coefficient μ_s is called the scattering mean free path (MFP). It represents the mean distance a photon propagates in the medium before it is scattered. The MFP for typical biological tissue (e.g. breast tissue) is of the order of $100\,\mu$m. It means that for every additional $100\,\mu$m that the light travels in the medium, the transmitted ballistic component is attenuated by 1/e due to scattering. This exponential decay with propagation distance in the sample implies that imaging using ballistic light may be performed only through relatively thin samples (few millimeters). In comparison, the scattering MFP of X-ray photons in biological tissue is ~ 5 cm. Hence X-ray photons are only weakly scattered by biological tissue and can penetrate much deeper than NIR light in the body [95, 96].

Combining the effects of absorption (equation A.1) and scattering (equation A.2), the actual depth that can be reached by ballistic imaging depends on the total attenuation coefficient of the medium, the intensity of incident light and the quality of the detector. In the case of a detector with perfect quantum efficiency, the limit to the ballistic imaging depth is that the level of ballistic signal must be detectable above the quantum shot-noise limit. Assuming a signal-to-noise ratio (SNR) of one, the theoretical ballistic imaging depth L_b is given by [97]

$$L_b = \frac{1}{\mu_t} \ln\left(\frac{1}{2} \frac{E}{h\nu} \right),$$ <div align="right">A. 3</div>

where $\mu_t = \mu_s + \mu_a$ is total attenuation coefficient due to scattering and absorption, E the optical energy delivered to the sample per spatial resolution element and $h\nu$ the photon energy. From equation (A.3), one can see that increasing the illuminating optical power, the acquisition time, and the number of averages can affect the maximum ballistic imaging depth in a logarithmic fashion and do not therefore change the fundamental limit appreciably. Moreover, the maximum intensity that can be delivered to a biological sample is limited by the tissue optical damage threshold. Based on the ANSI Z136 (American National Standards Institute, 1986) laser safety standard on human skin, Hee *et al* [97] used the maximum permissible optical intensity around 800 nm wavelength and estimated that the maximum ballistic imaging depth L_b below which the ballistic signal falls bellow shot noise level is approximately 36 MFP. For biological tissues such as breast tissue having a scattering MFP

of the order of 100 µm, the ballistic imaging depth is inherently limited to ~ 4 mm. If we work on reflection mode, considering round-trip scattering, the effective depth of ballistic imaging in such biological tissues will be limited to 2 mm. This shows that for many practical thicknesses of biological tissue that we would like to image, the ballistic signal will fall below the detection limit (shot noise) and all the detected photons will have been scattered.

However, one is helped by the fact that most scattering media, including biological tissue, are highly forward scattering. This means that a large fraction of the scattered photons will only be slightly deviated from their original direction upon each scattering event and follow snake-like path as shown in Figure A.3. As a consequence, for scattering depths at which there is effectively no ballistic light, there may be a significant number of photons that have been only slightly deviated from the ballistic direction. Hence when ballistic signal gets weaker than the noise level, detecting snake-like photons can extend the imaging depth at the expense of image resolution.
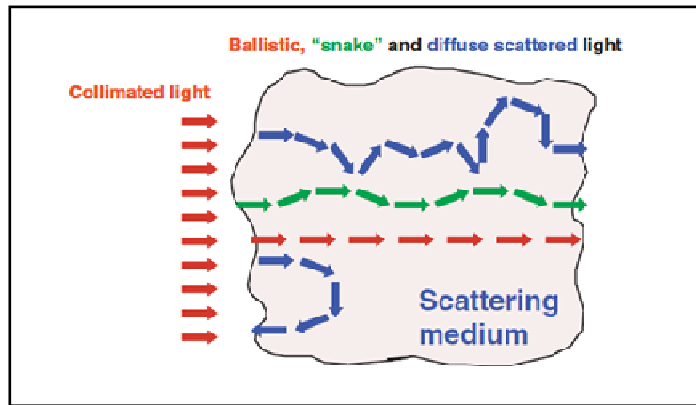
Figure A.3 Illustration of ballistic (red), snake-like (green) and scattered (blue) photons. For practical tissue imaging depth, ballistic imaging alone may not be sufficient and one will have to sacrifice resolution in order to increase the imaging depth by detecting the weakly scattered snake-like photons (taken from [94]).

The weakly scattered snake-like signal itself decays exponentially according to the following equation:

$$I_t = I_o e^{(-\mu_s' l)} ,$$
A. 4

where $\mu_s' = \mu_s (1-g)$ is the transport scattering g is anisotropy of scattering and its inverse is the transport scattering length. For biological tissues, g ~ 0.9. This implies that the scattering coefficient of snake-like photons is 10 times lower than that of ballistic photons. According to equation A.4, this means that the signal from snake-like photons in biological tissues can be detected up to a depth of 360 MFP, which corresponds to a thickness of ~ 4 cm in tissue.

In comparison, if the medium is less scattering, ballistic imaging alone allows to significantly increase the imaging depth. For example, for a coastal seawater with MFP ~ 2 m [97], the corresponding ballistic imaging can reach 80 m. Moreover, when working with such medium, the constraints on maximum permissible incident intensity will greatly be relaxed compared to biological tissues and so the maximum ballistic imaging depth can be increased according to equation A.4.

In contrast, for a significant imaging depth, the strong scattering coefficient of biological tissues decreases the number of ballistic photons that are available for detection. The ballistic photons will therefore be masked by the multiply scattered photons which will saturate the detector and obscure the image. In order to discriminate ballistic photons from the multiply scattered photons and enhance the quality and depth of optical imaging, various techniques are available.

A.3 Techniques for optical imaging in scattering media

The current drive towards the need of optical biopsy and functional imaging has led many researchers to develop various techniques for *in vivo* and *in situ* high-resolution imaging inside scattering media. In order to reject all or some of the scattered light and improve the quality of optical tomographic imaging in a scattering medium, a number of techniques are available: time-gating, spatial-gating and coherence-gating. Optical coherence tomography (OCT) as the name indicates hence uses the coherence property of light to reject the highly scattered photons coming from unwanted regions in the tissue in order to make tomographic images.

A.3.1 Time-gating

When we send a short pulse collimated light to a scattering medium, different types of photon trajectories are possible: *ballistic, snake-like and diffuse* paths (see Figure A.4). And if we look at the time-of-arrival of photons on a detector located on the other side of the medium (transmission mode), ballistic photons take the shortest path and are the ones that arrive at the detector first. Weakly scattered snake-like photons and multiply scattered diffuse photons will arrive later respectively. As a result, the incident short pulse light is modified by propagation through the scattering medium. If we observe the total envelope of the distribution of transmitted photon arrival times, it gives us the temporal point spread function (TPSF), which typically extends over several nanoseconds.
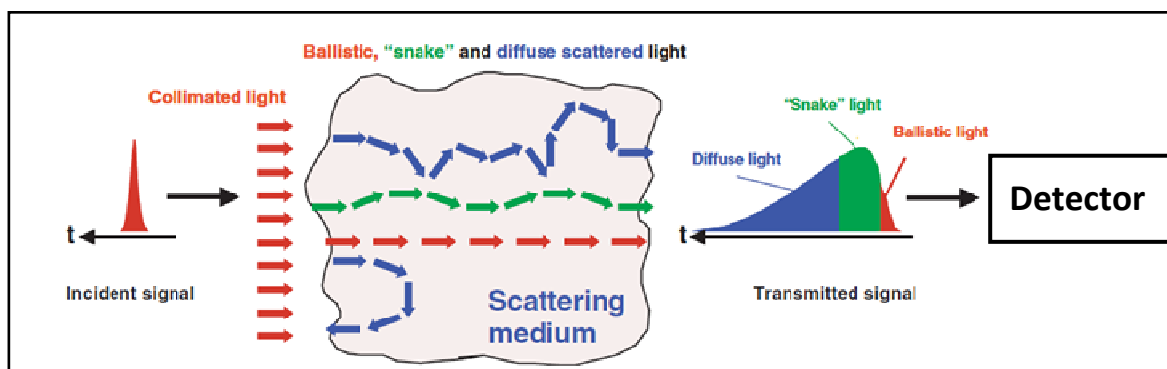
Figure A.4 Schematic of temporal point spread function (TPSF) observed when a light pulse is modified by propagation through a scattering medium (taken from [94]).

Time-gating techniques for imaging in scattering media use the concept time-of-flight of photons to be able to discriminate early arriving photons from those photons which arrive late. Time-gating may be realized using fast electronic instrumentation, such as streak camera[14] [98] and gated optical image intensifier (GOI)[15] [99]. However, the typical depth resolution that can be achieved using such electronic time-gating is still very low. For example, a time-gating as short as 100 ps will correspond to a depth resolution of 1.5 cm in air. In order to use the time-gating approach to realize three dimensional imaging with micrometer resolution, one requires a temporal discrimination (resolution) faster than 100 fs. Unfortunately, such a high-resolution time discrimination is beyond the detection limit of electronics and direct electronic realization of time-gating imaging that requires micrometer resolution is impossible. However a better temporal discrimination (than possible with direct detection) can for example be achieved by intensity-dependent nonlinear optical time-gating techniques based on harmonic generation [100, 101], stimulated Raman scattering [102, 103], parametric amplification [104-107] and the Kerr effect [108, 109].

A.3.2 Spatial-gating

When a photon is scattered, it deflects from its original direction of propagation. Hence if one illuminates a scattering medium with a collimated light beam, most scattered photons will deviate to new propagation directions corresponding to higher spatial frequencies. By putting a collimating grid in front of a detector (see Figure A.5, a), one can discriminate collinear ballistic photons which travel in parallel to the direction of the incidence beam from the non-collinear multiply scattered photons.

---

[14] A streak camera is an ultra-high speed detector which captures light emission phenomena occurring in extremely short time periods.

[15] GOI is a microchannel plate intensifier that may be rapidly switched ON and OFF, effectively providing a fast shutter with an exposure time as short as 70 ps.
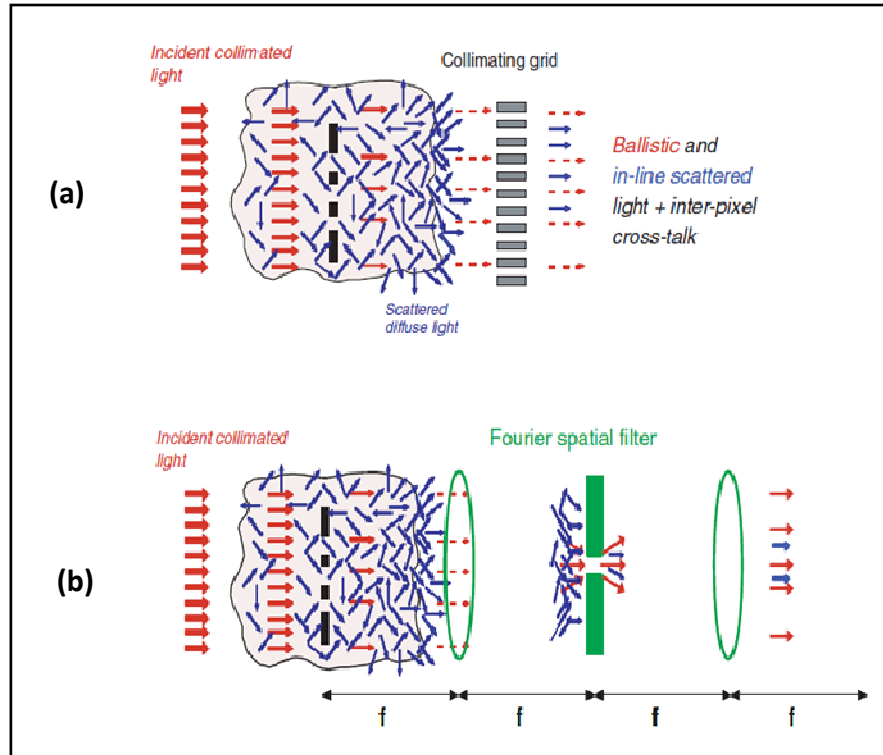
Figure A.5 Wide-field spatial filtering by **(a)** collimating grid and **(b)** Fourier plane spatial filter, taken from [94].

For optical imaging, a more practical approach to this technique will be rather to put a spatial filter in the Fourier plane (see Figure A.5, b). This simple technique is effective to image shallow depths up to 5 MFP (10 MFP in the round trip) in reflection mode and even deeper in transmission mode [94]. However, the use of a spatial filter in a wide-field imaging system will increasingly limit the achievable spatial resolution of the image. Another limitation of spatial filtering in wide-field imaging through strongly scattering media is cross-talk. Many multiply scattered photos may eventually appear parallel to the incident direction causing both axial cross-talk and inter-pixel cross-talk.

Confocal microscopy is the limit of wide-field imaging where inter-pixel cross-talk is eliminated by acquiring image pixels sequentially. A confocal microscopy therefore uses a spatial-gating method in order to improve the detrimental effects of scattered light. It is a point-by-point imaging technique (see Figure A.6) which involves two dimensional scanning to record an image. It can be employed either in reflection mode or transmission mode. Confocal microscopes offer superior resolution compared to conventional whole-field microscopes, particularly in the longitudinal direction [94].
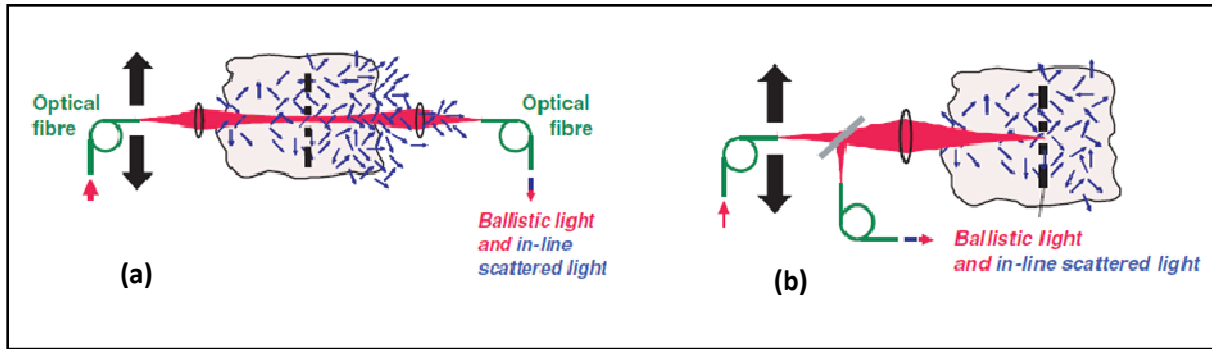
Figure A.6 Sequential pixel acquisition trough turbid media using confocal scanning microscope in (a) transmission and (b) reflection (taken from [94]).

When used in reflection mode, confocal microscopy provides a three dimensional imaging facility that has become the instrument of choice for imaging objects embedded in semi-transparent medium. It has been applied to imaging strongly scattering biological tissues (such as human skin and oral Mucosa) *in vivo* [110]. Thanks to the highly effective filter of confocal microscopy, images with reasonably high longitudinal resolution have been obtained with the imaging ranging from $300\,\mu\text{m}$ to $500\,\mu\text{m}$, depending on the type of the tissue. Though inter-pixel cross-talk is eliminated by imaging a point at a time, confocal microscopy with high numerical aperture (NA) still suffers from longitudinal pixel cross-talk that ultimately limits its imaging depth.

The use of nonlinear confocal microscopy (for which the signal is proportional to the square or cube of the incident intensity at the focal volume) can increase the imaging depth even further. In biomedical imaging, confocal microscopy can also be combined with fluorescence imaging techniques. Multi-photon microscopy, which records the fluorescence signal arising from the intensity dependent two [111]1 or three [112] photon absorption has been shown to provide increased penetration into scattering media. This increase in penetration is partly due to the use of longer excitation wavelength, which is less attenuated in biological tissues. The other reason is that nonlinear excitation provides effective point-source localization and only fluorescence light is collected, hence scattered excitation light does not produce cross-talk. However the attenuation of the excitation light itself is still a problem and this technique is also restricted to fluorescent samples.

A.3.3 Coherence-gating

As light scatters, it loses its coherence properties. Hence one can use the concept of optical heterodyne detection (mixing of reference beam with signal beam at a light detector) to

discriminate ballistic photons from scattered photons. In coherence-gating technique, one uses a light source with low temporal coherence to illuminate an object in a scattering medium, and the optical signal coming from the sample is mixed with a reference light at the light detector (e.g. photodiode) – low-coherence interferometry (see Figure A.7). Ballistic light remains coherence and interferes with the reference light whereas multiply scattered light from unwanted region of the sample can become effectively incoherent and will no more interfere with reference light. Hence by employing low-coherence interferometry, one can discriminate coherent ballistic photons from the unwanted multiply scattered incoherent photons using the concept of coherence-gating.
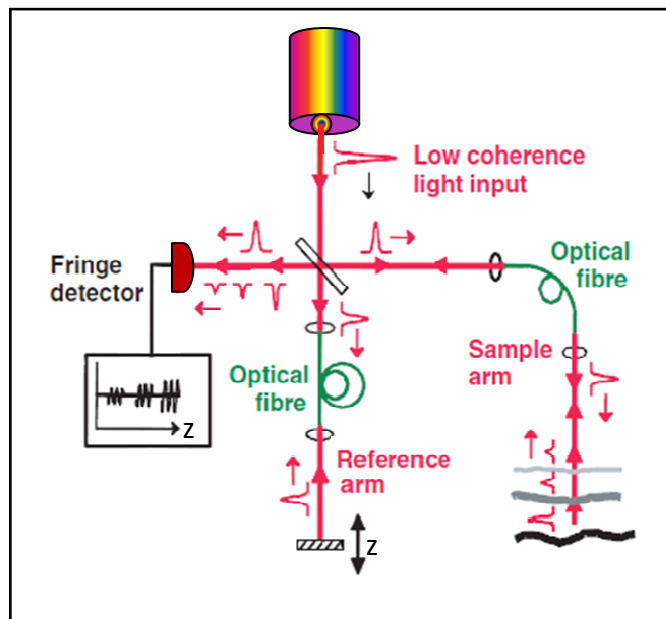
Figure A.7 Low-coherence interferometry

The selectivity of low-coherence interferometry in rejecting scattered photon from unwanted regions depends on the coherence length L_c of the light source that is used for imaging. Coherence length refers to the propagation length from a coherence source to a point where the light wave maintains a specified degree of coherence. The significance of coherence length is that interference will be strong only within the coherence length of the source. As a result any photon that is collected from outside coherence length will not participate in the interference process and will eventually be discriminated and can easily be removed later as background signal by simple arithmetic process such as subtraction. The coherence length of a light source is inversely proportional to its spectral bandwidth and is given by:

$$L_c = \frac{4\ln 2}{\pi n} \times \frac{\lambda_o^{\,2}}{\Delta\lambda},$$

<div align="right">A. 5</div>

where λ_o is the centre wavelength of the source spectrum, n the refractive index of the medium and $\Delta\lambda$ the spectral width given by the full-width-at-half maximum (FWHM). If the source has a Gaussian spectrum, then a path offset of $\pm L_c/2$ will reduce the fringe visibility to 50%.

If a light source with short L_c is used for imaging a sample in such a way that L_c is short compared to the scattering MFP of the medium, the path offset of any multiply scattered photon will exceed the coherence length and will not be able to interfere. Hence the shorter the coherence length, the more selective the discrimination of ballistic photons against scattered photons.

Apart from effectively discriminating ballistic photons against scattered photons, low-coherence interferometry also provides a high-resolution ranging capability when used in reflection mode. The imaging depth is given by the time-of-flight of the detected photons and the depth (axial) resolution is determined by half of the coherence length. OCT uses the principle of low-coherence interferometry combined with transverse scanning to perform optical imaging at micrometric resolution with few millimeters of imaging depth [22].

Implementing low-coherence interferometry in a confocal microscope configuration provides a high-resolution three-dimensional imaging capability with a very strong discrimination capability against scattered light. Such technique is called optical coherence microscopy (OCM). In OCM, 2-dimensional *en face* scans (in the plane normal to the beam axis) are performed using a pair of galvo scanning mirrors. After each *en face* scan, the depth is incremented by moving the focusing lens while the position of the reference mirror is adjusted to keep the equal path length position of the OCM interferometer coincident with the beam waist [113]. This procedure maintains the same transverse resolution throughout depth of the image. The complex 3-D scanning is the main drawback of OCM for fast imaging applications.

References

[1]   K. Plamann, F. Aptel, C. L. Arnold *et al.*, "Ultrashort pulse laser surgery of the cornea and the sclera," *J. Opt.,* vol. 12, no. 8, 2010.

[2]   "Anatomy of the Human Eye," *http://www.mastereyeassociates.com/eye-anatomy-eye-problems*, 2012.

[3]   C. Crotti, "Chirurgie du segment antérieur de l'oeil et traitement du glaucome assistés par laser femtoseconde et imagerie de tomographie par cohérence optique, PhD dissertation," Laboratoire d'Optique Appliquée, ENSTA ParisTech - École Polytechnique, http://hal-ensta.archives-ouvertes.fr, 2011.

[4]   "Clinical optics and refraction," *http://www.eyeweb.org/optics.htm*, 2012.

[5]   I. S. Solomon, "Aqueous humor dynamics," *The New York Eye and Ear Infirmacy*, 2002.

[6]   "Eyecare Associates of Prescocotte," *http://www.prescotteyedoctor.com/eye-library*, 2012.

[7]   A. Ram, and S. Rashmi, "Aqueous outflow in Schlemm's canal," *Applied Mathematics and Computation,* vol. 174, no. 1, pp. 316-328, 2006.

[8]   "Open Angle Glaucoma & Angle Closure Glaucoma," *http://www.vision-and-eye-health.com/glaucoma-types.html*, 2012.

[9]   "Progression of Glaucoma Symptoms as Seen Through the Eyes of the Patient," *http://www.ahaf.org/glaucoma/about/understanding/progression-of-glaucoma.html*, 2012.

[10]   "Glaucoma," *http://en.wikipedia.org/wiki/Glaucoma*, 2012.

[11]   P. Jaret, "A New Understanding of Glaucoma," *New York Times*, 2009.

[12]   "Glaucoma Filtration Surgery," *http://eyecareamerica.org/eyecare/treatment/glaucoma-filtration/*, 2012.

[13]   "FItration Surgery (Trabeculectomy)," *http://health.nytimes.com/health/guides/disease/glaucoma/surgery.html* 2012.

[14]   G. M. Michel, "Five steps Canaloplasty Success," *Ochsner Clinic Foundation, http://www.youtube.com/watch?v=8QC3RcS9pOY*, 2011.

[15]   "Surgical treatment of glaucoma," *http://www.ophthalmotext.com/surgical-treatment-of-glaucoma-what-is-surgical-treatment-of-glaucoma/*, 2012.

[16]   C. Crotti, "Chirurgie du segment antérieur de l'oeil et traitement du glaucome assistés par laser femtoseconde et imagerie de tomographie par cohérence optique," Laboratoire d'Optique Appliquée - ENSTA ParisTech - École polytechnique – CNRS UMR 7639, l'École Polytechnique, l'École Polytechnique, 2011.

[17]   J. B. Wise, *Lasers in Ophthamology, Chapter 24,* : McGraw-Hill 2003.

[18]   S. Melamed, G. J. Ben Simon, and H. Levkovitch-Verbin, "Selective laser trabeculoplasty as primary treatment for open-angle glaucoma: a prospective, nonrandomized pilot study," *Arch. Ophthalmology,* vol. 21, no. 7, pp. 957-960, 2003.

[19]   F. S. Roger, "Bringing a Versatile Tool To the Anterior Segment Surgeon," *http://www.ophthalmologymanagement.com/articleviewer.aspx?articleid=100597*, 2012.

[20]   L. Artur, and G. A. Xavier, Gual, "Understanding Trabecular Meshwork Physiology: A Key to the Control of Intraocular Pressure?," *Physiology,* vol. 18, no. 5, pp. 205-209, 2003.

[21]   H.-J. Merté, "Genesis of glaucoma," *Wessely Symposium, Munich,* vol. 16, pp. 61-66, 1974.

[22]   D. Huang, E. A. Swanson, C. P. Lin *et al.*, "Optical coherence tomography," *Science,* vol. 254, no. 5035, pp. 1178-1181, 1991.

[23] D. Sampson. "Introduction to Optical Coherence Tomography, Optical+Biomedical Engineering Laboratory, OBEL, University of Western Australia, http://obel.ee.uwa.edu.au/research/oct/intro."

[24] T. L. Szabo, "Diagnostic Ultrasounf Imaging: Inside Out," *Elsevier*, 2004.

[25] W. R. Hedrick, D. L. Hykes, and D. E. Starchman, *Ultrasound Physics and Instrumentation,* , 2005.

[26] J. Fujimoto, and W. Drexler, *Optical Coherence Tomography: Technology and Apllications,* : Springer Berlin Heidelberg, 2008.

[27] J. G. Fujimoto, "Optical coherence tomography for ultrahigh resolution in vivo imaging," *Nat. Biotechnol.,* vol. 21, pp. 1361 - 1367 31 October 2003, 2003.

[28] K. Wiesauer, M. Pircher, E. Götzinger *et al.*, "En-face scanning optical coherence tomography with ultra-high resolution for material investigation," *Opt. Express,* vol. 13, pp. 1015-1024, 2005.

[29] E. A. Swanson, J. A. Izatt, M. R. Hee *et al.*, "In vivo retinal imaging by optical coherence tomography," *Opt. Lett.,* vol. 18, no. 21, pp. 1864-1866, 1993.

[30] M. Wojtkowski, R. Leitgeb, A. Kowalczyk *et al.*, "In-vivo human retinal imaging by Fourier domain optical coherence tomography," *J. Biomed. Opt.,* vol. 7, pp. 457-463, 2002.

[31] J. A. Izatt, M. R. Hee, E. A. Swanson *et al.*, "Micrometer-scale resolution imaging of the anterior eye in vivo with optical coherence tomography," *Arch. Ophthalmol.,* vol. 112, pp. 1584-1589, 1994.

[32] S. Trefford, and F. Desmond, "Optical Coherence Tomography of the Anterior Segment," *Ocul. Surf.,* vol. 6, pp. 117-127 2008.

[33] K. Takada, I. Yokohama, K. Chida *et al.*, "New measurement system for fault location in optical waveguide devices based on an interferometric technique, ," *Appl. Opt. ,* vol. 26, pp. 1603-1608, 1987.

[34] R. C. Youngquist, S. Carr, and D. E. N. Davies, "Optical coherence-domain reflectometry: a new optical evaluation technique," *Opt. Lett.,* vol. 12, no. 3, pp. 158-160, 1987.

[35] H. H. Gilgen, R. P. Novak, R. P. Salathe *et al.*, "Submillimeter optical reflectometry," *IEEE J. Lightwave Technol. ,* vol. 7, pp. 1225–1233, 1989.

[36] A. F. Fercher, K. Mengedoht, and W. Werner, " Eye-length measurement by interferometry with partially coherent light," *Opt. Lett.,* vol. 13, pp. 1867–1869, 1988.

[37] D. Huang, J. Wang, C. P. Lin *et al.*, " Micron-resolution ranging of cornea and anterior chamber by optical reflectometry," *Lasers Surgery Med.,* vol. 11, pp. 419–425, 1991.

[38] A. M. Rollins, and J. A. Izatt, "Optimal interferometer designs for optical coherence tomography," *Opt. Lett.,* vol. 24, no. 21, pp. 1484-1486, 1999.

[39] W. Drexler, U. Morgner, F. X. Kärtner *et al.*, "In vivo ultrahigh-resolution optical coherence tomography," *Opt. Lett.,* vol. 24, no. 17, pp. 1221-1223, 1999.

[40] !!! INVALID CITATION !!!

[41] W. Drexler, and J. G. Fujimoto, *Optical Coherence Tomography: Technology and Applications,* : Springer, 2008.

[42] F. Lexer, A. F. Fercher, H. Sattmann *et al.*, "Dynamic coherent focus for transversal resolution enhancement of OCT," pp. 85-90, 1998.

[43] A. Vogel, and V. Venugopalan, "Mechanisms of Pulsed Laser Ablation of Biological Tissues," *Chem. Rev. ,* vol. 103, pp. 577-644, 2003.

[44]   A. Fercher, F. , W. Drexler, C. Hitzenberger, K . *et al.*, "Optical coherence tomography—principles and applications," *Rep. Prog. Phys.,* vol. 66 pp. 239–303, 2003.

[45]   R. Leitgeb, C. Hitzenberger, and A. Fercher, "Performance of fourier domain vs. time domain optical coherence tomography," *Opt. Express,* vol. 11, no. 8, pp. 889-894, 2003.

[46]   E. A. Swanson, D. Huang, M. R. Hee *et al.*, "High-speed optical coherence domain reflectometry," *Opt. Lett.,* vol. 17, no. 2, pp. 151-153, 1992.

[47]   A. Rollins, S. Yazdanfar, M. Kulkarni *et al.*, "In vivo video rate optical coherence tomography," *Opt. Express,* vol. 3, no. 6, pp. 219-229, 1998.

[48]   S. Yun, G. Tearney, B. Bouma *et al.*, "High-speed spectral-domain optical coherence tomography at 1.3 μm wavelength," *Opt. Express,* vol. 11, no. 26, pp. 3598-3604, 2003.

[49]   B. Cense, N. Nassif, T. Chen *et al.*, "Ultrahigh-resolution high-speed retinal imaging using spectral-domain optical coherence tomography," *Opt. Express,* vol. 12, no. 11, pp. 2435-2447, 2004.

[50]   R. Huber, M. Wojtkowski, and J. G. Fujimoto, "Fourier Domain Mode Locking (FDML): A new laser operating regime and applications for optical coherence tomography," *Opt. Express,* vol. 14, no. 8, pp. 3225-3237, 2006.

[51]   M. Wojtkowski, V. Srinivasan, J. G. Fujimoto *et al.*, "Three-dimensional Retinal Imaging with High-Speed Ultrahigh-Resolution Optical Coherence Tomography," *Ophthalmology,* vol. 112, no. 10, pp. 1734-1746, 2005

[52]   M. Choma, M. Sarunic, C. Yang *et al.*, "Sensitivity advantage of swept source and Fourier domain optical coherence tomography," *Opt. Express,* vol. 11, no. 18, pp. 2183-2189, 2003.

[53]   N. Nassif, B. Cense, B. Hyle Park *et al.*, "In vivo human retinal imaging by ultrahigh-speed spectral domain optical coherence tomography," *Opt. Lett.,* vol. 29, no. 5, pp. 480-482, 2004.

[54]   M. D. Bayleyegn, H. Makhlouf, C. Crotti *et al.*, "Ultrahigh resolution spectral-domain optical coherence tomography at 1.3 μm using a broadband superluminescent diode light source," *Opt. Comm.,* vol. 285, no. 24, pp. 5564-5569, 2012.

[55]   A. F. Fercher, C. K. Hitzenberger, G. Kamp *et al.*, "Measurements of intraocular distances by backscattering spectral interferometry," *Opt. Comm.,* vol. 117, no. 43-48, 1995.

[56]   E. Wolf, "Three-dimensional structure determination of semi-transparent objects from holographic data," *Optics Communications,* vol. 1, no. 4, pp. 153-156, 1969.

[57]   J. F. de Boer, B. Cense, B. H. Park *et al.*, "Improved signal-to-noise ratio in spectral-domain compared with time-domain optical coherence tomography," *Opt. Lett.,* vol. 28, no. 21, pp. 2067-2069, 2003.

[58]   R. A. Leitgeb, C. K. Hitzenberger, A. F. Fercher *et al.*, "Phase-shifting algorithm to achieve high-speed long-depth-range probing by frequency-domain optical coherence tomography," *Opt. Lett.,* vol. 28, no. 22, pp. 2201-2203, 2003.

[59]   M. Wojtkowski, A. Kowalczyk, R. Leitgeb *et al.*, "Full range complex spectral optical coherence tomography technique in eye imaging," *Opt. Lett.,* vol. 27, no. 16, pp. 1415-1417, 2002.

[60]   Y. Pan, and F. D. L., "Noninvasive imaging of living human skin with dual-wavelength optical coherence tomography in two and three dimensions," *J. Biomed. Opt.Vol.3, pp. 446-455.,* vol. 3, pp. 446-455, 1998.

[61]   D. Sacchet, J. Moreau, P. Georges *et al.*, "Simultaneous dual-band ultra-high resolution full-field optical coherence tomography," *Opt. Express,* vol. 16, no. 24, pp. 19434-19446, 2008.

[62]   I. Hartl, X. D. Li, C. Chudoba *et al.*, "Ultrahigh-resolution optical coherence tomography using continuum generation in an air-silica microstructure optical fiber," *Opt. Lett.,* vol. 26, no. 9, pp. 608-610, 2001.

[63]   T. Ko, D. Adler, J. Fujimoto *et al.*, "Ultrahigh resolution optical coherence tomography imaging with a broadband superluminescent diode light source," *Opt. Express,* vol. 12, no. 10, pp. 2112-2119, 2004.

[64]   M. Wojtkowski, V. Srinivasan, T. Ko *et al.*, "Ultrahigh-resolution, high-speed, Fourier domain optical coherence tomography and methods for dispersion compensation," *Opt. Express,* vol. 12, no. 11, pp. 2404-2422, 2004.

[65]   H. Makhlouf, "Integrated multimodal-spectral fluorescence confocal microscope and spectral-domain optical coherence tomography imaging system for tissue screening," 2011, p. 181.

[66]   R. Leitgeb, W. Drexler, A. Unterhuber *et al.*, "Ultrahigh resolution Fourier domain optical coherence tomography," *Opt. Express,* vol. 12, no. 10, pp. 2156-2165, 2004.

[67]   T. Bajraszewski, M. Wojtkowski, M. Szkulmowski *et al.*, "Improved spectral optical coherence tomography using optical frequency comb," *Opt. Express,* vol. 16, no. 6, pp. 4163-4176, 2008.

[68]   G. Häusler, and M. W. Lindner, ""Coherence Radar" and "Spectral Radar"—New Tools for Dermatological Diagnosis," *J. Biomed. Opt.,* vol. 3, pp. 21-31, 1998.

[69]   M. Wojtkowski, R. Leitgeb, A. Kowalczyk *et al.*, "In-vivo human retinal imaging by Fourier domain optical coherence tomography," *J. Biomed. Opt. ,* vol. 7, pp. 457-463, 2002.

[70]   K. Wang, Z. Ding, T. Wu *et al.*, "Development of a non-uniform discrete Fourier transform based high speed spectral domain optical coherence tomography system," *Opt. Express,* vol. 17, no. 14, pp. 12121-12131, 2009.

[71]   Z. Wang, Z. Yuan, H. Wang *et al.*, "Increasing the imaging depth of spectral-domain OCT by using interpixel shift technique," *Opt. Express,* vol. 14, no. 16, pp. 7014-7023, 2006.

[72]   Z. Hu, and A. M. Rollins, "Fourier domain optical coherence tomography with a linear-in-wavenumber spectrometer," *Opt. Lett.,* vol. 32, no. 24, pp. 3525-3527, 2007.

[73]   G. Popescu, and A. Dogariu, "Ballistic Attenuation of Low-Coherence Optical Fields," *Appl. Opt.,* vol. 39, no. 25, pp. 4469-4472, 2000.

[74]   Thorlabs, "OCS1300SS Swept Source OCT System: User Guide," 2011.

[75]   R. Avtar, and R. Srivastava, "Aqueous outflow in Schlemm's canal," *Applied Mathematics and Computation,* vol. 174, no. 1, pp. 316-328, 2006.

[76]   R. S. Figueiredo, S. V. Araujo, E. J. Cohen *et al.*, "Management of coexisting corneal disease and glaucoma by combined penetrating keratoplasty and trabeculectomy with mitomycin-C," *Ophthalmic Surgery and Lasers,* vol. 27, no. 11, pp. 903-909, 1996.

[77]   F. Bigar, and R. Witmer, "Corneal endothelial changes in primary acute angle-closure glaucoma," *Ophthalmology,* vol. 89, no. 6, pp. 596-599, 1982.

[78]   G. O. Waring, M. M. Rodrigues, and P. R. Laibson, "Corneal dystrophies. II. Endothelial dystrophies," *Surv Ophthalmol.,* vol. 23, no. 3, pp. 147-68, 1978

[79]   J. Ytteborg, and C. Dohkman, "Corneal Edema and Intraocular Pressure: Animal Experiments," *Arch Ophthalmol.,* vol. 74, no. 3, pp. 375-381, 1965.

[80]   W. S. Vanmeter, W. B. Lee, and D. G. Katz, "Corneal Edema (Chapter 16A), Duane's Clinical Ophthalmology," Lippincott Williams and Wilkins 2006.

[81]   Wikipedia, "Spectral absorption of water," *http://en.wikipedia.org/wiki/File:Water_absorption.png*, 2012.

[82] D. A. Peyrot, F. Aptel, C. Crotti *et al.*, "Effect of Incident Light Wavelength and Corneal Edema on Light Scattering and Penetration: Laboratory Study of Human Corneas," *Journal of Refractive Surgery,* vol. 26, no. 10, 2010.

[83] F. Deloison, "Greffe de cornée automatisée assistée par laser femtoseconde optimisé en longueur d'onde, PhD thesis," Laboratoire d'Optique Appliquée, ENSTA ParisTech - École Polytechnique, http://pastel.archives-ouvertes.fr/docs/00/57/72/21/PDF/thA_se_Florent_Deloison.pdf, 2010.

[84] M. D. Bayleyegn, H. Makhlouf, C. Crotti *et al.*, "Guiding glaucoma laser surgery using Fourier-domain optical coherence tomography at 1.3 μm," *Proc. SPIE 8427*, 2012.

[85] M. H. Niemz, *Laser-Tissue Interactions: Fundamentals and Applications, chapter 3*, 3rd ed., Berlin: Springer, 2007.

[86] A. Vogel, "Nonlinear absorption: intraocular microsurgery and laser lithotripsy," *Phys Med Biol.,* vol. 42, no. 5, 1997.

[87] Y. Liu, H. Nakamura, T. E. Witt *et al.*, "Femtosecond Laser Photodisruption of Porcine Anterior Chamber Angle: An Ex Vivo Study," *Ophthalmic surgery, lasers & imaging,* vol. 39, no. 6, 2008.

[88] A. Heisterkamp, T. Ripken, H. Lubatschowski *et al.*, "Intrastromal cutting effects in rabbit cornea using femtosecond laser pulses," *Proc. SPIE,* vol. 4161, 2000.

[89] F. Williams, S. P. Varma, and S. Hillenius, "Liquid water as a lone-pair amorphous semiconductor," *The Jounal of Chemical Physics,* vol. 64, no. 4, pp. 1549-54 1976.

[90] J. Neev, "Ultrashort-pulse lasers: a new tool for biomedical applications," *Proc. SPIE,* vol. 3255, pp. 2-7, 1998.

[91] V. Nuzzo, K. Plamann, and M. Savoldelli, "In situ monitoring of second-harmonic generation in human corneas to compensate for femtosecond laser pulse attenuation in keratoplasty," J. Biomed. Opt., 12(6), 064032 (2007)." *J. Biomed. Opt.,* vol. 12, no. 6, 2007.

[92] M. Bellis, "History of the Microscope," *http://inventors.about.com/od/mstartinventions/a/microscope.htm*, 2012.

[93] G. E. Pierard, "In vivo confocal microscopy: a new paradigm in dermatology," *Dermatology,* vol. 186, no. 4, 1993.

[94] C. Dunsby, and P. M. W. French, "Techniques for depth-resolved imaging through turbid media including coherence-gated imaging," *J. Phys. D: Appl. Phys.,* vol. 36, no. 14, 2003.

[95] H. Key, E. R. Davies, P. C. Jackson *et al.*, "Optical attenuation characteristics of breast tissues at visible and near-infrared wavelengths," *Phys. Med. Biol. ,* vol. 36, 1991.

[96] W. F. Cheong, S. A. Prahl, and A. J. Welch, "A review of the optical properties of biological tissues," *Quantum Electronics, IEEE Journal of,* vol. 26, no. 12, pp. 2166-2185, 1990.

[97] M. R. Hee, J. A. Izatt, J. M. Jacobson *et al.*, "Femtosecond transillumination optical coherence tomography," *Opt. Lett.,* vol. 18, no. 12, pp. 950-952, 1993.

[98] Hamamatsu, "Guide to streak cameras," *http://sales.hamamatsu.com/assets/pdf/catsandguides/e_streakh.pdf*.

[99] Hamamatsu, "High-speed gated image intensifier units," *http://sales.hamamatsu.com/assets/pdf/parts_misc/Bildverstaerker.pdf*.

[100] J. G. Fujimoto, S. De Silvestri, E. P. Ippen *et al.*, "Femtosecond optical ranging in biological systems," *Opt. Lett.,* vol. 11, no. 3, pp. 150-152, 1986.

[101]   K. M. Yoo, Q. Xing, and R. R. Alfano, "Imaging objects hidden in highly scattering media using femtosecond second-harmonic-generation cross-correlation time gating," *Opt. Lett.,* vol. 16, no. 13, pp. 1019-1021, 1991.

[102]   M. D. Duncan, R. Mahon, L. L. Tankersley *et al.*, "Time-gated imaging through scattering media using stimulated Raman amplification," *Opt. Lett.,* vol. 16, no. 23, pp. 1868-1870, 1991.

[103]   J. A. Moon, R. Mahon, M. D. Duncan *et al.*, "Three-dimensional reflective image reconstruction through a scattering medium based on time-gated Raman amplification," *Opt. Lett.,* vol. 19, no. 16, pp. 1234-1236, 1994.

[104]   G. E. Anderson, F. Liu, and R. R. Alfano, "Microscope imaging through highly scattering media," *Opt. Lett.,* vol. 19, no. 13, pp. 981-983, 1994.

[105]   C. Doulé, T. Lépine, P. Georges *et al.*, "Video rate depth-resolved two-dimensional imaging through turbid media by femtosecond parametric amplification," *Opt. Lett.,* vol. 25, no. 5, pp. 353-355, 2000.

[106]   G. Le Tolguenec, F. Devaux, and E. Lantz, "Two-dimensional time-resolved direct imaging through thick biological tissues: a new step toward noninvasive medical imaging," *Opt. Lett.,* vol. 24, no. 15, pp. 1047-1049, 1999.

[107]   G. Le Tolguenec, E. Lantz, and F. Devaux, "Imaging through scattering media by parametric amplification of images: study of the resolution and the signal-to-noise ratio," *Appl. Opt.,* vol. 36, no. 31, pp. 8292-8297, 1997.

[108]   M. A. Duguay, and J. W. Hansen, "An ultrafast light gate," *Applied Physics Letters,* vol. 15, no. 6, pp. 192-194, 1969.

[109]   L. Wang, P. P. Ho, X. Liang *et al.*, "Kerr-Fourier imaging of hidden objects in thick turbid media," *Opt. Lett.,* vol. 18, no. 3, pp. 241-243, 1993.

[110]   M. Rajadhyaksha, R. R. Anderson, and R. H. Webb, "Video-Rate Confocal Scanning Laser Microscope for Imaging Human Tissues In Vivo," *Appl. Opt.,* vol. 38, no. 10, pp. 2105-2115, 1999.

[111]   W. Denk, J. H. Strickler, and W. W. Webb, "2-Photon laser scanning fluorescence microscopy " *Science* vol. 248, pp. 73, 1990

[112]   M. Schrader, K. Bahlmann, and S. W. Hell, "Three-photon-excitation microscopy: theory, experiment and applications," *Optik,* vol. 104, pp. 116, 1997.

[113]   B. Hoeling, A. Fernandez, R. Haskell *et al.*, "An optical coherence microscope for 3-dimensional imaging in developmental biology," *Opt. Express,* vol. 6, no. 7, pp. 136-146, 2000.

Optical coherence tomography for monitoring the glaucoma laser surgery

The ability of optical coherence tomography (OCT) to deliver tomographic images of biological tissues *in vivo* non-invasively and in real-time has been a growing interest in many biomedical applications, mainly in ophthalmology for imaging the retina and the anterior segment of the eye. However, developing high-resolution OCT for imaging strongly scattering biological tissues like sclera and edematous cornea has still been the main challenge. In this PhD work, an ultrahigh-resolution ($< 4\,\mu$m) Fourier-domain OCT (FD-OCT) system optimized at $1.3\,\mu$m center wavelength was developed in Laboratoire Charles Fabry – Institut d'Optique *Graduate School*. Using this OCT system, we have, for the first time, properly visualized the Schlemm's canal of the human eye that is located in the strongly scattering corneal limbus at depth of ~ 0.8 mm. Schlemm's canal has been our target for OCT imaging because it plays an important role for the management of the aqueous humor that is responsible for causing glaucoma - an eye disease that can potentially lead to blindness. In collaboration with Laboratoire d'Optique Appliquée at ENSTA ParisTech, we have also demonstrated real-time OCT imaging of the femtosecond laser surgery in excised human cornea. These studies have thus shown that the surgery of glaucoma by femtosecond laser, monitored by OCT, would be possible.

Key words: Optical coherence tomography (OCT), ophthalmology, glaucoma, femtosecond laser, laser surgery.

Tomographie par cohérence optique pour la chirurgie laser du Glaucome

La capacité de la tomographie par cohérence optique (OCT) à délivrer des images tomographiques de tissus biologiques *in vivo*, de manière non invasive et en temps réel, a suscité un intérêt croissant pour de nombreuses applications biomédicales, principalement en ophtalmologie pour l'imagerie de la rétine et du segment antérieur de l'œil. Toutefois, pour l'imagerie à haute résolution de tissus biologiques fortement diffusants, comme la sclérotique et la cornée œdémateuse, la technique nécessitait des améliorations technologiques. Dans cette thèse, un système d'OCT « Fourier-domain » (FD-OCT) à très haute résolution spatiale ($< 4\,\mu$m), à la longueur d'onde de 1,3 µm, a été développé dans la Laboratoire Charles Fabry – Institute d'Optique *Graduate School*. Avec ce système original, nous avons réussi, pour la première fois, à visualiser correctement le canal de Schlemm de l'œil humain qui se trouve à une profondeur d'environ 0,8 mm dans le limbe de la cornée, milieu fortement diffusant. L'imagerie du canal de Schlemm est capitale afin d'envisager la chirurgie par laser du glaucome, qui consiste à inciser cette partie de l'œil afin d'améliorer l'écoulement de l'humeur aqueuse. Par ailleurs, en collaboration avec le Laboratoire d'Optique Appliquée de l'ENSTA ParisTech, nous avons démontré la possibilité de contrôler en temps réel par OCT des découpes par laser femtoseconde pratiquées dans la cornée humaine *in vitro*. Ces travaux ont montré que l'opération du Glaucome par laser femtoseconde, contrôlée par OCT, devrait être possible.

Mots clés : Tomographie par cohérence optique (OCT), ophtalmologie, glaucome, laser femtoseconde, chirurgie laser.